



THE HONG KONG
POLYTECHNIC UNIVERSITY

香港理工大學

Pao Yue-kong Library

包玉剛圖書館

Copyright Undertaking

This thesis is protected by copyright, with all rights reserved.

By reading and using the thesis, the reader understands and agrees to the following terms:

1. The reader will abide by the rules and legal ordinances governing copyright regarding the use of the thesis.
2. The reader will use the thesis for the purpose of research or private study only and not for distribution or further reproduction or any other purpose.
3. The reader agrees to indemnify and hold the University harmless from and against any loss, damage, cost, liability or expenses arising from copyright infringement or unauthorized usage.

IMPORTANT

If you have reasons to believe that any materials in this thesis are deemed not suitable to be distributed in this form, or a copyright owner having difficulty with the material being included in our database, please contact lbsys@polyu.edu.hk providing details. The Library will look into your claim and consider taking remedial action upon receipt of the written requests.

**A FACILE ELECTROCHEMICAL
METHOD TO SYNTHESIZE NICKEL
COMPOSITES FOR HIGH-
PERFORMANCE ENERGY STORAGE**

LIU Yan

Ph.D

The Hong Kong Polytechnic University

2017

The Hong Kong Polytechnic University

Department of Applied Physics

**A Facile Electrochemical Method to Synthesize
Nickel Composites for High-Performance Energy
Storage**

LIU Yan

A thesis submitted in partial fulfillment of the requirements for
the degree of Doctor of Philosophy

June 2016

CERTIFICATE OF ORIGINALITY

I hereby declare that this thesis is my own work and that, to the best of my knowledge and belief, it reproduces no material previously published or written, nor material that has been accepted for the award of any other degree or diploma, except where due acknowledgement has been made in the text.

(Signed)

LIU Yan

(Name of student)



Abstract

Nickel-based compounds have drawn much attention as promising electrode materials for high performance supercapacitor. Currently, many fabrication methods including chemical precipitation, hydrothermal synthesis, sol-gel, thermal oxidation and electrochemical deposition have been used to produce various kinds of nickel-based nanostructures. However, these ways more or less suffers from some problems, such as the mixture of the nickel-based materials with binder and conducting agent, the relatively weak adhesion between the nickel-based materials and the current collector. Nevertheless, synthesizing nickel-based composites with high electrochemical performance utilizing a simple method still faces significant challenges.

In this thesis, an anodization method in an organic electrolyte to synthesize porous layered nickel-based composite electrode for supercapacitor is demonstrated. These organic electrolytes provide slow diffusion and transfer rates of ions which contribute to the formation of the homogeneous oxide layer. Simultaneously, the absence of water in the electrolyte improves the rate performance of the nickel composite electrode. Additionally, due to the direct growth of nickel-based composite on the substrate, the contact resistance between the active materials and the substrate is reduced. As a result, the hierarchical porous $\text{Ni}(\text{OH})_2/\text{Ni}_2\text{O}_3$ electrode shows a high specific capacitance of 3280 F g^{-1} at 1 A g^{-1} . After 5,000 charge/discharge cycles, the as-prepared material remains 95.6% of the initial capacitance. By this fine controlled



one-step and low cost electrochemical process without the need for hard/soft template, the hierarchical porous nickel composite shows good capacity. The strategy used here provides an easy and effective method to achieve excellent performance for supercapacitor materials.

In order to further enhance the intrinsic conductivity of nickel-based composite based on a simple preparation method, we exploit the cathodic deposition. Cathodic deposition is a simple, cost-effective and easily scaled-up method to deposit active materials on many complex substrates. Normally the deposited materials come from electrolytes. Herein, we develop a novel electrodeposition method in a source-free electrolyte. Dendritic Ni@NiO core@shell electrode (DNE) is successfully fabricated by electrodeposition in a Ni-free electrolyte, with the Ni anode providing Ni ions through dissolution and diffusion. The as-prepared DNE demonstrates a high specific capacitance of 1930 F g^{-1} and a high areal capacitance of 1.35 F cm^{-2} , with super-long cycle stability. Owing to the newly formed electrochemically active NiO and Ni(OH)₂ during the cycling test, the gravimetric capacitance of DNE hardly shows any decay after 70,000 cycles at a scan rate of 100 mV s^{-1} . It is also demonstrated that our method is universal to deposit dendritic Ni-compound on many other types of substrates, versatile for different applications.

It is also noted that the fabrication process for supercapacitor electrode is always one-side, that is, either anodization or cathodic deposition. One-step process has been developed to produce two kinds of nickel composites by the simultaneous occurrence



of anodization and cathodic deposition. The porous anodic film electrode and dendritic structure cathodic film electrode yield high areal capacitance of 3.25 and 2.02 F cm⁻² at a scan rate of 5 mV s⁻¹, respectively. Moreover, the cathodic film electrode presents long cycling stability. Due to the continuous formation of electrochemically active no during the cycling process, the areal capacitance of the cathodic film electrode keeps very steady and almost exhibits no decay after 10,000 cycles. Furthermore, the anodic and cathodic films are directly contacted with current collector, therefore, it is avoided to use conducting agents or binders, which increases the effective active materials and facilitates the electrode preparation process.

Finally, on the base of studies of single metal nickel-based composite, the introduction of extra cobalt to improve electrochemical performance is investigated. Hierarchical Ni-Co@Ni-Co layered double hydroxide (Ni-Co@Ni-Co LDH) nanotube arrays (NTAs) are fabricated on carbon fiber cloth (CFC) by template-assisted electrodeposition for high-performance supercapacitors. The synthesized Ni-Co@Ni-Co LDH NTAs/CFC (Ni:Co=1:1) shows high capacitance of 2385 F g⁻¹ at a current density of 5 A g⁻¹, while 98.8% of its initial capacitance is retained after 5,000 cycles. When the current density increases from 2 to 20 A g⁻¹, the capacitance loss is less than 20%, demonstrating an excellent rate capability. A highly flexible all-solid-state asymmetric supercapacitor is successfully fabricated with Ni-Co@Ni-Co LDH NTAs/CFC as the positive electrode and electrospun carbon fibers/CFC as the negative electrode, showing a maximum specific capacitance of 319 F g⁻¹, a high energy density of 100 W h kg⁻¹ at 1.5 kW kg⁻¹, and good cycling stability (98.6% after



3,000 cycles). These fascinating electrochemical properties result from the novel structure of electrode materials and synergistic contributions from the two electrodes, showing great potential for energy storage applications. The material structure design can be hopeful for fabricating supercapacitors with excellent performance.



List of Publications

1. **Yan Liu**, Nianqing Fu, Guoge Zhang, Wei Lu, Limin Zhou and Haitao Huang*. Ni@NiO Core/Shell Dendrites for Ultra-Long Cycle Life Electrochemical Energy Storage. *Journal of Materials Chemistry A*, **2016**, 4, 15049-15056.
2. **Yan Liu**, Nianqing Fu, Guoge Zhang, Ming Xu, Wei Lu, Limin Zhou and Haitao Huang*. Design of Hierarchical Ni-Co@Ni-Co Layered Double Hydroxide Core-Shell Structured Nanotube Array for High-Performance Flexible All-Solid-State Battery-type Supercapacitors. *Advanced Functional Materials*, 2016. DOI: 10.1002/adfm.201605307.
3. Shuijing Lei, **Yan Liu**, Linfeng Fei, Ruobing Song, Wei Lu, Chee Leun Mark, Yu Wang and Haitao Huang*. Commercial Dacron Cloth Supported Cu(OH)₂ Nanobelt Arrays for Wearable Supercapacitors. *Journal of Materials Chemistry A*, **2016**, 4, 14781-14788.
4. Guoge Zhang, Lan Wang, **Yan Liu**, Wenfeng Li, Fei Yu, Wei Lu and Haitao Huang*. Cracks Bring Robustness: a Pre-Cracked NiO Nanosponge Electrode with Greatly Enhanced Cycle Stability and Rate Performance. *Nanoscale*, **2016**, 8, 11256-11263.



5. Luoyuan Wang, Guoge Zhang, **Yan Liu**, Wenfang Li, Wei Lu and Haitao Huang*. Facile Synthesis of a Mechanically Robust and Highly Porous NiO Film with Excellent Electrocatalytic Activity towards Methanol Oxidation. *Journal of Materials Chemistry A*, **2016**, 4, 8211-8218.
6. Nianqing Fu, Chun Huang, **Yan Liu**, Xing Li, Wei Lu, Limin Zhou, Feng Peng, Yanchun Liu and Haitao Huang*. Organic-Free Anatase TiO₂ Paste for Efficient Plastic Dye-Sensitized Solar Cells and Low Temperature Processed Perovskite Solar Cells. *ACS Applied Materials and Interfaces*, **2015**, 7, 19431-19438.
7. Nianqing Fu, **Yan Liu**, Yanchun Liu, Wei Lu, Limin Zhou, Feng Peng and Haitao Huang*. Facile Preparation of Hierarchical TiO₂ Nanowire-Nanoparticle/Nanotube Architecture for Highly Efficient Dye-Sensitized Solar Cells. *Journal of Materials Chemistry A*, **2015**, 3, 20366-20374.
8. Yizhu Xie, **Yan Liu**, Yuda Zhao, Yuenhong Tsang, Shuping Lau, Haitao Huang and Yang Chai*. Stretchable All-Solid-State Supercapacitor with Wavy Shaped Polyaniline/Graphene Electrode. *Journal of Materials Chemistry A*, **2014**, 24, 9142-9149.



Acknowledgments

Time flies as fast as fleeting and three years' Ph.D candidacy is coming to an end. That worked well for about three years. Some people are always there to help whatever happened. I would like to take this opportunity to express my sincere gratitude to them for their full help and strong supports.

First, I would like to express my most sincere gratitude, to my supervisor, Dr. Haitao Huang, for giving me the opportunity to pursue my research work in a fascinating field, and providing me invaluable guidance throughout my three years of studies in Hong Kong Polytechnic University. He always makes tireless and selfless efforts in improvement of my academic ability. His administration provides us a dynamic and free atmosphere to conduct our research work. More importantly, his support for overseas conference gave me great opportunities to connect with the top scientists and researchers around world. Besides, his kind and patient personality also unconsciously affects me to make a better person in later life. I would also like to thank my co-supervisor, Prof. Limin Zhou for his academic advising and help during my Ph.D study.

I would like to express my thanks to my group mates, Dr. Nianqing Fu, Dr. Tao Li, Dr. Shanming Ke, Dr. Biaolin Peng, Dr. Ming Guo, Dr. Xiaolin Liu, Dr. Chun Huang, Mr. Xing Li, Ms. Shu Zhu, Ms. Ying Wang and Ms. Sinyi Pang, for their useful help and discussion in experiments. Many thanks go to my colleagues, Dr. Wei Lu, Mr.



Man Hon Wong, and Ms. Ruobing Song, Ms. Jing Hu and the entire department for their consistent support. I would also like to express my sincere appreciation to Dr. Guoge Zhang in South China University of Technology with his guidance and help.

I would like to acknowledge The Hong Kong Polytechnic University, Department of Applied Physics, and Materials Research Center for the research support during my Ph.D study period. I appreciate the assistance from all the technicians in laboratories.

Finally, I am particularly grateful to my parents for their understanding, selfless loves, and giving without any expectation of return.



Table of Contents

Abstract	I
List of Publications	V
Acknowledgments	VII
Table of Contents	IX
List of Figures	XII
List of Tables	XXIII
Chapter 1 Introduction	1
1.1 Background	1
1.2 Objectives and scope of research	5
1.3 Synopsis of thesis	9
Chapter 2 Literature Review of Nickel-Based Composites for Supercapacitor	
Electrodes	12
2.1 Supercapacitor: energy storage device	12
2.1.1 Energy storage mechanism.....	14
2.1.2 Supercapacitor electrode materials	26
2.2 Approaches for synthesizing nickel-based composites as supercapacitor electrode	34
2.2.1 Hydrothermal method	35
2.2.2 Chemical bath precipitation	36
2.2.3 Electrochemical synthesis	36
2.3 Anodization for nickel-based composite as supercapacitor electrode.....	43
2.3.1 Basics of anodization process.....	43
2.3.2 Influences of processing parameters—aqueous and non-aqueous electrolyte.....	46
2.3.3 Structure and properties of anodized oxide film	52
2.4 Cathodic deposition for nickel-based composite as supercapacitor electrode	56



2.4.1 Synthesis	56
2.4.2 Formation mechanism of structured cathodic deposits.....	58
2.4.3 Specific advantages of cathodic deposition	67
2.5 Summary.....	70
Chapter 3 Experimental Methods	71
3.1 Electrochemical synthesis of nickel-based composites.....	71
3.1.1 Anodization of nickel foil in organic electrolytes with different water contents	71
3.1.2 Cathodic deposition of nickel-based composite in nickel-free organic electrolyte.....	72
3.1.3 Anodization of nickel foil and cathodic deposition of nickel-based composite in a bath with nickel-free organic electrolyte.....	73
3.1.4 Design of the Ni-Co@Ni-Co layered double hydroxide nanotube arrays and the assembly of the device	73
3.2 Characterization and analysis of nickel-based composites.....	77
3.2.1 Structural and elemental characterizations.....	77
3.2.2 Electrochemical characterizations	78
3.2.3 Flexible device test	79
Chapter 4 Porous Layered Nickel-Based Composite by Anodization in Organic Electrolyte for Supercapacitor	82
4.1 Motivation.....	82
4.2 Structural and elemental characterizations	83
4.3 Electrochemical characterizations.....	86
4.3.1 Characterization of layered nickel-based composite	86
4.3.2 Role of deionized water in electrochemical performance	94
4.3.3 Influence of reaction time on film thickness.....	95
4.5 Summary.....	96
Chapter 5 Ni@NiO Core/Shell Dendrites by Nickel-Free Cathodic Deposition for Ultra-long Cyclic Life Supercapacitor	97
5.1 Motivation.....	97
5.2 Structural and elemental characterizations	98
5.3 Electrochemical characterizations.....	106
5.4 Crystal growth mechanism of dendritic structure	114
5.5 Summary.....	122



Chapter 6 Nickel-Based Nanosheets and Dendrites in Nickel-Free Organic Electrolyte for High-Capacitance and Long-Life Supercapacitor.....	124
6.1 Motivation.....	124
6.2 Optimization of applied voltage.....	125
6.3 Structural and elemental characterizations	126
6.4 Electrochemical characterizations of anodic and cathodic films.....	131
6.5 Summary.....	136
Chapter 7 Design of Hierarchical Ni-Co@Ni-Co Layered Double Hydroxide Core-Shell Structured Nanotube Array for High-Performance Flexible All-Solid-State Battery-Type Supercapacitors	138
7.1 Motivation.....	138
7.2 Structural and elemental characterizations	141
7.2.1 Positive electrode: Ni-Co@Ni-Co LDH NTAs/CFC	141
7.2.2 Negative electrode: CNFs/CFC.....	155
7.3 Electrochemical characterizations.....	156
7.3.1 Positive electrode: Ni-Co@Ni-Co LDH NTAs/CFC	156
7.3.2 Negative electrode: CNFs/CFC.....	163
7.3.3 Battery-type supercapacitor.....	166
7.4 Relationship between Faradaic reaction active sites and nickel-cobalt composition	172
7.5 Summary.....	175
Chapter 8 Conclusion and Future Outlook.....	176
8.1 Conclusion	176
8.2 Future Recommendations	178
References	183



List of Figures

<i>Figure #</i>	<i>Captions</i>	<i>Page</i>
Figure 1.1	Primary energy consumption by source and sector in 2013.	2
Figure 1.2	The power density as a function of energy density for various energy storage devices.	3
Figure 2.1	(a) Schematic presentations of a supercapacitor device and (b) its potential drop at the electrode/electrolyte interface.	14
Figure 2.2	The types of Faradaic mechanisms giving rise to pseudocapacitance	19
Figure 2.3	The general electrochemical features of pseudocapacitive materials.	20
Figure 2.4	Comparison of the charge–discharge profiles of Ni(OH) ₂ in (a) bulk and (b) nanostructured forms.	22
Figure 2.5	Volumetric and gravimetric specific capacitance of different carbon materials for supercapacitors.	27
Figure 2.6	A schematic diagram of electrochemical synthesis device with two electrodes in a divided mode.	38
Figure 2.7	Pathway of a general electrode reaction.	39
Figure 2.8	(a) Schematic diagram of the growing processes of Co _x Ni _{1-x} hydroxides on NiCo ₂ O ₄ nanowires which has been grown on CFP. (b) SEM images of CFP before (inset) and after the growth of NiCo ₂ O ₄ nanowires. (c) Large magnification of (b). (d) SEM image of Co _x Ni _{1-x} hydroxides on NiCo ₂ O ₄ nanowires grown on CFP. (e) TEM image of Co _x Ni _{1-x} hydroxides on NiCo ₂ O ₄ nanowires grown on CFP.	42
Figure 2.9	Pourbaix diagram of the Ni-H ₂ O system at 25 °C.	46



Figure 2.10	A schematic diagram of the possible steps towards the formation of porous oxide film. Oxide thickness is not drawn to scale.	47
Figure 2.11	(a) Schematic for the fabrication process of 3D nanoporous Ni(OH) ₂ thin film, (b) top and (c) magnified-cross sectional SEM images of anodic nanoporous thin film	50
Figure 2.12	(a) Current-time curve for Ti anodization with and without fluorides in the electrolyte. (b) Corresponding evolution of TiO ₂ morphologies with different current behaviour.	51
Figure 2.13	The general electrochemical reaction scheme at a nickel hydroxide electrode.	54
Figure 2.14	Unit cells of (a) α -Ni(OH) ₂ and (b) β -Ni(OH) ₂ . XRD pattern of α -Ni(OH) ₂ and β -Ni(OH) ₂ (c). Raman spectra of α -Ni(OH) ₂ and β -Ni(OH) ₂ (d). CV curve of nickel oxide electrode in 1 mol L ⁻¹ KOH.	54
Figure 2.15	The schematic of α -Ni(OH) ₂ and β -Ni(OH) ₂ interstratification, in which both phases coexist with a crystal.	55
Figure 2.16	The pH-Eh diagram corresponding to different cathodic deposition equations.	58
Figure 2.17	Scheme of the electrodeposition process on planar electrodes.	60
Figure 2.18	General shape of the transients of time-current curve observed for nickel electrodeposition under most conditions.	61
Figure 2.19	(a) Schematic of the fabrication process of Co ₃ O ₄ @NiCo ₂ O ₄ nanowire arrays. (b) top-view SEM images of Co ₃ O ₄ @NiCo ₂ O ₄ nanowire arrays on Ni foam. (c) The magnification of (b). (d) Cycling performance of	63

- $\text{Co}_3\text{O}_4@\text{NiCo}_2\text{O}_4$ nanowire arrays at various current densities.
- Figure 2.20 (a) Schematic illustration of the synthesis procedure of $\text{MnO}_x/\text{NTNA}/\text{CFP}$. (b) SEM image of NTNA on CFP. (c) Side-view SEM image of $\text{MnO}_x/\text{NTNA}/\text{CFP}$. (d) CV curves of $\text{MnO}_x/\text{NTNA}/\text{CFP}$, MnO_x/CFP , $\text{MnO}_x/\text{TiO}_2/\text{CFP}$, TiO_2/CFP , and NTNA/CFP at a scan rate of 50 mV s^{-1} . (e) The rate capability of $\text{MnO}_x/\text{NTNA}/\text{CFP}$, MnO_x/CFP and $\text{MnO}_x/\text{TiO}_2/\text{CFP}$. (f) Cyclic stability of $\text{MnO}_x/\text{NTNA}/\text{CFP}$ and MnO_x/CFP at a current density of 1 mA cm^{-2} for up to 5000 cycles The inset is CV curves of $\text{MnO}_x/\text{NTNA}/\text{CFP}$ before and after cycling at 50 mV s^{-1} . 64
- Figure 2.21 (a) Scheme for the preparation process of H-Ni@NiO core/shell NH electrodes. (b) FESEM, (c) TEM and (d) HRTEM micrographs of H-Ni@NiO core/shell NH electrodes. 66
- Figure 2.22 Schematic illustration of three-dimension self-supported structure by electrochemical deposit. 67
- Figure 2.23 Illustration of the thesis structures and the following possible approaches for enhancing battery-type supercapacitor performance. 70
- Figure 4.1 Schematic diagramme showing the fabrication process of layered nickel composite thin film. Anodization is done in a two-electrode system in the EG electrolyte. 83
- Figure 4.2 Characterization of the structure: (a) SEM images of $\text{Ni}(\text{OH})_2/\text{Ni}_2\text{O}_3$. (b) TEM characterization of $\text{Ni}(\text{OH})_2/\text{Ni}_2\text{O}_3$. Inset: SAED pattern and high resolution (HRTEM) of the marked area). (c) XRD patterns of $\text{Ni}(\text{OH})_2/\text{Ni}_2\text{O}_3$. (d) Raman spectrum of $\text{Ni}(\text{OH})_2/\text{Ni}_2\text{O}_3$. 84



-
- Figure 4.3 XPS spectra of Ni(OH)₂/Ni₂O₃. (a) Ni 2p and (b) survey. 85
- Figure 4.4 (a) CV curves of Ni(OH)₂/Ni₂O₃ prepared in the electrolyte containing 0.1% NH₄F and 0% water for 4 h. Inset: the relationship between cathodic peak current and square root of scan rate. (b) The variation of specific capacitance with scan rate from 5 to 50 mV s⁻¹. 86
- Figure 4.5 CV curves of the samples prepared for 4 h in the electrolyte containing 0.1% NH₄F and different water contents. (a) 2% water with scan rates from 5 to 50 mV s⁻¹. (b) 3% water with scan rates from 5 to 50 mV s⁻¹. (c) CV curves of the samples prepared in the electrolyte with different water contents at a scan rate of 5 mV s⁻¹. Inset: the variation of specific capacitance with the water content. 88
- Figure 4.6 CV curves of the samples prepared in the electrolyte containing 0.1% NH₄F and no water for different reaction time: (a) 3 h, (b) 5 h, and (c) CV of different samples scanned at 5 mV s⁻¹. Inset: comparison of specific capacitance. 90
- Figure 4.7 CV curves of the sample prepared in the electrolyte containing 0.5% NH₄F and 0% water for 4 h. 91
- Figure 4.8 (a) GCD curves of Ni(OH)₂/Ni₂O₃. Inset: magnified curves. (b) Specific capacitance as a function of current density. (c) EIS plots of Ni(OH)₂/Ni₂O₃ from 0.01 Hz to 100 kHz after 10,000 scans in 1 mol L⁻¹ NaOH. Inset: magnified EIS at high frequency region. (d) Cyclic test of Ni(OH)₂/Ni₂O₃ by CV measurement at a scan rate of 100 mV s⁻¹ in 1 mol L⁻¹ NaOH aqueous solution. The inset shows the initial 2000 cycles. 92



Figure 4.9	Typical transient anodization current in the electrolyte containing 0.1% NH_4F and no water.	95
Figure 5.1	Schematic illustration of the formation of DNE material.	99
Figure 5.2	Surface morphologies of (a) anode and (b) cathode after electro-deposition in EG electrolyte at 40 °C.	100
Figure 5.3	SEM image with (a) top view and (b) cross-sectional view of the microstructure of DNE material.	100
Figure 5.4	Characterizations of the DNE. (a) XRD. (b) Low and (c) high magnification TEM images. (d) HRTEM of the marked area of (c). Red dotted line is a guide to the eye to show roughly the Ni/NiO interface. (e) SAED pattern from (c). (f) and (g) Fourier transformation (FFT) patterns of the marked areas of (d).	102
Figure 5.5	TEM characterizations of DNE materials in different selected areas of the same sample.	103
Figure 5.6	The element Ni (a) and O (b) mapping of DNE materials. (c) The corresponding EDS. The Cu signal comes from the TEM sample holder.	103
Figure 5.7	(a) Ni 2p XPS on the fresh sample. (b) Depth profile of Ni 2p XPS on DNE from 0 to 290 nm. (c) Variation of O and Ni concentrations as a function of etch depth. (d) Raman spectrum of DNE. (e) Full XPS pattern of DNE material.	105
Figure 5.8	Electrochemical characterizations of DNE. (a) CV curves of the 1 st and the 801 st cycles at a scan rate of 100 mV s^{-1} . (b) CV curves at different scan rates from 5 to 100 mV s^{-1} . (d) Specific capacitance at different scan rates. (e) GCD curves at a current density of 2.9 A g^{-1} (2 mA cm^{-2}). (f) EIS spectra of MNE from 0.01 to 100 kHz in 1 mol L^{-1} NaOH. Inset: magnified EIS in high frequency region.	106



Figure 5.9	(a) BET isothermal of DNE material. (b) The rate capability of the DNE at the different current densities.	109
Figure 5.10	(a) Cyclability test of the DNE at a scan rate of 100 mV s^{-1} . (b) CV curves of DNE at different cycle numbers at the scan rate of 100 mV s^{-1} . (c) Specific capacitance as a function of the scan rate. (d) Coulombic efficiency at different cycling stages.	111
Figure 5.11	(a) Raman spectra of the DNE material at different cycle numbers. (b) SEM image of the DNE material after 70,000 cycles.	112
Figure 5.12	(a) High and low (the inset) magnification TEM images of the DNE material after 70,000 cycles. (b, c) HRTEM image of the marked areas in (a). (d) SEAD pattern. Red dotted line is a guide to the eye to show roughly the boundary between Ni and crystalline NiO.	113
Figure 5.13	(a) The current transient of the cathodic deposition process at different temperatures. (b) The CV curves of samples prepared in different deposition time. (c) CV curves of samples in different electrolytes at a scan rate of 20 mV s^{-1} in different electrolytes, including EG+ NH_4F , water+ NH_4F in which the nickel foil was used as the anode and water+ $\text{NH}_4\text{F} + 0.05 \text{ M Ni}(\text{Ac})_2$ where Pt was used as the anode. (d) The current transient of the cathodic deposition process at $40 \text{ }^\circ\text{C}$ in (a) electrolytes at 20 (red line) and 7 V (black line), respectively.	116
Figure 5.14	SEM images of samples prepared in different electrolytes containing (a) water+ NH_4F in which the nickel foil was	120



- used as the anode and (b) water+ NH_4F +0.05 M $\text{Ni}(\text{Ac})_2$ where Pt was used as the anode.
- Figure 5.15 (a) Cyclic test of samples prepared in different electrolytes containing (1) water+0.1% NH_4F in which nickel anode was the nickel source and (2) water+ 0.1% NH_4F +0.05 M $\text{Ni}(\text{Ac})_2$ where Pt was used as the anode at the scan rate of 100 mV s^{-1} . (b) The CV curves of samples prepared in EG electrolyte containing 0.1% NH_4F with different water contents at the scan rate of 100 mV s^{-1} . 120
- Figure 5.16 (a) Digital pictures of samples prepared in different electrolytes at 40°C , containing EG+ NH_4F (①), EG+ NH_4Cl (②), water+ NH_4Cl (③), and water+ NH_4F (④). The bottles presented electrolyte solutions after cathodic deposition reaction. (b) The current transient of the cathodic deposition process in (a) electrolytes at 40°C . The applied voltages are 60, 30, 7, and 7 V, respectively. 121
- Figure 5.17 The morphology evolution of cathode surface at 40°C after cathodic deposition of (a) 0 min, (b) 0.5 min, (c) 2 min, (d) 5min, (e) 10 min, (f) 20 min,(g) 30 min, and (h, i) 60 min. 122
- Figure 5.18 Surface morphologies of the electro-deposited cathodes at 40°C on (a, b) Fe foil, (c, d) TiO_2 nanotube array, and (e, f) stainless steel net. 123
- Figure 6.1 (a) Digital pictures of samples prepared under an applied voltage from 0 to 70 V. (b) Transient current density recorded under different applied voltages. The inset shows the curves under 20, 30, 40, and 50 V. 126
- Figure 6.2 SEM images of (a) anodic and (b, c) cathodic films. TEM images of (d, e, and f) anodic and (g, h, and i) cathodic films. The insets of (f) and (i) are corresponding SAEDs. 129



Figure 6.3	(a) XRD pattern and (b) Raman spectra of anodic and cathodic films.	129
Figure 6.4	XPS spectra of (a) anodic and (b) cathodic films.	131
Figure 6.5	CV curves of (a) anodic and (b) cathodic films at different scan rates in 1 mol L ⁻¹ NaOH. Insets: linear relationship between cathodic peak current and the square root of scan rate. The variation of areal specific capacitance as a function of scan rate: (c) anodic and (d) cathodic films.	132
Figure 6.6	GCD curves of (a) anodic and (b) cathodic films. Cyclability test of (c) anodic and (d) cathodic films. Insets: the CV curves for cycle 1 and cycle 10,000.	135
Figure 6.7	CV curves of the anodic and cathodic film electrodes at a scan rate of 50 mV s ⁻¹ .	136
Figure 6.8	The variation of capacitance of the anodic and cathodic film electrodes as a function of scan rate.	137
Figure 7.1	A schematic diagram of the preparation procedures of hierarchical Ni-Co@Ni-Co LDH NTAs on CFC.	141
Figure 7.2	(a) Low and (b) high magnification SEM images of carbon nanofibers of the CFC. The inset: the optical image of CFC.	143
Figure 7.3	SEM images of ZnO NRAs grown on CFC by electrodeposition at different current densities: (a) and (b) 0.8 mA cm ⁻² , (c) 0.6 mA cm ⁻² and (d) 1 mA cm ⁻² .	144
Figure 7.4	(a) TEM image of a single ZnO nanorod and (b) HRTEM image taken from the edge of the ZnO nanorod. Inset: Corresponding SAED pattern.	144
Figure 7.5	SEM images of Ni-Co@Ni-Co LDH NRAs on ZnO template, which are electrodeposited by different current density: (a) and (b) 4 mA cm ⁻² , (c) 1 mA cm ⁻² and (d) 6 mA cm ⁻² .	145



Figure 7.6	SEM images. (a) Magnified Ni-Co@Ni-Co LDH NRAs and (b) a single Ni-Co@Ni-Co LDH NR grown on a ZnO NR by electrodeposition. Ni:Co=5:5.	145
Figure 7.7	(a) and (b) SEM images of Ni-Co@Ni-Co LDH NTAs/CFC with different magnifications (Ni:Co=5:5).	146
Figure 7.8	SEM images and the EDX spectra of Ni-Co@Ni-Co LDH NTAs/CFC with different Ni:Co ratios: (a, b) 10:0, (c, d) 7:3, (e, f) 3:7, and (g, h) 0:10.	147
Figure 7.9	Body of the Ni-Co@Ni-Co LDH NTAs (Ni:Co=5:5): (a) TEM image, (b) HRTEM image and SAED pattern (inset) of the selected area in (a), (c) STEM bright field image, and (d-f) elemental mapping of Ni, Co and O.	148
Figure 7.10	Top of the Ni-Co@Ni-Co LDH NTA (Ni:Co=5:5): (a) and (b) TEM image; (c) HRTEM image and (d) SAED pattern of the selected area in (b).	149
Figure 7.11	EDX spectra of (a) the body and (b) the top of the Ni-Co@Ni-Co LDH NTAs (Ni:Co=5:5).	149
Figure 7.12	The BET isothermal of the the Ni-Co@Ni-Co LDH (Ni:Co=5:5) at 77 K. The inset: the Barret-Joyner-Halenda (BJH) pore size distribution	151
Figure 7.13	(a) XRD patterns and (b) Raman spectra of CFC, ZnO and Ni-Co@Ni-Co LDH NTAs/CFC with different Ni:Co ratios.	151
Figure 7.14	(a) Ni 2p XPS, (b) Co 2p XPS, (c) depth profile of Ni 2p XPS, and (d) depth profile of Co 2p XPS of the as-obtained Ni-Co@Ni-Co LDH NTAs/CFC (Ni:Co=5:5). Etching depth is from 0 to 290 nm.	153
Figure 7.15	Variation of O, Co, and Ni concentrations of the Ni-Co@Ni-Co LDH (Ni:Co=5:5) as a function of etching depth.	154



Figure 7.16	CNFs: (a, b, c) TEM images with different magnifications. (d) The SAED pattern of CNFs in a selected area of (b).	156
Figure 7.17	(a) CVs of Ni-Co LDHs/CFC, and CVs of Ni-Co@Ni-Co LDH NTAs/CFC at different scan rates in 1 mol L ⁻¹ NaOH aqueous solution with different Ni:Co ratios: (b) 5:5, (c) 10:0, (d) 7:3, (e) 3:7, and (f) 0:10. Inset of (b): CVs of Ni-Co@Ni-Co LDH NTAs/CFC and Ni-Co LDHs/CFC at a scan rate of 10 mV s ⁻¹ .	157
Figure 7.18	SEM image of Ni-Co@Ni-Co LDHs/CFC.	159
Figure 7.19	CVs of samples of different Ni:Co ratios.	159
Figure 7.20	GCD curves of Ni-Co@Ni-Co LDH NTAs/CFC at different current densities with different Ni:Co ratios: (a) 5:5, (b) 10:0, (c) 7:3, (d) 3:7, and (e) 0:10. (f) GCD curves of samples with different Ni:Co ratios at a current density of 5 A g ⁻¹ .	161
Figure 7.21	(a) Specific capacitance vs. current density. (b) Comparison of the specific capacitance and retention rate. (c) Nyquist plots. Inset: magnified EIS spectra at the high frequency region. (d) Cycling performance at a current density of 5 A g ⁻¹ . The measurement is based on for Ni-Co@Ni-Co LDH NTAs/CFC with different Ni:Co ratios.	163
Figure 7.22	(a) CV curves of CNFs/CFC electrode at different scan rates. (b) GCD curves of CNFs/CFC at different current densities. (c) Specific capacitance of CNFs/CFC electrode at different current densities. (d) Cycling performance of CNFs/CFC electrode at a current density of 5 A g ⁻¹ .	166
Figure 7.23	A schematic illustration for the preparation process of FBSC Ni-Co@Ni-Co LDH NTAs/CFC and CNFs/CFC and the assembly of FBSC device.	167



Figure 7.24	CV curves of (a) Ni-Co@Ni-Co LDH NTAs/CFC and CNFs/CFC electrodes at a scan rate of 10 mV s^{-1} , and (b) an optimized FBSC device in various voltage windows at a scan rate of 100 mV s^{-1} .	168
Figure 7.25	(a) CVs at different scan rates, (b) GCD curves at different current densities, (c) specific capacitance at different current densities, and (d) Cycling performance at a current density of 5 A g^{-1} of an optimized FBSC device.	170
Figure 7.26	(a) CVs of the FBSC device under flat and bending conditions at a scan rate of 100 mV s^{-1} . Inset: digital image of a 90° bended device. (b) Digital image of a LED lit up by two tandem devices. (c) GCD curves of two FBSCs in series and in parallel at a current density of 5 A g^{-1} . A single device is also plotted for comparison. (d) Ragone plot of our device in comparison with those reported ones.	172
Figure 7.27	The relationship between the cathodic peak current and scan rate fitted using the Randles-Sevcik equation for Ni-Co@Ni-Co LDH NTAs/CFC different Ni:Co ratios: (a) 10:0, (b) 7:3, (c) 5:5, (d) 3:7, and (e) 0:10.	175
Figure 8.1	The schematic of interdigitated plate electrodes based on three-dimension architecture.	182



List of Tables

<i>Table</i>	<i>Captions</i>	<i>Page</i>
Table 2.1	Carbon materials for EDLCs reported in recent years.	28
Table 2.2	Summary of recent reports on pseudocapacitive electrode materials.	30
Table 5.1	Comparison of the maximum specific capacitance of some reported nickel-based electrode and the present work.	108
Table 7.1	Elemental distribution of the Ni-Co@Ni-Co LDH NTAs with different Ni:Co ratios.	148
Table 7.2	Comparison of the specific capacitance of the present work with those reported ones based on nickel or cobalt oxide/hydroxide.	164



Chapter 1 Introduction

1.1 Background

As the development of mankind and society, the demand on petroleum, coal and natural gas are kept on increasing. It is believed that these natural resources will eventually dry up. The energy crisis influences not only today's economy and national security, but also the future of the next generations. Significant progress has been made in the development of technologies to harvest renewable energies such as, solar, hydrodynamic, wind, geothermal, biofuels, and tidal energies. One of the main challenges is that the provision of these renewable energies is decentralized, intermittent and strongly depends on the geographic location. The imbalanced regional distribution of these renewable resources is another issue. In this regard, the best possible solution is to transform them into the electricity for energy consumption in the industrial, commercial and residential demands. Figure 1.1 shows the primary energy consumption by source and sector in 2013.^[1] It presents that electricity is of importance in the structure of energy consumption. Thus, the storage of generated electricity with high efficiency is a very important process especially during the off-peak hour of electricity usage. At present, the development of highly efficient, stable and green energy storage technologies is mainly dominated by pumped hydrodynamic power which constitutes 99% of a worldwide storage capacity of 127,000 MW of

discharge power.^[2] In addition, compressed air, flywheel, hydrogen storage, batteries and supercapacitors are also applied in electricity storage. Among them, supercapacitors are emerging as an essential class for advancing the economical use of renewable energies. In general, they possess many desirable features, such as high power and energy storage efficiency, long cycle life, pollution-free operation and almost zero maintenance. Moreover, they can be used as in a variety of applications, including back-up power systems, electric vehicles, hybrid electric vehicles, roll-up displays and wearable devices. Supercapacitors have attracted increasing interest in recent years because of these advantages.

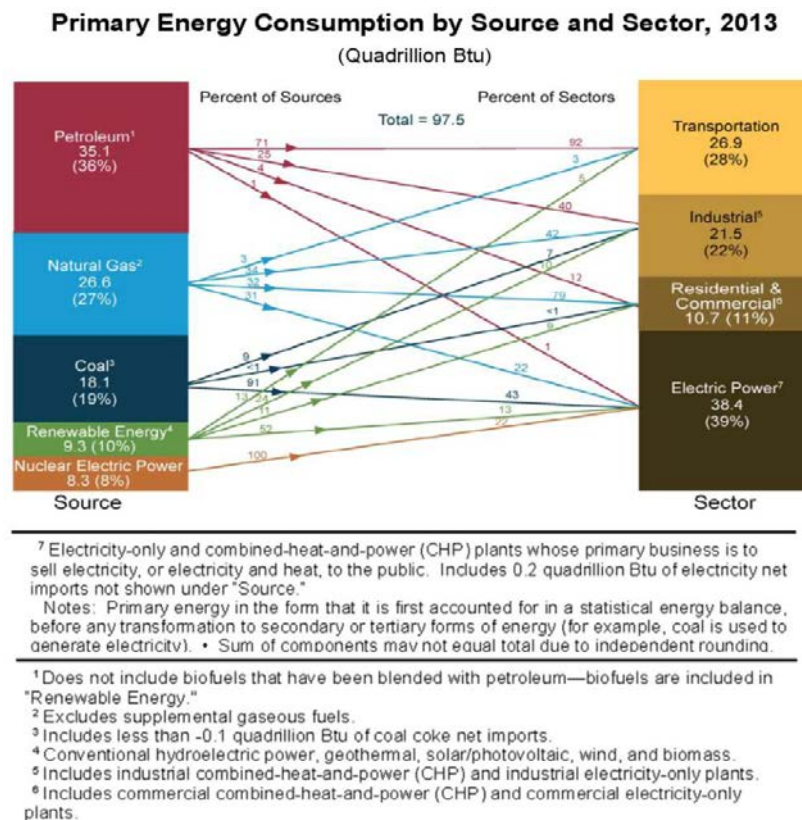


Figure 1.1 Primary energy consumption by source and sector in 2013.^[1]

Supercapacitors, also called electrochemical capacitors, are a kind of electrochemical energy storage devices (EESDs), which can satisfy high power requirement. Unlike batteries, which are able to store more energy, but deliver it slowly, supercapacitors can deliver energy fast and discharge in a short period of time (e.g., several seconds). For example, commercially available carbon-based supercapacitors can supply a power density of more than 40 kW kg^{-1} at an energy density of 10 W h kg^{-1} (Skeleton Tech., SCA4500 type). Due to the above characteristic, supercapacitors can bridge the gap between conventional capacitors and batteries/fuel cells (Figure 1.2). Currently, the energy storage technology of supercapacitors is attractive and plays an important role in complementing batteries in the power quality application, such as alleviating short-term interruptions of a few minutes until a generator or battery can be placed in service.

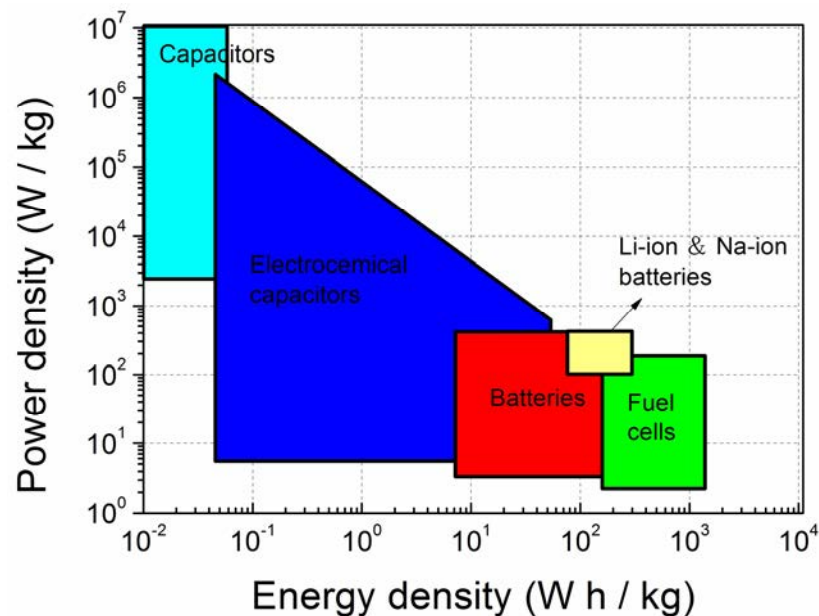


Figure 1.2 The specific power density as a function of energy density for various energy storage devices ^[3].



Supercapacitors are generally classified into electrochemical double layer capacitors (EDLCs) and pseudocapacitors according to their different energy storage mechanisms. EDLCs store energy by reversible ion adsorption from an electrochemical double layer at the electrode-electrolyte interface. Due to non-Faradaically surface charge storage, and fast energy uptake and delivery, EDLCs often have a long cycle life ($>100,000$ cycles) ^[4] and high power density. Typical electrode materials for EDLCs are carbon-based active materials with high surface area, such as activated carbon, carbon nanotube, graphene and so on. These materials often possess ease of processing, relatively inert electrochemistry, controllable porosity and electrochemical active sites for ion adsorption. Due to the limitation of charge storage at the interface between electrolyte and electrode, the capacitance of carbon-based materials is relatively low which results in low energy density. Pseudocapacitors utilize fast and reversible Faradaic reactions at the vicinity of the surface which involves the passage of charges across the double layer, and in the bulk materials with two-dimensional transport pathways to store charges. The most commonly known pseudocapacitor materials are transition metal oxides/hydroxides (e.g. RuO_2 , MnO_2 , Nb_2O_5 , TiO_2 , etc.) and conducting polymers (e.g. polyaniline, polypyrrole and polythiophene). Besides, battery-type supercapacitor electrode materials (Ni(OH)_2 , NiO , Co_3O_4 , etc.) can be also considered (next chapter will discuss). Fast and reversible redox reactions take place at the vicinity of the material surface and in the bulk materials with two-dimensional transport pathways, which allows higher capacitance than EDLCs. However, pseudocapacitors suffer from the drawbacks of a low power density and lack of stability during cycling. The low power density can be



attributed to the poor electric conductivity of materials (e.g. metal oxides/hydroxides), which hinders the electron transfer rate. At the same time, the destruction of structure caused by repeated swelling and shrinking of electrode materials during cyclic charging and discharging raises the issue of the lack of cycling stability. Different strategies have been used to balance the power and energy densities of supercapacitors. One strategy is to prepare composites utilizing carbon-based active material as the backbone to support pseudocapacitor materials with high capacitance. However, the agglomeration of the carbon material makes the decoration of pseudocapacitor materials inhomogeneous. Besides, using nanostructured electrode materials has been demonstrated effectively to solve these problems. The resulting nanomaterials have a number of interesting properties, which are distinct from their bulk counterparts. For example, carefully designed nanostructure can relax the stress due to volume change in the cyclic process, provide many active sites for ion adsorption or charge transfer reactions and shorten ion diffusion length. However, it is not always an easy task to control nanostructured materials for excellent electrochemical performance. There is a long way to develop materials with proper components and nanostructures for excellent energy storage.

1.2 Objectives and scope of research

The ability to quickly charge and discharge electrical energy makes supercapacitors ideal devices for short-term energy storage. Numerous efforts have been conducted to fabricate the electrode material which is the bottleneck of energy storage capability.



Pseudocapacitive materials, such as metal oxides/hydroxides have been demonstrated to be the potential candidates for electrode materials. At present, the most commonly used metal oxides/hydroxides can be classified into two types: noble (RuO_2 , IrO_2) and cheap metal oxides/hydroxides (MnO_2 , TiO_2 , Nb_2O_5 , etc.). Besides, nickel-based compounds have drawn much attention as promising electrode materials for high performance supercapacitor because high theoretical specific capacitance (3750 F g^{-1}), the diversity of morphology and battery-type material feature. However, nickel-based electrode materials for EESDs have the poor cycle performance, high resistivity and low rate capability (capacitance retention at a high scan rate or current density). With an aim to achieve superb electrode performance, it is necessary to improve the electrochemical properties (cycling stability, specific capacitance and rate capability) of nickel-based electrodes. At present, most of researchers try to solve these problems by controlling the structure and composition of nickel-based materials. One strategy is to synthesize nanoparticles by a variety of techniques such as hydrothermal synthesis, chemical bath deposition, sol-gel and so on. Due to various controllable processing parameters, the as-prepared nickel-based materials can exhibit the diversity of the structure and morphology. Those nanoparticles have to be slurry-coated on the current collector in the traditional slurry-coating electrode preparation procedure with the addition of binder and conducting agent, which is time-consuming and complicated. Other strategies include the growth of nickel-based materials directly on the current collector by sputtering and electrochemical methods (e.g., anodization and cathodic deposition). Specifically, electrochemical methods are fast and simple, and there is a potential to accomplish different structured nickel-based materials with a



low cost. However, the relatively poor adhesion between nickel-based materials and the current collector results in the flake-off of active materials and hence short cyclic life. Therefore, to date, it is still a challenge to prepare electrode materials with excellent electrochemical performance towards high capacitance, superior rate capability, and long cyclic stability.

The main objectives of the current research work are:

- To explore and fabricate metal oxides/hydroxides and/or their composites by electrochemical reactions in different electrolytes for improved performance of supercapacitor electrodes.
- To comprehend the influence of organic electrolyte on the morphologies of the materials and their electrochemical performance, and the correlation between morphology and performance.
- To design new structure and components for the electrode materials for supercapacitor application.

Three approaches are proposed to accomplish the above objectives.

First of all, for the preparation techniques, electrochemical methods including anodization and cathodic deposition were employed to deposit the electrode materials directly on the current collector with strong adhesion, which effectively decreases the



contact resistance to provide fast electron transfer between active materials and the current collector.

Secondly, the structure and morphology of nickel-based materials were controlled by tuning the processing parameters. On the one hand, anodization of nickel foil in organic electrolyte was proposed to achieve nickel-based composite with high specific capacitance as well as good cycle life. On the other hand, core/shell structured metal/metal oxides or hydroxide structure was proposed to further enhance the electron transfer, and charge transfer of the electrode. Particularly, Ni@NiO was synthesized by cathodic deposition in nickel-free organic electrolyte. With the knowledge gained from the above work, two types of nickel-base composites with good electrochemical performance are simultaneously accomplished in a single cell. Under fine control of the electrochemical synthesis conditions, hierarchical nickel composite nanosheets and dendritic Ni@NiO core@shell structure were synthesized simultaneously in a single electrochemical cell.

Finally, the composition of the nickel-based material was optimized. Nickel-cobalt bimetal oxides/hydroxides were fabricated as scalable alternatives for supercapacitor electrodes. The introduction of extra cobalt can boost electric conductivity of the materials to support fast electron transport required under higher rates. Three dimensional hybrid nanostructures were proposed to fulfill high rate performance and long cycle life. Core/shell Ni-Co@Ni-Co double layered hydroxide nanotube arrays were fabricated by a template method. The designed nanotube arrays increases the



surface area and shortens the charge diffusion path. Flexible asymmetric supercapacitors were assembled and tested, showing the potential for application.

1.3 Synopsis of thesis

This thesis presents the synthesis and characterization of nickel-based composites for enhanced electrochemical energy storage application. The mechanism of the synthesis of nickel-based composite through electrochemical reaction and the microstructure-property relationship are systematically studied. The nickel-cobalt composite with a designed structure was demonstrated to be applicable in a flexible energy storage device.

The thesis is organized as follows:

Chapter 1 presents an overview of the global energy sources and the necessity of the pattern transformation for energy generation. The objectives and relevant research approaches for realizing enhanced electrochemical energy storage performance are carefully exhibited.

In Chapter 2, a comprehensive literature review on nickel-based composite materials for energy storage devices is provided. It contains the basic working principles of the energy storage device, the design of the electrode structure, the selection of the electrode materials, and the preparation methods. Particular emphasis is placed on the current status of the development of electrochemical methods for the preparation of



nickel-based composites for energy storage devices. Strategies to achieve excellent electrochemical performance of the energy storage devices are reviewed.

Chapter 3 introduces the experimental approaches used in the current work, including the material synthesis and characterizations, and the device assembly and testing.

In Chapter 4, synthesis and characterizations of hierarchical nickel-based composite for high capacitance energy storage device is introduced. Inspired by the anodization of titanium, a porous layer of Ni-based composite was prepared by anodization in organic electrolyte. Due to the direct anodization on a Ni foil, the Ni-based composite layer shows good mechanical/electrical contact with the current collector (Ni foil) and facilitates improved cycling performance with a capacitance approaching the theoretical value.

Chapter 5 presents the synthesis and characterizations of dendritic nickel-based composite by electrodeposition in nickel-free organic electrolyte. The metal@metal oxide core@shell structure results in an enhanced electrochemical activity of the composite material and an ultra-long life during cycling process. The crystal growth mechanism in a source-free environment and the microstructure-property relationship are discussed with systematic experimental work.

Chapter 6 introduces the synthesis of both anode and cathode at the same time in a single cell under optimized electrochemical reaction. The synthesized anodic and



cathodic nickel-based composite electrodes exhibit excellent electrochemical performance.

Chapter 7 studies double-metal composite fabricated by electrochemical reaction. Nickel-cobalt nanotube arrays were synthesized and characterized. The designed structure benefits charge transfers, leading higher capacitance and better rate performance.

Chapter 8 summarizes the work on the nickel-based composites for enhanced electrochemical energy storage performance and provides a better understanding on the working principles. Suggestions of the future work on nickel-based composites for energy storage applications are also given.



Chapter 2 Literature Review of Nickel-Based Composites for Supercapacitor Electrodes

In this chapter, a methodical review of nickel-based composites for supercapacitor electrodes is presented. It contains four sections in details. Firstly, supercapacitors as a kind of EESDs will be introduced, with an emphasis on its energy storage mechanism and performance. Secondly, electrode materials applied in supercapacitors will be reviewed with an emphasis on transition metal oxides/hydroxides. Thirdly, approaches for nickel-based composites will be summarized, with an emphasis on electrochemical synthesis methods, such as anodization and cathodic deposition. Finally, nickel-based composites for supercapacitor electrodes in the thesis will be summarized and strategies for enhancing performance will be proposed.

2.1 Supercapacitor: energy storage device

Energy storage in supercapacitors is done in the form of an electric field between two electrodes.^[5] A supercapacitor as an EESD is similar to batteries in design and manufacturing. As shown as in Figure 2.1a, a supercapacitor consists of two electrodes, an electrolyte and a separator that isolates the two conducting electrodes.^[6] Active porous electrode materials are coated onto conducting current collectors as anode and



cathode. In general, nanostructured materials with high specific surface area and porosity are used to fabricate supercapacitor electrodes. A separator is often a porous film, which allows ion in and out and avoids the direct contact between cathode and anode. The electrolyte occupies the voids of electrode materials, and provides ions for energy storage. The potential drop is shown in Figure 2.1b. During charging, the cations from electrolyte react with cathode while the anions from electrolyte react with anode. The electrochemical reaction causes directional movement of ions and then forms the potential difference between cathode and anode of the supercapacitor. The cathode reaction will increase the potential of the cathode over open circuit potential (OCP). The anode reaction will lower the potential of anode over OCP. In the discharge process, it is the other way round. The anode and cathode materials should be electrochemical active in the electrochemical potential range.

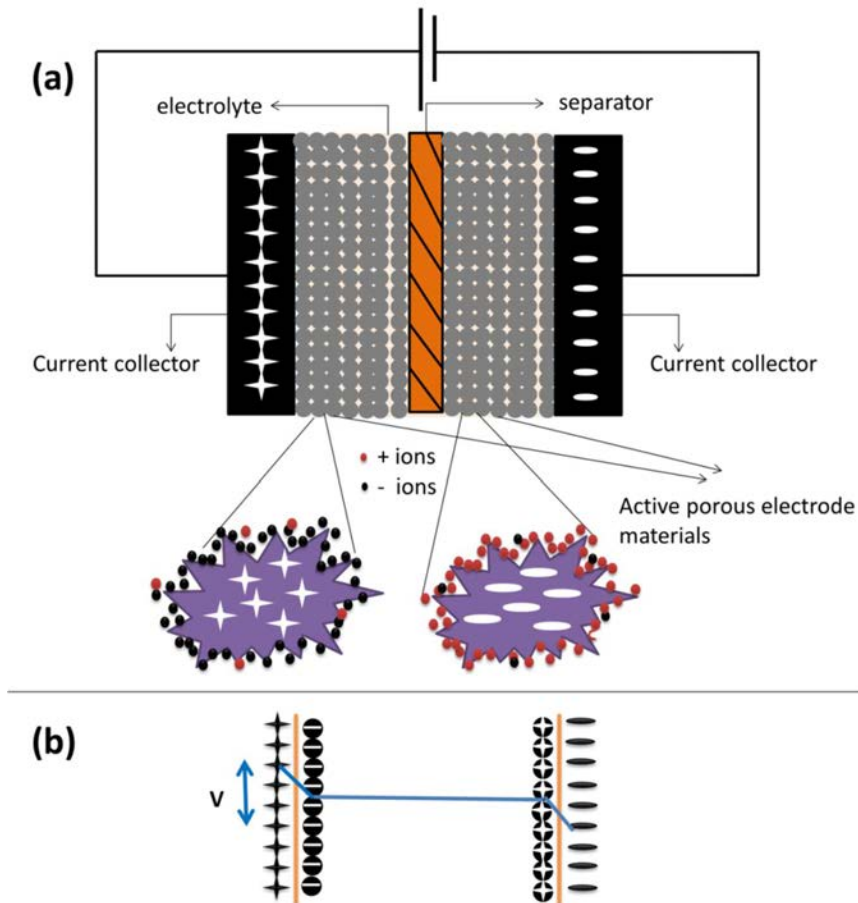


Figure 2.1 (a) Schematic presentations of a supercapacitor device and (b) its potential drop at the electrode/electrolyte interface.^[3a]

2.1.1 Energy storage mechanism

As described in the introduction, supercapacitors based on the energy storage mechanism are categorized into EDLCs whose capacitance is from an electrostatic charge accumulation at the interface of electrode and electrolyte, and pseudocapacitors

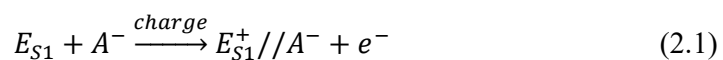


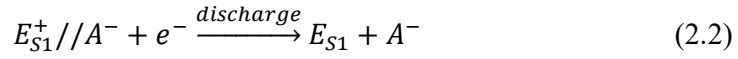
where Faradaic redox reactions take place at the vicinity of the surface involving the passage of charge across the double layer, and in the bulk materials with two-dimensional transport pathways to store charges. Yet, they usually work together, especially in realizing excellent supercapacitor performance.

2.1.1.1 Energy storage mechanism of electrochemical double-layer capacitor

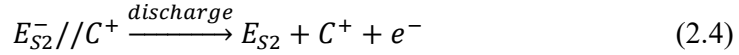
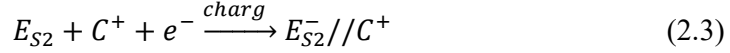
EDLCs are electrostatic capacitors which store charges by reversible adsorption of ions from electrolyte onto the surface of active materials. The most common active electrode materials in EDLCs are carbon materials, such as active carbon^[7], ordered mesoporous carbon,^[8] carbon nanotube,^[9] and graphene.^[10] As shown in Figure 2.1, electrical double layer capacitance happens at the interface between the active materials and electrolyte, where an excess or deficiency of charges is accumulated on the electrode surface, and electrolyte ions with counterbalancing charges are arranged on the electrolyte side to meet electroneutrality. During charging/discharging process, ions and electrons charge at the electrode-electrolyte interface move under electrical balance with electrostatic interaction in nature. For this reason, charging/discharging is greatly reversible and thousands of cycles are easily achievable. Equation (2.1)-(2.6) are listed below in order to understand charging/discharging process of EDLCs more clearly:^[6]

On one electrode:

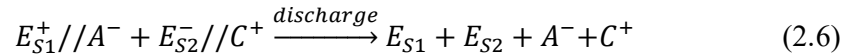
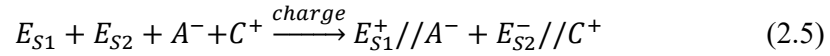




On the other electrode:



The overall charging/discharging process can be described as Equations (2.5) and (2.6):



where E_{S1} and E_{S2} represent the two electrode surfaces, A^- and C^+ are anion and cation respectively, and the interface between electrode and electrolyte is described as //.

Besides, charge separation at the interface of electrode and electrolyte is induced by polarization. The double layer capacitance C described by Helmholtz in 1853 ^[11] is calculated by Equation (2.7), assuming a parallel-plate capacitance.

$$C = \frac{\epsilon_r \epsilon_0 A}{d} \quad (2.7)$$

where ϵ_r is the dielectric constant of electrolyte, ϵ_0 is the dielectric constant of vacuum, d is the effective thickness of electrical double layer and A is the electrode surface area. Based on Equation (2.7), with the increase of pore volume by developing high surface area (A) the capacitance of carbon electrode (C) will be effectively



improved. However, the capacitance increase is restricted and some reported results are against this simple relationship between the surface area and the capacitance.^[12] In general, it is believed that submicropores of an electrode do not take part in the formation of electrical double layer because of inaccessibility of the submicropore surfaces to the large solvated ions. Simon and Gogotsi^[13] reported that the maximum pore size of carbon electrodes was close to the ion size (0.8 nm in their case). Some of the new finding cannot be interpreted by electrical double-layer theory. Hence, Huang *et al.*^[14] presented an electric double-cylinder capacitor model to describe the capacitance behavior of microporous carbon electrodes. Their study provides some methods to enhance capacitance. However, it is still challenging to fully understand the energy storage mechanism of EDLC in nanoscale.

2.1.1.2 Energy storage mechanism of pseudocapacitor

Different from EDLCs, pseudocapacitors store energy by fast and reversible redox reactions between the electrolyte and electrochemical active species at the vicinity of the surface involving the passage of charge across the double layer, and in the bulk materials with two-dimensional transport pathways to store charges. Conway divided the pseudocapacitive mechanisms into three types:^[15] (i) underpotential deposition (UPD), (ii) redox system, and (iii) intercalation system. These processes are shown in Figure 2.2. UPD happens when metal ions form a monolayer upon a different metal surface by electrosorption, e.g., Pb on the surface of Au or Pt. Redox system takes place when ions are electrosorbed at the surface or near-surface of the electrode (RuO_2 ,



MnO₂,...) followed by a Faradaic charge-transfer. Intercalation system happens when ions intercalate into the quasi-two-dimensional transport pathways or the layer-lattice structures (e.g., TiS₂, MoS₂, or Nb₂O₅) accompanied by a Faradaic charge-transfer, where phase transformation will not occur although charges are stored in the bulk. The difference among these three types of mechanisms is that the processes occur due to the types of materials. The similarity is that they describe the behaviour of materials which have electrochemical signature of a capacitive electrode (of EDLCs), i.e., a linear dependence of the charged stored with the potential:

$$C = \frac{\Delta Q}{\Delta V} \quad (2.8)$$

where ΔQ is the charge stored (C , or mA h), and ΔV is a potential window (V). Ideally, the capacitance, C , is constant over a given potential window. However, since the plot of ΔQ vs. ΔV is not completely linear, the capacitance is not always constant, and so it is termed pseudocapacitance. As a matter of fact, “pseudocapacitance” is used to designate electrode materials that have the features of a capacitive electrode such as observed in carbon materials, where charge storage originates from different reaction mechanism. Yet, based on the kinetic behavior and same as the capacitive electrode materials, the pseudocapacitive electrode materials require reactions to occur on the surface, or be limited by the surface, not to be limited by solid-state diffusion.^[16] Equation (2.9) with b-value is 1 exhibits kinetics indicative of surface-controlled electrochemical processes where electrode materials perform high rate capability.^[17]

$$i = av^b \quad (2.9)$$

Where i is the current (A), and v is the sweep rate (mV s^{-1}) of a cyclic voltammetry experiment. a and b are adjustable values. When b is 0.5, the current is controlled by semi-infinite diffusion. The electrode materials in the rechargeable batteries often satisfy this condition where charge storage occurs in the bulk and meanwhile is limited by solid-state diffusion. Therefore, battery materials often experience high energy densities but limited power densities and the rate capability.

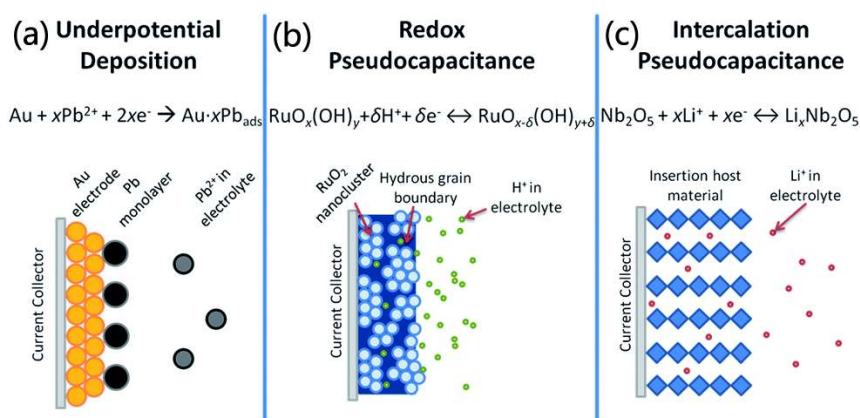


Figure 2.2 The types of Faradaic mechanisms giving rise to pseudocapacitance.^[16]

Unfortunately, despite the clear definition of pseudocapacitance, it is still confusing in the cases where battery-type materials like $\text{Ni}(\text{OH})_2$ and V_2O_5 can show the electrochemical behaviour of pseudocapacitance (Figure 2.3). Therefore, this type of materials often exhibits very good electrochemical performance in specific capacitance, cyclic life and rate capability, which absorbs advantages of supercapacitors. Dunn *et al.*^[17] describe such situation as “extrinsic pseudocapacitance”, different from “intrinsic pseudocapacitance” such as RuO_2 , MnO_2 and Nb_2O_5 . The former can emerge by proper material engineering. When the electrode materials (film, powder, ...) reach a critical size (nanoscale, increasing the

surface area), where diffusion distance is shortened and in some cases, the phase change is suppressed, giving rise to “capacitive-like” performance such as high rate capability. In those cases, the charge storage takes place at or near the surface following the surface-controlled process ($b=1$ in Equation 2.9). However, extrinsic materials do not show pseudocapacitance in the bulk state due to the phase transformation, following solid-state diffusion ($b=0.5$ in Equation 2.9), the same as battery materials like spinel $\text{Li}_4\text{Ti}_5\text{O}_{12}$ and LiFePO_4 . The latter are materials that display the characteristics of capacitive charge storage for a wide range of particle sizes and morphologies, i.e., the material engineering will not affect their electrochemical behaviors. In a word, materials like $\text{Ni}(\text{OH})_2$ and V_2O_5 are not strictly regarded as supercapacitor or battery materials based on their electrochemical behaviour. Therefore, the term “battery-type pseudocapacitive materials” (BPMs) is used in the thesis to avoid the confusion with the traditional concepts. The supercapacitors based on BPMs can be named after “battery-type supercapacitor”.

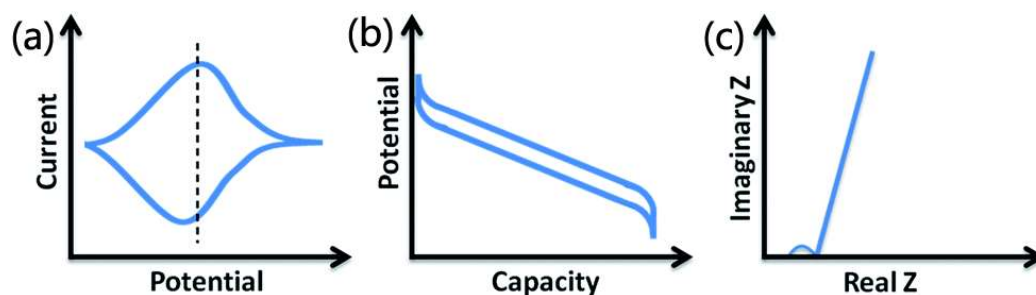


Figure 2.3 The general electrochemical features of pseudocapacitive materials.^[16]

Nanostructured $\text{Ni}(\text{OH})_2$ is taken as an example to illustrate the electrochemical mechanism and behavior based on the concept of BPM. Charge storage in



nanostructured $\text{Ni}(\text{OH})_2$ involves at least one diffusion-controlled phase transformation during a redox reaction, which results in a constant potential during the galvanostatic charge–discharge test, indicative of a low rate behavior. This indicates that nanostructured $\text{Ni}(\text{OH})_2$ behaves as a battery material. On the other hand, due to nanostructuring, increasing surface charge storage sites results in a decrease in diffusion distance and to some extent, suppresses the phase transformation, which benefits the improvement of the rate capability and cyclic stability. Meanwhile, a large percentage of the charge storage sites are limited to the surface or near the surface of the nanostructured $\text{Ni}(\text{OH})_2$.

Charge storage in $\text{Ni}(\text{OH})_2$ takes place via reversible redox of $\text{Ni}^{2+}/\text{Ni}^{3+}$ couple in an alkaline KOH electrolyte: $\text{Ni}(\text{OH})_2 + \text{OH}^- \rightleftharpoons \text{NiOOH} + \text{H}_2\text{O} + e^-$.

Figure 2.4a showed the charge-discharge curves in a bulk $\text{Ni}(\text{OH})_2$ electrode that presents a battery-type potential plateau. However, nanostructure $\text{Ni}(\text{OH})_2$ electrode performs both a flat potential region and a sloping capacitive region in Figure 2.4b. The sloping regions likely correspond to pseudocapacitive contributions from the surface or near-surface charge storage sites. Therefore, the capacitance of the nanostructured $\text{Ni}(\text{OH})_2$ is very high because of the contributions of both the battery-capacity and supercapacitor-capacitance.

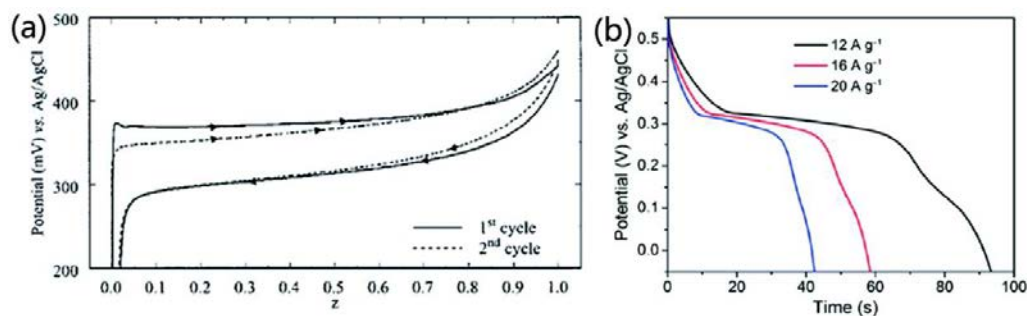


Figure 2.4 Comparison of the charge–discharge profiles of $\text{Ni}(\text{OH})_2$ in (a) bulk ^[18] and (b) nanostructured forms ^[19].

Compared with EDLCs, the pseudocapacitors have higher capacitance.^[20] In order to realize the optimal supercapacitor performance (energy density), it is necessary to integrate the electrode configuration (e.g. hybrid supercapacitors containing two different electrodes with one carbon electrode and another metal oxide Faradaic capacitance electrode). In this kind of hybrid supercapacitor, the electrical double-layer and Faradaic redox processes occur simultaneously and are utilized based on their different charge storage behaviors in a supercapacitor cell. Essentially, capacitor-like cyclic durability is achieved by limiting discharge depth of the pseudocapacitive electrode. What's more, operating voltage window can be extended because the positive and negative electrodes are made of dissimilar materials. Thus, it is very important to optimize electrode design and balance charge and potential of the electrodes to achieve the maximum capacitance and energy density.



2.1.1.3 The performance of supercapacitors

The performance of supercapacitors is usually evaluated by the capacitance, power density, energy density, and cyclic durability, which will be discussed in the following.

As shown in Figure 2.1, a supercapacitor cell can be regarded as two capacitors in series. The capacitances of positive and negative electrodes can be expressed as C_p and C_n . The overall cell capacitance is described in Equation (2.10):

$$\frac{1}{C_T} = \frac{1}{C_p} + \frac{1}{C_n} \quad (2.10)$$

If the two electrodes are made from the same material, the corresponding supercapacitor is called a symmetric supercapacitor. When the positive and negative electrodes are made from different materials, the supercapacitor is called an asymmetric supercapacitor. The capacitance of C_T is always controlled by the electrode with a smaller capacitance. In general, the maximum capacitance of a supercapacitor mainly depends on the electrode materials.

Besides the cell capacitance, the theoretical energy (E) and power (P) densities of supercapacitors can be expressed by Equation (2.11) and (2.12):

$$E = \frac{1}{2} CV^2 = \frac{QV}{2} \quad (2.11)$$

$$P = \frac{1}{4R_S} V^2 \quad (2.12)$$



where Q is the total stored charge in the supercapacitor, R_s represents the equivalent series resistance (ESR). From the equations, it can be seen that C , V and R_s are important parameters determining the performance of supercapacitors. Among them, the capacitance C has been discussed above and strongly depends on the electrode materials and the construction of electrodes. ESR is the inner resistance which associates with a mass transfer resistance of the ions in the electrode matrix, contact resistance between the current collector and active materials, and electrolyte resistance. The voltage (V) is limited by the thermodynamic stability of electrolyte solution. For example, when carbon is used as the electrode materials in aqueous electrolyte, the voltage window of a symmetric supercapacitor is about 1.0 V, while the voltage can reach 3.0-5.0 V in the ionic liquid electrolyte.^[21]

According to Equation (2.11) and (2.12), the improvement of both energy and power densities can be more easily achieved by increasing the voltage window than increasing the capacitance or reducing ESR because of the square power law. To increase the voltage window, electrode materials and electrolytes should be optimized. However, it should be noted that the capacitance increase can be compromised by the voltage window increase because electrolytes with a large electrochemical window often suffer from low ionic conductivity due to high viscosity.

Equation (2.11) tells that the energy density of a supercapacitor is proportional to its capacitance, indicating that increasing the capacitance can effectively enhance the



energy density. Hence, the electrode material is a key factor for developing supercapacitors with excellent performance.

It can be seen from Equation (2.12) that the lower the ESR, the higher the power density of a supercapacitor. In general, supercapacitors have higher power densities than batteries due to lower inner resistance because of the rapid transfer of positive and negative charges. To reduce ESR, the electrode structure and electrolyte should be optimized.

In conclusion, developing electrode materials should be one of the crucial approaches to supercapacitors with improved energy density and/or power density.

In order to realize a high performance supercapacitor electrode, factors that determine the capacitance, rate capability, and cyclic stability should be considered. (i) Specific surface area: since the kinetics of charge storage is limited by surface processes, a electrode with a high specific surface area are able to provide a high capacitance and rate capability. Nanostructured electrode material is a choice for increasing the specific surface area of the electrode. (ii) Electronic and ionic conductivity: Good electric and ionic conductivity can contribute to the enhancement of specific capacitance and rate capability. During cycling or charging/discharging process, the rectangular nature of cyclic voltammetry and symmetry of galvanostatic charging/discharging curves can be kept in good condition, indicative of the good double-layer capacitive behaviors. (iii) Mechanical and chemical stability: cyclic stability is often determined by mechanical and chemical stability of electrodes. Phase



change, dissolution, and side reaction of electrode materials are main factors for reduced cyclic durability.

2.1.2 Supercapacitor electrode materials

As discussed above, the capacitance and charge storage mechanism of supercapacitors intrinsically rely on the electrode materials used. Hence, preparing electrode materials with high capacitance and enhanced performance is very important to advance energy storage technology.

2.1.2.1 Carbon materials

A variety of carbon materials are the most commonly applied in EDLCs, which adsorbs electrolyte ions at the surface between electrode and electrolyte to store charge. Carbon materials, e.g., activated carbons (ACs), templated carbons (TCs), carbon nanofibers (CNFs), carbide-derived carbons (CDCs), carbon nanotubes (CNTs) and graphene, have been widely studied as electrode materials for EDLCs because of their high specific surface area, high electrical conductivity, and good thermo-chemical stability (Figure 2.5). Different carbon materials have their advantages and disadvantages. A condensed summary of notable research in the development of carbon materials for supercapacitors with excellent performance is presented in Table 2.1. In fact, the specific capacitance of carbon materials is usually below 500 F g^{-1} . Therefore, the energy density of carbon material is not very high. According to Conway,^[15] carbon materials for EDLCs must have (i) high specific surface area, on

the order of $1000 \text{ m}^2 \text{ g}^{-1}$; (ii) good intra- and interparticle conductivity in porous matrices; and (iii) easy electrolyte accessibility to intrapore surface area. This means that future research directions in carbon materials are to develop carbon electrodes with high specific-surface area, proper pore distribution and pore size, rational surface conditioning with modification so as to achieve better performance, namely, good specific capacitance and conductivity without compromising cyclic stability.

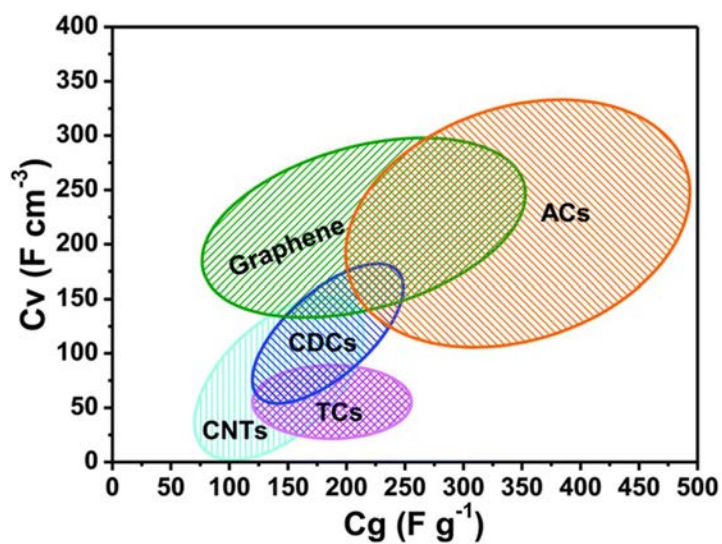


Figure 2.5 Volumetric and gravimetric specific capacitance of different carbon materials for supercapacitors.^[22]

**Table 2.1** Carbon materials for EDLCs reported in recent years.

Materials	Electrolyte	Scan rate/ Current density	C_g (F g ⁻¹)	C_v (F cm ⁻³)	Ref.
AC	EMIMBF ₄	1 A g ⁻¹	207 (two)	104	[23]
AC	1 M H ₂ SO ₄	1 mV s ⁻¹	510 (two)	390	[24]
HFAC-2	1 M H ₂ SO ₄	0.25 A g ⁻¹	556 (three)	611	[25]
CDCs	1 M TEABF ₄	—	—	180	[26]
CDCs	1 M H ₂ SO ₄	—	—	160	[26]
CDCs	1.5M TEMABF ₄ /AN	20 mV s ⁻¹	—	180	[27]
CNT/MXene	1 M H ₂ SO ₄	2 mV s ⁻¹	134 (three)	390	[28]
Graphene	H ₂ SO ₄ /PVA	1 V s ⁻¹	—	71.6	[29]
3D porous carbon	6 M KOH	0.5 A g ⁻¹	318 (three)	118	[30]
VArGO	6 M KOH	0.05 A g ⁻¹	145 (two)	171	[31]
Graphene/CNT	EMIMBF ₄	0.5 A g ⁻¹	199 (two)	211	[32]
N-doped porous carbon	1 M H ₂ SO ₄	0.2 A g ⁻¹	298 (three)	161	[33]
N-doped CNFs	6 M KOH	1 A g ⁻¹	202 (three)	200	[34]

Annotation: “two” means two-electrode system; “three” means three-electrode system.



2.1.2.2 Faradaic materials

As mentioned above, EDLCs based on the electrochemical double-layer mechanism have limited capacitance, which results in relatively low energy density. However, pseudocapacitors which store charges in some electrosorption processes and redox reactions at the interface between electrode and electrolyte can have 10-100 times stronger energy-storage ability than EDLCs. Therefore, great efforts have been made in recent years to develop electrode materials with pseudocapacitance. Currently, the main material types contain conducting polymers and metal oxides/hydroxides, such as polyaniline (PANi), polypyrrole (PPy), RuO_2 , MnO_2 , and Nb_2O_5 . And battery-type pseudocapacitive materials, such as V_2O_5 , NiO , Ni(OH)_2 , Co_3O_4 , and Co(OH)_2 , are also included. The summary of popular pseudocapacitive electrode materials is listed in Table 2.2.



Table 2.2 Summary of recent reports on pseudocapacitive electrode materials.

Materials	Theoretical Value (F g ⁻¹)	Electrolyte	Scan rate/ Current density	C _g (F g ⁻¹)	Ref.
PANi hydrogel	750	1 M H ₂ SO ₄	0.2 A g ⁻¹	480 (three)	[35]
PPy	620	0.5 M H ₂ SO ₄	1.1 A g ⁻¹	566 (three)	[36]
PPy	620	5 M LiCl	1 A g ⁻¹	699 (three)	[37]
RuO ₂	2000	0.5 M H ₂ SO ₄	2 mV s ⁻¹	900 (three)	[38]
RuO ₂	2000	0.5 M H ₂ SO ₄	20 mV s ⁻¹	1190 (three)	[39]
Ni(OH) ₂	2069	1 M KOH	1 mV s ⁻¹ 5 mV s ⁻¹	2188 (three) 153 (two)	[40]
NiO	2584	2 M KOH	2 A g ⁻¹	1126 (three)	[41]
Hydrogenated NiO	—	1 M KOH	5 mV s ⁻¹	1272 (three)	[42]
Ni(OH) ₂	2069	6 M KOH	2 mV s ⁻¹ 0.9 A g ⁻¹	1765 (three) 192 (two)	[43]
α-MnO ₂ δ-MnO ₂	—	0.25 M Na ₂ SO ₄	1 A g ⁻¹	200 (three) 190 (three)	[44]



MnO₂	1370	1 M Na ₂ SO ₄	0.5 A g ⁻¹	371.2 (three)	[45]
β-MnO₂	—	1 M Na ₂ SO ₄	0.5 A g ⁻¹	453 (three)	[46]
V₂O₅	—	1 M KCl	100 mV s ⁻¹	1024	[47]
V₂O₅	—	2 M KOH	—	350	[48]
Co₃O₄	3560	2 M KOH	2 A g ⁻¹	2735 (three)	[49]
Co₃O₄	3560	1 M KOH	0.5 A g ⁻¹	781 (three)	[50]
β-Co(OH)₂	3600-3700	1 M KOH	1 A g ⁻¹	416 (three)	[51]

Conducting polymers are polymers with highly π -conjugated polymeric chains. By chemical or electrochemical redox “doping”, the conductivity can be tuned in a wide range up to 10000 S cm⁻¹. The reversible redox “doping-dedoping” in the conducting polymer backbone does not involve structural change and is highly reversible. However, swelling and shrinking of conducting polymers during the intercalating/deintercalating process may lead to mechanical degradation of the electrode and then poor cyclic durability.^[36-37,52]

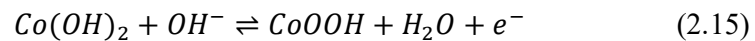
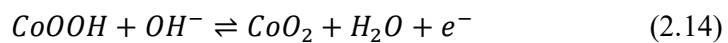
In general, metal oxides/hydroxides have higher energy density than carbon materials and better electrochemical stability than conducting polymer materials. RuO₂ is one of the earliest studied metal oxides, because of its high theoretical capacitance (2000



F g^{-1}), good conductivity, wide potential window and good electrochemical reversibility.^[38-39] Despite so many advantages, RuO_2 is still not popular for commercial application in supercapacitors due to its high cost, toxicity and scarce source. In order to reduce the cost of supercapacitor electrode materials, some metal oxides/hydroxides are alternative candidates to replace RuO_2 . These materials include MnO_2 and Nb_2O_5 , as well as BPMs (V_2O_5 , NiO , Co_3O_4 , $\text{Ni}(\text{OH})_2$ and $\text{Co}(\text{OH})_2$). MnO_2 ^[44-46,52a] is an attractive electrode material due to its environmental harmlessness, large abundance, low cost and high theoretical capacitance (1370 F g^{-1}). Although the theoretical capacitance is high, the practical capacitance of MnO_2 is usually low due to its poor conductivity and electrochemical dissolution during cycling. The poor electronic and ionic conductivities hinder the electron and ion transfer, and cause low rate performance and low power density. V_2O_5 as BPM is also reported as a traditional metal oxide for supercapacitor (battery-type) application.^[38,47] The energy storage behavior of V_2O_5 is attributed to pseudocapacitance as well as battery-type Li/Na ion intercalation. The battery type capacity is the main contributor to energy storage. It has a higher theoretical capacitance than RuO_2 due to its smaller molar mass and more oxidation states of V ions. However, a bottleneck for V_2O_5 is still its low conductivity. Apart from RuO_2 , MnO_2 , and V_2O_5 , nickel and cobalt-based metal oxides/hydroxides have attracted a large number of interests from researchers in recent years. These VIII B metal elements present similar electrochemical reactions as well as high specific capacitance when they are applied in (battery-type) supercapacitor electrode materials.^[40,42-43,49-51] At the same time, $\text{NiO}/\text{Ni}(\text{OH})_2$ and $\text{Co}_3\text{O}_4/\text{Co}(\text{OH})_2$ have higher electrical conductivity than MnO_2 and V_2O_5 (2~3 orders of magnitude), which



is good for realizing high rate capacity and power density. The pseudocapacitive mechanism of NiO/Ni(OH)₂ has been discussed in the prior section (2.1.1.2), and they belong to BPMs. The redox reactions are $NiO + OH^- \rightleftharpoons NiOOH + e^-$ and $Ni(OH)_2 + OH^- \rightleftharpoons NiOOH + H_2O + e^-$. Nickel-based materials can only be used in alkaline solution. Neutral aqueous solution or organic electrolyte cannot supply enough OH⁻ for electrochemical reactions. Although NiO/Ni(OH)₂ has higher electrical conductivity than MnO₂ and V₂O₅, it is still not enough for the supercapacitor (battery-type) electrodes, especially compared with carbon material. There are two main issues for NiO/Ni(OH)₂: relatively low electrical conductivity and short cycle life. It is a good method to introduce other metal ions or conducting additives into the nickel oxide/hydroxide matrix.^[53] Co₃O₄/Co(OH)₂ has similar properties and structure to NiO/Ni(OH)₂. Their supercapacitive reactions can be described by Equations (2.13) - (2.15):



In fact, nickel and cobalt-based oxides/hydroxides can give the much higher capacitance than RuO₂, MnO₂ and other metal oxides/hydroxides. However, their high capacitance is located in a low potential window, which limits their practical application as supercapacitors (battery-type).



In summary, pseudocapacitive electrode materials play an important role in next generation high-performance supercapacitor (battery-type). However, in order to improve their poor conductivity, short cycling life, and low bulk material utilization, much and fresh efforts need to be made. As introduced in Chapter 1.1, these problems are to be tackled by the following methods. For example, developing nanostructured materials and composites will be effective approaches to enhancing supercapacitor performance. What's more, these two methods can also relieve the swelling and shrinking stress of the electrodes during charging/discharging process, and weaken the dissolution of materials into the electrolyte, which can enhance cyclic life. Besides, ionic and electronic conductivity can be further improved due to nanostructured porosity and conducting agent addition, which is beneficial to rate capacity and power density.

2.2 Approaches for synthesizing nickel-based composites as supercapacitor electrode

Based on the above discussions, pseudocapacitive electrode materials have incomparable advantages due to their high theoretical specific capacitance, especially BPMs, such as nickel and cobalt-based materials. In the past few years, nickel-based materials have attracted much attention for application in the field of energy storage. Researchers are looking for easy and feasible preparation methods for electrode materials with good electrochemical performance. In this section, several approaches



on the preparation of nickel-based materials for high performance supercapacitors (battery-type) will be discussed.

2.2.1 Hydrothermal method

Hydrothermal synthesis is a method to produce different compounds and materials from high-temperature aqueous solutions at high vapor pressure. Its advantages include the ability to synthesize large crystals with high quality and high quantity. Lu et al.^[54] reported ultrathin Ni(OH)₂ nanowall film on the nickel foam by hydrothermal method in Ni(NO₃)₂ and HMT aqueous solution. Because of direct growth of nanowalls on the substrate, the product showed high specific capacitance (2675 F g⁻¹) and good cycling performance (>96% for 500 cycles). Similarly, Su et al.^[55] used Teflon-lined stainless steel autoclave which was heated to 220 °C for 12 h to produce NiC₂O₄ precursor nanowires. The as-prepared porous NiO nanowires demonstrated a specific capacitance of 348 F g⁻¹ as electrodes in supercapacitors (battery-type). The generation of CO₂ during annealing at 400 °C created a porous structure which increases the specific surface area. However, high temperature annealing can also give rise to high crystallinity which may decrease the number of active defects and be adverse to the improvement of electrochemical performance. Moreover, the hydrothermal method also has its natural drawbacks, including high requirement for equipment and the inability to monitor crystal growth process.



2.2.2 Chemical bath precipitation

Chemical bath precipitation (CBD) is a method to deposit thin films on a substrate by chemical reaction in a solution container. It yields stable and uniform films with good reproducibility in a simple process. By adjusting different deposition temperature, duration, and composition, the growth of thin films can be well controlled. For example, Yuan et al.^[56] prepared β -Ni(OH)₂/ γ -NiOOH composite film on nickel-foam substrate by CBD. The as-obtained porous composite film showed an interconnected net-like structure composed of nanowall flakes. This structure can accommodate volume change caused by the electrochemical reaction, increase the contact between electrolytes and active materials, and shorten ion diffusion path. The composite film exhibited a noticeable pseudocapacitance (battery-type) of 1420 F g⁻¹ at 2 A g⁻¹ and 1098 F g⁻¹ at 40 A g⁻¹. Although the CBD method is facile, it suffers from relatively weak adhesion between nickel-based materials and the current collector. Therefore, its cycling performance is not very good (1000 cycles with 81% retention).

2.2.3 Electrochemical synthesis

Electrochemical synthesis is also called electrosynthesis, and is a method to produce chemical compounds in an electrochemical cell. It takes place at the electrode-electrolyte interface. The reaction parameters contain electrodes (anode and cathode), electrolyte, temperature, and the cell with divided or undivided mode. A schematic diagram of electrochemical synthesis device with two electrodes in a divided mode is



shown in Figure 2.6. As a matter of fact, this device is an electrolytic cell in a divided mode. Electrical energy is used to drive nonspontaneous redox reaction. There are several features of electrochemical synthesis which are different from other synthetic methods:^[57] (i) Electrochemical synthesis takes place near the electric double layer with a high potential gradient of 10^5 V cm^{-1} . The reaction happens and forms new materials which can be obtained in a chemical reaction. (ii) The product is grown on the electrode in the form of a thin film or a coating. If a suitably shaped counter electrode is used for uniform polarization, conformal coatings can be grown on a substrate of arbitrary shape. (iii) Kinetic and thermodynamic controls can be achieved by controlling the current passed through the cell and applied potential, respectively. (iv) The film or coating composition can be varied by controlling the bath composition. (v) By fine-tuning the applied cell potential, an oxidation or a reduction reaction happens, which is difficult for chemical synthesis. These features of electrochemical synthesis qualify itself a high level of preparation method for nickel-based materials with an easy of controlling structures and components. For example ^[58], (i) the crystal growth can be suitably adjusted by applied potential, current densities or electrolyte concentration, and thus designed nanostructured nickel-based materials can be easily synthesized; (ii) the nanostructured nickel-based materials can be directly grown on the conductive substrate; and (iii) the hybrid element, such as Co, can be easily introduced into the nickel-based material matrix by electrochemical method. It will provide fast electron transport pathways and improve the rate capability.

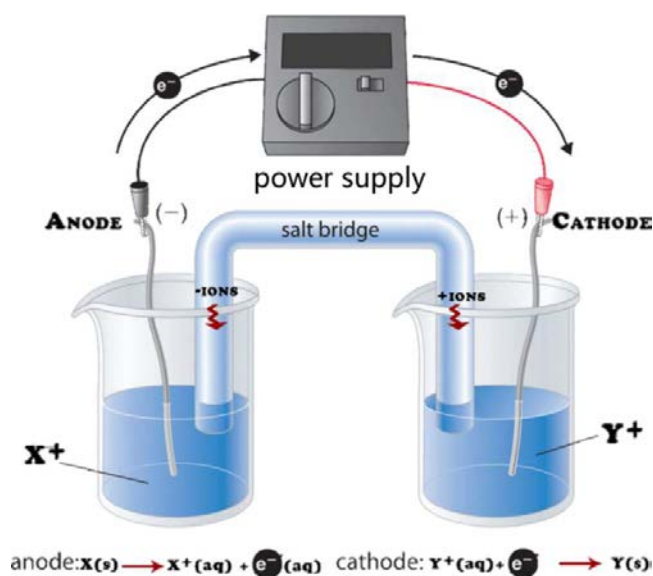


Figure 2.6 Schematic diagram of electrochemical synthesis device with two electrodes in a divided mode.

In theory, the production of nanostructured nickel-based materials confirms the electrode reaction mechanism. An overall electrochemical reaction in an electrode, $O + e^- \rightleftharpoons R$, involves a series of steps. As shown in Figure 2.7, these steps are mass transfer (e.g., O from the bulk solution to the surface of the electrode), electron transfer at the electrode surface, chemical reactions preceding or following the electron transfer, and other surface reactions (e.g., adsorption, desorption or crystallization).^[59] Generally, electrode reaction rate is controlled by the rates of these processes. Therefore, theoretically, any improvement in mass transfer, electron transfer and ion diffusion in the bulk material will facilitate the enhancement of electrochemical performance. Experimentally, strategies should be focused on the increase of material

conductivity for electron transfer, the increase of specific surface area for more electrolyte contact, and the mechanical and chemical stability.

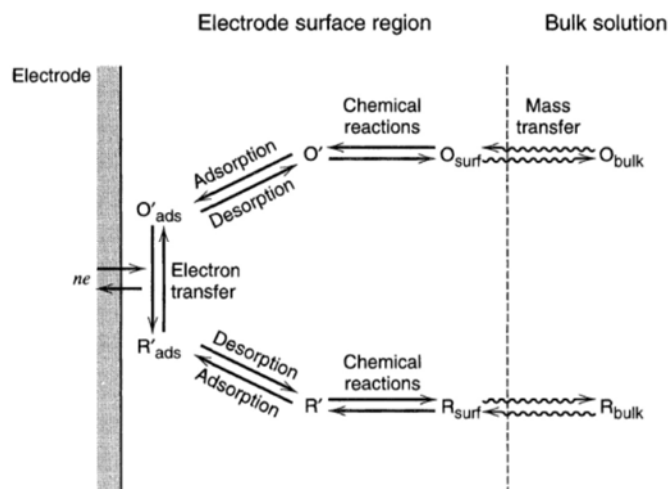


Figure 2.7 Pathway of a general electrode reaction.^[59]

Generally, according to different reaction locations, the electrochemical synthesis method can be classified into two types: anodization and cathodic deposition. They are surface modification techniques, and happen on the anode and cathode, respectively. In recent years, these two methods are often used to prepare monolithic nickel-based materials. Zhang *et al.*^[60] used a facile one-step anodization method to prepare hierarchical nickel compound. The fine control of anodization condition made the compound film with 3D nanoflake structure exhibit robust mechanical behavior and excellent rate capacity (only 20% reduction with 50 times of scan rate). The film remained intact even after 30 min ultrasonication, which guarantees a good stability. The corresponding contact resistance between the substrate and active material was



small. However, the specific capacitance of the hierarchical nickel compound was only 167 mF cm^{-2} at 500 mV s^{-1} . The performance of the composite was expected to be further improved by increasing the thickness of anodic film. After the change of the electrolyte composition, Zhang's group ^[61] produced sponge-like $\text{Ni(OH)}_2\text{-NiF}_2$ composite film as supercapacitor electrode materials. Similar to anodization of titanium, fluoride containing solution was used as the electrolyte, which contributes to the formation of porous layered structure. The as-obtained composite presented a high specific capacitance of 2090 F g^{-1} at 10 mV s^{-1} and a high discharge performance with 1680 F g^{-1} at 100 A g^{-1} . Although the capacitance and high rate discharge is fascinating, the capacitance after 2000 cycles kept only 71% of the initial value, including a poor cycle life.

Yang *et al.*^[62] directly electrodeposited $\alpha\text{-Ni(OH)}_2$ on nickel foam and this nanostructure has ultrahigh capacitance of 3152 F g^{-1} at a current density of 4 A g^{-1} . By constant potential deposition in nickel nitrate solution, loosely packed nanoscale porous Ni(OH)_2 was obtained and maintained large surface area for reaction, which resulted in effective utilization of electrode materials. The porous architecture helped electrolyte penetration and fast proton exchange, which enhanced the capacitance performance. However, the capacitance loss was about 48% after 300 cycles due to the flake off of Ni(OH)_2 from the substrate. Similarly, Hu's group^[63] cathodically deposited Ni(OH)_2 with particle-like morphology. The loosely packed structure allows the electrolyte ions to easily access the active materials for pseudocapacitive reaction (battery-type). As a result, the maximum specific capacitance of 2595 F g^{-1} was



obtained at a current density of 1 A g^{-1} . They also discussed the electrodeposition conditions, such as the applied potential and concentration of $\text{Ni}(\text{NO}_3)_2$. When the applied potential and concentration of $\text{Ni}(\text{NO}_3)_2$ were $-0.9 \text{ V vs Ag/AgCl}$ and 0.008 mol L^{-1} , respectively, the maximum specific capacitance was obtained. Thus, it can be seen that the performance of as-deposited material is affected by various parameters of cathodic deposition.

The addition of other metal element can sometimes further improves the electrochemical performance of nickel-based materials. Hybrid metal can be easily introduced into nickel-based material matrix. By electrochemical synthesis, Huang's group^[64] fabricated nickel cobalt hydroxide nanosheets on porous NiCo_2O_4 nanowires grown vertically on CFP by hydrothermal reaction and cathodic deposition (Figure 2.8a). SEM images of NiCo_2O_4 nanowire template were shown in Figure 2.8b and 2.8c. After electrodeposition, the NiCo_2O_4 nanowires were decorated by $\text{Co}_x\text{Ni}_{1-x}$ hydroxide coating in sheet-like morphology (Figure 2.8d). $\text{Co}_x\text{Ni}_{1-x}$ hydroxide coating can be found under TEM in Figure 2.8e. Among different stoichiometries of the $\text{Co}_x\text{Ni}_{1-x}$ hydroxide sheets studied, $\text{Co}_{0.66}\text{Ni}_{0.33}$ hydroxides/ NiCo_2O_4 /CFP exhibited the highest capacitance of about 1.64 F cm^{-2} at 2 mA cm^{-2} and the best stability with 18.7% of capacitance loss after 2000 cycles. The hybrid composite electrode also presented excellent rate capability (less than 33% capacitance loss with 45 times rate increase). The high performance of the hybrid composite electrode is attributed to some features of the electrode, such as high conductivity of CFP for current collector, porous NiCo_2O_4 nanowires and the ultrathin sheet coating of $\text{Co}_x\text{Ni}_{1-x}$ hydroxides for large

surface area with short electron and ion diffusion path. However, the specific capacitance and cycling life are not good enough compared with reported nickel-based composites. There's still room for improvement in the electrochemical performance of this kind of material.

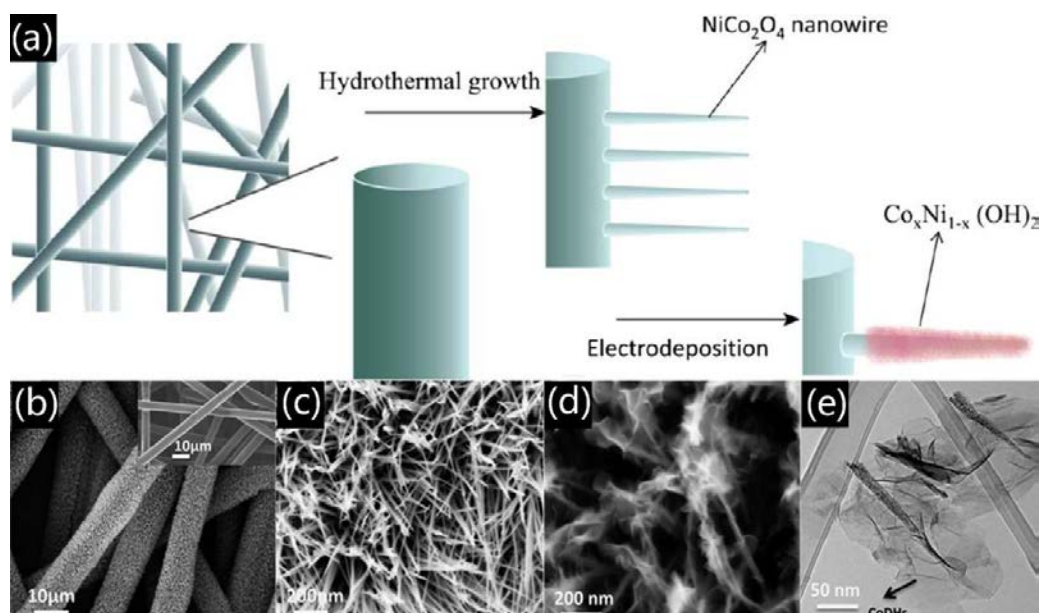


Figure 2.8 (a) Schematic diagram of the growing processes of $\text{Co}_x\text{Ni}_{1-x}$ hydroxides on NiCo_2O_4 nanowires which has been grown on CFP. (b) SEM images of CFP before (inset) and after the growth of NiCo_2O_4 nanowires. (c) Large magnification of (b). (d) SEM image of $\text{Co}_x\text{Ni}_{1-x}$ hydroxides on NiCo_2O_4 nanowires grown on CFP. (e) TEM image of $\text{Co}_x\text{Ni}_{1-x}$ hydroxides on NiCo_2O_4 nanowires grown on CFP.^[64]

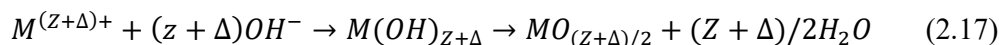


2.3 Anodization for nickel-based composite as supercapacitor electrode

Anodization for monolithic nickel-based composite as supercapacitor (battery-type) electrode will be introduced in details in this section. The content contains basics of anodization process, structure and properties of anodized oxide film, and advantages of anodization. Anodization is different from cathodic deposition, and has its characteristic features and merits. Nickel-based material synthesis will benefit from this technique.

2.3.1 Basics of anodization process

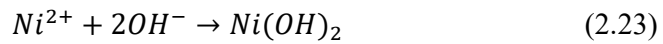
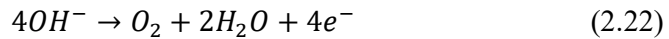
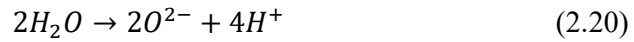
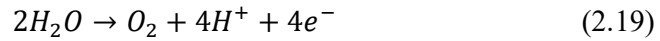
Anodization, also called anodic oxidation, is a technique where a metal ion in a lower oxidation state is oxidized to a higher oxidation on the anode electrode. When a constant voltage or current is applied between the anode and cathode, the metal ion in a higher oxidation state under field-driven ion diffusion yields the formation of oxide or hydroxide which happened in the nickel/water interface. The main electrochemical reactions on the anode are listed below.^[57]



For anodizing nickel foil, the electrochemical reactions are commonly as follows.



At the nickel/water interfaces:



Based on the above reactions, the surface of nickel foil by anodization might form nickel oxide or nickel hydroxide under the electrolyte without reactive anion. Because nickel oxide/hydroxide has higher resistance than the electrolyte and the nickel foil, the applied potential will drop over the oxidized film on the anode. As long as the applied electrical field is strong enough to drive the ions into the oxidized film, the oxidized film will continue growing. Taking TiO_2 as an example, the thickness d is almost linearly dependent on the applied voltage U :

$$d \approx \alpha U \quad (2.25)$$

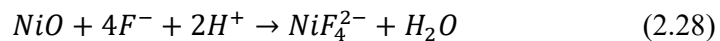
where α is a constant. The α -value of TiO_2 is in the range of 1.5~3 nm V^{-1} .^[65]

However, if the applied voltage exceeds the dielectric breakdown limit of the newly formed oxide, the newly formed film will no longer be resistive to prevent further current flow and oxide growth, which will be accompanied by more gas evolution and sparking. Therefore, the thickness of the oxide film is limited by the dielectric



breakdown voltage. Generally, under the dielectric breakdown limit, the anodic film is relatively thin and ordinarily nonporous or less porous. Hence, it is easy to understand that metals can be protected by forming a layer of oxide film using anodization because at a relatively low applied voltage there is no bubble formation. When a high voltage anodization is adopted, the ions in the electrolyte will be embedded into the deep oxide coating, giving rise to a micro-porous structure due to the localized dissolution of the oxide. The anodic film forms a rough surface, and a balance between oxide film formation rate and oxide dissolution rate in the electrolyte determines the anodic film growth.^[66] These phenomena often exist in the anodization of valve metals (such as titanium, aluminium, niobium, hafnium and so on).^[67]

Although nickel is not a valve metal, the anodization behaviour of nickel can be borrowed from that of titanium. In fluorine-containing electrolyte anodization, nickel often undergoes inhomogeneous field-assisted dissolution at a high applied voltage, and forms porous structure.^[68] The possible electrochemical reaction is as follows:^[69]



2.3.2 Influences of processing parameters—aqueous and non-aqueous electrolyte

The properties of the resulting nickel-based oxide, such as morphologies, electrochemical performance and stability, depend on the processing parameters such as applied voltage, electrolyte composition, current density, temperature, reaction time and stirring condition. Among them, electrolyte composition and applied voltage are key factors that determine the film composition and morphologies. As shown in the Pourbaix diagram (Figure 2.9), in solutions with different pH values, the anodic oxidation of Ni proceeds in stages, resulting in the formation of nickel oxides and hydroxides with various valences. If the electrolyte contains other anions which are able to react with nickel ions, the anodic film composition would be more complex.

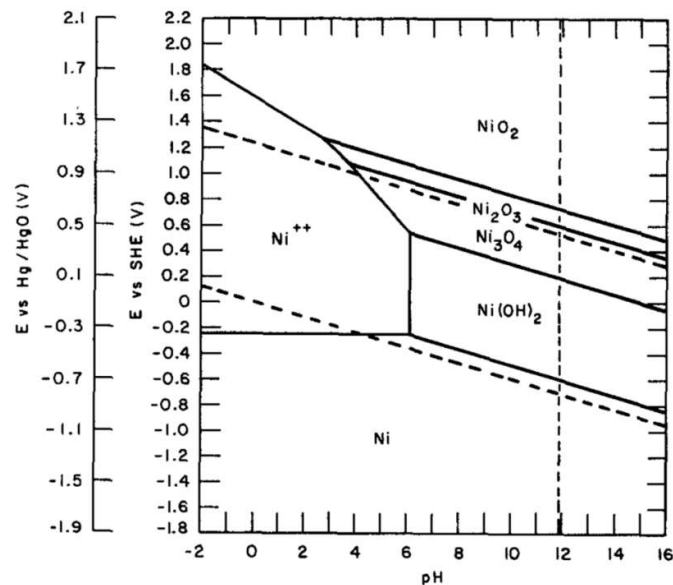


Figure 2.9 Pourbaix diagram of the Ni-H₂O system at 25 °C.^[70]

Using proper applied voltage and electrolyte, one can obtain porous oxide. A possible mechanism is described in Figure 2.10.^[71] Under open circuit potential, i.e., without any external applied voltage, a balance between mass transfer and electron transfer is reached. Specifically, Ni oxidation at the inner interface and oxygen reduction at the outer interface are balanced (Figure 2.10a). However, when a positive voltage is applied, film growth can take place in the absence of electron transfer through the film because oxygen reduction occurs at the cathode. The electrons will move into the external circuit (Figure 2.10b). The thickness of the oxide film is closely related to electrolyte composition, applied potential and so on. During this process, the oxide film begins to dissolve, forming pits under the assistance of electrical field as the film continues to grow (Figure 2.10c). As time goes on, under enough high voltage applied, ions in electrolyte solution are immersed into the oxide coating and meanwhile, Ni ions are migrated into the electrolyte, resulting in the observed porous structure (Figure 2.10d).

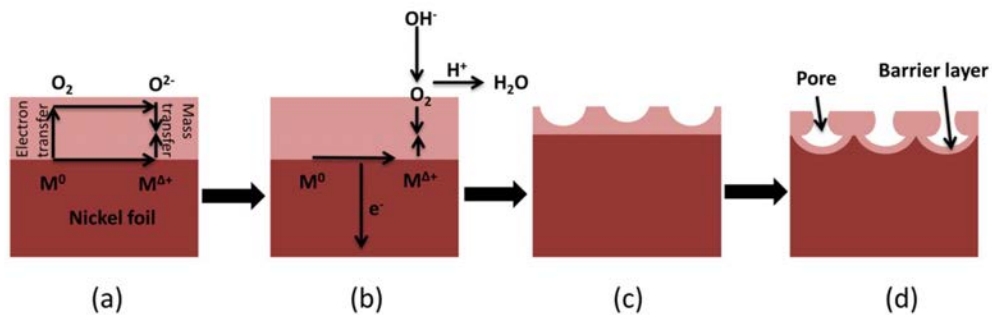


Figure 2.10 A schematic diagram of the possible steps towards the formation of porous oxide film. Oxide thickness is not drawn to scale.



Porous nickel-based films can be used as supercapacitor electrode materials. In order to form porous films, acids, neutral salts, and alkaline all positively take part in the anodization of nickel foil. Herein, aqueous and nonaqueous electrolytes for nickel foil anodization will be discussed.

According to the Einstein-Stokes relation (Equation 2.29),^[72] it is easy to understand the influence of aqueous and nonaqueous electrolytes on the porous structure formation at nickel.

$$D = \frac{K_B T}{6\pi\eta r} \quad (2.29)$$

where η is the dynamic viscosity, T is the absolute temperature, D is the diffusion rate constant, r is the radius of the particle, and K_B is Boltzmann's constant.

In aqueous electrolytes, due to the fast ion diffusion and mass transfer (Equation 2.29), the field-assisted dissolution of nickel is very quick and the oxide film is often very thin. In general, adjustment of pH value of electrolytes can improve the oxide film growth. Importantly, the oxide formation ability in acidic electrolytes exceeds that in alkaline solutions.^[65] For example, Yang *et al.*^[73] fabricated NiO nanorod-anchored Ni foam electrode by anodization in the aqueous electrolyte containing 0.3 mol L⁻¹ oxalic acid. After calcination of NiC₂O₄ at 400 °C ($\text{NiC}_2\text{O}_4 \cdot 2\text{H}_2\text{O} + \text{O}_2 \rightarrow \text{NiO} + 2\text{H}_2\text{O} + 2\text{CO}_2$), NiO nanorod-anchored Ni foam electrode was completed. Kruse and his coworkers^[74] produced porous nickel oxide layer using 99% sulfuric acids. The aforementioned Zhang's group prepared hierarchical nickel compound^[60] in aqueous



electrolyte of $0.15 \text{ mol L}^{-1} \text{ H}_2\text{SO}_4 + 0.0375 \text{ mol L}^{-1} \text{ CsCl}$, and sponge-like $\text{Ni}(\text{OH})_2$ - NiF_2 composite ^[61] in very concentrated acidic electrolyte of 1 wt% $\text{NH}_4\text{F} + 80\text{wt}\%$ H_3PO_4 .

A variety of organic electrolytes including dimethyl sulfoxide (DMSO), formamide, (FA), ethylene glycol (EG), and N-methylformamide (NMF), dimethyl formamide (DMF), 1-methyl-2-pyrrolidinone (NMP), etc., are widely-used. Motivated by the fact that EG is presented as an ideal electrolyte during the anodization of Ti to prepare various nanostructures, nickel foil is anodized in EG-containing electrolyte to realize porous nickel-based film. The donation of oxygen from organic electrolyte is more difficult in comparison with that from de-ionized (DI) water, thus reducing the ability to form oxides. At the same time, due to the viscosity of organic electrolyte, ion diffusion becomes slow (Equation 2.29), which has an influence on the pH value at the vicinity and consequently on the chemical dissolution of the oxide.^[67a,75] Overall, the use of EG as the electrolyte greatly change the anodization kinetics and resulting film morphologies.^[76] Besides, it is worth noting that F^- -based electrolyte is commonly known as etchants for many metals.^[67c,77] F^- ion addition may cause a dissolution of the formed oxide film and triggers the formation of a porous structure (Equations 2.26-2.28). Same as Ti anodization, the addition of NH_4F promotes porous structure formation. For example, Yang *et al.*^[43] recently used EG electrolyte containing $0.2 \text{ mol L}^{-1} \text{ NH}_4\text{F} + 2 \text{ mol L}^{-1} \text{ DI water}$ to anodize nickel foil for supercapacitor electrode material. The as-prepared porous NiF_2/NiO was treated by hydrothermal method ($\text{NiF}_2 + 2\text{NaOH} \rightarrow \text{Ni}(\text{OH})_2 + 2\text{NaF}_2$) in order to obtain 3D

porous $\text{Ni}(\text{OH})_2$ (Figure 2.11). The as-fabricated 3D film delivered a promising capacitance of 1765 F g^{-1} and the as-assembled device showed 90% of retention after 10,000 charge/discharge cycles. The high capacitance indicates that 3D open channel in the nanoporous structure provides more electrochemically active sites for redox reactions and fast ion transfer. The anodic film adheres strongly on to the nickel foil. Meanwhile, nanoporous structure can buffer the volume change during charging/discharging process. These factors result in good cycle life of the 3D nanoporous $\text{Ni}(\text{OH})_2$ thin film.

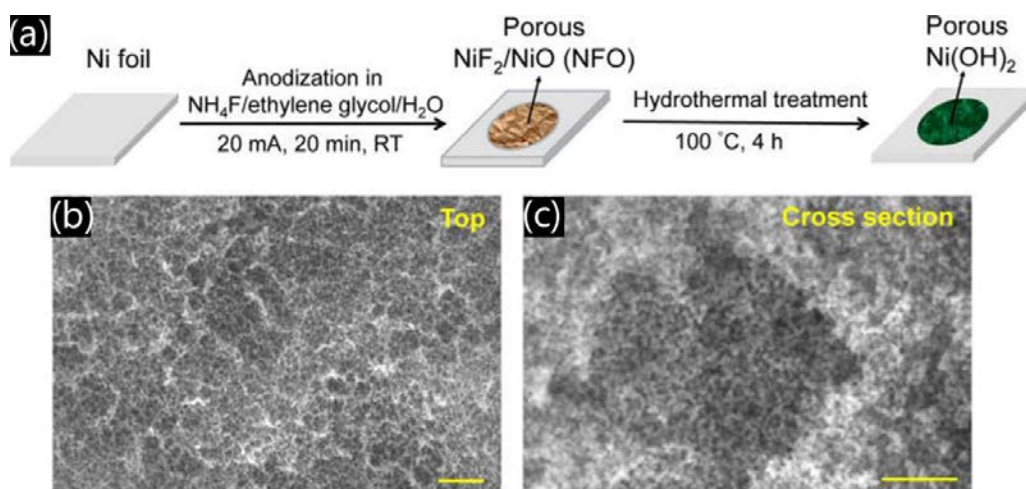


Figure 2.11 (a) Schematic for the fabrication process of 3D nanoporous $\text{Ni}(\text{OH})_2$ thin film, (b) top and (c) magnified-cross sectional SEM images of anodic nanoporous thin film.^[43]

Since the detailed theoretical modelling of pore formation in anodic nickel is not very clear,^[70,78] the mechanism of Ti anodization will be introduced instead. Macack *et*

al.^[79] previously reported the importance of F^- ion in the self-assembled pore formation of Ti. The current-time curve for electrolyte containing F^- ion during anodization process can be attributed to different stages in the pore formation process (Figure 2.12). For anodization of Ti in a fluoride-free electrolyte (e.g. H_2SO_4), the oxide film formation causes the decreased field strength, which leads to a sharp current decay and hence to the growth of a compact oxide layer with a finite thickness. When the electrolyte contains fluoride ions, chemical dissolution and field-enhanced dissolution due to the formation of TiF_6^{2-} complexes contribute to the tubular structure of TiO_2 .

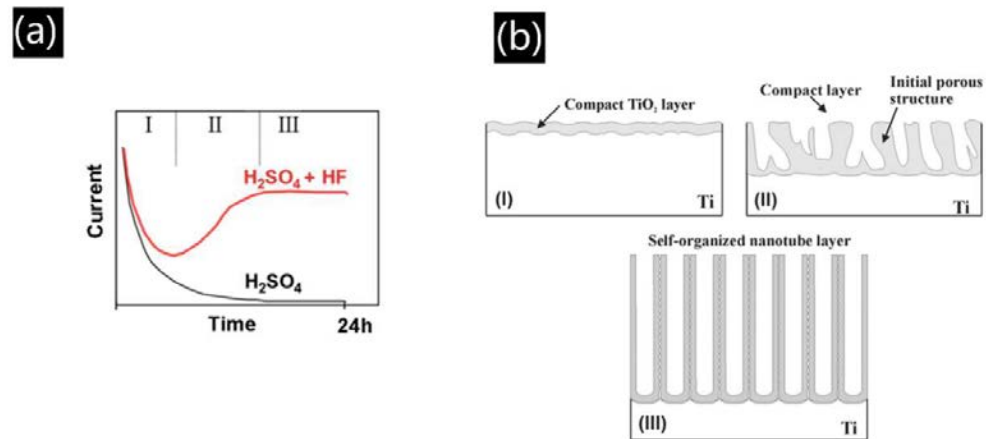


Figure 2.12 (a) Current-time curve for Ti anodization with and without fluorides in the electrolyte. (b) Corresponding evolution of TiO_2 morphologies with different current behavior.^[79]



2.3.3 Structure and properties of anodized oxide film

The samples prepared from a high constant potential generally have a rougher surface than that from a low constant potential.^[65] The high roughness of the samples results from quick field-enhanced dissolution. The rough surfaces provide enough space for the electric double layer charge storage.

As shown in Figure 2.11, the structure of the as-grown nickel-based film is strongly dependent on the specific electrochemical parameters, such as applied potential, electrolyte composition, anodization time, current density and temperature. For example, anodic oxide film on nickel electrodes in different pH solutions has been studied several decades ago. In 1976, MacDougall^[80] put forward that the oxide formed by steady-state oxidation of nickel at pH=8.4 had the same electrochemical characteristics as that formed under similar conditions at pH=4.5 or 2.8. The oxide films formed by steady-state oxidation for one hour at pH=2.8 and 8.4 in Na₂SO₄ aqueous solution were 9-10 Å in thickness. It is obvious that this behaviour cannot be explained by the aforementioned formation mechanism of porous anodic oxide film at nickel substrate. Another possible mechanism proposed by the author was the direct oxidation of the metal surface which involves a reaction such as: $Ni + H_2O \rightarrow NiO + 2H^+ + 2e^-$. This is direct electrochemical reaction between nickel foil electrode and water from the electrolyte solution. Due to the absence of chemical dissolution process, there is a tendency to form a compact structure instead of a porous one.



According to Equations 2.23 and 2.24, anodization for nickel foil generally generates NiO or Ni(OH)₂. For Ni(OH)₂, there exist two different phases: α-Ni(OH)₂ and β-Ni(OH)₂. The structure of α-Ni(OH)₂ contains many anions and water molecules and the formula of α-Ni(OH)₂ is generally written as Ni(OH)_{2-x}(Aⁿ⁻)_{x/n} · yH₂O, where x=0.2~0.4, y=0.6~1, and A= chloride, sulfate, nitrate, carbonate, or other anions.^[81] β-Ni(OH)₂ is isostructural with brucite and made up of closely stacked two-dimensional Ni(OH)₂ principle layers. Due to the large interlayer spacing of α-Ni(OH)₂ that allows the interlayer ions and molecules to move, its structure is more unstable than β-Ni(OH)₂. α-Ni(OH)₂ can be transferred to β-Ni(OH)₂ under concentrated alkaline, higher temperature, chemical aging, and electrochemical oxidation. The electrochemical processes that occurs at a nickel hydroxide electrode for supercapacitors is shown in Figure 2.13 which was initially proposed by Bode *et al.*^[82] From the scheme, α-Ni(OH)₂/γ-NiOOH is a reversible redox pair, where more electrons are exchanged per nickel atom because the oxidation state of nickel in γ-NiOOH is close to 3.5. Hence, it is likely that α-Ni(OH)₂ is more suitable for supercapacitor electrode than β-Ni(OH)₂, which has stronger electrocatalytic activity.^[83] The structural and electrochemical characteristics of α-Ni(OH)₂ and β-Ni(OH)₂ are presented in Figure 2.14. It can be seen that α-Ni(OH)₂ and β-Ni(OH)₂ have obviously different structure features and electrochemical potential, which leads to their different electrochemical performance. However, by electrochemical method, it is always difficult to obtain very pure α-Ni(OH)₂ electrode material. α-Ni(OH)₂ and β-Ni(OH)₂ often coexist in the materials.

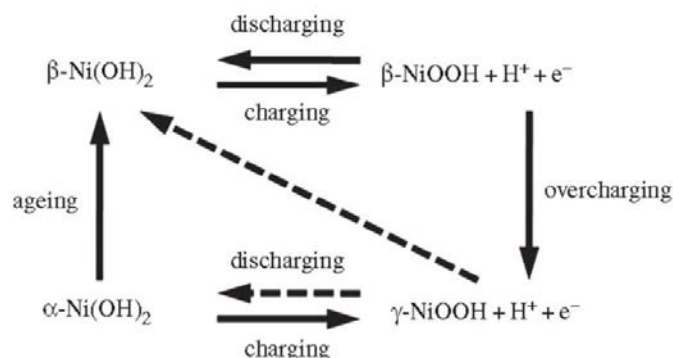


Figure 2.13 The general electrochemical reaction scheme at a nickel hydroxide electrode.

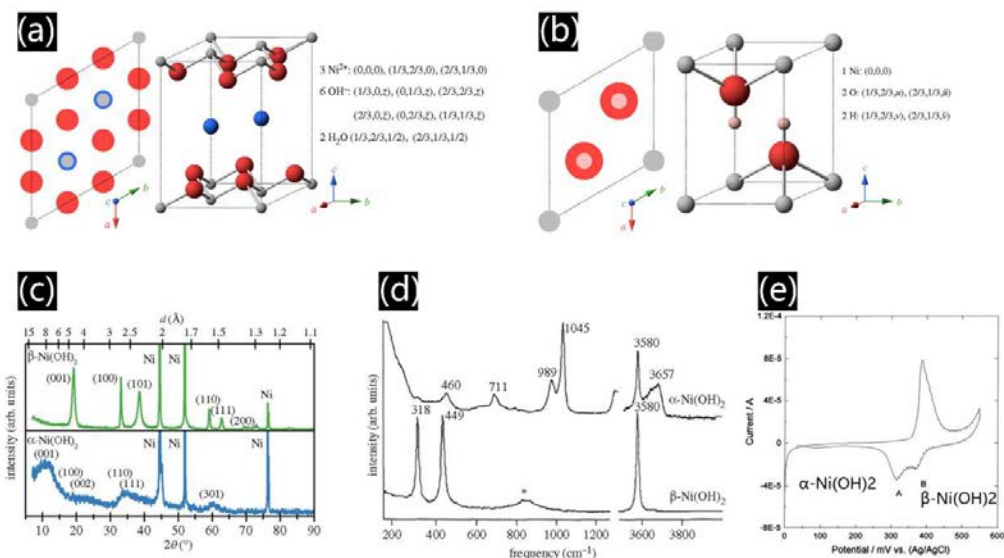


Figure 2.14 Unit cells of (a) α -Ni(OH)₂ and (b) β -Ni(OH)₂. (c) XRD pattern of α -Ni(OH)₂ and β -Ni(OH)₂. (d) Raman spectra of α -Ni(OH)₂ and β -Ni(OH)₂. (e) CV curve of nickel oxide electrode in 1 mol L⁻¹ KOH.^[84]

Considering that the theoretical capacitance of NiO (2573 F g⁻¹) is higher than that of Ni(OH)₂ (2069 F g⁻¹), it is necessary to carry out calcination treatment of Ni(OH)₂. Cheng *et al.*^[85] discussed the impact of calcination temperature on crystalline structure



and the specific capacitance. The result shows that a maximum specific capacitance of 696 F g^{-1} can be obtained at $250 \text{ }^\circ\text{C}$. Yet, when the calcination temperature of $\text{Ni(OH)}_2/\text{CNT}$ electrode increased to $300 \text{ }^\circ\text{C}$, the specific capacitance significantly decreased to 586 F g^{-1} . Although high crystallinity can result in higher conductivity, the decrease of specific surface area also reduces the number of active sites. On the other hand, low crystallinity can give rise to rich porous nanostructure as well as the high specific surface area. Therefore, the annealing temperature plays an important role in realizing the optimal specific capacitance.

As shown in Figure 2.15, Ni(OH)_2 has interstratification effect, and can be conveniently modified by doping with other divalent, trivalent elements (Co, Mn, Mo, N, S and so on).^[86] Therefore, many strategies can be devised for nickel hydroxide in order to achieve high performance electrode materials.

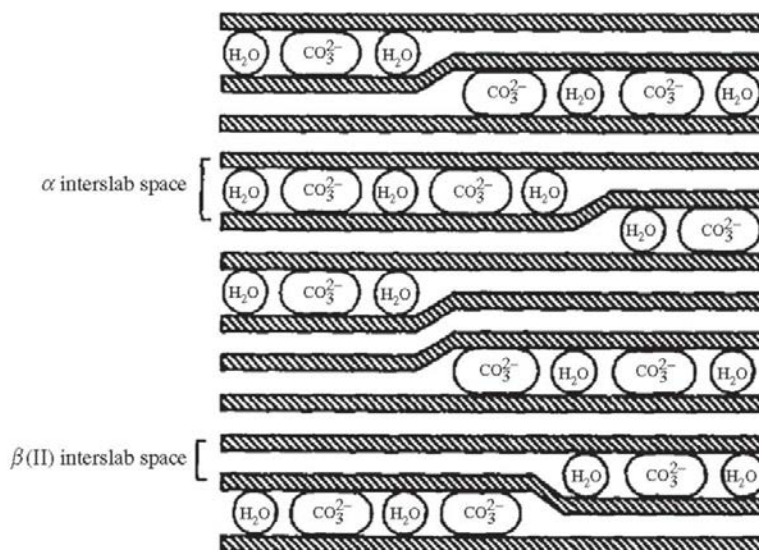


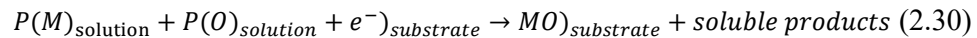
Figure 2.15 The schematic of α - Ni(OH)_2 and β - Ni(OH)_2 interstratification, in which both phases coexist with a crystal.^[84]



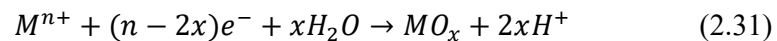
2.4 Cathodic deposition for nickel-based composite as supercapacitor electrode

2.4.1 Synthesis

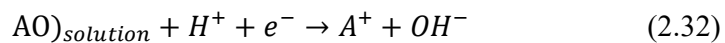
The reaction of oxide formation by cathodic deposition can be summarized as follows.^[57,87]



Where P(M) and P(O) is dissolved precursor species for the metallic M and oxygen O in a solution. The mechanism of cathodic electrodeposition of oxide can be split into two categories depending on which of the precursor P(i) receives electrons on the cathode. First case: the redox precursor is the metal species. By reduction, metal oxide or metal is directly deposited onto the electrode. The variation of valence state of metal ions from M(+n) to M(n-x) is illustrated in Equation 2.31.

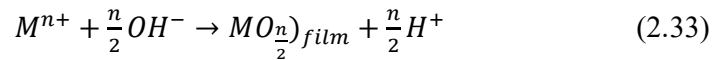


Second case: the redox precursor is the oxygen precursor (noted as AO) such as O₂, NO₃⁻, H₂O, or H₂O₂.





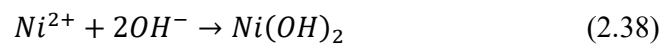
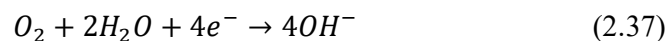
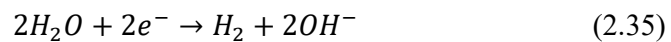
All these reduction reactions cause an increase in the pH of the electrolyte nearby the electrode surface, either by the consumption of H^+ ions or by the generation of OH^- ions. The metal ions precipitate directly onto the electrode surface as a form of an oxide or hydroxide (Equation 2.33).



Although there are two types of reactions, the reaction with the most positive potential value would be preferred over the others on purely thermodynamic considerations. The main reaction is the second type, i.e., the metal ions deposits in the form of a hydroxide or oxide on the cathode.

By the above theories, mixed oxide films can be achieved by mixing the precursors in the deposition bath, such as Ni-Co composite, Ni-Mn composite, Ni-Fe composite and so on. However, the co-deposition of multinary compound requires similar physico-chemical parameters of every oxide or hydroxide, including the deposition potentials, pH, and their kinetics.

The possible cathodic deposition reaction of nickel oxide/hydroxide can be described as follows.



Based on the above reactions, the surface of cathode in a cathodic deposition might form metal nickel, nickel oxide or nickel hydroxide in the electrolyte without reactive anion. The composition of deposits is decided by pH of the electrolyte and standard electrode potential of electrochemical reaction (see Figure 2.16). By cathodic deposition, the synthesis of nanometric nickel-based composite can be realized in the various morphologies of nanoparticles, nanowires, and nanoclusters for the application of supercapacitor electrode application. Overall, cathodic deposition is a versatile and low-cost tool for the synthesis of metal oxides/hydroxides.

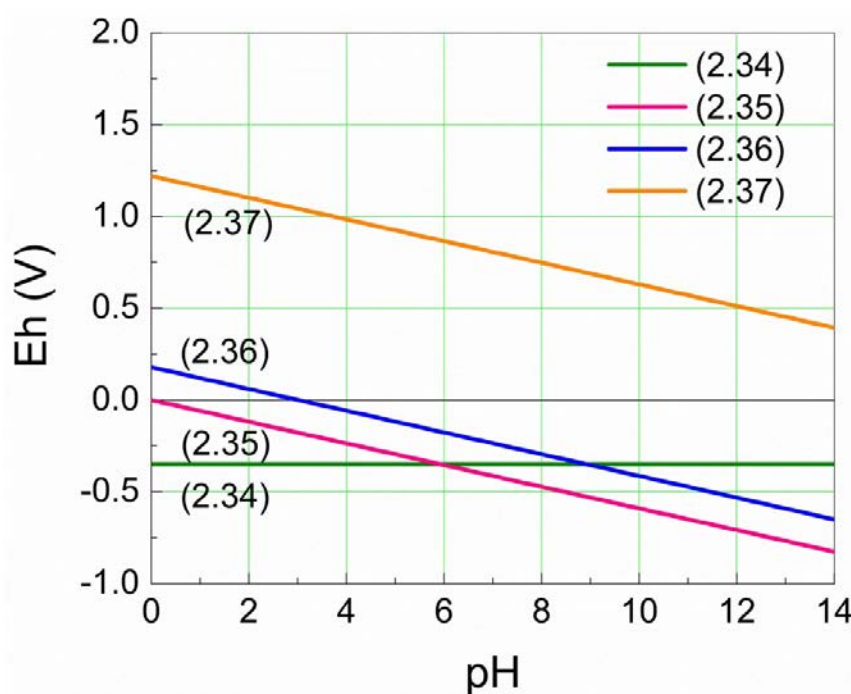


Figure 2.16 The pH-Eh diagram corresponding to different cathodic deposition equations.

2.4.2 Formation mechanism of structured cathodic deposits



The formation of nonstructured electrodeposits is related to their nucleation and growth. The formation mechanism involves surface adsorption of species for nucleation and selective growth of crystals due to the inhibited growth of certain crystal facets (Figure 2.17). In absence of organic additives, species^[88] like H_2 , H_{ads} , $(NiOH)_{ads}$, Ni^{2+} , $Ni(OH)_2$, $Ni_4(OH)_4^{4+}$ and $Ni(OH)^+$ which form due to the reduction of hydrogen ions, determine the microstructural features of electrodeposits. For example, electrodeposits of different textures normally have different hydrogen content.^[89] In the presence of unsaturated organic additives, these molecules are adsorbed on the surface via the unsaturated bonds, blocking certain sites on the nickel lattice and thus changing the growth rates of different crystal faces. The unsaturated bond reacts with hydrogen on the surface of the cathode and the resulting reduction products are desorbed from the surface and/or embedded into the deposit. The rates of these processes are affected by the characteristics of the organic molecules (size, shape, unsaturation degree, and functional groups, etc.) For example, the active group of sodium benzene sulfonate is =C-S. The sulfur anions after hydrogenolysis of =C-S prefer to be adsorbed on the (110) crystallization direction, causing the [100] texture to predominate.^[90]

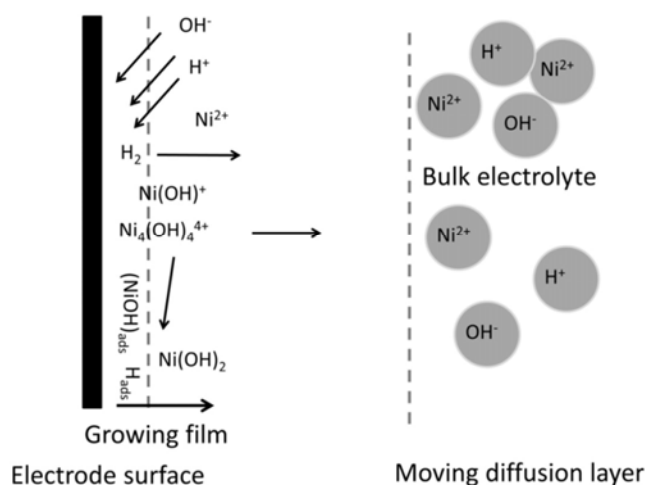


Figure 2.17 Scheme of the electrodeposition process on planar electrodes.^[88b]

In the nucleation processes, the overpotential plays an important role. Nickel with a high overpotential, tends to have a high nucleation rate ($R=A\exp[-B/\eta^2]$,^[91] where R is nucleation rate and η is overpotential) and the growth of crystals is therefore reduced. The growth process contains two steps: (i) lateral growth and coalescence of the nuclei (A-B segment of Figure 2.18) and (ii) outwards growth of electrodeposits by continuous nucleation growth (B-D segment). The former step plays a fundamental role in the determination of the structure of the initial deposition layer. The latter step has a bearing on crystal defects and granularity in the bulk of the electrodeposited layer. Due to different growth rate, the crystal faces are formed. Fast-growing faces grow to die out and slow-growing faces survive. In order to realize two/three-dimension microstructures by massive nucleation and promotion or suppression of

grain growth, high cathodic overvoltage, high adion surface coverage and low surface mobility are required.

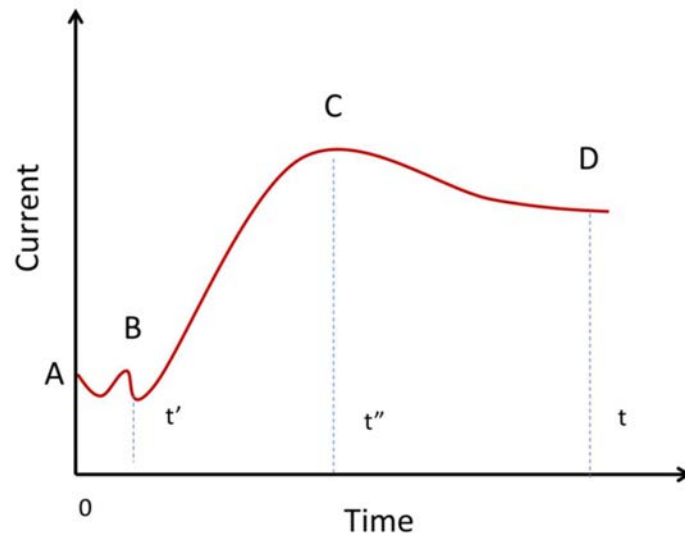


Figure 2.18 General shape of the transients of time-current curve observed for nickel electrodeposition under most conditions.^[92]

Figure 2.18 illustrates the general features of current-time curve which is observed in the initial stages of electro-crystallization of nickel.^[92] The current variation highlights two/three-dimension nucleation and crystal growth. A-B is the electrodeposition of a monolayer of nickel via two-dimensional nucleation and crystal growth accompanied by hydrogen evolution on both the edges and tops of the growth centers. B-C is three-dimensional nucleation and crystal growth on top of the first monolayer with hydrogen evolution. C-D is the overlap of growth centers followed by the outward growth into the solution accompanied by the death and rebirth of nuclei.



The nucleation and growth of nanometric electrodeposits are influenced by many factors, and the final textures are a combination of two/three-dimension growth, the death and rebirth of nuclei, and the secondary three-dimension growth on the top of the first layer.

Besides, cathodic deposition of nanostructured materials can be influenced by the surface of the cathode, which acts as a template. Various desired architectures or morphologies can be achieved by adjusting the surface morphology of the cathode. Such template-assisted electrodeposition can be divided into two types: active template-assisted and regular template-based electrodeposition. The former templates can be used as part of the substrate as an active current collector. The former templates are generally removed after deposition. The formation of nanostructures by assisted method arises from the growth of nuclei that conformally nucleate on the substrate surface. The subsequent growth of these nuclei at the templates generates the desired surface morphology of the surface.

Zhang *et al.*^[93] synthesized nano-forest of hierarchical $\text{Co}_3\text{O}_4@\text{NiCo}_2\text{O}_4$ nanowire arrays. As shown in Figure 2.19a, Co_3O_4 nanowire array template which were vertically grown on the Ni foam substrate was synthesized by a hydrothermal reaction (step i), followed by the co-deposition of Ni-Co oxide nanoflakes on Co_3O_4 nanowires was finished (step ii). The SEM images demonstrated the core-shell structure (Figures 2.19b and 2.19c). On the one hand, the introduction of Co_3O_4 nanowire array avoided the aggregation and benefited sufficient ion diffusion. On the other hand, NiCo_2O_4 can

also reduce the charge-transfer resistance of Co_3O_4 , resulting in fast electron transport within active materials. The synthesized nanoforest-like hierarchical structure exhibited excellent electrochemical performance. A high areal capacitance of 2.04 F cm^{-2} at a scan rate of 5 mV s^{-1} and 0.79 F cm^{-2} even at 30 mA cm^{-2} after 6000 cycles were achieved, almost 2.5 times higher than pristine Co_3O_4 (Figure 2.19d).

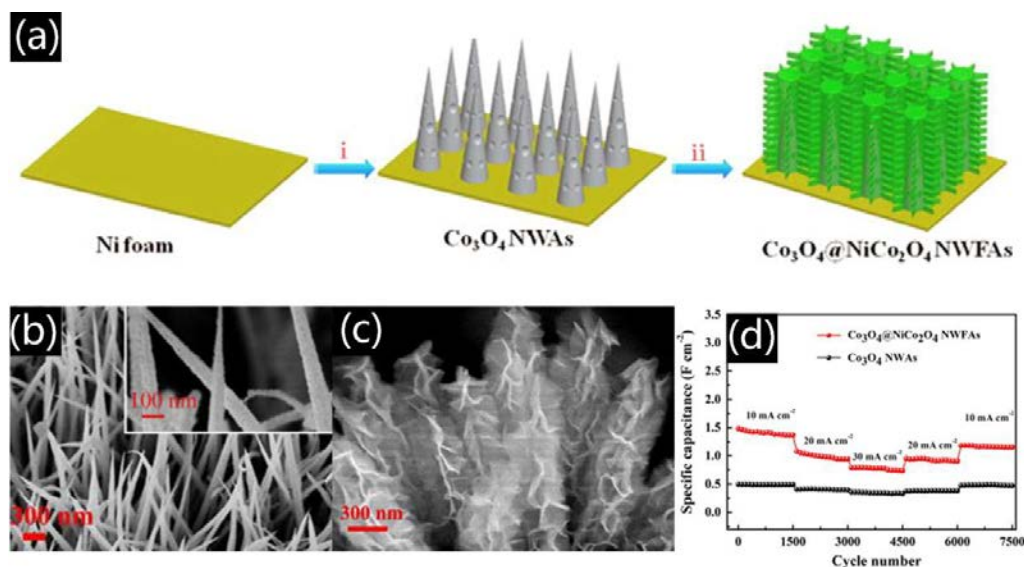


Figure 2.19 (a) Schematic of the fabrication process of $\text{Co}_3\text{O}_4@/\text{NiCo}_2\text{O}_4$ nanowire arrays. (b) top-view SEM images of $\text{Co}_3\text{O}_4@/\text{NiCo}_2\text{O}_4$ nanowire arrays on Ni foam. (c) The magnification of (b). (d) Cycling performance of $\text{Co}_3\text{O}_4@/\text{NiCo}_2\text{O}_4$ nanowire arrays at various current densities.^[93]

Chu *et al.*^[94] utilized the nitrated TiO_2 nanorod arrays (NTNA) on the carbon fiber paper (CFP) as three-dimension nanostructured current collector for supercapacitor electrode, where MnO_x was electrodeposited on NTNA/CFP (Figure 2.20a). The as-prepared $\text{MnO}_x/\text{NTNA}/\text{CFP}$ showed the larger current density than other electrodes

(Figure 2.20d), indicating higher specific capacitance. When the current density was increased from 0.25 to 2 mA cm⁻², MnO_x/NTNA/CFP exhibited only 22% loss in areal capacitance, which was smaller than the 57% loss of MnO_x/CFP, and 77% loss of MnO_x/TiO₂/CFP (Figure 2.20e). The better rate capability resulted from the introduction of nitrated TiO₂ nanorod arrays which improved the accessible active surface and reduced ion diffusion path compared with MnO_x/CFP. The cyclic stability of MnO_x/NTNA/CFP was better than MnO_x/CFP, remaining 96% of the initial capacitance for up to 5,000 cycles (Figure 2.20f).

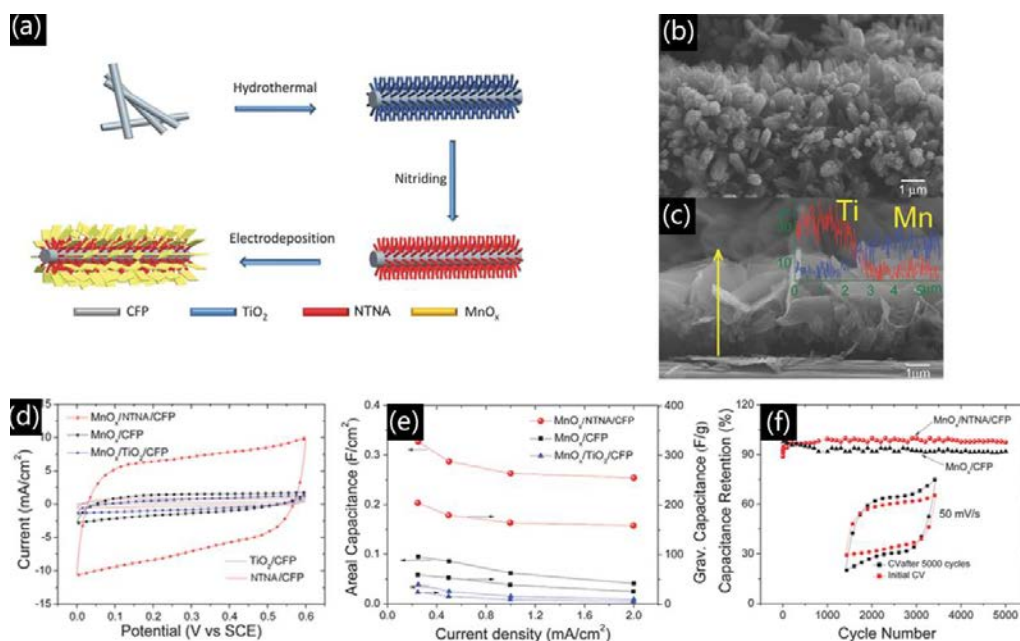


Figure 2.20 (a) Schematic illustration of the synthesis procedure of MnO_x/NTNA/CFP. (b) SEM image of NTNA on CFP. (c) Side-view SEM image of MnO_x/NTNA/CFP. (d) CV curves of MnO_x/NTNA/CFP, MnO_x/CFP, MnO_x/TiO₂/CFP, TiO₂/CFP, and NTNA/CFP at a scan rate of 50 mV s⁻¹. (e) The rate



capability of $\text{MnO}_x/\text{NTNA}/\text{CFP}$, MnO_x/CFP and $\text{MnO}_x/\text{TiO}_2/\text{CFP}$. (f) Cyclic stability of $\text{MnO}_x/\text{NTNA}/\text{CFP}$ and MnO_x/CFP at a current density of 1 mA cm^{-2} for up to 5000 cycles. The inset is CV curves of $\text{MnO}_x/\text{NTNA}/\text{CFP}$ before and after cycling at 50 mV s^{-1} .^[94]

Using the similar strategy, Singh *et al.*^[95] fabricated Ni@NiO core/shell nano-heterostructures (NHs) using the anodic aluminium oxide (AAO) template (Figure 2.21). After the removal of AAO, the hydrogenated Ni/NiO (H-Ni/NiO) nanowires showed a high specific capacitance of about 1722 F g^{-1} at a current density of 8.6 A g^{-1} . When the scan rate increased from 2 to 100 mV s^{-1} , the specific capacitance of H-Ni@NiO core/shell NHs electrode decreased from 1635 to 627 F g^{-1} , with only a loss of 38.4% of the initial capacitance. The good performance may be attributed to the one-dimensional nano-heterostructures with high aspect ratio and the increased reactive surface area.

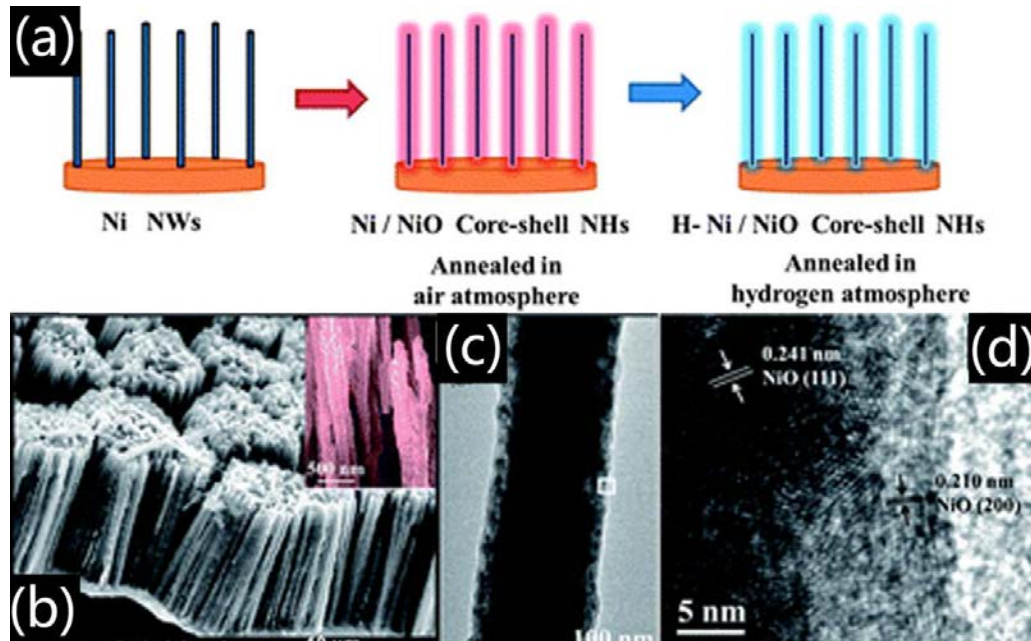


Figure 2.21 (a) Scheme for the preparation process of H-Ni@NiO core/shell NH electrodes. (b) FESEM, (c) TEM and (d) HRTEM micrographs of H-Ni@NiO core/shell NH electrodes.^[95]

In summary, by template-assisted electrodeposition, the growth of deposits can be controlled and well-defined morphologies of deposits can be achieved. The surface characteristics of the electrode substrate seriously affect the electrodeposits. Therefore, further studies on electrode surfaces and multi-dimensional substrate are essential for the successful preparation of nanostructures using electrodeposition.

2.4.3 Specific advantages of cathodic deposition

Cathodic deposition is a technique that holds many advantages for the fabrication of nanostructured materials for supercapacitors, such as rapidity, potential to solve shape limitation, material production on widely different substrates, and the ability to prepare composites unachievable by other techniques. Particularly, cathodic deposition as a strategy of self-supported electrodes has become a hot research field. Three-dimensional self-supported nanostructures can be easily fabricated by cathodic deposition. Electrodes fabricated by self-supported techniques give attracting features over slurry-cast electrodes in terms of surface area and electron transport. A schematic illustration of an idealized three-dimensional self-supported electrode by cathodic deposition is shown in Figure 2.22.^[3b]

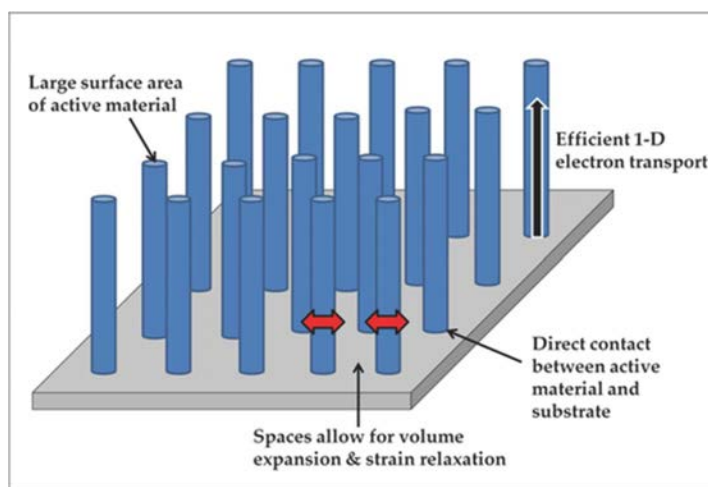


Figure 2.22 Schematic illustration of three-dimensional self-supported structure by electrochemical deposit.^[3b]



The fabricated self-supported electrodes offer many advantages for energy storage over electrodes composed of nanoparticles of active materials dispersed in a matrix of binder and conducting agent.

(i) High surface area: Porous or hierarchical structure increases the specific surface area of electrode material, which is very important for supercapacitor to improve its energy density, power density and specific capacitance.

(ii) Tunable free space of the electrode: The porous structure allows the swelling and shrinking of the electrode during charge/discharge, and avoids structural collapse of the electrode, which is beneficial to the improvement of cycling performance.

(iii) Nanostructured active electrode: The nanostructured materials are directly bonded to the surface of the substrate, which reduces contact resistance and increases electronic conductivity.

(iv) Improved electronic and ionic conductivity. The hierarchical structure by cathodic deposition often leads to out of equilibrium lattice defects. By KrogerVink nomenclature:^[96] $O_o \rightleftharpoons V_o^{\cdot\cdot} + 2e^- + 1/2O_2(g)$, positively charged oxide ion vacancies ($V_o^{\cdot\cdot}$) are compensated by the injection of electrons (e^-) into the conduction band. That is, oxides with a large surface area will present a large oxygen deficiency and consequently a large electronic conductivity, due to excess electrons.^[97] At the same time, nanostructured oxides by cathodic deposition may be doped with other ions in the reaction medium, which may be adsorbed at the surface resulting in surface sites



and/or space charge regions^[98] or incorporated into the oxide bulk leading to further ionic defects.^[99] A large number of adsorbed or dissolved dopant ions will enhance the ionic conductivity of oxides in nanostructured form.^[100]

(v) Assortment of possible structure and composition. By cathodic deposition, hierarchical structure and various morphologies can be obtained by adjusting deposition conditions such as applied voltage, temperature, current density, pH value, electrolyte composition and so on. Besides, by changing the surface of the conductive substrate, different structures and morphologies can be realized. The co-deposition of multi-metal oxides/hydroxides by electrochemical method can resolve the synthesis of different metal composites.

2.5 Summary

Based on the above literature review, the thesis structures and the following strategies adopted to achieve excellent supercapacitor performance are proposed in Figure 2.23.

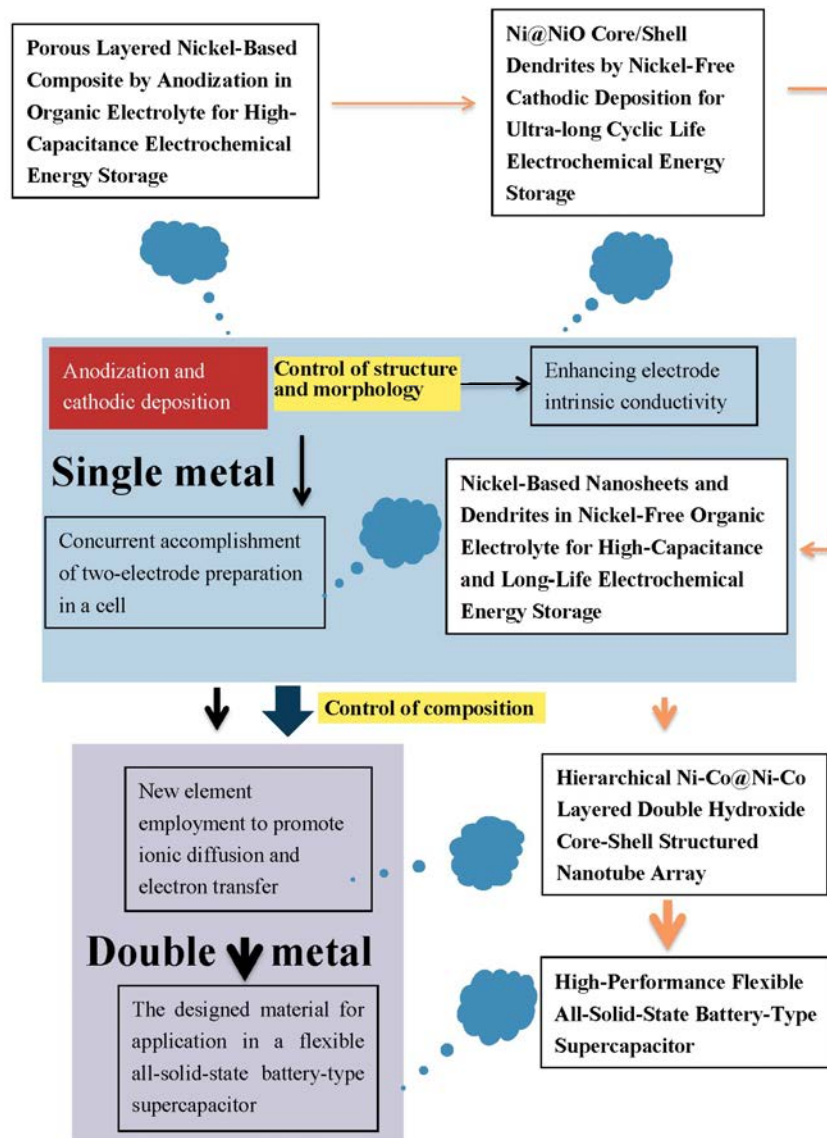


Figure 2.23 Illustration of the thesis structures and the following possible approaches for enhancing battery-type supercapacitor performance.



Chapter 3 Experimental Methods

3.1 Electrochemical synthesis of nickel-based composites

All the chemicals (purchased from Sigma-Aldrich Corp) used were of analytical grade and were used as received without further purification.

3.1.1 Anodization of nickel foil in organic electrolytes with different water contents

Prior to the experiment, nickel foils (0.2 mm thickness, 99.6% purity, Yirun Pte. Ltd., China) was degreased in ultrasonic bath using acetone, and ethanol for 30 min, respectively, followed by washing with DI water and drying in hot air. The anodization was carried out by a DC Supply System (N5751A, Agilent Technologies Ltd, US) in ethylene glycol (EG) electrolyte containing NH_4F (0.1% w/w) and DI water (from 0 to 5% v/v) without unstirring. Both anode and cathode were nickel foils (0.5 cm \times 4 cm). The Ni foils were subjected to potentiostatic anodization at 60 V for different time. All experiments were carried out at 40 °C (controlled by a thermostat water bath). After that, the as-synthesized samples on the anode were soaked in ethanol for 2 hours and then rinsed with DI water, followed by drying in hot air for further usage.



3.1.2 Cathodic deposition of nickel-based composite in nickel-free organic electrolyte

Prior to the experiment, nickel foils (0.2 mm in thickness, 99.6% in purity, Yirun Pte. Ltd., China) was degreased ultrasonically in acetone and ethanol, consecutively, for 30 min, followed by washing with de-ionized (DI) water and drying in hot air. The electro-deposition of active materials was carried out by a DC power supply (N5751A, Agilent Technologies Ltd, US) in EG electrolyte containing NH_4F (0.1% w/w) and DI water (3% v/v), with two nickel foils (0.5 cm \times 4 cm) for both anode and cathode. The foils were subjected to potentiostatic electrodeposition at 60 V for 60 min. All the experiments were carried out at 40 °C in a controlled thermostat water bath. The deposited cathodic electrodes were soaked in ethanol for 2 hours, then rinsed with DI water and followed by drying in hot air.



3.1.3 Anodization of nickel foil and cathodic deposition of nickel-based composite in a bath with nickel-free organic electrolyte

Prior to the experiment, nickel foils (0.2 mm thickness, 99.6% purity, Yirun Pte. Ltd., China) was degreased in ultrasonic bath using acetone, and ethanol for 30 min, respectively, followed by washing with DI water and drying in hot air. The anodization was carried out by a DC Supply System (N5751A, Agilent Technologies Ltd, US) in EG electrolyte containing NH_4F (0.5% w/w) and DI water (3% v/v) without stirring. Two nickel foils (0.5 cm \times 4 cm) were used for both anode and cathode, and they were subjected to potentiostatic electrodeposition at 60 V for 60 min. All experiments were carried out at room temperature. After that, the as-synthesized samples on the anode and cathode were soaked in ethanol for 2 hours and then rinsed with DI water, followed by drying in hot air for further usage.

3.1.4 Design of the Ni-Co@Ni-Co layered double hydroxide nanotube arrays and the assembly of the device

Electrodeposition was carried out in a two-electrode electrolytic cell by galvanostatic electrodeposition. Platinum plate was used as the counter electrode (1cm \times 5cm) and the commercial CFC (WOS1002) was utilized as the working electrode (1cm \times 5cm).



Preparation of ZnO NRAs on CFC: ZnO NRAs were grown on CFC by electrodeposition in the solution of 1 mmol L⁻¹ Zn(NO₃)₂ and 5 mmol L⁻¹ NH₄NO₃ at a current density of 0.8 mA cm⁻² for 1.5 h at 75 °C. During the electrodeposition process, the electrolytic cell was kept sealed to avoid water evaporation. After the deposition, CFC appeared white with the coating. As-deposited CFC was then washed thoroughly by deionized water and ethanol.

Preparation of Ni-Co@Ni-Co LDH NRAs on ZnO: Ni-Co@Ni-Co LDH NRAs were fabricated by electrodeposition of Ni-Co LDHs on the ZnO NRA-coated CFC with a current density of 4 mA cm⁻² at 50 °C for 1.5 h. The electrolyte was 60 mL of 4 mM metal ion solution with various Ni²⁺/Co²⁺ feeding concentration ratios of 10:0, 7:3, 5:5, 3:7 and 0:10. The deposited CFC appeared black and was rinsed with deionized water and ethanol for several times. Finally, the obtained materials were dried at 60 °C for 24 h. For comparison, Ni-Co@Ni-Co LDHs/CFC without ZnO template (Ni:Co=5:5) was prepared based on above process.

Preparation of Ni-Co@Ni-Co LDH NTAs on CFC: The ZnO NRA template was completely removed by immersing the sample in 1 mol L⁻¹ NaOH for 6 h to produce Ni-Co@Ni-Co LDH NTAs/CFC.

Preparation of MgCO₃/Ni(Ac)₂/PAN suspension: 1.0 g MgCO₃·3H₂O and 0.2 g Ni(Ac)₂·4H₂O were added in 10 mL DMF. After stirring for 2 h, a dispersed suspension was obtained. Meanwhile, 1.9 g PAN was dissolved in 10 mL DMF at 70°C with continuous stirring for 1 h. The suspension was then transferred to PAN



solution with vigorous stirring for 3 h. Finally, the $\text{MgCO}_3/\text{Ni}(\text{Ac})_2/\text{PAN}$ suspension was obtained.

Electrospinning of $\text{MgCO}_3/\text{Ni}(\text{Ac})_2/\text{PAN}$ suspension: The suspension was spun into nanofibers using electrospinning. In a typical process, the suspension was loaded into a 20 mL plastic syringe with a stainless steel pinhead connected with a 17 kV DC supply, and extruded at room temperature in air at a feeding rate of 0.06 mm min^{-1} . A distance of 20 cm was kept between the needle tip and the aluminum foil collector.

Preparation of CNFs: $\text{MgCO}_3/\text{Ni}(\text{Ac})_2/\text{PAN}$ nanofibers were firstly dried at $60 \text{ }^\circ\text{C}$ for 3 h, and then annealed at $250 \text{ }^\circ\text{C}$ for 2 h in air for composite stabilization. Subsequently, carbonization was carried out at $450 \text{ }^\circ\text{C}$ for 1 h and $800 \text{ }^\circ\text{C}$ for 3 h in N_2 to obtain $\text{MgO}/\text{Ni}/\text{carbon}$ nanofiber with a heating rate of $5 \text{ }^\circ\text{C min}^{-1}$. After that, a mixture of $\text{MgO}/\text{Ni}/\text{carbon}$ nanofiber with KOH was added into 200 ml deionized water followed by vigorous stirring at $120 \text{ }^\circ\text{C}$ until the formation of a slurry. The slurry was then calcined at $250 \text{ }^\circ\text{C}$ for 30 min and $750 \text{ }^\circ\text{C}$ for 1 h in a tube furnace under N_2 atmosphere with a heating rate of $5 \text{ }^\circ\text{C min}^{-1}$. Finally, the as-obtained product was further treated using diluted HNO_3 solution to remove Ni, MgO and KOH , then filtrated and washed with deionized water until the filtrate became neutral. CNFs were obtained after subsequent drying at $60 \text{ }^\circ\text{C}$ for 12 h.

Preparation of CNFs on the CFC: A slurry was obtained by mixing carbon nanofibers (as the active material), with acetylene black (as conductive agent) and polyvinylidene fluoride (as the binder) in a mass ratio of 80:10:10 in 1-methyl-2-pyrrolidinone. The



paste was then pressed onto carbon fiber cloth (1cm×3 cm) and dried at 80 °C for 24 h.

Preparation of PVA-KOH gel electrolyte: PVA-KOH gel electrolyte was prepared using PVA (molecular weight: 6450 g mol⁻¹) and KOH. Firstly, 2 g PVA was dissolved in 20 mL deionized water by continuous stirring and kept at 90 °C for 2 h until a clear viscous solution was obtained. When it was cooled down, 2 g of concentrated KOH solution was added to the viscous solution slowly under stirring until a clear solution was prepared.

Fabrication of battery-type supercapacitor: The as-prepared Ni-Co@Ni-Co LDH NTAs/CFC and CNFs/CFC were soaked into the hot PVA-KOH gel electrolyte (50~60 °C) for 10 min and hung for 15 min under ambient condition to allow the electrolyte to diffuse into the nanoporous structure of the active materials. This coating process was repeated three times. Then the two electrodes were pressed against each other and dried in hot air until the gel electrolyte was solidified and the deionized water evaporated. Silver paste was used for electric contact between CFC and the instrument. The as-fabricated battery-type supercapacitor is labeled as Ni-Co@Ni-Co LDH NTAs/CFC || CNFs/CFC.



3.2 Characterization and analysis of nickel-based composites

3.2.1 Structural and elemental characterizations

Scanning electron microscope (SEM, TM 3000, Hitachi, Japan) was used to characterize the morphology of different samples.

Transmission electron microscope (TEM, JOEL JEM-2010, Japan) was used to investigate the detailed morphologies and microstructures of the samples. The active materials were scraped-off from the substrates and dispersed in the ethanol, followed by dropping onto the specialized TEM copper grids with carbon membrane.

Energy dispersive spectroscopy (EDS) was employed to both qualitatively and quantitatively analyze the sample composition. EDS sample preparation is the same as the preparation for TEM samples.

X-ray diffraction (XRD, Rigaku D/max IIIA, Cu α , $\lambda=0.15418$ nm, Japan) was performed to examine the crystalline structure of the samples. Nickel-based composites by anodization were directly measured together with the substrate. For nickel-based composites by cathodic deposition, the active materials were flaked-off from the substrate, and the as-obtained powders were used for XRD measurement.



Indexing of the diffraction data can be performed using software like “Jade” with ICDD database.

Raman spectra were taken on a HORIBA HR800 Raman spectrometer at 488 nm to analyze the chemical bonding of functional groups in the samples.

X-Ray photoelectron spectroscopy (XPS, ESCALAB 250Xi) measurements were employed to study the surface chemical state of elements in the as-prepared samples inside an ultrahigh vacuum chamber. Depth profile XPS was used to indirectly analyze the elemental distribution of samples along the direction perpendicular to the substrate. Samples were etched at a rate of 3 nm min⁻¹ by Ar⁺ ions.

Brunauer–Emmett–Teller (BET) measurements (Micromeritics ASAP2020) were used to determine the N₂ adsorption/desorption surface area of samples.

3.2.2 Electrochemical characterizations

Electrochemical characterizations, such as cyclic voltammetry (CV), galvanostatic charge/discharge (GCD) and electrochemical impedance spectroscopy (EIS, 5 mV amplitude, 0.01~100 kHz frequency range) were carried out by an electrochemical workstation (CHI660e) in 1 mol L⁻¹ NaOH with a three-electrode system. The as-prepared samples were directly used as the work electrode. Platinum was used as the counter electrode, and saturated calomel electrode (SCE) was used as the reference electrode.



Gravimetric or areal specific capacitance (C) of different electrodes can be measured by CV curves according to the following equation:

$$C = \frac{\int I(V)dV}{2\nu VS} \quad (3.1)$$

where $I(V)$ is the response current density (A), ν is the scan rate ($V s^{-1}$), V is the potential window (V), and S is the active weight or area of the electrode (g or cm^2).

Alternatively, gravimetric or areal specific capacitance (C) of different electrodes can be calculated from GCD tests based on the following equation:

$$C = \frac{I\Delta t}{\Delta VS} \quad (3.2)$$

where I is the discharge current (A), Δt is the discharge time (s), ΔV is the potential window (V), and S is the active weight or area of the electrode (g or cm^2).

Besides, long-term cycling tests were carried out using either CV or GCD test.

3.2.3 Flexible device test

The electrochemical performance of the as-assembled flexible device (Ni-Co@Ni-Co LDH NTAs/CFC || CNFs/CFC) was evaluated by CV, GCD and EIS techniques using a two-electrode system. CV curve was performed in the range of 0 to 1.7 V, EIS in the frequency range of 10 mHz to 100 kHz with a 5 mV AC amplitude, and GCD test in the range of 0 to 1.5 V at the current densities of 2, 5, 10, and 20 $A g^{-1}$. All electrochemical tests were carried out at room temperature (20 °C).



For supercapacitors with the optimized capacitance, it is known that the charge (Q) should be carefully balanced using the following Equations 3.3 and 3.4.

$$Q^+ = Q^- \quad (3.3)$$

$$Q = C\Delta Em \quad (3.4)$$

where C is gravimetric specific capacitance ($F\ g^{-1}$), + and – represent positive and negative electrodes, respectively. ΔE is the potential range during charge/discharge process. m is the mass of the electrode material. As a result, the mass balance will be expressed as follows.

$$\frac{m_+}{m_-} = \frac{C_- \Delta E_-}{C_+ \Delta E_+} \quad (3.5)$$

Gravimetric specific capacitance (C_{cell}) of the whole device can be calculated from GCD tests based on the following equation:

$$C_{cell} = \frac{I\Delta t}{\Delta V m} \quad (3.6)$$

where I is the discharge current (A), Δt is the discharge time (s), ΔV is the voltage window of the device (V), and m is the whole active weight of positive and negative electrode (g).

What's more, the power density and energy density were calculated to illustrate the energy delivery characteristics of the device, which is eventually plotted as Ragone plot. The power density and energy density of the device can be calculated by the following equations:

$$W = \frac{1}{2 \times 3.6} CV^2 \quad (3.7)$$



$$P = \frac{3600W}{t} \quad (3.8)$$

Where W is energy density (W h kg^{-1}), C is gravimetric specific capacitance of the device (F g^{-1}), V is the voltage window of the device, P is the power density (W kg^{-1}), t is the discharge time of the device (s).



Chapter 4 Porous Layered Nickel-Based Composite by Anodization in Organic Electrolyte for Supercapacitor

4.1 Motivation

In this chapter, layered nickel compound film ($\text{Ni}(\text{OH})_2/\text{Ni}_2\text{O}_3$) was fabricated in an organic electrolyte for battery-type supercapacitor application by a one-step anodization process. Compared with previous reports ^[60,101] where aqueous solution was used as the electrolyte for anodization, nickel compound prepared in ethylene glycol electrolyte achieved higher specific capacitance and more stable cycling life (3280 F g⁻¹ at 1 A g⁻¹, 95.6 % retention after 5,000 cycles). This method has several advantages: (i) the organic electrolyte suppresses the ion diffusion, and the rate of crystal nucleation, which may further influence the material structure. (ii) (ii) the growth of active material directly on the substrate simplifies the preparation process; and (iii) porous layered structure increases the number of active sites and shortens the ion diffusion and transfer paths, beneficial to high specific capacitance. As a result, the layered nickel compound exhibited excellent specific capacitance (3280 F g⁻¹). Herein, we utilize a simple and cost-effective method to realize good performance of electrode materials for battery-type supercapacitors.

4.2 Structural and elemental characterizations

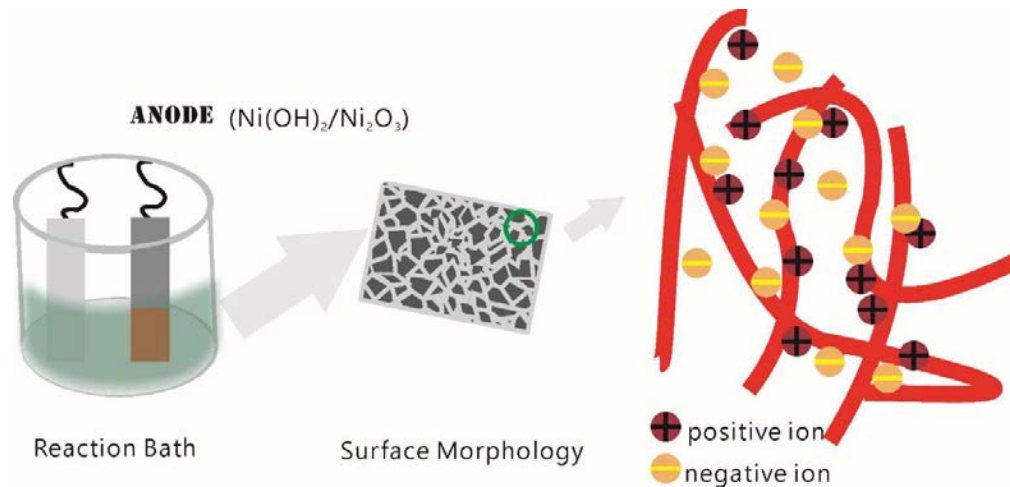


Figure 4.1 Schematic diagramme showing the fabrication process of layered nickel composite thin film. Anodization is done in a two-electrode system in the EG electrolyte.

Figure 4.1 shows the method used to prepare porous layered Ni(OH)₂/Ni₂O₃ electrode materials. First, plain nickel foil was immersed in the organic electrolyte for anodization. Then layered porous structure of the active material was deposited on the surface of anode.

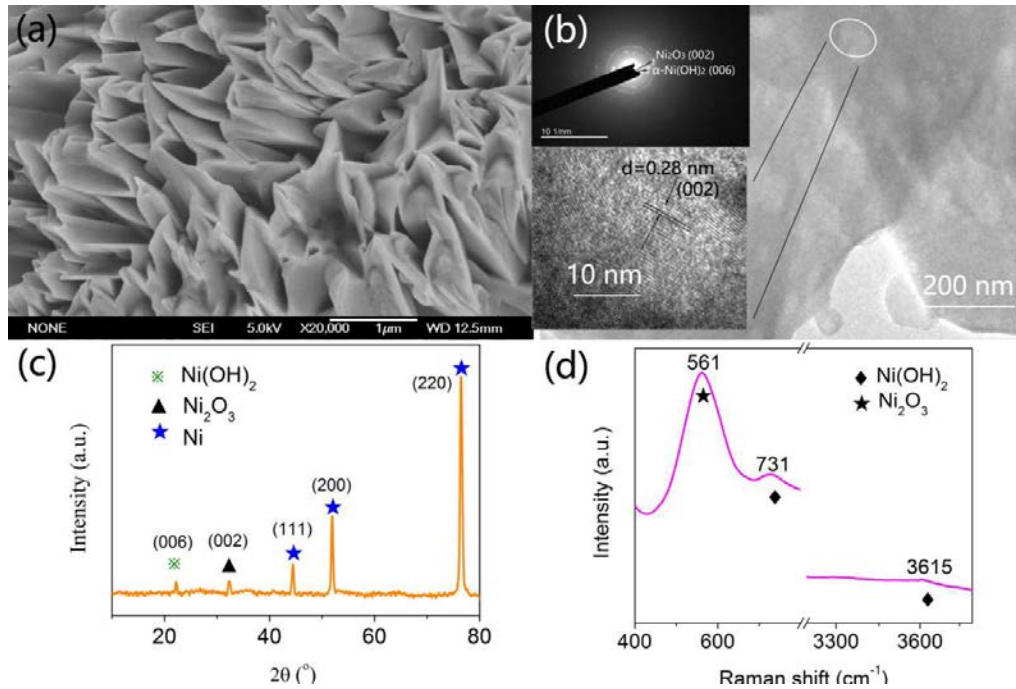


Figure 4.2 Characterization of the structure: (a) SEM images of Ni(OH)₂/Ni₂O₃. (b) TEM characterization of Ni(OH)₂/Ni₂O₃. Inset: SAED pattern and high resolution (HRTEM) of the marked area. (c) XRD patterns of Ni(OH)₂/Ni₂O₃. (d) Raman spectrum of Ni(OH)₂/Ni₂O₃.

The morphologies of Ni(OH)₂/Ni₂O₃ were characterized by SEM and TEM. SEM image (Figure 4.2a) reveals a layered structure formed for Ni(OH)₂/Ni₂O₃. Interestingly, as can be seen in the high resolution TEM (Figure 4.2b), some mesopores were found in the layers. These mesopores provide increased the number of electrochemical active sites and facilitate ion diffusion during the charge/ discharge process. The corresponding lattice fringes of Ni₂O₃ could be found in the HRTEM (Figure 4.2b), displaying a d-spacing of 0.28 nm, consistent with the (002) plane of

Ni₂O₃. The structure of Ni(OH)₂/Ni₂O₃ composite is characterized by X-ray diffraction (XRD, Figure 4.2c). Besides the peaks from Ni substrate, those at 22° and 32° could be indexed as (006) plane of Ni(OH)₂ phase (JCPDS No. 38-0715) and ((002) plane of Ni₂O₃ (JCPDS No. 14-0481)), respectively. The result is in accordance with the selected area electron diffraction pattern (inset of Figure 4.2b). Raman spectrum of Ni(OH)₂/Ni₂O₃ (Figure 4.2d) shows three bands at 561, 730, and 3616 cm⁻¹, which are attributed to Ni₂O₃ and α-Ni(OH)₂, respectively.^[102]

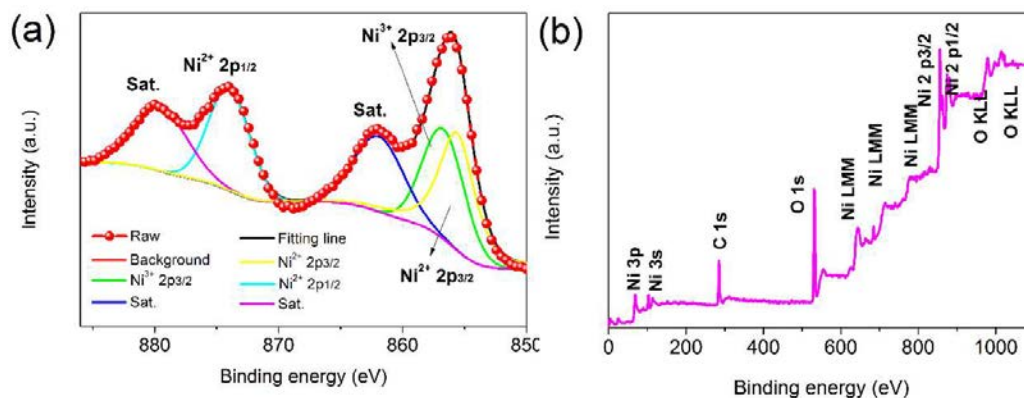


Figure 4.3 XPS spectra of Ni(OH)₂/Ni₂O₃. (a) Ni 2p and (b) a full XPS.

The existence of Ni(OH)₂/Ni₂O₃ is also confirmed by the XPS spectra. Figure 4.3a showed the Ni2p XPS spectrum with two shake-up satellites (denoted as Sat.). The peaks observed at 855.6 and 873.8 eV correspond to Ni²⁺ 2p_{3/2} and Ni²⁺ 2p_{1/2} signals of Ni(OH)₂ while the peak at 856.7 eV is ascribed to Ni³⁺ 2p_{3/2} signal of Ni₂O₃.^[61,103] The XPS survey spectrum showed no detectable signals other than Ni, O, indicative of the purities of the sample (Figure 4.3b).

4.3 Electrochemical characterizations

4.3.1 Characterization of layered nickel-based composite

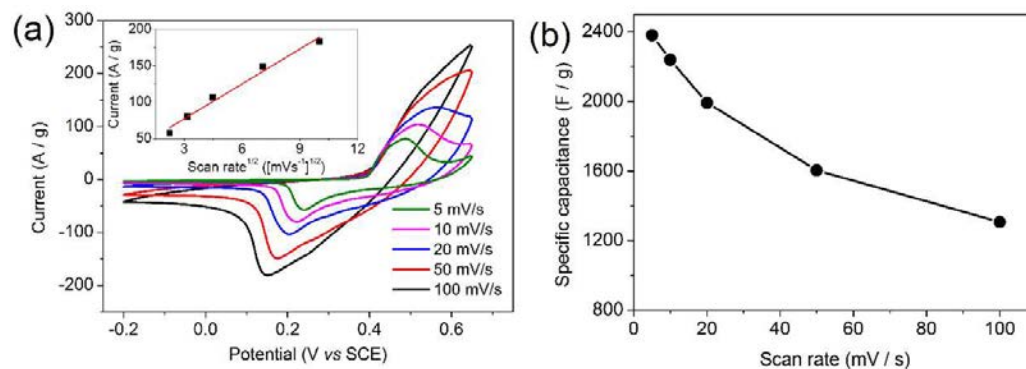


Figure 4.4 (a) CV curves of Ni(OH)₂/Ni₂O₃ prepared in the electrolyte containing 0.1% NH₄F and 0% water for 4 h. Inset: the relationship between cathodic peak current and square root of scan rate. (b) The variation of specific capacitance with scan rate from 5 to 50 mV s⁻¹.

As indicated by SEM and TEM results, Ni(OH)₂/Ni₂O₃ with porous layered structure may be promising for energy storage and catalysis. To determine its potential for supercapacitor applications, its electrochemical properties were fully characterized. Due to direct growth of Ni(OH)₂/Ni₂O₃ on the surface of anode, it is not necessary to add binder and/or conducting agent for the electrode preparation and was used directly for the following electrochemical characterizations. CV measurements (Figure 4.4a) show a pair of redox peaks, indicating that Ni(OH)₂/Ni₂O₃ possesses battery-type



pseudocapacitive electrochemical activity in KOH electrolyte. All the CV curves show similar shapes and the peak current density increases with increasing scan rate, revealing good rate property and excellent capacitive behavior of Ni(OH)₂/Ni₂O₃. At the same time, the color change of the sample was clearly observed during CV scan. When the sample was anodically polarized, it turned dark, while the color faded in reverse scan. The reversible color change was attributed to the reaction of Ni(II) ⇌ Ni(III).^[60,104] The oxidation and reduction peaks are almost symmetrical, indicating good reversibility of the electrochemical reactions which implies rapid charge transport and long life time. The linear relationship between cathodic peak current and the square root of scan rates (inset of Figure 4.4a) suggests that the reaction was controlled by the diffusion of OH⁻. The specific capacitances calculated by CV curves are 2381, 2240, 1993, 1605 and 1307 F g⁻¹ at scan rates of 5, 10, 20, 50 and 100 mV s⁻¹ (Figure 4.4b), respectively. The decrease of the specific capacitance with increasing scan rates indicates the increasing of the number of inaccessible active sites due to diffusion effect. At a low scan rate, the Ni(OH)₂/Ni₂O₃ electrode material demonstrated higher electrochemical performance than many other previous reports.^[61,105]

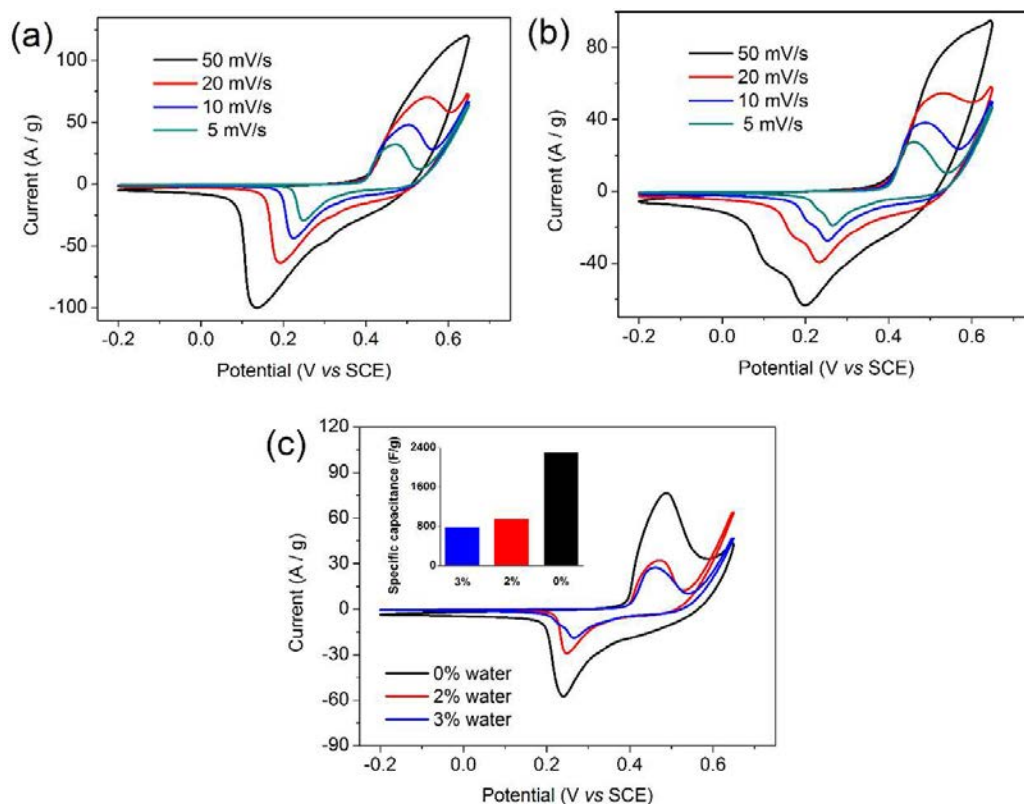


Figure 4.5 CV curves of the samples prepared for 4 h in the electrolyte containing 0.1% NH_4F and different water contents. (a) 2% water with scan rates from 5 to 50 mV s^{-1} . (b) 3% water with scan rates from 5 to 50 mV s^{-1} . (c) CV curves of the samples prepared in the electrolyte with different water contents at a scan rate of 5 mV s^{-1} . Inset: the variation of specific capacitance with the water content.

In order to achieve excellent capacitance performance, the preparation conditions including reaction time, water and NH_4F contents were optimized via CV tests which were used for the screening of the electrochemical properties of electrode materials. The CV curves of nickel compounds prepared in the solutions with 0.1% NH_4F and



various water contents were shown in Figure 4.5. The sample prepared with 2% water exhibits a typical pair of redox peaks from nickel oxide/hydroxide (Figure 4.5a). However, the CV curve in Figure 4.5b shows two cathodic peaks at 100 and 200 mV, even there is only one single anodic peak. It is due to the transformation of γ -NiOOH and reduction of β -NiOOH, respectively.^[83] According to Bode diagramme (Figure 2.11),^[82] the reduced states of γ - and β -NiOOH are α - and β -Ni(OH)₂, respectively. It is believed that α -Ni(OH)₂ is more suitable for supercapacitor/battery electrode applications than β -Ni(OH)₂ because of the higher theoretical capacity.^[106] Therefore, it is easy to understand that when a single reduction peak was developed into two peaks (as seen from Figure 4.4a to Figure 4.5a), the capacitance declined from 2381 to 1226 F g⁻¹ at 5 mV s⁻¹. It can also be seen that the addition of water in the preparation electrolyte possibly resulted in the formation of β -Ni(OH)₂, which was detrimental to the electrochemical capacity. The sample prepared in the water-free electrolyte exhibited the best electrochemical properties. Figure 4.5c showed CV curves of samples prepared in the electrolyte with different water contents (0%, 2% and 3%) at a scan rate of 5 mV s⁻¹. With the increasing water content, the as-fabricated samples demonstrated better catalytic activity towards oxygen evolution reaction.

CV curves of electrode materials fabricated in three hours are shown in Figure 4.6a. Two cathodic peaks at 0.25 and 0.30 V can be seen, similar to the samples prepared in electrolytes with 3% water. However, two anodic peaks at 0.45 and 0.55 V are also observed, which correspond to γ - and β -NiOOH, respectively. When the reaction time was extended to five hours (Figure 4.6b), the utilization of active material was

decreased due to limited conductivity of thickened anodic film. Consequently, the gravimetric specific capacitance was not the highest. The specific capacitances were 2381, 1050, and 801 F g^{-1} for samples prepared with reaction time of 4, 3, and 5 h, respectively (Figure 4.6c). The area of CV curve of the sample prepared in 0.5% NH_4F (Figure 4.7) is less than that in 0.1% NH_4F . The optimized conditions to maximize capacity are 0.1% NH_4F , no water, and 4 hours (Figure 4.4).

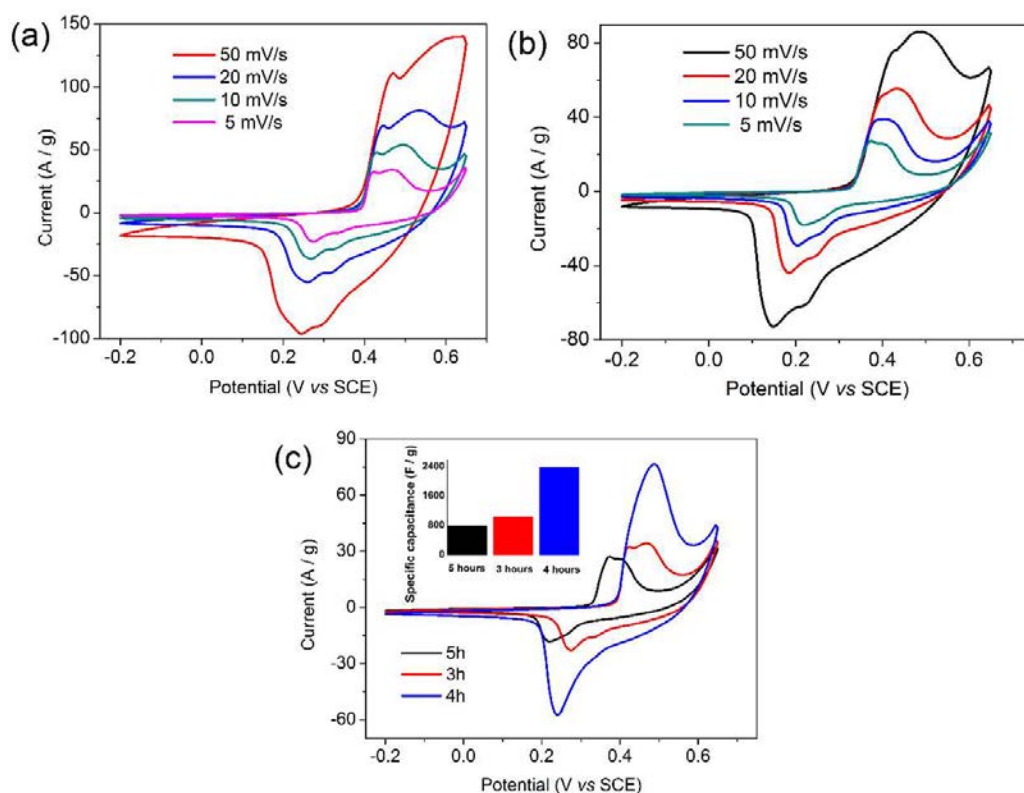


Figure 4.6 CV curves of the samples prepared in the electrolyte containing 0.1% NH_4F and no water for different reaction time: (a) 3 h, (b) 5 h, and (c) CV of different samples scanned at 5 mV s^{-1} . Inset: comparison of specific capacitance.

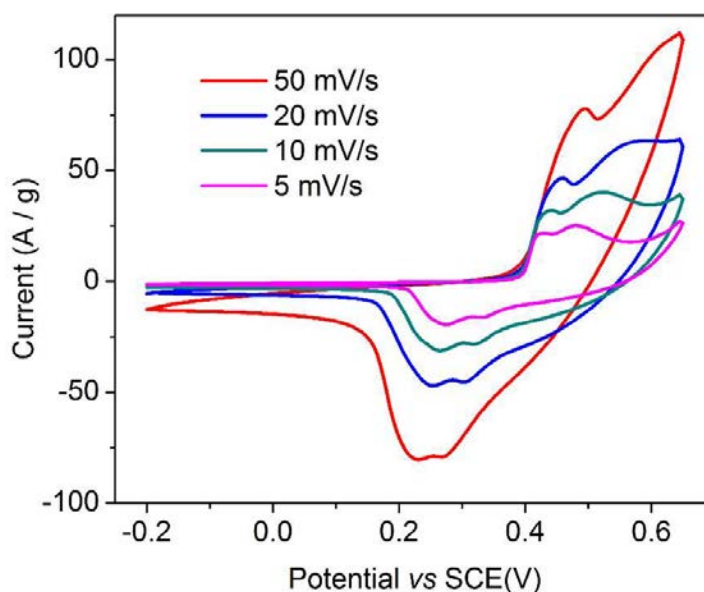


Figure 4.7 CV curves of the sample prepared in the electrolyte containing 0.5 % NH_4F and 0% water for 4 h

The electrochemical performance of $\text{Ni}(\text{OH})_2/\text{Ni}_2\text{O}_3$ was further evaluated by the galvanostatic charge-discharge (GCD) technique (Figure 4.8). The performance was stable in a potential window from 0 to 0.5 V at various GCD current densities from 1 to 40 A g^{-1} . A quasi-plateau and sloping line during the charge/discharge process were observed, indicating the battery-like pseudocapacitive behavior. Figure 4.8b shows that the specific capacitance is as high as 3248 F g^{-1} at a current density of 1 A g^{-1} . When the current density was increased by 40 times to 40 A g^{-1} , the specific capacitance still remained 56 % of the initial value (79.1 % at 10 A g^{-1}), suggesting a good rate performance compared with many other nickel-based electrodes reported recently, such as Ni/NiO (38.1 % retention for 40 times rate increase),^[107] $\text{Ni}(\text{OH})_2/\text{MnO}_2$ (40.6% retention for 40 times rate increase),^[108] graphene/NiO (64.3%

retention for 3 times rate increase),^[109] $\text{Co}_3\text{O}_4/\text{Ni-Co-O}$ (72% retention for 6 times rate increase),^[110] ZnO/NiO (78.4% retention for 5 times rate increase),^[111] $\text{Ni}/\text{NiO}/\text{GO}$ (70% retention for 10 times rate increase).^[112]

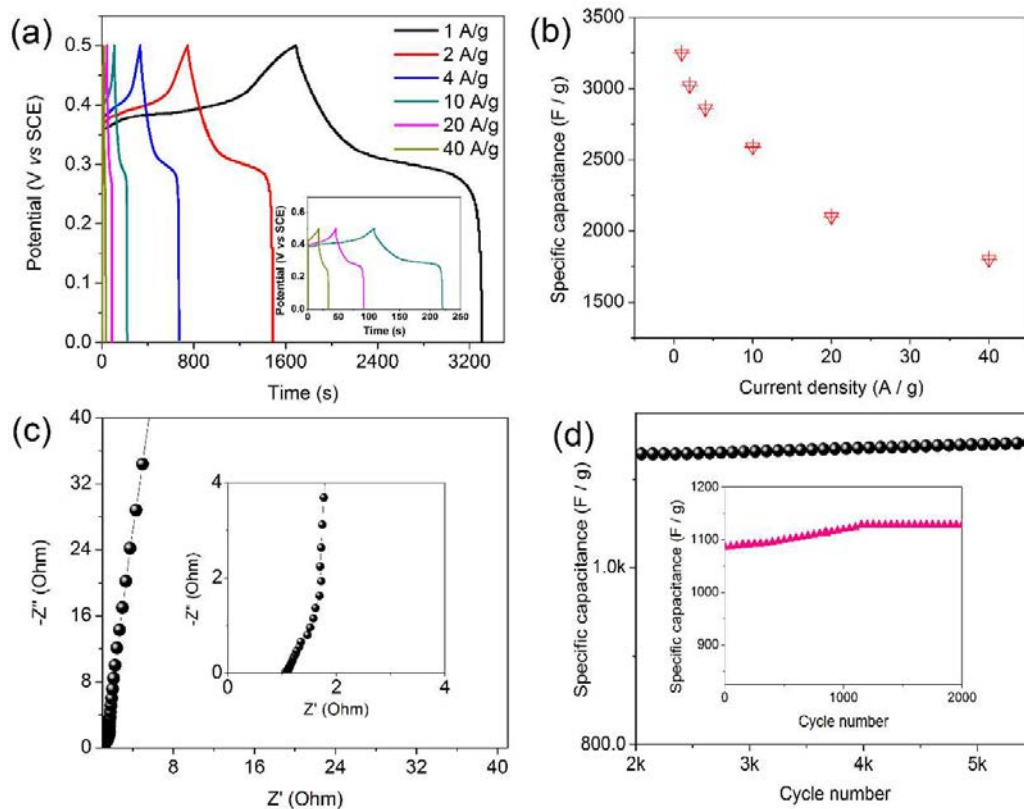


Figure 4.8 (a) GCD curves of $\text{Ni}(\text{OH})_2/\text{Ni}_2\text{O}_3$. Inset: magnified curves. (b) Specific capacitance as a function of current density. (c) EIS plots of $\text{Ni}(\text{OH})_2/\text{Ni}_2\text{O}_3$ from 0.01 Hz to 100 kHz after 10,000 scans in 1 mol L^{-1} NaOH. Inset: magnified EIS at high frequency region. (d) Cyclic test of $\text{Ni}(\text{OH})_2/\text{Ni}_2\text{O}_3$ by CV measurement at a scan rate of 100 mV s^{-1} in 1 mol L^{-1} NaOH aqueous solution. The inset shows the initial 2000 cycles.



Figure 4.8c shows the EIS Nyquist plots of Ni(OH)₂/Ni₂O₃ electrodes. The small equivalent series resistance ($\sim 1.0 \Omega \text{ cm}^{-2}$) is attributed to the low electrolyte resistance and the low contact resistance between active material and current collector. The high frequency region was expressed in the form of a depressed semicircle and was associated with a charge transfer resistance of $1.0 \Omega \text{ cm}^{-2}$ (inset of Figure 4.8c), much lower than those reported elsewhere, suggesting the potential to provide high power density.^[113] The low frequency portion is composed of a straight line representing the Warburg resistance, which is resulted from the kinetics of ion diffusion/migration in the electrolyte. The Ni(OH)₂/Ni₂O₃ electrode material shows a steep slope of the line, indicating fast ion diffusion in the interface between the electrode and the electrolyte that is able to catch up with the frequency change.

Cyclic test was carried out by CV measurement at the scan rate of 100 mV s^{-1} (Figure 4.8d). In the first 2,000 cycles (the inset), the specific capacitance is raised from 1087 F g^{-1} to 1129 F g^{-1} due to the electrochemical activation of the electrode. It further reveals that the electrochemical reaction is mainly controlled by the insertion/extraction of OH⁻ ions in the electrolyte. After 2000 cycles, the capacitance is steady and is maintained at 1141 F g^{-1} with negligible degradation, implying good electrochemical stability.



4.3.2 Role of deionized water in electrochemical performance

Figure 4.5 shows that the $\text{Ni(OH)}_2/\text{Ni}_2\text{O}_3$ electrode has the highest specific capacitance when it is prepared in the electrolyte containing 0.1% NH_4F and no water. The role of DI water will be analyzed in this section.

Since ethylene glycol can easily absorb water, the electrolyte without intentional addition of DI water still contains a tiny amount of moisture water, coming from the open air. Therefore, those absorbed water molecules will take part in the electrochemical reaction. According to Equations 2.19-2.22, a small quantity of O_2 and OH^- , etc., will be produced on the surface of the anode. Meanwhile, the nickel foil also participates in the reactions of $\text{Ni} \rightarrow \text{Ni}^{2+} + 2e^-$ (2.18), $\text{Ni}^{2+} + 2\text{OH}^- \rightarrow \text{Ni(OH)}_2$ (2.23), and $\text{Ni(OH)}_2 \rightarrow \text{NiO} + \text{H}_2\text{O}$ (2.24). If the water content is high, severe oxidation of H_2O takes place and the nickel that participates in the oxidation is more likely to be dissolved rather than the formation of hydroxide/oxide. At the same time, during the anodization process in fluorine-containing electrolyte, nickel often undergoes inhomogeneous field-assisted dissolution at a high applied voltage^[68] with the corresponding electrochemical reactions following Equations 2.26-2.28.^[69] As discussed in Figure 2.10, the growth of the porous structure depends on a balance between hydroxide/oxide film formation rate and oxide dissolution rate in the electrolyte. Therefore, it is reasonable to conjecture that porous nickel compound with suitable thickness will be formed in a low level of water content. On the contrary, it



can be difficult to form nickel film with good electrochemical performance owing to the domination of H_2O oxidation.

4.3.3 Influence of reaction time on film thickness

Figure 4.6 exhibits the effect of anodization time on the specific capacitance. When the reaction time reached 4 hours, the sample exhibited the highest specific capacitance of 2400 F g^{-1} . Figure 4.9 shows the transient current at an anodization voltage of 60 V. With the increasing reaction time, the current density decreases accordingly, indicating increasing film thickness. This allows us to control the film thickness by reaction time for optimized specific capacitance of the samples.

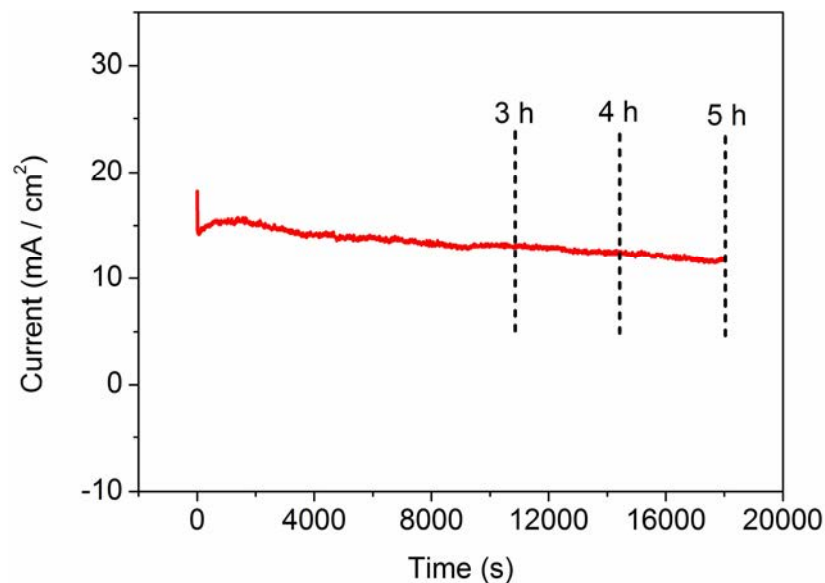


Figure 4.9 Typical transient anodization current in the electrolyte containing 0.1% NH_4F and no water.



4.5 Summary

In summary, layered porous $\text{Ni}(\text{OH})_2/\text{Ni}_2\text{O}_3$ composite was successfully synthesized by anodization of nickel foil in organic electrolyte containing NH_4F and EG without DI water. As a result of layered structure, and strong adhesion to the conducting substrate, $\text{Ni}(\text{OH})_2/\text{Ni}_2\text{O}_3$ presented not only a high specific capacitance, but also a superior rate capability and a long cycle life. The preparation strategy of the anodization in the organic electrolyte might be promisingly extended to the fabrication of other metal composites for supercapacitor electrodes.



Chapter 5 Ni@NiO Core/Shell Dendrites by Nickel-Free Cathodic Deposition for Ultra-long Cyclic Life Supercapacitor

5.1 Motivation

Cathodic deposition has gained more and more attention because the electroactive material can be directly grown on a current collector without the need to use any binder or conducting agent^[114]. It is well known that the morphology of the electro-deposited material is closely related to the nucleation and growth process of crystallites. Normally, the lower the concentration of the deposited ions, the lower the nucleation and growth rates of crystallites are in favor of an anisotropic growth with larger surface area^[115]. In addition, the adhesion strength between the deposited material and the substrate becomes stronger due to less defects and/or lower stress. In a conventional electro-deposition process of nickel-based material, the electrolyte is the only source of nickel ions, which will be depleted as the deposition process goes on. It is difficult to maintain a steady supply of low-concentrated nickel ions during the whole deposition process, leading to weak adhesion in most of the electro-deposited nickel-based materials.



In this chapter, we demonstrate that by using the electrode instead of the electrolyte as the nickel source, it is possible to keep a stable and a low nickel ion concentration to realize the low nucleation rate and anisotropic growth of nickel-based material. With the simultaneous control of OH^- ion generation speed, a novel core/shell structured dendritic Ni@NiO electrode (DNE) was produced with a large specific surface area. The vertically aligned dendrite structure not only provides efficient ion diffusion paths, but also facilitates electrolyte penetration. Specific capacitance as high as 1930 F g^{-1} was achieved at a current density of 2.9 A g^{-1} (areal capacitance $\sim 1.35 \text{ F cm}^{-2}$). The cyclability of the as-prepared material was also excellent, with the capacitance remaining almost 100% of its original value after 70,000 charge-discharge cycles. Moreover, the DNE material assumed a core/shell structure with highly conductive metallic nickel as the core and amorphous nickel oxide as the shell. Hence, the power density of the DNE was greatly enhanced, compared with other electro-deposited nickel-based materials [105a,116]. The technique reported here was facile and effective in microstructure engineering, and can be extended to the cathodic deposition of other electrode materials with high performance for battery-type supercapacitor.

5.2 Structural and elemental characterizations

In our method, cathodic deposition was conducted in a nickel-free organic electrolyte and a novel dendritic Ni@NiO core/shell structure was formed with excellent electrochemical properties. The construction of DNE material is schematically illustrated in Figure 5.1. In the initial state of cathodic deposition, there were no nickel

ions in the nickel-free electrolyte. The nickel ions (Ni^{2+}) mainly came from field-assisted anodic dissolution of nickel foil, which provided the slow nucleation and growth of nickel and nickel oxide/hydroxide on the cathode. When Ni^{2+} ions arrived at the cathode surface via diffusion and electric field drifted migration, nickel nucleated and grew, involving the reactions as shown in Equation 2.34, 2.38 and 2.39 [83]. As schematically shown in Figure 5.1, after the nucleation and growth of nickel composite, the surfaces of cathode were covered by dendritic structures (inserted SEM images also have shown), although the anode seemed to be neat (Figure 5.2 and 5.3).

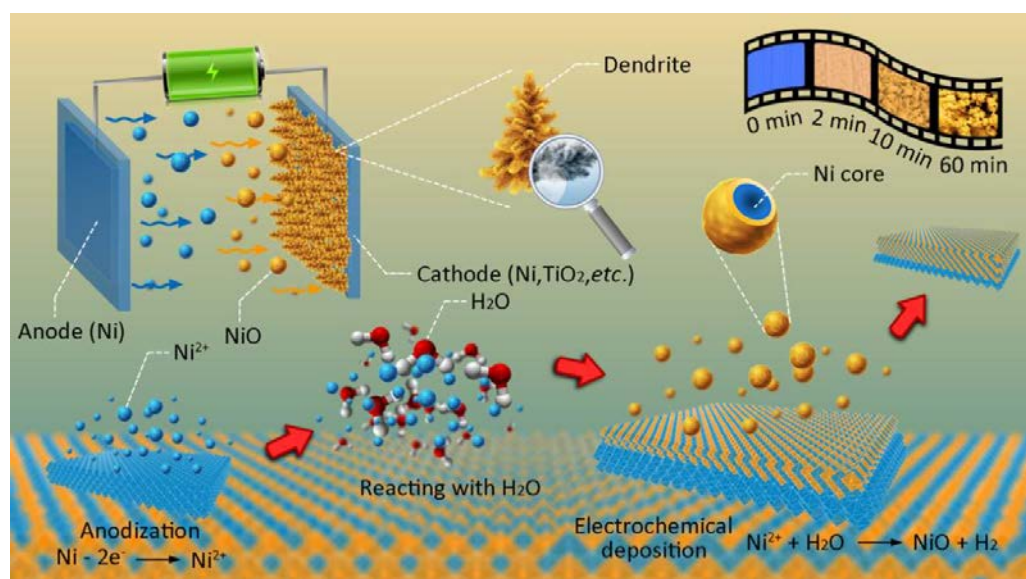


Figure 5.1 Schematic illustration of the formation of DNE material.

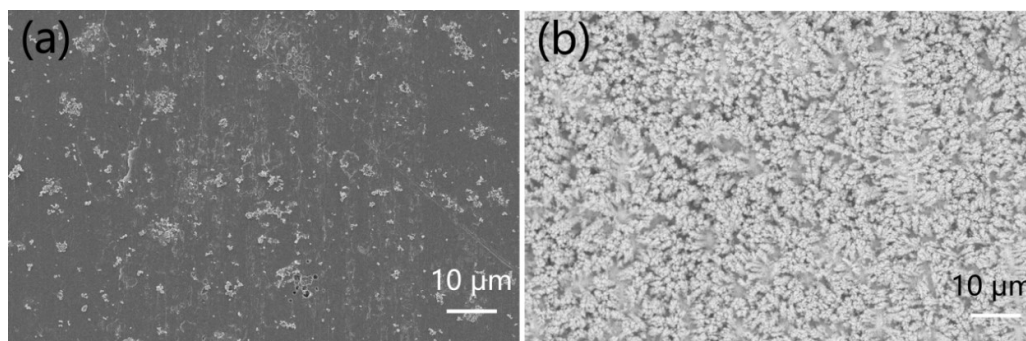


Figure 5.2 Surface morphologies of (a) anode and (b) cathode after cathodic deposition in EG electrolyte at 40°C.

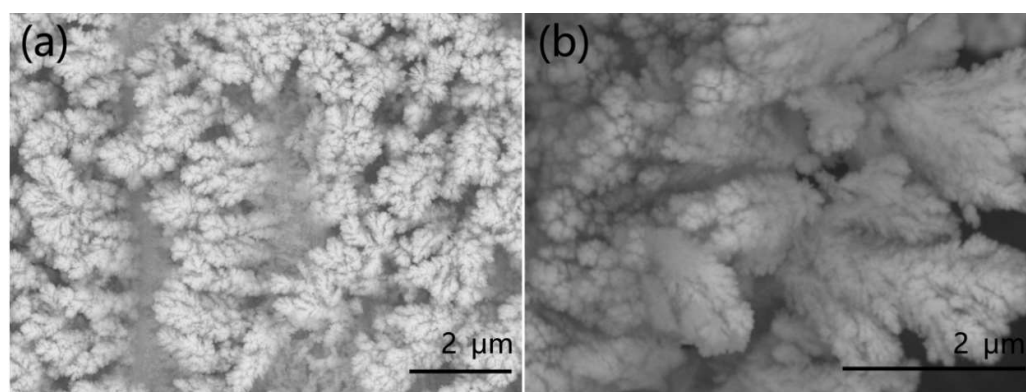


Figure 5.3 SEM image with (a) top view and (b) cross-sectional view of the microstructure of DNE material.

Figure 5.4a shows the XRD pattern of the DNE material whose particle size is ~ 4.8 nm (estimated by the Debye-Scherrer method). Three relatively strong diffraction peaks at 44.5° , 51.8° and 76.2° are resulted from the cubic nickel (JCPDF 87-0712) deposited on the substrate. Compared with the bare Ni substrate, the electrodeposited DNE, consisting of crystallized Ni, showed preferred growth along $\langle 111 \rangle$ direction, characteristic for a dendritic morphology of Ni.^[117] The dendritic structure can also be easily identified from TEM (Figure 5.4b), with micro- to nano-branches (Figures 5.4c



and 5.5). High-resolution TEM (HRTEM) image (Figure 5.4d) shows a d -spacing of 0.207 nm in the core of dendrites, corresponding to the interplanar distance of (111) planes of Ni and is consistent with the XRD results. In the corresponding selected area electron diffraction pattern (SAED, Figure 5.4e), a distinct ring is observed, corresponding to the (111) plane of Ni nanocrystals.^[118] The shell of dendrites is, however, amorphous. This core-shell structure is also verified by the fast Fourier transformation (FFT) patterns, as shown in Figure 5.4f and 5.4g. The element mapping of Figure 5.4b is shown in Figure 5.6a and 5.6b. EDS (Figure 5.6c) reveals that the as-prepared dendrites contain both Ni and O elements, suggesting that the outer surface (shell) of the as-prepared dendrites be amorphous nickel oxides.

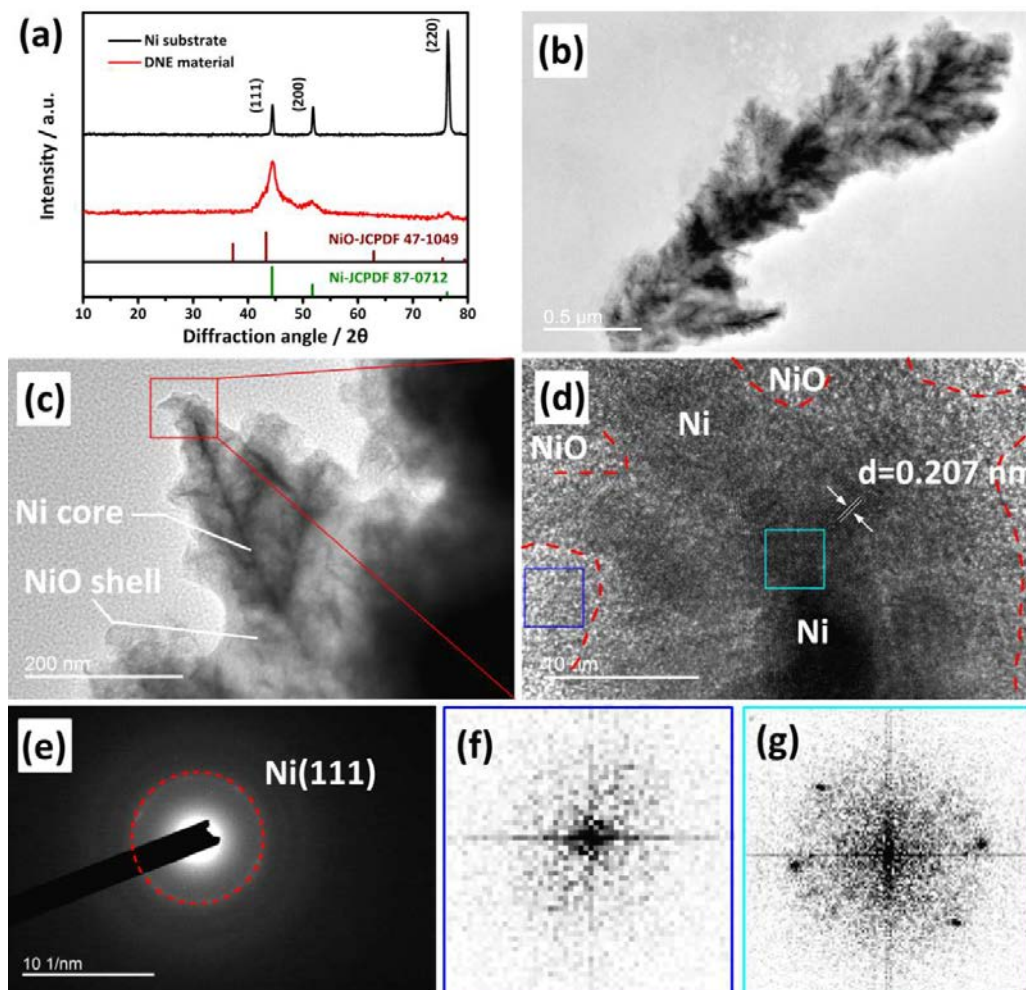


Figure 5.4 Characterizations of the DNE. (a) XRD. (b) Low and (c) high magnification TEM images. (d) HRTEM of the marked area of (c). Red dotted line is a guide to the eye to show roughly the Ni/NiO interface. (e) SAED pattern from (c). (f) and (g) Fourier transformation (FFT) patterns of the marked areas of (d).

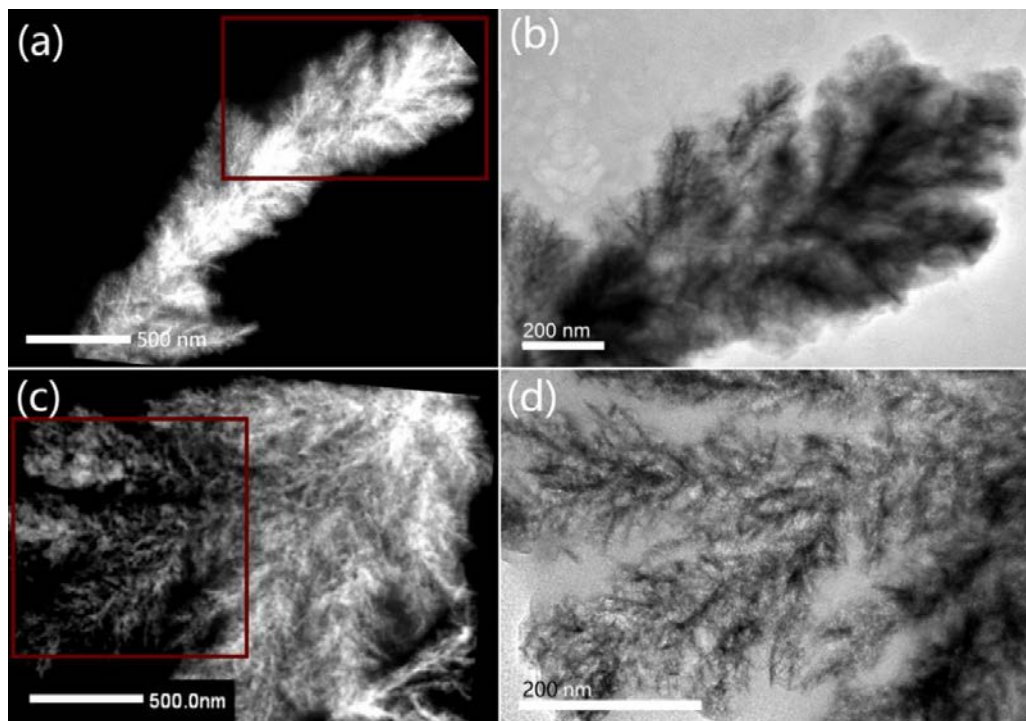


Figure 5.5 TEM characterizations of DNE materials in different selected areas of the same sample.

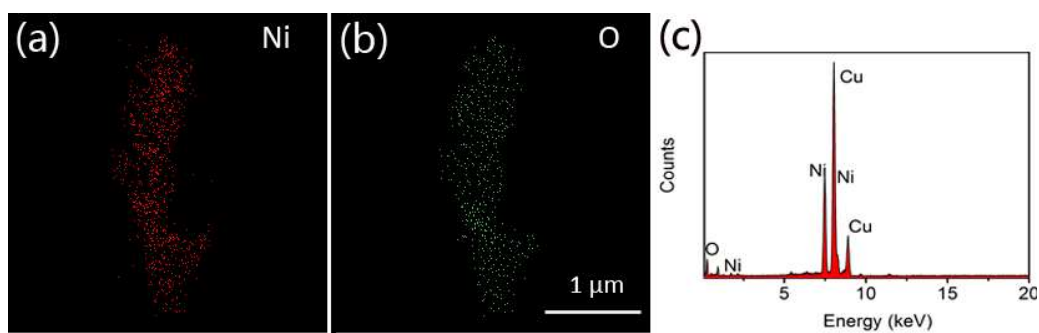


Figure 5.6 The element Ni (a) and O (b) mapping of DNE materials. (c) The corresponding EDS. The Cu signal comes from the TEM sample holder.



This core/shell structure was further studied by XPS. Figure 5.7a shows the Ni 2p XPS spectrum with two shake-up satellites (denoted as Sat.) near the two spin-orbit doublets at 856.1 and 873.8 eV, which can be assigned to Ni 2p_{3/2} and Ni 2p_{1/2} signals of NiO, respectively^[119]. In addition, another Ni 2p_{3/2} peak at 852.9 eV, corresponding to elemental nickel,^[120] can be identified. The atomic ratio of Ni to Ni²⁺ was 1:10, as estimated from the peak areas. This result implies that the surface of dendrites mainly consists of NiO, as XPS normally probes a depth in the order of 10 nm^[121]. In order to support our speculation, a destructive depth profile from XPS (Figure 5.7b) is carried out. New peaks centred at 858.2 and 869.5 eV are observed in the depth profile XPS, corresponding to the characteristic Ni 2p_{3/2} satellite and Ni 2p_{1/2} peaks of Ni metal, respectively.^[122] What's more, the intensity of peaks of Ni⁰ at 852.9, 858.2, and 869.5 eV is increased with increasing etching depth while the intensity of peaks located at 856.1 and 873.8 eV representing the characteristic Ni 2p_{3/2} and Ni 2p_{1/2} peaks of Ni²⁺ is reduced. In conjunction with Figure 5.7c, the variation of content of nickel has negative relation with oxygen content change, indicating that the metal nickel increases with increasing etching depth. Because of the uneven surface and irregular feature of dendrites, the as-obtained result strongly relies on being fixed in position when shot at with the sputtering gun.^[123] However, the result can support the core/shell structure of dendrites. The XPS survey spectrum (Figure 5.7d) shows that no signals other than Ni, O and the adventitious carbon can be detected on the surface of dendrites, indicating that no impurities were introduced during the cathodic deposition.

Figure 5.7e shows Raman spectra of the DNE material, where the bands at 529.5 and 1078.1 cm^{-1} correspond to the one-phonon LO mode, and the two-phonon 2LO mode of NiO, respectively [124]. All these results confirm that the DNE material has a Ni@NiO core/shell structure. This unique structure enables the DNE material to possess excellent electrochemical properties because of the high electric conductivity in the core that greatly shortens the electron transport pathways and a large amount of structural disorders or defects on the amorphous shell that ensure a large active sites.

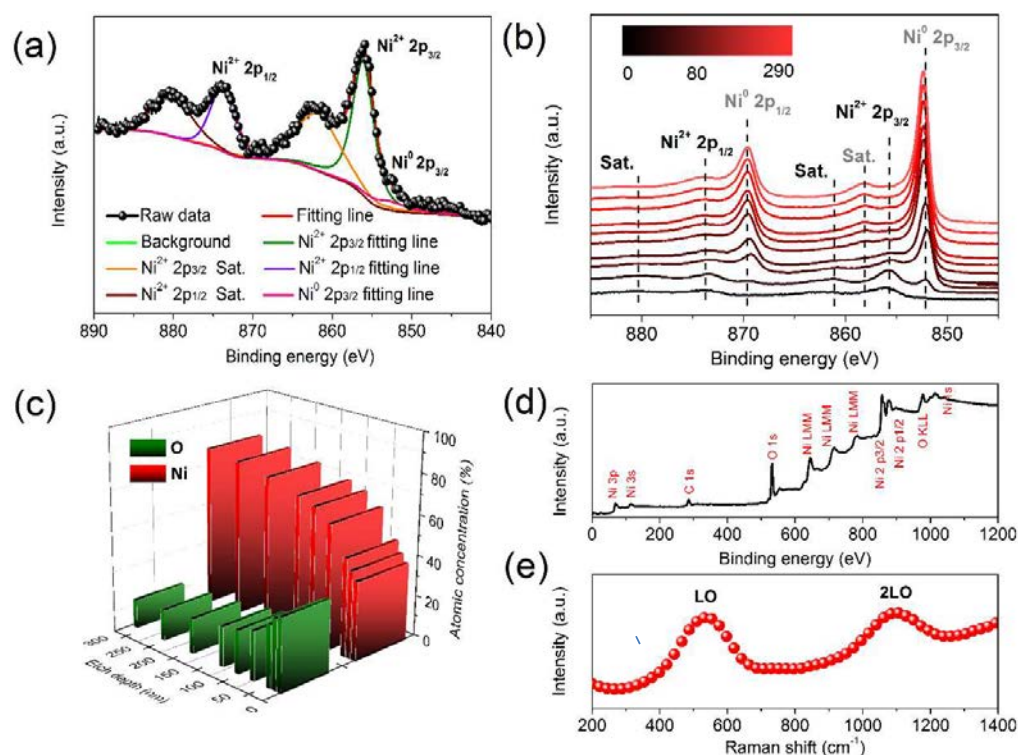


Figure 5.7 (a) Ni 2p XPS on the fresh sample. (b) Depth profile of Ni 2p XPS on DNE from 0 to 290 nm. (c) Variation of O and Ni concentrations as a function of etch depth. (d) Raman spectrum of DNE. (e) Full XPS pattern of DNE material.

5.3 Electrochemical characterizations

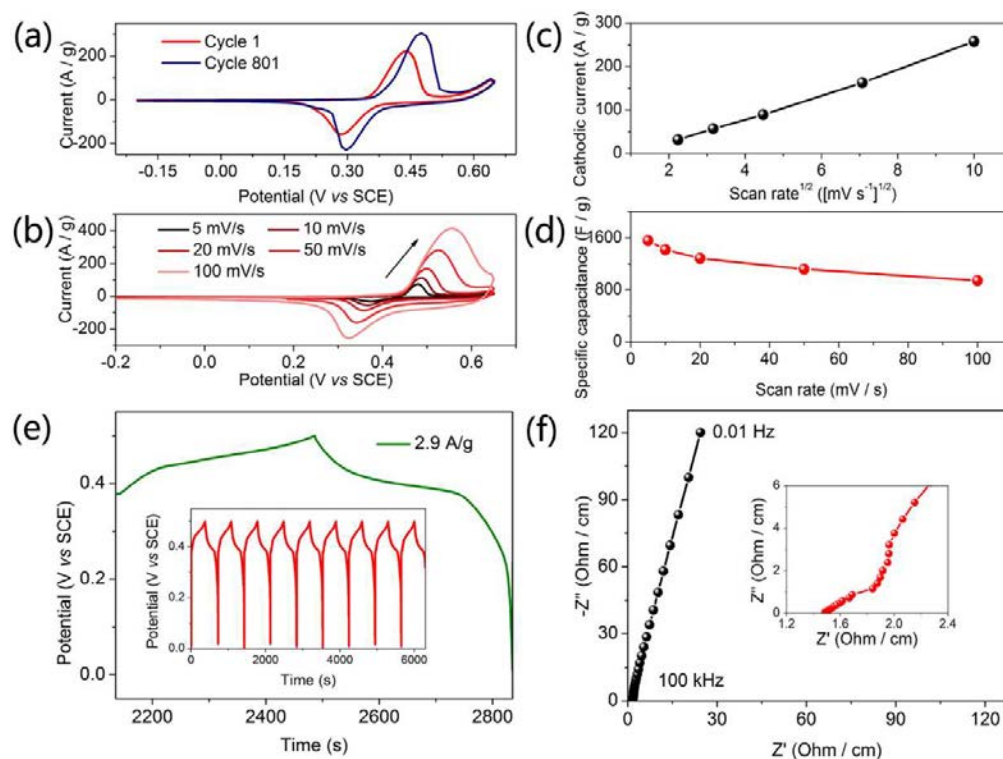


Figure 5.8 Electrochemical characterizations of DNE. (a) CV curves of the 1st and the 801st cycles at a scan rate of 100 mV s⁻¹. (b) CV curves at different scan rates from 5 to 100 mV s⁻¹. (c) The cathodic peak current in (b) as a function of the square root of scan rate. (d) Specific capacitance at different scan rates. (e) GCD curves at a current density of 2.9 A g⁻¹ (2 mA cm⁻²). (f) EIS spectra of DNE from 0.01 to 100 kHz in 1 mol L⁻¹ NaOH. Inset: magnified EIS in high frequency region.

Before the evaluation of the electrochemical performance of DNE, the electrode was electrochemically activated in a three-electrode system using 1 mol L⁻¹ NaOH aqueous



solution as the electrolyte. As shown in Figure 5.8a, a gradual increase of the current density with cycle number was observed. A distinctive pair of redox peaks between -0.2 and 0.65 V is due to the insertion/extraction of OH^- ions in the electrolyte^[81], illustrating characteristic battery-type pseudocapacitive behaviour of DNE.

Figure 5.8b shows the typical CV curves of the as-prepared DNE after the electrochemical activation. With the increase of scan rate, the current density also increases accordingly, and there is no big difference in the shape of CV curves, indicating that the DNE is a good conductor with a small equivalent series resistance (ESR) and exhibits an excellent rate property. At the scan rate of 5 mV s^{-1} , the specific capacitance of DNE was calculated to be 1557 F g^{-1} (1.02 F cm^{-2}), better than previous reports.^[60,125] As shown in Figure 5.8c, when the scan rate was increased to 100 mV s^{-1} , the DNE had a good rate capability with more than 60.7 % retention of the capacitance (945 F g^{-1} , 0.66 F cm^{-2}). Meanwhile, the linear relation between the cathodic peak current and the square root of scan rate (Figure 5.8d) shows that the reaction process at the electrode was diffusion controlled rather than surface limited.

The excellent electrochemical performance of DNE was further confirmed by GCD measurement as shown in Figure 5.8e. The GCD curves exhibited both a battery-type plateaus at 0.35 V and sloping potential region below 0.35 V, in agreement with signatures of BPMs. At a current density of 2.9 A mg^{-1} (2 mA cm^{-2}), the specific capacitance of DNE is 1928.5 F g^{-1} (1.35 F cm^{-2}). This value is superior to those of the state-of-the-art nickel-based electrodes reported (Table 5.1). The high specific surface



area ($85.5 \text{ m}^2 \text{ g}^{-1}$, Figure 5.9a) of the DNE is one of the factors that contribute to this outstanding electrochemical performance. The rate capability of the DNE at different current densities is also good, with only 29.2% decay when the current is increased from 2.9 A g^{-1} to 58 A g^{-1} (Figure 5.9b).

Table 5.1 Comparison of the maximum specific capacitance of some reported nickel-based electrode and the present work.

Electrode materials	Mass loading (mg/cm^2)	Electrolyte	Current density (A g^{-1})	Specific capacitance (F g^{-1})	Ref.
Ni/NiO	0.7	1 M NaOH	2.9	1928.5	Present work
Ni(OH) ₂ /NiF ₂	0.15	1 M NaOH	2	350.0	[61]
Ni-Co LDH	0.23	6 M KOH	1	1760.0	[126]
NiO/Co ₃ O ₄	N/A	1 M KOH	4	1190.0	[127]
Ni-CNTs@β-Ni(OH) ₂	N/A	1 M KOH	2	1807.0	[128]
Ni/NiO NTs	N/A	1 M NaOH	1	<1000	[129]
rGO/a-Ni(OH) ₂	0.8	1 M KOH	1	1671.1	[130]

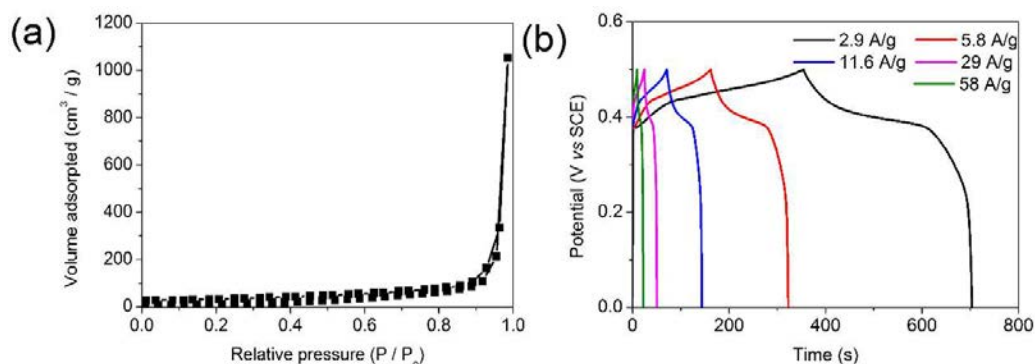


Figure 5.9 (a) BET isothermal of DNE material. (b) The rate capability of the DNE at the different current densities.

The electrochemical impedance spectroscopy (EIS) of the DNE was also studied. Figure 5.8f shows that ESR of the as-prepared DNE in this study is about 1.4Ω , indicative of a low electrolyte resistance and a low contact resistance between the active material and the current collector. The high frequency region of the EIS shows a depressed semicircle with a charge transfer resistance of 1.2Ω (inset of Figure 5.8f) that is much lower than reported elsewhere, ^[60,131] implying a high power density. The low frequency portion of EIS shows a straight line, representing the Warburg impedance which is resulted from the ion diffusion/migration in the electrolyte. The EIS of DNE shows a large slope of the line, indicating that the ion diffusion at the interface between the electrode and the electrolyte was fast enough to catch up with the frequency change.

Figure 5.10a shows the variation of the gravimetric capacitance of the DNE in the cyclic test up to 70,000 cycles at a scan rate of 100 mV s^{-1} . During the first 800 cycles,



the augmented specific capacitance was much greater than that at the first cycle (Figure 5.8a). Notably, the galvanic capacitance of the DNE continuously increases in the initial 20,000 cycles. Importantly, from 20,000 to 60,000 cycles, there was not an obvious drop in the capacitance (945 F g^{-1}), demonstrating the excellent electrochemical stability of the DNE. After 60,000 cycles, the capacitance is still 110% of the initial value (859 F g^{-1}), which slightly declines to 100% up to 70,000 cycles. In order to explore more details of the unique electrochemical reaction during cycling, CVs at different cycling stages are compared in Figure 5.10b. After 800 cycles, the shift of anodic peak potential from 0.48 to 0.55 V was clearly observed while the cathodic peak potential remained unchanged at 0.3 V. This phenomenon is attributed to the phase transition from γ -Ni(OOH) to β -Ni(OOH).^[82-83,132]

From 10,000 to 40,000 cycles, there is a continuous increase in the capacitance of the DNE, which is contradictory to the fact that β -Ni(OOH) has poorer electrochemical activity than γ -Ni(OOH) ^[83]. We ascribe the increased capacitance to the gradual transition of the Ni core of the dendrites into β -Ni(OOH) during cycling process ^[122b,133], resulting in exceptionally superior cycle life and good capacitance as compared with recent reports ^[53a,60,134]. This gradual transition of Ni into β -Ni(OOH) during cycling does not affect the Coulombic efficiency or the rate capability too much (Figure 5.10c and 5.10d). After 70,000 cycles, the flaking-off and dissolution of active materials, the electrochemical performance becomes poor. To understand the origin of the improved gravimetric capacitance and such a long cycle life of the DNE, Raman characterizations were conducted at different cycling stages.

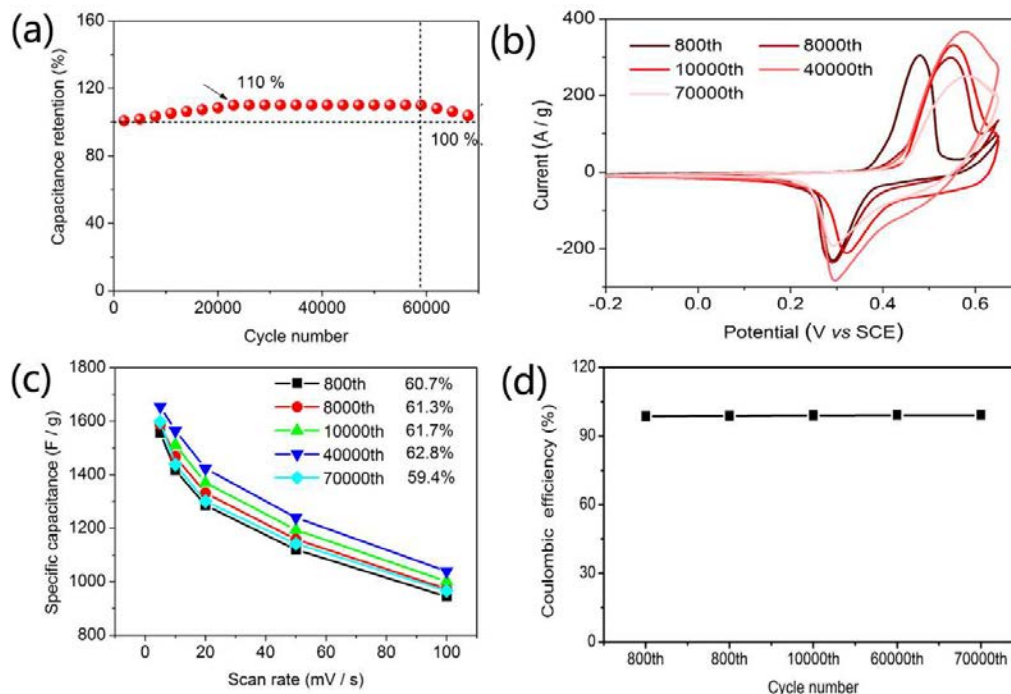


Figure 5.10 (a) Cyclability test of the DNE at a scan rate of 100 mV s^{-1} . (b) CV curves of DNE at different cycle numbers at the scan rate of 100 mV s^{-1} . (c) Specific capacitance as a function of the scan rate. (d) Coulombic efficiency at different cycling stages.

Figure 5.11a shows that the characteristic Raman peaks of NiO (LO and 2LO) can still be observed in the DNE material after 800 cycles, indicating that no new phase was formed. After 8000 cycles, new Raman peak at 714.2 cm^{-1} can be found, which belongs to $\text{Ni}(\text{OH})_2$ [135] due to the electrochemical oxidation of Ni, commonly found in alkaline electrolyte. Meanwhile, more and much stronger characteristic Raman peaks at 370.6 , 506.7 , 690.1 and 1078.1 cm^{-1} are found, which correspond to TO, 2TO and 2LO modes of NiO, respectively, confirming also the gradual transformation of

Ni (core of DNE) into electrochemical active NiO [136]. The transformation of Ni into NiO and Ni(OH)₂ continues up to 40,000 cycles, as the intensities of the corresponding Raman peaks kept on increasing. After 70,000 cycles, however, the Raman peaks of Ni(OH)₂ disappeared and the intensities of the NiO peaks became remarkably weaker, indicating that the Ni core stopped its reaction with the electrolyte and the NiO and Ni(OH)₂ was partially dissolved in the electrolyte repeated ion intercalation/deintercalation during cycling. This result agrees with the cyclic test where the capacitance decays after 70,000 cycles. Hence, the ultra-long cycle life of the DNE results from the continuous transformation of newly exposed Ni core into NiO and Ni(OH)₂ during the cycling process.

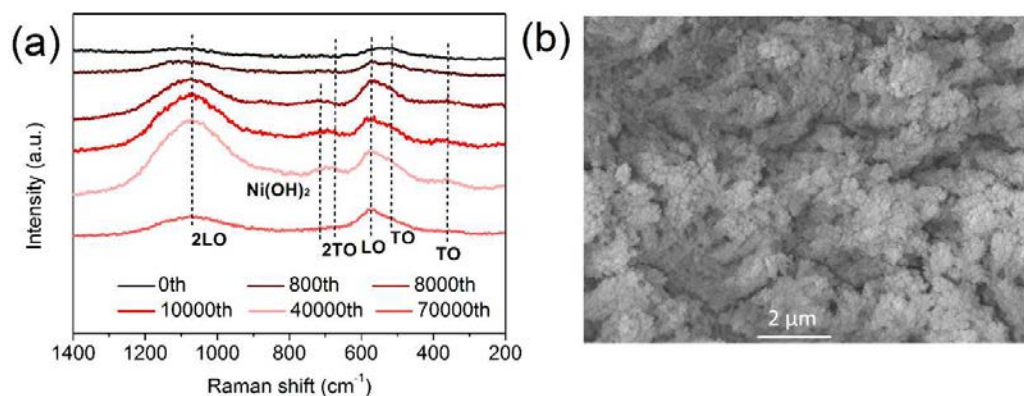


Figure 5.11 (a) Raman spectra of the DNE material at different cycle numbers. (b) SEM image of the DNE material after 70,000 cycles.

The dendritic core/shell morphology of the DNE (Figures 5.11b and 5.12a) remains almost unchanged even after 70,000 cycles, revealing a remarkable structural stability. Moreover, partial transformation of the Ni core boundary into crystalline NiO that has

a d -spacing of 0.147 nm corresponding to the interplanar distance of (220) plane of NiO was also observed after 70,000 cycles (Figure 5.12b and 5.12c). The corresponding SAED pattern (Figure 5.12d) shows the diffraction rings corresponding to the (111) and (220) planes of NiO nanocrystals. These results are consistent with the Raman spectra analysis.

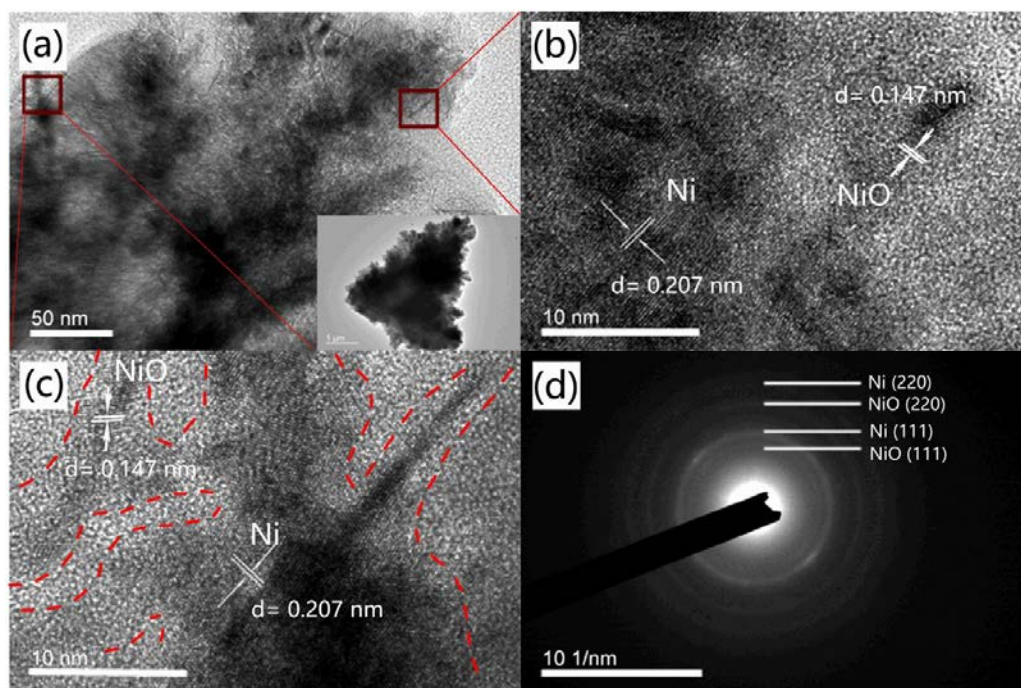


Figure 5.12 (a) High and low (the inset) magnification TEM images of the DNE material after 70,000 cycles. (b, c) HRTEM image of the marked areas in (a). (d) SAED pattern. Red dotted line is a guide to the eye to show roughly the boundary between Ni and crystalline NiO.



5.4 Crystal growth mechanism of dendritic structure

It can be seen from the above results that the key to the superior electrochemical performance of DNE is its unique dendritic core/shell microstructure, with the Ni core being a good conductor that shortens the electron transport path and the NiO shell possessing a large amount of electrochemically active sites for an excellent Faradaic capacitance. Moreover, the gradual transformation of the Ni core into electroactive material helps maintain the DNE an ultra-long cycle life. This unique microstructure resulted from the Ni-free electrolyte used in our work, where Ni^{2+} ions come from the Ni anode under potential or over-potential, different from previous reports where Ni^{2+} -containing electrolyte was used as the only Ni source for cathodic deposition [105a,137]. Here in this study, viscous organic electrolyte (EG) was used to control the diffusion of Ni^{2+} [138] in order to get a steady deposition on the cathode for the formation of dendritic DNE. A small amount of water is necessary for the reduction of Ni^{2+} and the deposition of Ni on the cathode. As water was gradually depleted, the local pH was increased and the surface of the electrode was gradually passivated, forming a layer of oxide or hydroxide [83,87,139] to cover the Ni core. Thus, dendritic Ni@NiO core/shell structure was finally formed.

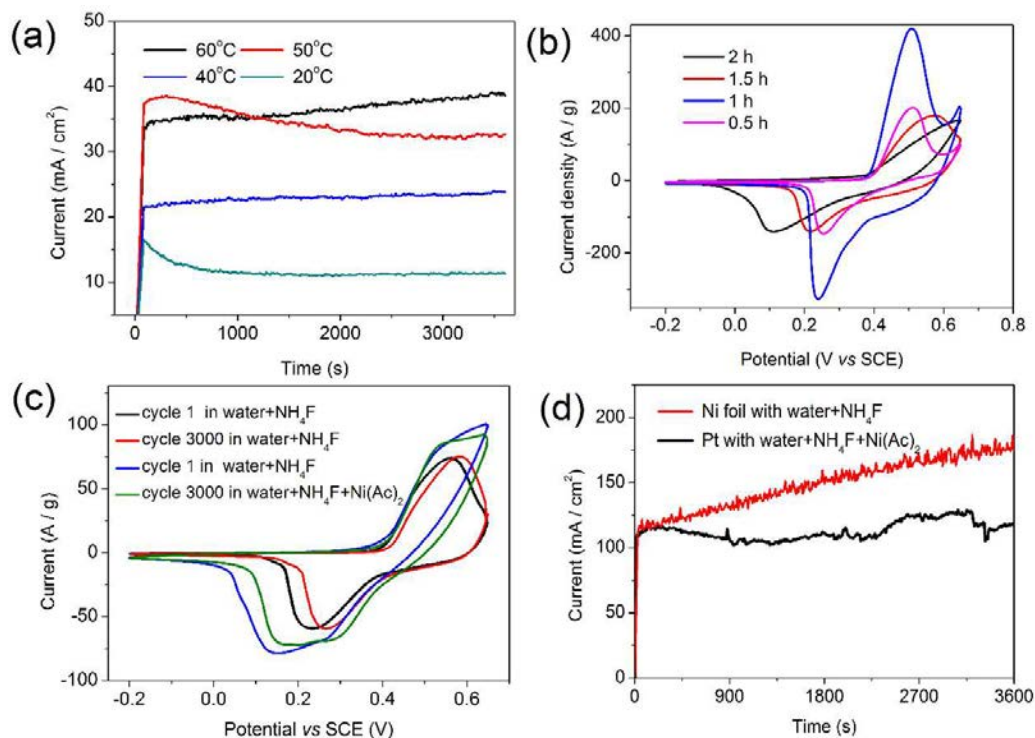


Figure 5.13 (a) The current transient of the cathodic deposition process at different temperatures. (b) The CV curves of samples prepared in different deposition time. (c) CV curves of samples in different electrolytes at a scan rate of 20 mV s^{-1} in different electrolytes, including EG + NH_4F , water + NH_4F in which the nickel foil was used as the anode and water + NH_4F + $0.05 \text{ M Ni}(\text{Ac})_2$ where Pt was used as the anode. (d) The current transient of the cathodic deposition process at $40 \text{ }^\circ\text{C}$ in (a) electrolytes at 20 V (red line) and 7 V (black line), respectively.

Similar to preferential free growth of dendrite silver or platinum^[140], which was driven by overpotential or thermal undercooling, the dendritic Ni core also grew along the $\langle 111 \rangle$ direction (**Figure 5.2**). In the cathodic deposition of nickel, dendrite growth



along the preferred orientation frequently occurs under high current density or overpotential [141]. Among the many factors that control the dendrite growth, the most important one is the H^+ ions from water electrolysis, whose content and migration rate affect metallic overpotential and thus the nucleation rate [89]. It is well known that hydrogen evolution reaction (HER) involving an intermediate H adsorption could make an important contribution to the preferential oriented growth [138,142]. At the cathode, H^+ is slowly consumed by hydrogen evolution. Reddy *et al.* proposed that the change of nickel texture is induced by variation in surface hydrogen adsorption which depends on temperature, additive and current density [89]. Since temperature affects the diffusion of Ni^{2+} and H^+ , and the viscosity of the electrolyte, to elucidate the effect of temperature on the growth of dendrites, several different temperatures of the cathodic deposition were tried. As shown in Figure 5.13a, the cathodic deposition current was the most stable at 40 °C under an applied voltage of 60 V, indicating steady ion diffusion and migration. The stable current density ensures a stable hydrogen evolution and bubbles can be observed on the surface of the cathode. Additionally, the deposition time also affects the electrochemical performance of the electrodes (Figure 5.13b). Too-short or too-long deposition time is detrimental to the specific capacitance of the electrodes, with 1 hour being the optimum deposition time for the growth of well-developed dendritic structure with a slim enough yet interconnected Ni core. Since the growth of dendritic DNE depends on the kinetic equilibrium of nickel dissolution, dissociation of DI water, hydrogen evolution and nickel deposition, the use of viscous EG could keep smooth and stable migration of Ni^{2+} , OH^- and H^+ , as well as proper hydrogen evolution (see Equation 2.34-2.39). In order to elucidate the effect of electrolyte,



different electrolytes were also tried. When EG was replaced by DI water and/or $\text{Ni}(\text{Ac})_2$, the as-prepared samples showed poor electrochemical performances (Figure 5.13c). As shown in Figure 5.13d, when the balance between the migration of Ni^{2+} , OH^- and H^+ ions and the generation of H_2 was disturbed, either the excess H_2 on the cathode caused the vigorous formation of H_2 bubbles, which seriously degraded the adhesion of active material on the electrode (the red line), or the gradually exhausted Ni^{2+} ions (in $\text{Ni}(\text{Ac})_2$ electrolyte) could not maintain the steady formation of $\text{Ni}@\text{NiO}$ (the black line). Same as the cases in previous reports [140b,141b,143], the as-obtained materials were made up of numerous flakes or particles (Figure 5.14a and 5.14b) and showed poor cycle life (Figure 5.15a). Besides, water content also affects the amount of H^+ ion and ion diffusion in the viscous electrolyte. Our results showed that the sample prepared in the electrolyte of 3 vol% water exhibited the best electrochemical performance (Figure 5.15b). NH_4F also took an importance role in the cathodic deposition Figure 5.16a exhibits the samples which were prepared in different electrolytes where NH_4Cl was instead of NH_4F and DI water was instead of EG. Sample ① was prepared by our work. The DNE material was uniformly grown on the surface of nickel foil. From Equation 2.26-2.28, fluorine ions could prevent the fast dissolution of nickel by the formation of NiF_4^- on the surface of the nickel. So, the electrolyte after the reaction was clear (Figure 5.16a①) and current response value kept unchanged (Figure 5.16b①). The results demonstrate that a stable nickel source is good for the formation of a stable coating layer. When NH_4Cl took place of NH_4F , the dissolution of nickel of sample ② as the anode was faster than that of sample ① which can be surmised from the larger current density (Figure 5.16b②). Moreover,



the colour of the electrolyte (Figure 5.16b②) was dark green belonging to nickel ions; the anode was seriously corroded; chloride ions can also strengthen the corrosion level. Amount of H_2 obstructs the adhesion of active materials on the cathode; therefore, it is difficult to form a coating layer. The experimental results of sample ① and ② express the role of NH_4F in the preparation of the DNE material. While EG was replaced by DI water and NH_4Cl was instead of NH_4F , it is impossible to form a coating layer (Figure 5.16a③). Almost all the active materials were flaked off into the electrolyte solution which exhibited the cloudiness state. The current response (Figure 5.16b③) was unstable and ratcheted upward, indicating the circulation between adhesion and flaking of the active materials on the cathode. If only EG was replaced by DI water, the coating layer of sample ④ was better than those of sample ② and ③. However, it was observed that the black materials fell in the electrolyte solution, and there were two kinds of materials with different colours on the surface of the cathode (Figure 5.16a④). What's more, the current response was stable (Figure 5.16b④). The results of sample ③ and ④ indicate that the fast ion diffusion in DI water due to its low viscosity harm the formation of the coating layer where active ions have no time to react or the products were washed off due much H_2 that originates from hydrogen evolution on the cathode (Equation 2.35).

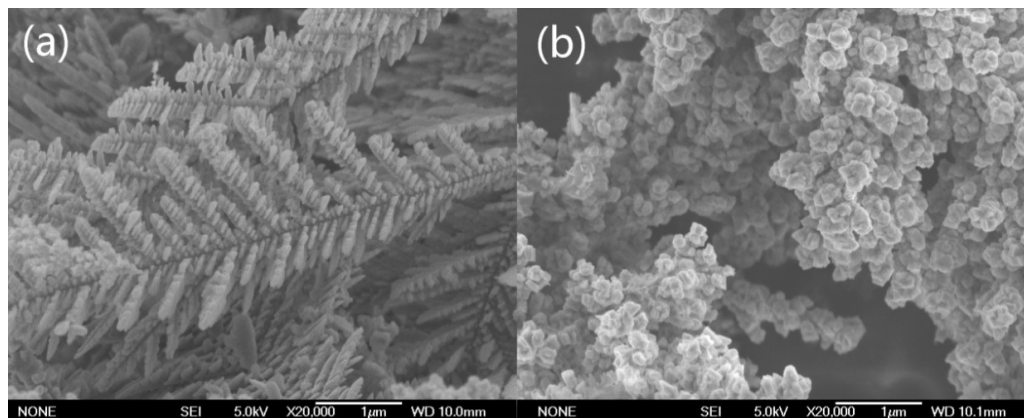


Figure 5.14 SEM images of samples prepared in different electrolytes containing (a) water+ NH_4F in which the nickel foil was used as the anode and (b) water+ NH_4F +0.05 M $\text{Ni}(\text{Ac})_2$ where Pt was used as the anode.

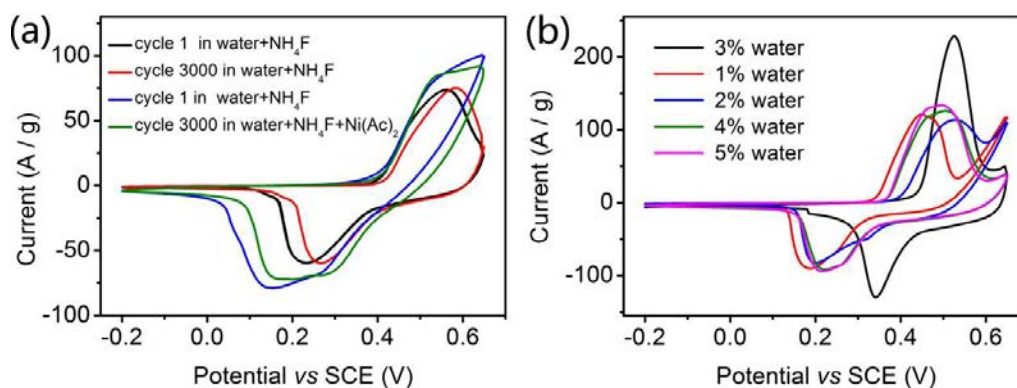


Figure 5.15 (a) Cyclic test of samples prepared in different electrolytes containing (1) water+0.1% NH_4F in which nickel anode was the nickel source and (2) water+ 0.1% NH_4F +0.05 M $\text{Ni}(\text{Ac})_2$ where Pt was used as the anode at the scan rate of 100 mV s^{-1} . (b) The CV curves of samples prepared in EG electrolyte containing 0.1% NH_4F with different water contents at the scan rate of 100 mV s^{-1} .

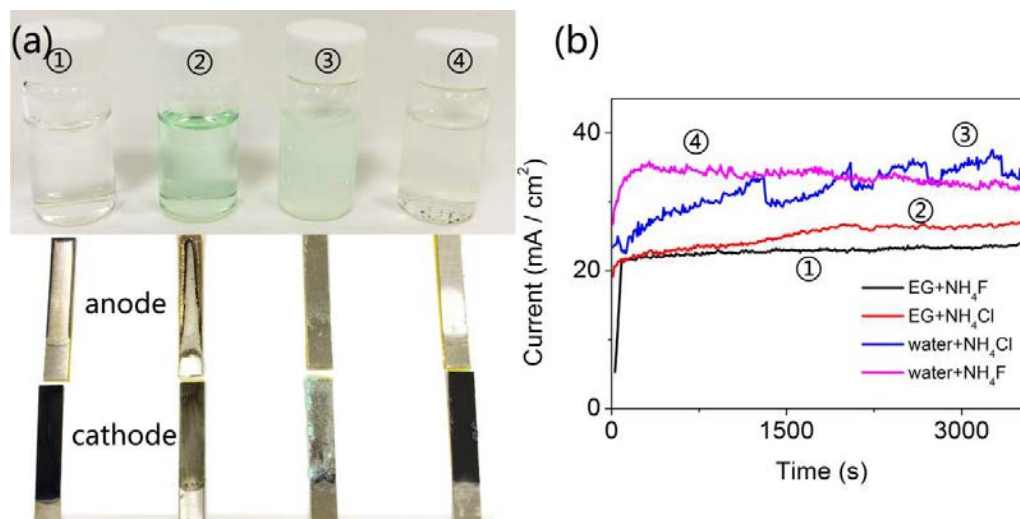


Figure 5.16 (a) Digital pictures of samples prepared in different electrolytes at 40 °C, containing EG+NH₄F (①), EG+NH₄Cl (②), water+NH₄Cl (③), and water+NH₄F (④). The bottles presented electrolyte solutions after cathodic deposition reaction. (b) The current transient of the cathodic deposition process in (a) electrolytes at 40°C. The applied voltages are 60, 30, 7, and 7 V, respectively.

To explore the details of the microstructure evolution during cathodic deposition process, SEM images were taken at different stages of the cathodic deposition in Figure 5.17. It can be found the microstructure has experienced three-level of structure evolution, i.e., from nanoneedle to microbranch and finally to dendrite.

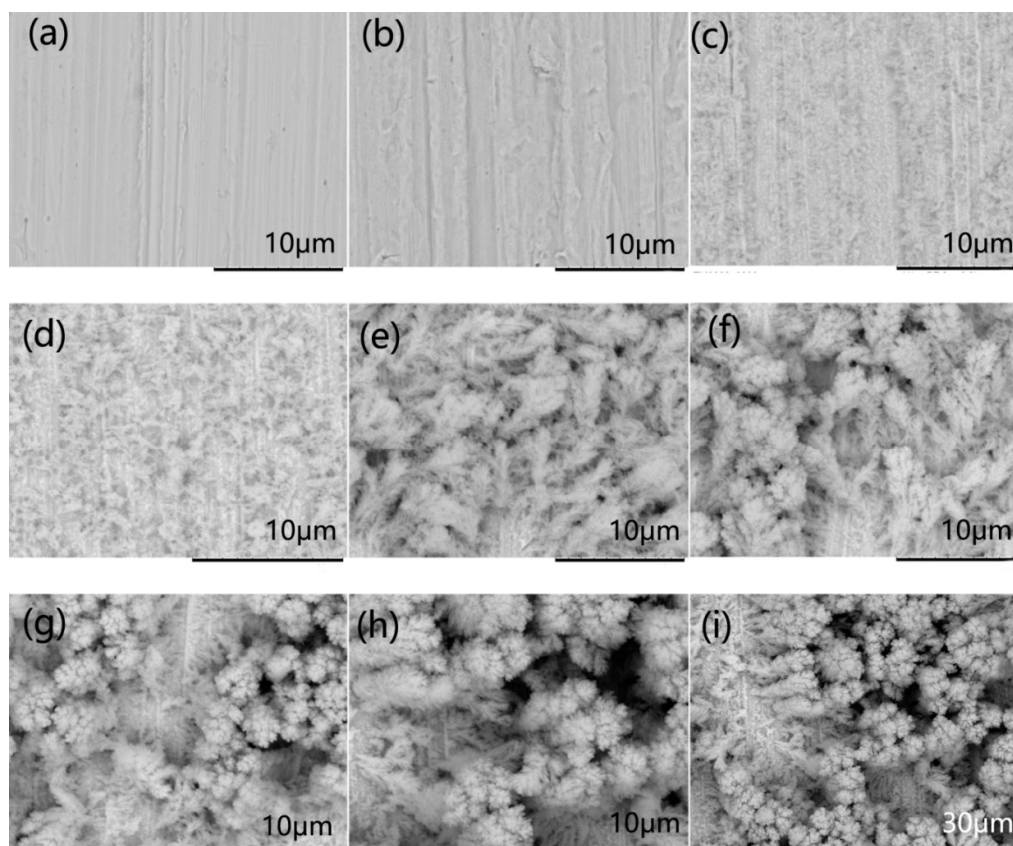


Figure 5.17 The morphology evolution of cathode surface at 40°C after cathodic deposition of (a) 0 min, (b) 0.5 min, (c) 2 min, (d) 5min, (e) 10 min, (f) 20 min,(g) 30 min, and (h, i) 60 min.

It is also interesting to note that such a morphology can not only be obtained by cathodic deposition on Ni foil, but can also be obtained on other substrates as well, such as, stainless steel plate, TiO₂ nanotube arrays, and stainless steel net (Figure 5.18), indicating that this cathodic deposition method (in Ni-free electrolyte) is universal to deposit dendritic Ni-compound on many types of substrates, versatile for different applications

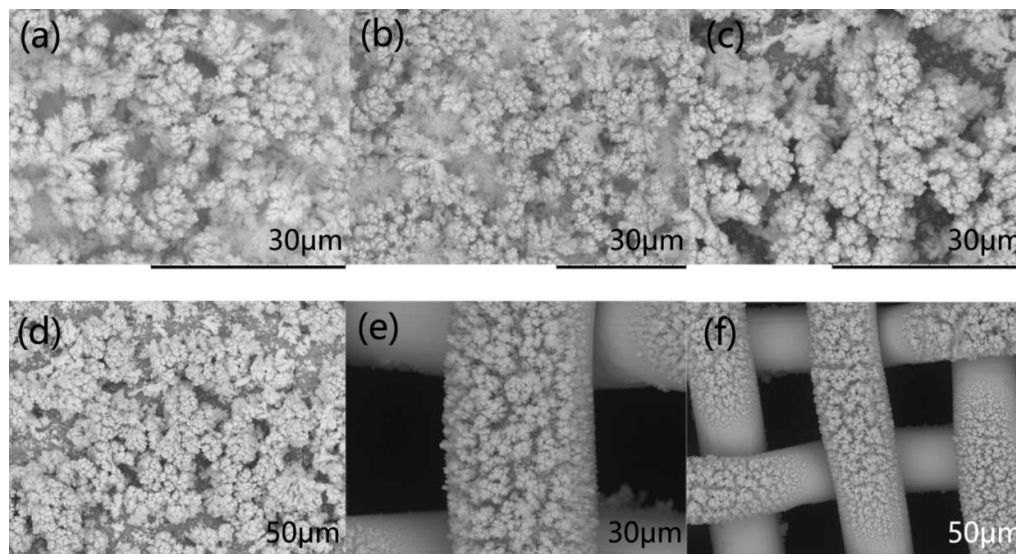


Figure 5.18 Surface morphologies of the electro-deposited cathodes at 40 °C on (a, b) Fe foil, (c, d) TiO₂ nanotube array, and (e, f) stainless steel net.

5.5 Summary

In summary, dendritic Ni@NiO core/shell material was fabricated by one-step cathodic deposition without soft/hard template or further annealing process. The DNE material in the form of dendrites directly grown on the substrate possessed good physical adhesion to the current collector (without the need to use a conductive binder to adhere the active electrode material to the current collector) and hence resulted in reduced electrode resistance and simplified preparation procedure. Additionally, the dendritic core/shell structure had high specific surface area, good connecting and favorable conductivity, providing abundant reaction sites and charge transport paths.



This unique architecture resulted in excellent gravimetric capacitance (1930 F g^{-1} at a current density of 2.9 A g^{-1}), high rate capability and ultra-long cycle life. The DNE material presented in this study shows a great potential for application in battery-type supercapacitor by direct use of Ni anode as the nickel source to realize low and steady nucleation rate, and anisotropic growth, which might be extended to other metal systems, such as $\text{Co@Co}_2\text{O}_3$ and $\text{Fe@Fe}_2\text{O}_3$ for the exploration of high-performance electrode.



Chapter 6 Nickel-Based Nanosheets and Dendrites in Nickel-Free Organic Electrolyte for High-Capacitance and Long-Life Supercapacitor

6.1 Motivation

In Chapters 4 and 5, the preparation of nickel-based composites has been demonstrated, which show high specific capacitance and impressive cycling life. In those studies, anodization and cathodic depositions were applied so as to improve electric and ionic conduction using simple electrochemical methods. In these ways, the as-prepared layered anodic nanosheets and dendrites with the core-shell structure greatly satisfy the requirement. To break the restriction that, in a three-electrode system, normally only one type of electrode material can be made by an electrochemical method, we developed a method to fabricate both anode and cathode at the same time for supercapacitor applications.

In this chapter, we report an approach to anodically and cathodically grow nickel composite thin-films with porous structure at the same time in a single bath. The architectures of anodic and cathodic films with porous nanosheets and dendrites respectively were achieved by fine NH_4F -containing source-free organic electrolyte.

The as-fabricated anodic and cathodic films delivered promising electrochemical performance (3.25 F cm^{-2} at 5 mV s^{-1}). The cathodic film electrode did not exhibit any decay after 10,000 cycles, while maintaining a high areal capacitance (2.02 F cm^{-2} at 5 mV s^{-1}). Our method is simple, low cost and can be easily scaled up. Additionally, the simultaneous preparation method improves the production efficiency, which provides an exciting direction to fabricate electrode materials with excellent performance.

6.2 Optimization of applied voltage

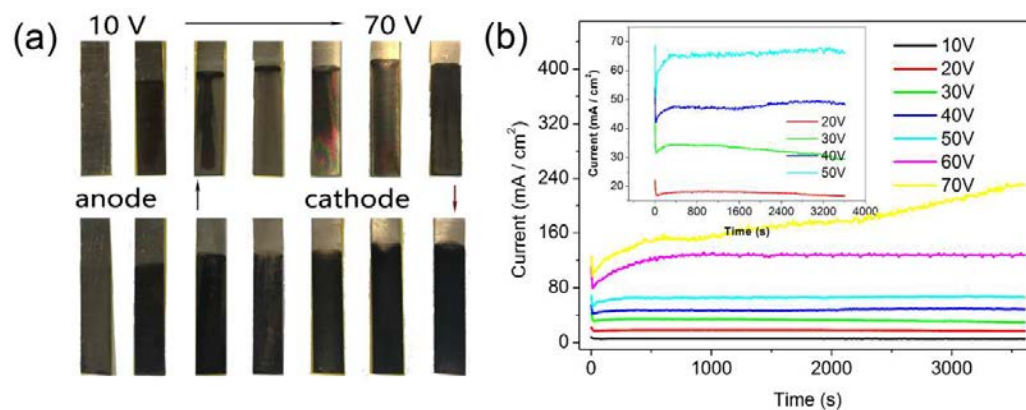


Figure 6.1 (a) Digital pictures of samples prepared under an applied voltage from 0 to 70 V. (b) Transient current density recorded under different applied voltages. The inset shows the curves under 20, 30, 40, and 50 V.

In order to elucidate the effect of applied voltage in our method, the nickel-based composites were fabricated under different voltages. Figure 6.1a shows that when the



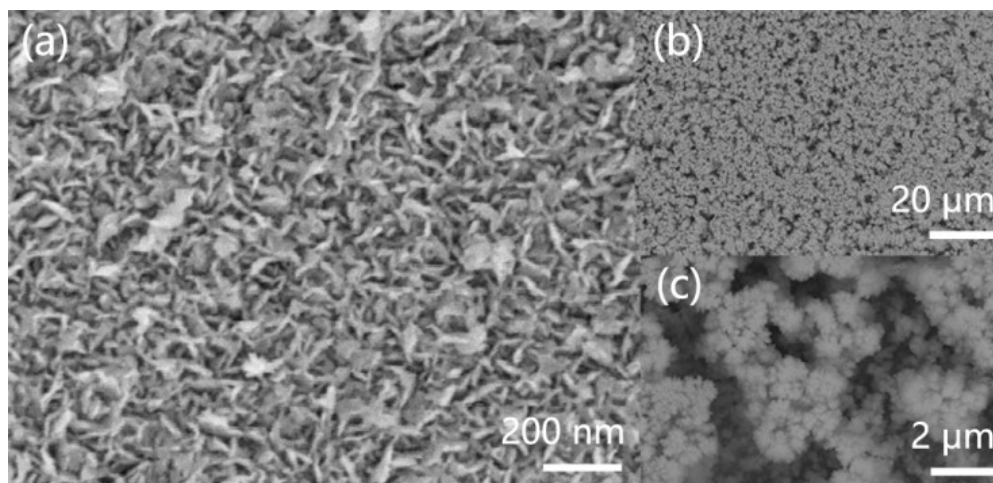
applied voltage is 10 V, it is difficult to grow the active material on both the anode and cathode nickel foils. One possible reason is that the current density is too low (15 mA cm⁻², Figure 6.1b). With increasing voltage, films were observed to be grown on the surface of both anode and cathode. Between an applied voltage of 20 and 50 V, the surface of the anode was covered by a small number of active material particles and the current density was not stable. When the applied voltage reached 60 V, a large and stable current density of 120 mA cm⁻² was achieved. If the applied voltage was increased to 70 V, the current density became unstable again and kept on increasing, indicating an unstable film growth. In order to deposit enough active materials on both anode and cathode with a stable structure, the applied voltage was chosen as 60 V.

6.3 Structural and elemental characterizations

Figure 6.2 shows the morphologies of anodic and cathodic electrode samples. The as-prepared anodic thin-film has a layered porous structure (Figure 6.2a). A porous structure can, to some extent, reduce the electrode resistance, increase number of reaction sites, and hence enhance the electrochemical performance. The as-prepared cathodic film shows fungus-like morphology (Figures 6.2b and 6.2c). Different from anodic film, it had a dendritic structure which is characteristic of metal deposition^[144]. XRD results also prove the metallic composition of this cathodic film (Figure 6.3a). TEM images of anodic film (Figure 6.2d-6.2e) clearly show that the nanosheets are full of pores with a diameter of 10 nm. Obviously the porous structure of nanosheets is beneficial for the ion transport during the charge/discharge process. The high-



magnification HRTEM image (Figure 6.2e) shows the lattice fringe with a d -spacing of 0.27 nm, consistent with the (100) plane of α -Ni(OH)₂ (PDF #22-0444). SAED pattern (inset in Figure 6.2f) presents polycrystalline rings which, from the inner to the outer, can be indexed as (101) plane for Ni₂O₃, (100) for α -Ni(OH)₂ and (102) for β -Ni(OH)₂. The above characterizations show that the anodic film is nickel-based composite. Figures 6.2g-6.2i show that the cathodic film is in dendritic structure with fungus-like morphology. HRTEM images exhibited a lattice fringe with a d -spacing of 0.2 nm, consistent with the (111) plane of nickel (PDF#87-0712). A dispersed diffraction ring of nickel in SAED (inset of Figure 6.2i) suggests nanocrystalline nickel.



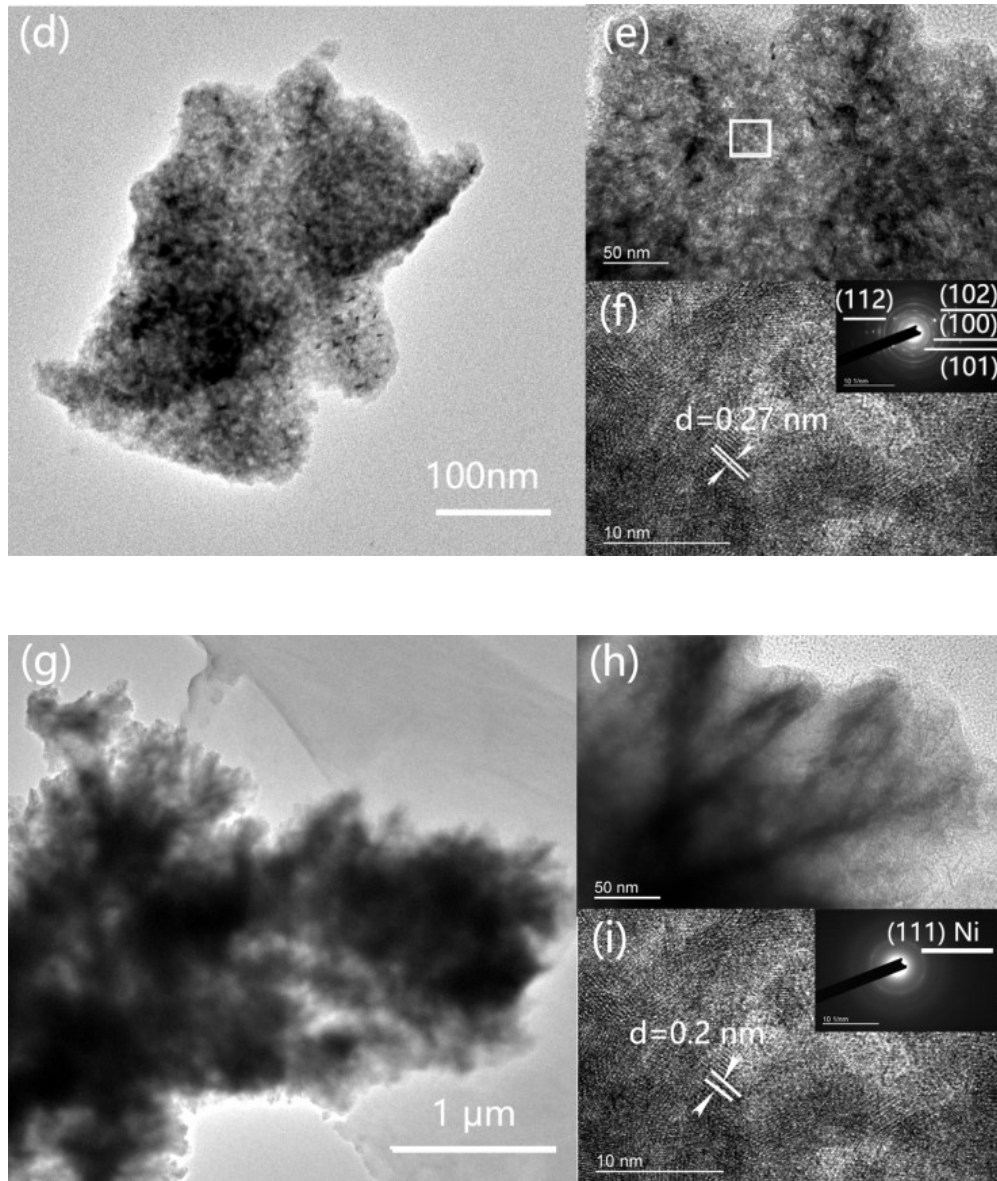


Figure 6.2 SEM images of (a) anodic and (b, c) cathodic films. TEM images of (d, e, and f) anodic and (g, h, and i) cathodic films. The insets of (f) and (i) are corresponding SAEDs.

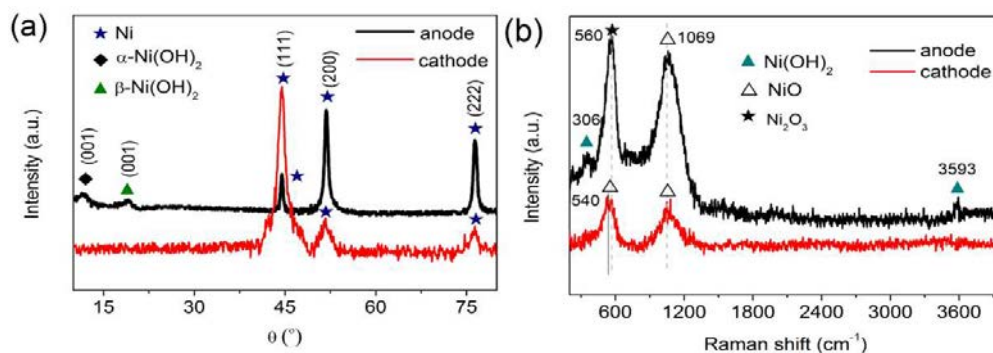


Figure 6.3 (a) XRD pattern and (b) Raman spectra of anodic and cathodic films.

The crystalline structure and chemical composition of anodic and cathodic films were investigated by XRD (Figure 6.3a) and Raman spectroscopy (Figure 6.3b). The anodic nanoporous film shows diffraction peaks at 11.6° and 19.3° , which can be indexed to (100) plane of α -Ni(OH)₂ (PDF #22-0444) and (100) plane of β -Ni(OH)₂ (PDF #14-0117) (Figure 6.3a). Besides, Ni peaks from the substrate beneath the anodic film were also detected at 44.5° , 51.9° , and 76.4° for (111), (200), and (222) planes, respectively (PDF# 87-0712). The Ni peaks can also be detected on the cathodic dendritic film, whose SAED pattern confirms its nanocrystal nature. The existence of metallic nickel can contribute to the improvement of the rate performance of the electrodes. The Raman bands for the anodic film confirm the existence of Ni(OH)₂, Ni₂O₃ and NiO (Figure 6.3b).^[133] Same as Ni₂O₃, the diffraction peaks of NiO were not detected in the XRD pattern, implying the amorphous nature of NiO. Generally, it is known that amorphous phase within materials can introduce more active sites for electrochemical reaction because of the existence of many defects and disorders.^[40] The Raman spectrum of the cathodic film shows features that are typical for NiO. In particular, the

two bands at 540 and 1069 cm^{-1} can be attributed to one-phonon (LO mode) and two-phonon (2LO mode) excitations.^[70,124a,145]

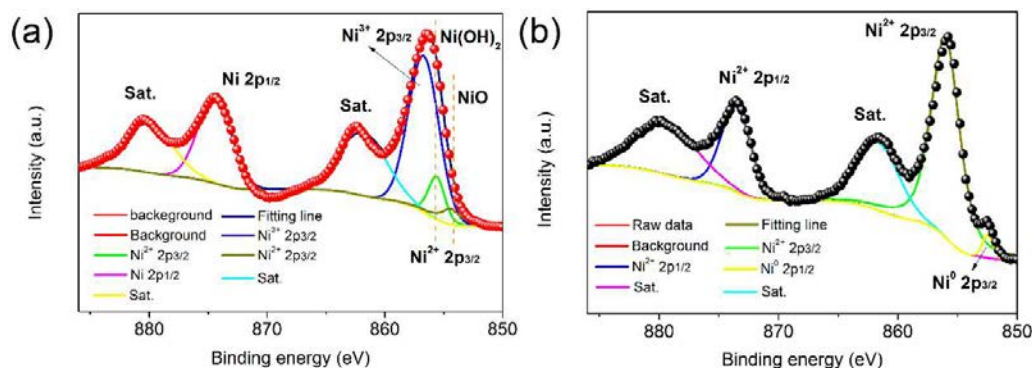


Figure 6.4 XPS spectra of (a) anodic and (b) cathodic films.

The composition of anodic and cathodic films is further revealed by XPS spectra. As shown in Figure 6.4a, three distinct Ni $2p_{3/2}$ peaks were exhibited at 856.7, 855.6, 854.4 eV, corresponding to the nickel compounds of Ni_2O_3 , $\text{Ni}(\text{OH})_2$ and NiO , respectively. The nickel composites from anodic film contain Ni_2O_3 , $\text{Ni}(\text{OH})_2$ and NiO , which is consistent with the result of XRD and Raman spectra. The atomic ratio of Ni^{3+} to Ni^{2+} was about 6.2:1 based on the calculation of peak areas. The presence of large amount of Ni^{3+} is beneficial to the electron conduction. Figure 6.4b showed the Ni $2p$ spectrum of NiO and Ni , with the Ni^{2+} peaks at 8056.1 eV and Ni^0 at 852.9 eV. The result confirms the existence of NiO on the surface of cathodic film. Besides, the weak Ni^0 component suggests that the film is made up of core/shell $\text{Ni}@\text{NiO}$, when XPS is only a surface characterization technique. The metallic nickel can improve the conductivity of the active materials on the cathode, which contributes to the rate performance.

6.4 Electrochemical characterizations of anodic and cathodic films

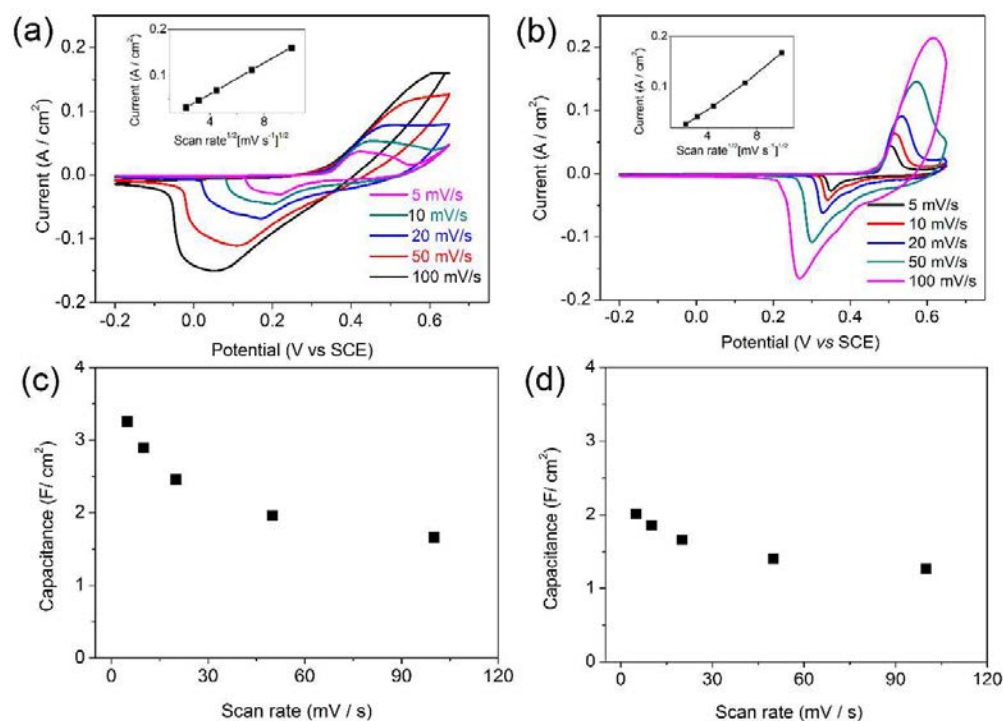


Figure 6.5 CV curves of (a) anodic and (b) cathodic films at different scan rates in 1 mol L⁻¹ NaOH. Insets: linear relationship between cathodic peak current and the square root of scan rate. The variation of areal specific capacitance as a function of scan rate: (c) anodic and (d) cathodic films.

To explore the advantages of anodic and cathodic films as electrodes for battery-type supercapacitor, their performance was studied by CV, GCD and EIS in a three-electrode cell using 1 mol L⁻¹ NaOH aqueous solution as shown in Figure 6.5. Figures 6.5a and 6.5b show CV curves of anodic and cathodic film electrodes, respectively, at



a scan rate from 5 to 100 mVs⁻¹. A pair of redox peaks are clearly seen in each curve, illustrating a typical battery-type faradaic behavior of anodic film. Additionally, the good symmetrical characteristics of the anodic and cathodic peaks indicated the redox reversibility. Noticeably, color change was observed during CV scan. When the sample was anodically polarized, the anodic film became black. At the reverse scan, it's color was immediately recovered. The color change refers to the reversible reaction of Ni(II)↔Ni(III). The linear relationship between cathodic peak current and the square root of scan rate indicates that the reaction was controlled by bulk diffusion of OH⁻. The faradic reaction kinetics is represented by redox peak separation, with small separation indicating fast kinetics. As shown in Figure 6.6, the anodic film electrode exhibits much higher areal capacitance than the cathodic film at a scan rate of 50 mV s⁻¹. However, the redox peak separation of the anodic film electrode is 0.5 V at 50 mV s⁻¹, higher than that of the cathodic film electrode (0.25 V). The reduced peak separation of the cathodic film electrode indicates enhanced reaction kinetics, which was important for electrode application to achieve high rate capability. Figures 6.5c and 6.5d show that the specific capacitances of the anodic and cathodic film electrodes decrease gradually with the increasing scan rate, which can be attributed to limited electrolytic ion diffusion and migration. At high scan rates, the diffusion effect caused some active surface areas to be inaccessible for charge storage and thus the utilization of active material was decreased. Meanwhile, the potential and the current at the redox peaks shifted towards more positive and negative axes during anodic and cathodic scans, respectively, because of the increase of internal diffusion resistance of active materials with increasing scan rate. Due to the fast reaction kinetics, the specific



capacitance of cathodic film electrode was only decreased by 37% from 2.02 to 1.27 F cm^{-2} as the scan rate was increased by 20 times (from 5 to 100 mV s^{-1}), while the specific capacitance of the anodic film electrode was reduced to 1.66 F cm^{-2} from 3.25 F cm^{-2} (49% reduction). The excellent rate performance of the cathodic film electrode is comparable to many other nickel-based electrodes reported recently, such as Ni@NiO electrode (63% capacitance reduction from 5 to 100 mV s^{-1}),^[145] amorphous Ni(OH)₂ (43% capacitance reduction from 1 to 20 mV s^{-1}),^[40] NiF₂/Ni(OH)₂ (42% capacitance reduction from 10 to 200 mV s^{-1}),^[61] Ni(OH)₂/graphene (54% reduction from 1 to 20 mV s^{-1}),^[146] Ni_xCo_{2x}(OH)_{6x}/TiN (37% reduction from 5 to 100 mV s^{-1}).^[114] Compared with the cathodic film electrode, the anodic one exhibits higher areal capacitance of 3.25 F cm^{-2} at a scan rate of 5 mV s^{-1} and relatively low rate capability (Figure 6.8). This outstanding electrochemical capacitance of the anodic film electrode could be attributed to the porous structure and morphology. By contrast, the metallic nickel enhances the rate capability of the cathodic film electrode.

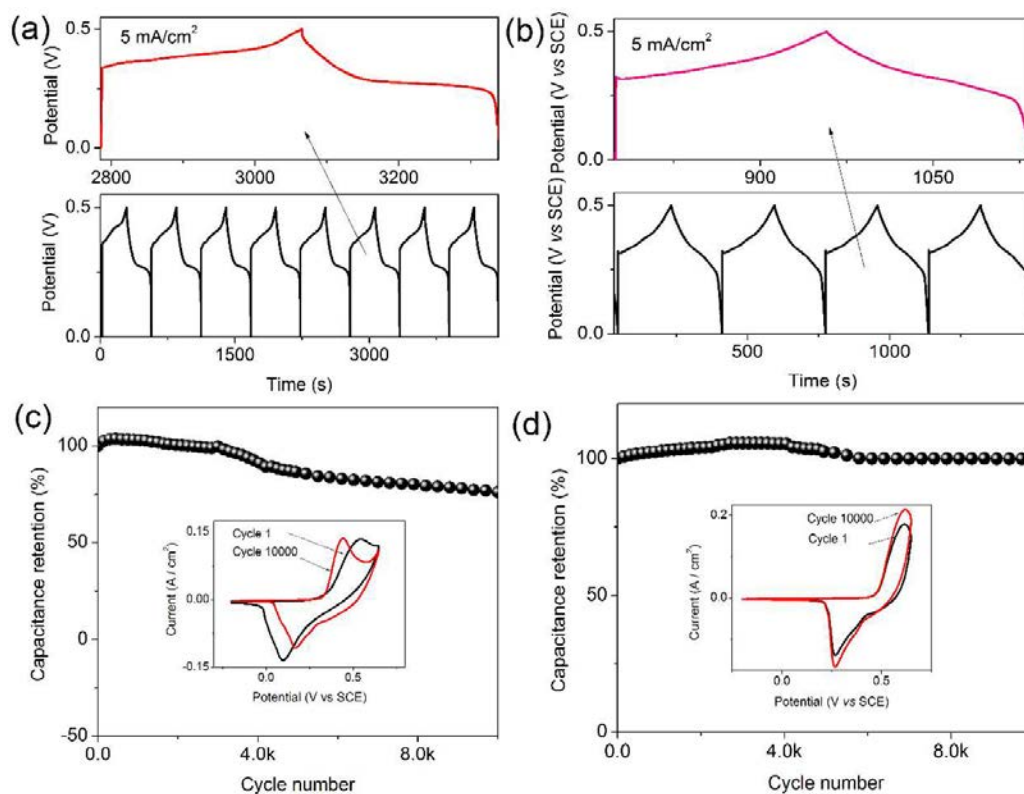


Figure 6.6 GCD curves of (a) anodic and (b) cathodic films. Cyclability test of (c) anodic and (d) cathodic films. Insets: the CV curves for cycle 1 and cycle 10,000.

The superior electrochemical performance of the anodic and cathodic film electrodes was further confirmed by GCD measurements (Figures 6.6a and 6.6b). The areal capacitances of anodic and cathodic film electrodes are 2.76 and 1.81 F cm⁻², respectively, at a current density of 5 mA cm⁻². The capacitances obtained are considerably higher than or comparable to those of recently reported Ni-based electrodes, such as Ni_xCo₂x(OH)_{6x}/TiN (0.18 F cm⁻² at 100 mV s⁻¹),^[114] Ni@NiO (2.07 F cm⁻² at 8 mA cm⁻²),^[145] hydrogenated NiO (371.8 mF cm⁻² at 5 mV s⁻¹),^[147] Ni₂O₃/Ni(OH)₂ (167 F cm⁻² at 500 mV s⁻¹).^[60] The cycling performance of the anodic

and cathodic film electrodes was also evaluated. Figure 6.6c and 6.6d show the variation of the areal capacitances of the anodic and cathodic electrodes, respectively, at a scan rate of 50 mV s^{-1} for 10,000 cycles. The areal capacitance of the anodic film electrode slowly increased in the initial 1,000 cycles and then remained comparatively steady as the cycling continued (Figure 6.6c). The capacitance began to decrease after 3,000 cycles, but still kept a retention rate of 79% of the initial capacitance after 10,000 cycles. The good cyclability may be due to the strong adhesion between the anodic film and its nickel substrate, minimizing the flaking-off of active materials. Notably, the areal capacitance of the cathodic film electrode continuously increased in the initial 4,000 cycles and kept steady without any decay up to 10,000 cycles (Figure 6.6d). The initial increase in capacitance is due to the activation of electrode.

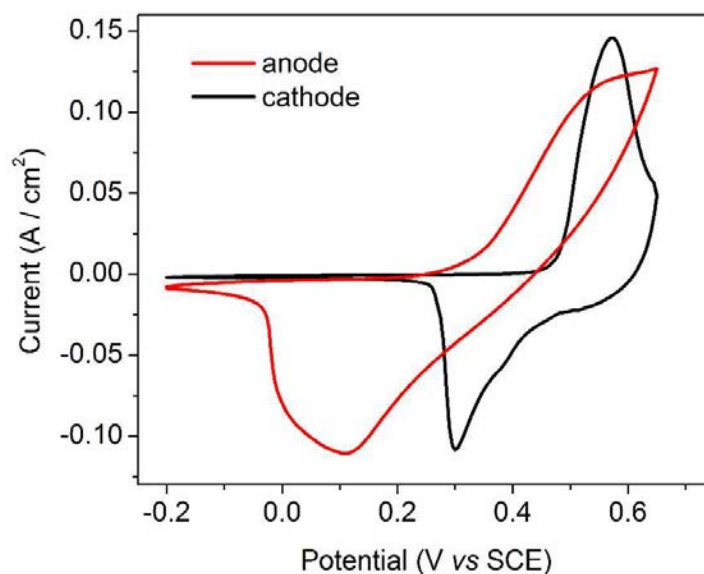


Figure 6.7 CV curves of the anodic and cathodic film electrodes at a scan rate of 50 mV s^{-1} .

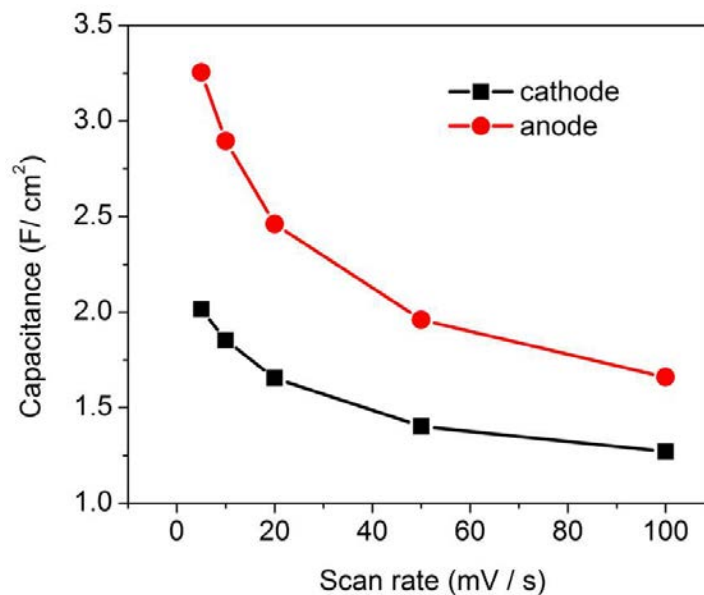


Figure 6.8 The variation of capacitance of the anodic and cathodic film electrodes as a function of scan rate.

6.5 Summary

In summary, a one-step method in NH_4F -containing ethylene glycol electrolyte has been developed to anodically fabricate porous nickel composite electrode and cathodically deposit dendritic structure $\text{Ni}@\text{NiO}$ electrode. As a result of pore-enriched architecture which provides abundant open channels for ion transport and a highly accessible interface for redox reactions, the as-prepared anodic film electrode yielded a very high areal capacitance of 3.4 F cm^{-2} at a scan rate of 5 mV s^{-1} . Moreover, the cathodic film electrode exhibited ultrahigh long-term cycling stability with few decay of capacitance after 10,000 cycles (0.1% decay) when the areal capacitance also



reached 2.0 F cm^{-2} . This work gives us a revelation that two kinds of metal-based materials can be simultaneously produced in a bath and used as electrodes.



Chapter 7 Design of Hierarchical Ni-Co@Ni-Co Layered Double Hydroxide Core-Shell Structured Nanotube Array for High-Performance Flexible All-Solid-State Battery-Type Supercapacitors

7.1 Motivation

In previous chapter, in order to achieve the excellent performance of electrode materials as battery-type supercapacitor, the strategies for enhancing the intrinsic conductivity and ionic conductivity of materials are focused on the structure and morphology control by simple metal oxide/hydroxide preparation (NiO/Ni(OH)₂). However, the introduction of other elements towards the composition control can further boost the electric conduction of materials and to support fast electron transport required by higher rates.

Nanotube arrays (NTAs) with well-defined pore structures have drawn great attention in the design of electrode materials due to the high surface area. It has been demonstrated that the well-oriented NTAs also contribute to the ion diffusion and substantially facilitate the electrolyte penetration/diffusion.^[148] However, most of the



NTAs reported had closely packed nanotubes (without top),^[129,149] which result in low surface area, low number of electrochemical active sites, and difficult electrolyte infiltration.

Based on the above discussions, in this chapter, we use low-cost and environment-friendly ZnO nanorod arrays (ZnO NRAs) grown on CFC as a template to design and fabricate Ni-Co@Ni-Co LDH NTAs (core-shell structured) with separated tubes and hierarchical top for efficient utilization of high surface area (Figure 7.1). The well-aligned Ni-Co@Ni-Co LDH NTAs designed in this work represent a new example of nanostructure engineering for better electrochemical performance, owing to the following features: (i) the Ni/Co metallic core provides a pathway for efficient charge transport, which effectively overcomes the weakness of Ni-Co LDH (relatively poor conductivity); (ii) the binary metal ions of Ni²⁺/Ni³⁺ and Co²⁺/Co³⁺ enhance capacitive properties since the mixed valence states can increase the number of active sites to trigger more redox reactions; (iii) the nanotube structure with a hierarchical top in addition to the separated tubes not only facilitates the transport of ions, but also provides numerous electrochemical reaction sites; (iv) well-aligned NTAs growing homogeneously on the CFC current collector enable almost all the nanotubes to participate in the electrochemical reactions without any dead volume. In a liquid-electrolyte-based three-electrode test, Ni-Co@Ni-Co LDH NTAs/CFC achieved a very high specific capacitance of 2414 F g⁻¹, in 1 mol L⁻¹ NaOH aqueous solution. An all-solid-state flexible battery-type supercapacitor (FBSC) was assembled using Ni-Co@Ni-Co LDH NTAs/CFC as the positive electrode and CNFs/CFC as the negative

electrode. The as-fabricated FBSC exhibited a fascinating electrochemical performance with the maximum specific capacitance of 319 F g^{-1} , high energy density of 100 W h kg^{-1} at a power density of 1.5 kW kg^{-1} , and good cycling stability (98.6% capacitance retention rate after 3,000 cycles). Our work reported here sheds light on the effective structural engineering of electrodes to improve electrochemical performance of energy storage devices.

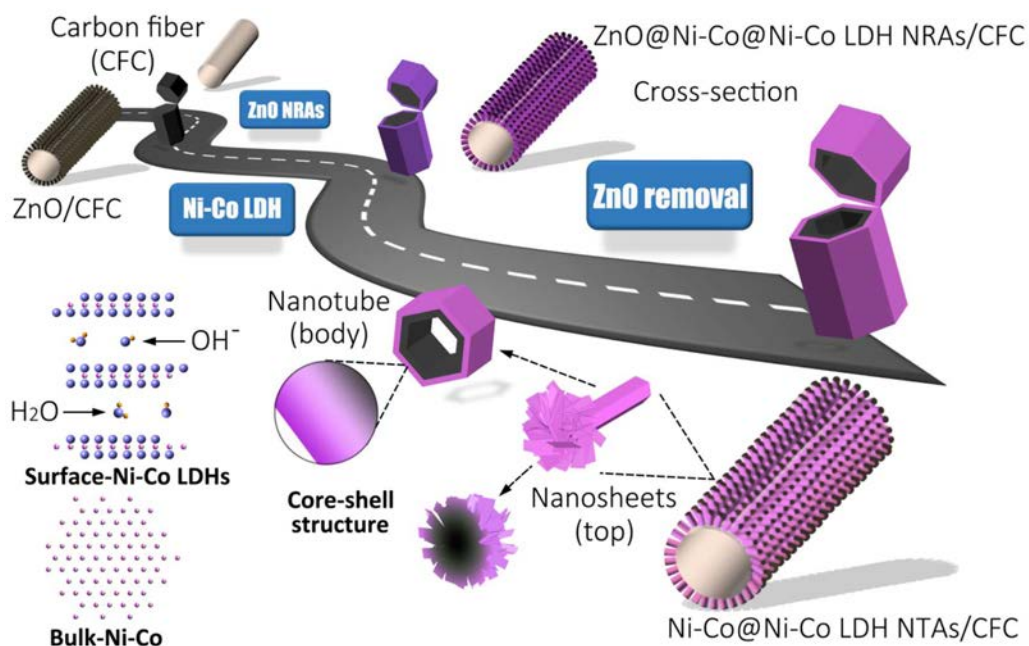


Figure 7.1 A schematic diagram of the preparation procedures of hierarchical Ni-Co@Ni-Co LDH NTAs on CFC.



7.2 Structural and elemental characterizations

7.2.1 Positive electrode: Ni-Co@Ni-Co LDH NTAs/CFC

In this work, CFC was used both as the current collector and the support for active materials. Figure 7.2 shows that CFC is composed of many carbon fibers with diameters of about 8 μm . For the electrochemical deposition of ZnO NRAs, only at a current density of 0.8 mA cm^{-2} were dense, homogeneous, and vertically aligned ZnO NRAs formed with a separation around 100-500 nm among NRAs (Figure 7.3a and 7.3b). ZnO NRAs electrodeposited at a too low or a too high current density are shown in Figure 7.3c and 7.3d. The diameter and length of ZnO NRAs are about 500 nm and 2 μm , respectively (Figure 7.4). From the HRTEM image and SAED pattern, the growth direction of ZnO NRA is determined to be along [001] direction, the polar c -axis of ZnO crystals.^[150] After the second electrodeposition, nickel and cobalt hydroxides were coated on the surfaces of ZnO NRAs. Similarly, only at a current density of 4 mA cm^{-2} can hierarchical Ni-Co@Ni-Co LDHs be conformally deposited on ZnO NRAs, with nanorods clearly separated to each other (Figure 7.5a and 7.5b), as compared with those deposited at a too low (1 mA cm^{-2}) or a too high (6 mA cm^{-2}) current density (Figure 7.5c and 7.5d). High magnification SEM image (Figure 7.6a) clearly shows that the Ni-Co@Ni-Co LDH NR looks like a fungus composed of a big top and a small body (marked by rectangles in Fig.7.6a). The big top is made of layered sheets (Figure 7.6b) which greatly enhance the specific surface area of the active material. After dissolving the ZnO NRAs template, Ni-Co@Ni-Co LDH NTAs/CFC

was fabricated (Figure 7.7). The morphologies of the Ni-Co LDH NTAs of different Ni:Co ratios (unless otherwise specified, all the Ni:Co ratio mentioned hereafter refers to the molar ratio of Ni:Co in the electrolyte for electrodeposition) are similar to each other (Figure 7.7, 7.8a, 7.8c, and 7.8e), with the nanotubes standing vertically and separated apart from each other. Exceptionally, the Ni-Co@Ni-Co LDH NTAs (Ni:Co=0:10) were composed of larger plates and the nanotube structure was completely destroyed (Figure 7.8g). This may be attributed to the fast electrodeposition of Co element. In general, as the content of cobalt was increased gradually, the coated Ni-Co@Ni-Co LDHs became more net-like until it appeared flaky. The chemical composition of Ni-Co@Ni-Co LDH NTAs/CFC is analyzed by EDX as shown in Table 7.1. The compositions are absolutely different from the starting feeding molar ratios of Ni:Co. This is expected and is due to different reaction resistances present in the solution (e.g. surface overpotential, concentration overpotential, and ohmic overpotential, etc.).^[151] The deposition of Co is always preferred due to its dominant electrochemical activity at 4 mA cm^{-2} .

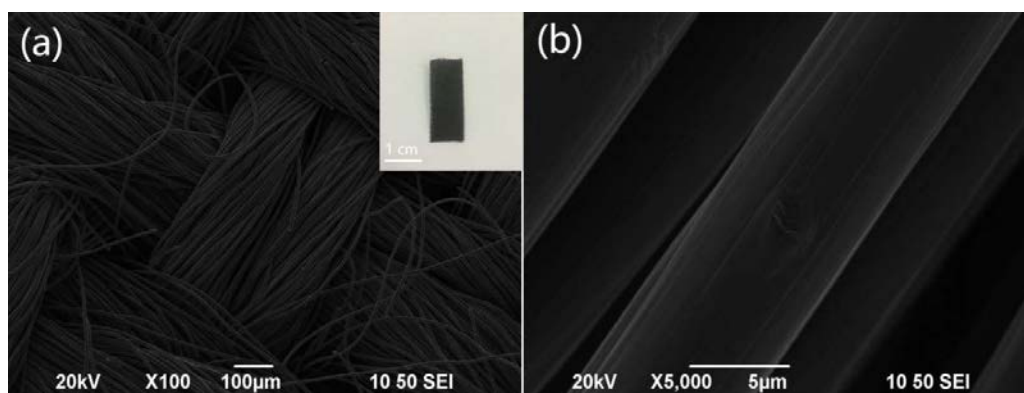


Figure 7.2 (a) Low and (b) high magnification SEM images of carbon nanofibers of the CFC. The inset: the optical image of CFC.

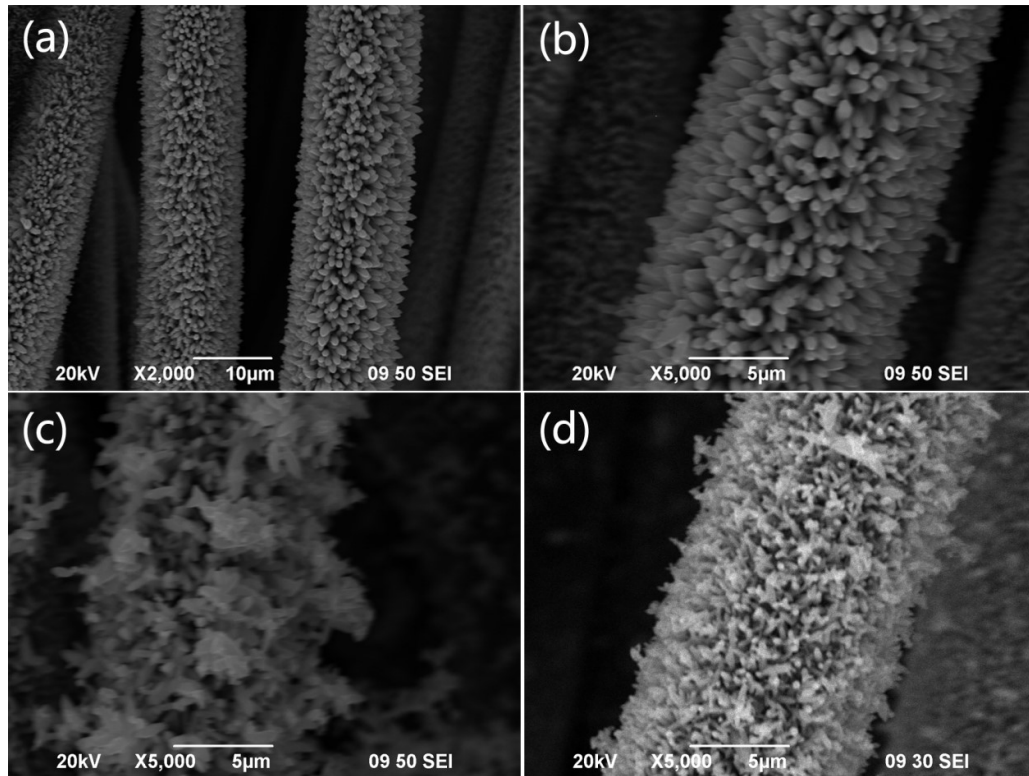


Figure 7.3 SEM images of ZnO NRAs grown on CFC by electrodeposition at different current densities: (a) and (b) 0.8 mA cm^{-2} , (c) 0.6 mA cm^{-2} and (d) 1 mA cm^{-2} .

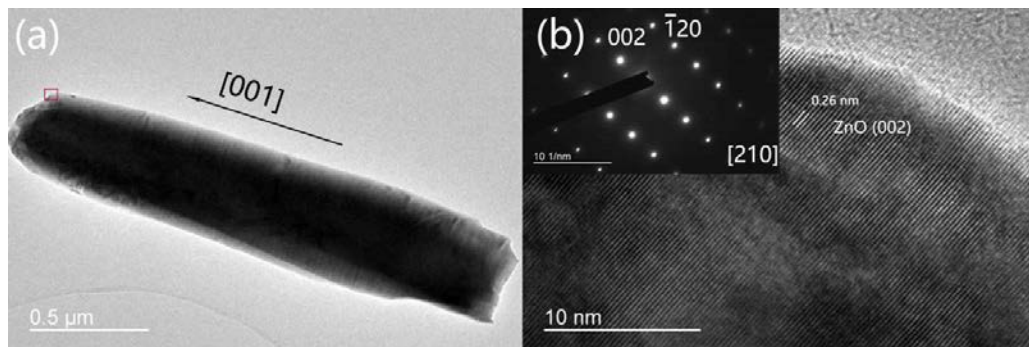


Figure 7.4 (a) TEM image of a single ZnO nanorod and (b) HRTEM image taken from the edge of the ZnO nanorod. Inset: Corresponding SAED pattern.

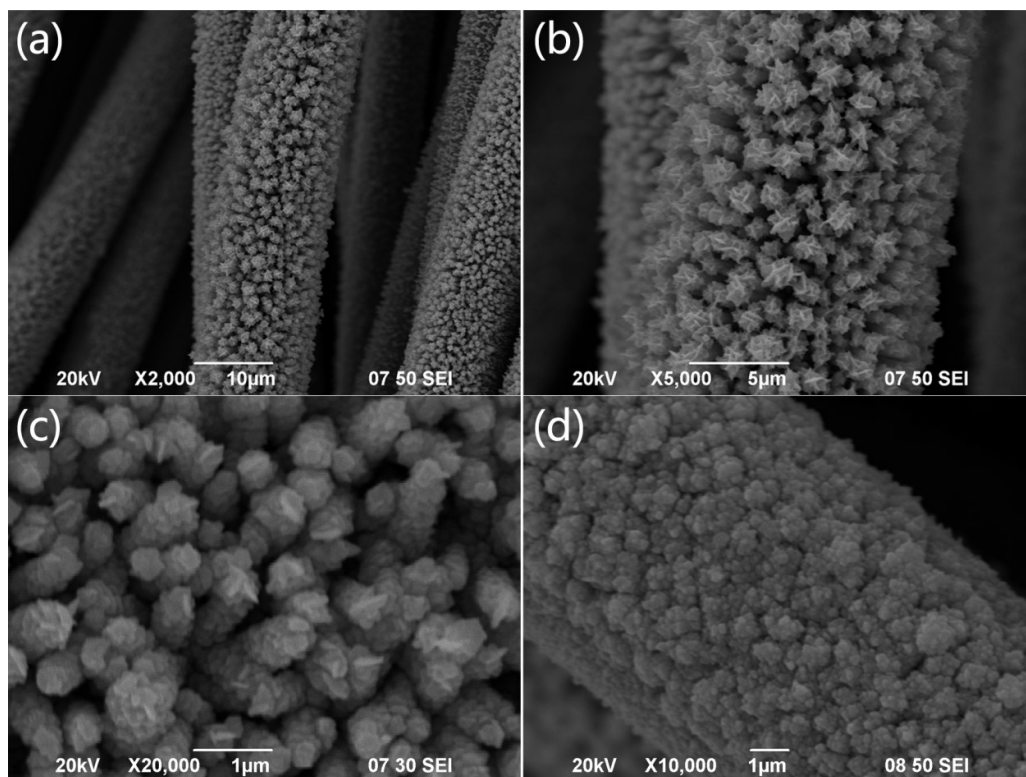


Figure 7.5 SEM images of Ni-Co@Ni-Co LDH NRAs on ZnO template, which are electrodeposited by different current density: (a) and (b) 4 mA cm^{-2} , (c) 1 mA cm^{-2} and (d) 6 mA cm^{-2} .

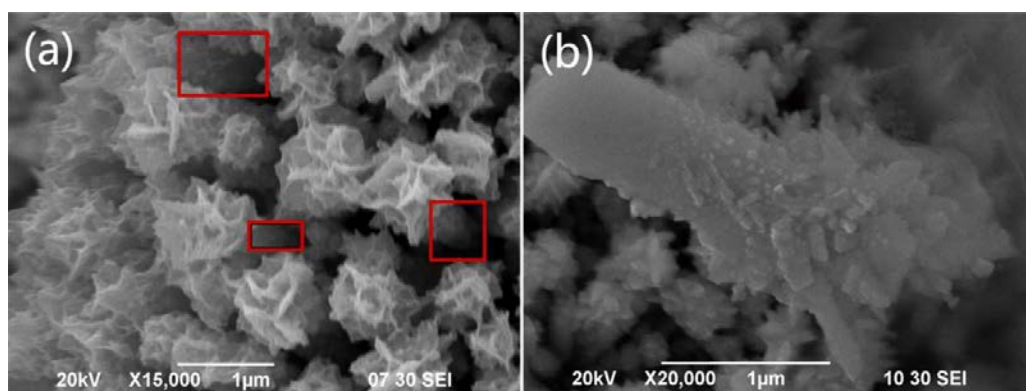


Figure 7.6 SEM images. (a) Magnified Ni-Co@Ni-Co LDH NRAs and (b) a single Ni-Co@Ni-Co LDH NR grown on a ZnO NR by electrodeposition. Ni:Co=5:5.

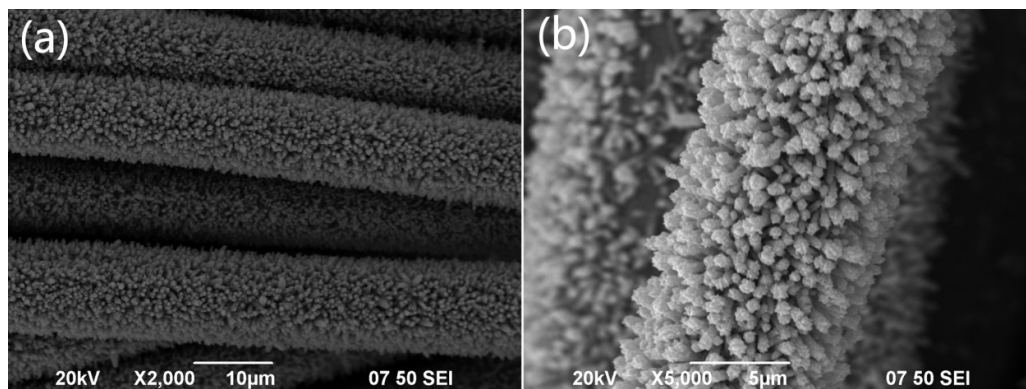


Figure 7.7 (a) and (b) SEM images of Ni-Co@Ni-Co LDH NTAs/CFC with different magnifications (Ni:Co=5:5).

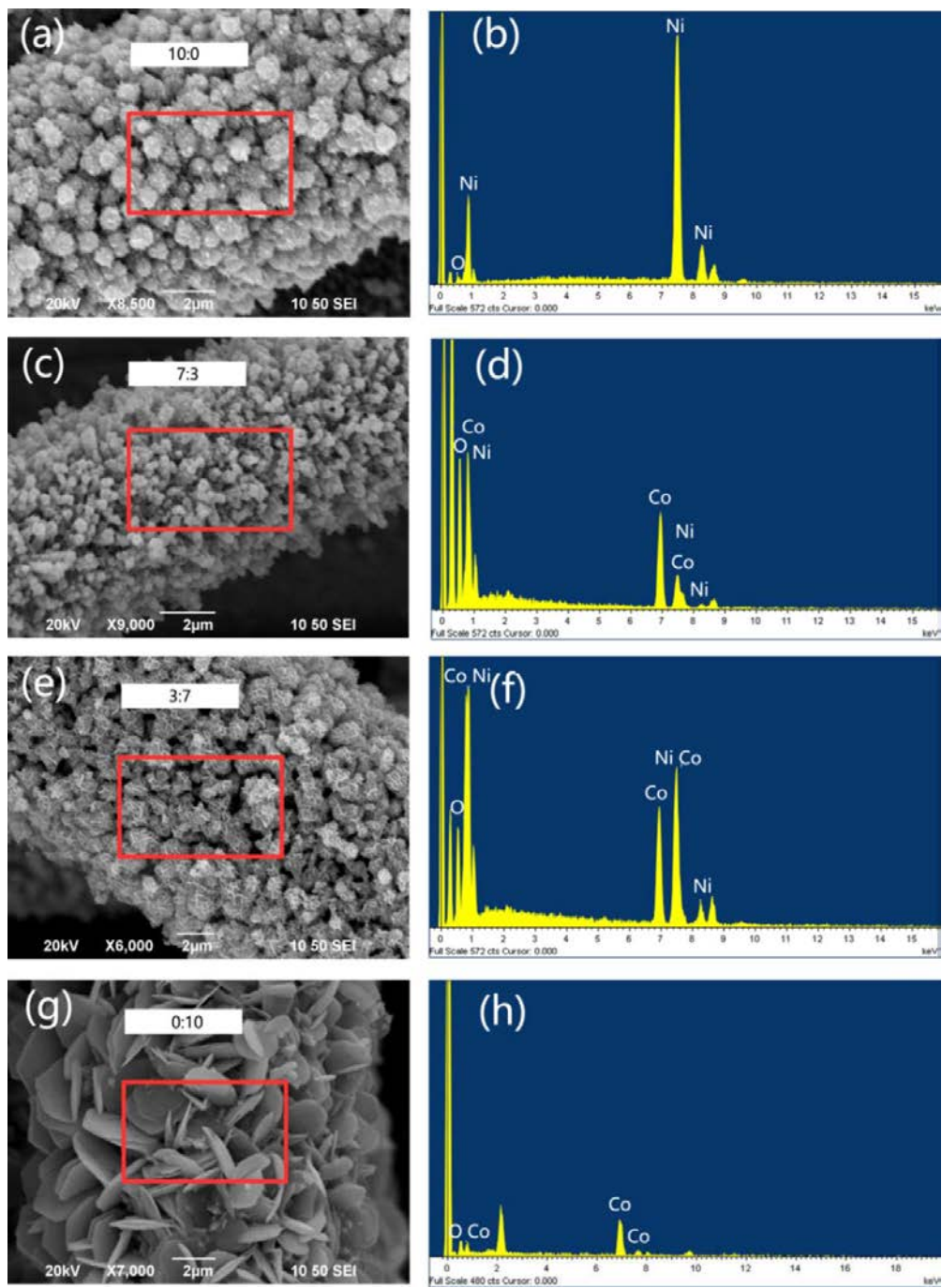


Figure 7.8 SEM images and the EDX spectra of Ni-Co@Ni-Co LDH NTAs/CFC with different Ni:Co ratios: (a, b) 10:0, (c, d) 7:3, (e, f) 3:7, and (g, h) 0:10.

Table 7.1 Elemental distribution of the Ni-Co@Ni-Co LDH NTAs with different Ni:Co ratios.

Ni:Co feeding ratio ^a	Measured atomic ratio by EDX (%) ^a		
	O ^a	Co ^a	Ni ^a
10:0 ^a	10.89±1% ^a	0 ^a	89.11±1% ^a
7:3 ^a	9.76±1% ^a	59.50±1% ^a	30.73±1% ^a
5:5 ^a	28.84±1% ^a	55.24±1% ^a	15.92±1% ^a
3:7 ^a	12.78±1% ^a	70.97±1% ^a	16.24±1% ^a
0:10 ^a	19.53±1% ^a	80.47±1% ^a	0 ^a

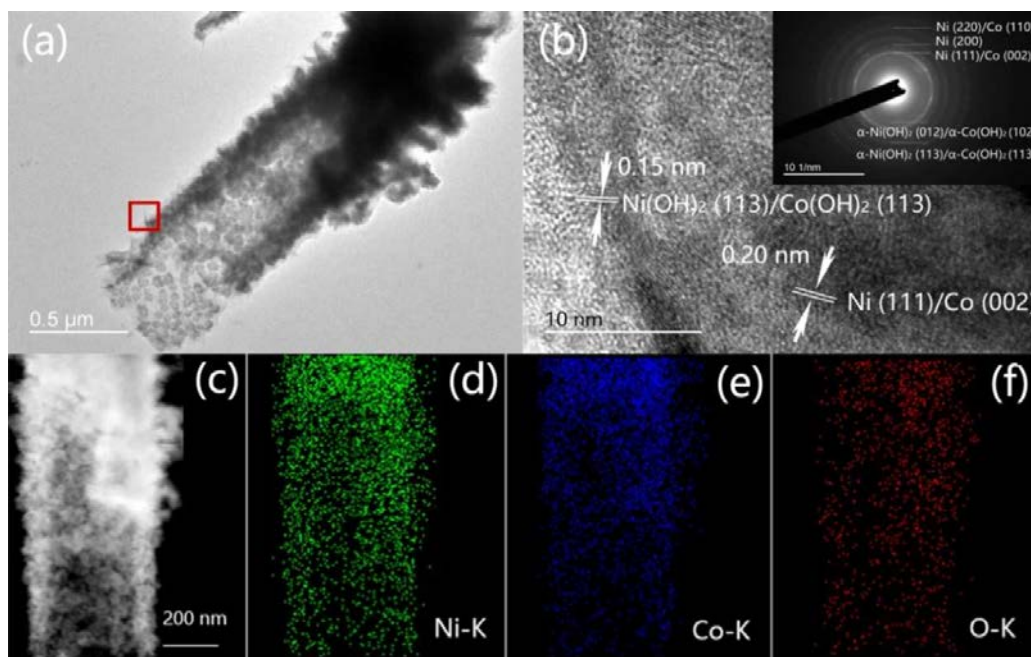


Figure 7.9 Body of the Ni-Co@Ni-Co LDH NTAs (Ni:Co=5:5): (a) TEM image, (b) HRTEM image and SAED pattern (inset) of the selected area in (a), (c) STEM bright field image, and (d-f) elemental mapping of Ni, Co and O.

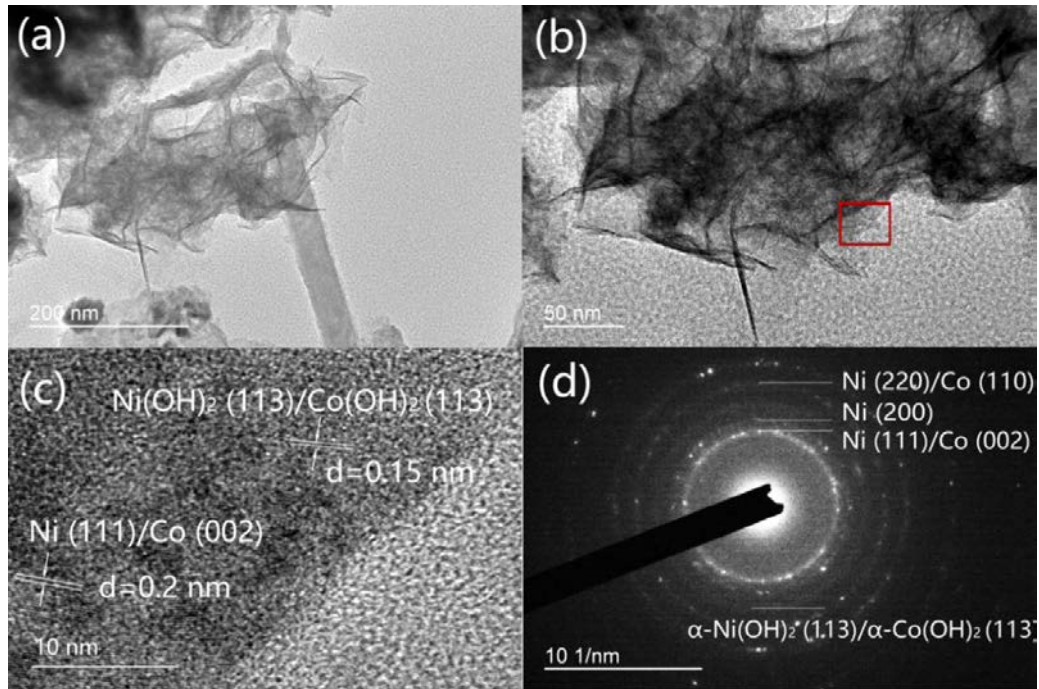


Figure 7.10 Top of the Ni-Co@Ni-Co LDH NTA (Ni:Co=5:5): (a) and (b) TEM image; (c) HRTEM image and (d) SAED pattern of the selected area in (b).

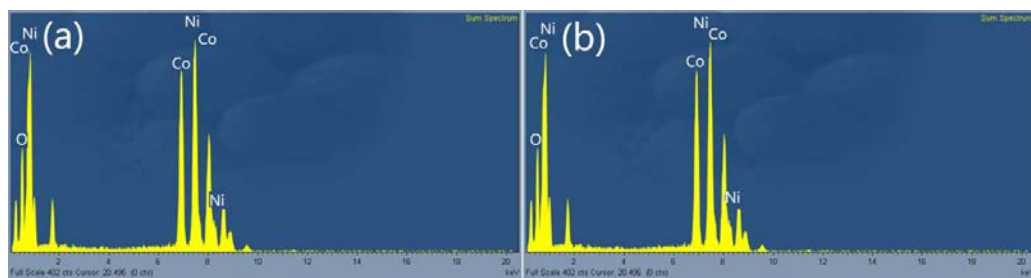


Figure 7.11 EDX spectra of (a) the body and (b) the top of the Ni-Co@Ni-Co LDH NTAs (Ni:Co=5:5).



Figure 7.9a shows that the top of the Ni-Co@Ni-Co LDH NT (Ni:Co=5:5) has a diameter of ~ 700 nm and consists of many nanosheets, while the body of NT has a diameter of ~ 550 nm and consists of nanocrystals (20-30 nm in size). The body of NT has a wall thickness of ~ 50 nm. The nanosheets on the top of the NT provide a large amount of active sites for electrochemical reaction and the void space between neighboring NTs is beneficial for electrolyte infiltration and ion diffusion without any blocks. HRTEM image of the Ni-Co@Ni-Co LDH NTA (Figure 7.9b) shows the lattice fringes corresponding to the (111) plane of nickel or (002) plane of cobalt and the (113) plane of α -Ni(OH)₂ or α -Co(OH)₂. The selected-area electron diffraction (SAED) pattern (inset of Figure 7.9b) reveals that the body of the Ni-Co@Ni-Co LDH NTA consists of many nanocrystals. The diffraction rings match the planes of Ni (or Co) and α -Ni(OH)₂ (or α -Co(OH)₂). EDX mapping (Figure 7.9d-7.9f) shows that Ni, Co and O are well-dispersed and homogeneously mixed in the NTA. It is worth noting that Ni:Co:O ratio in the Ni-Co@Ni-Co LDH NTAs (Ni:Co=5:5) is around 1:3.4:1.8 (Table 7.1), deviating from the stoichiometric ratio of Ni(OH)₂ (or Co(OH)₂) and implying the existence of metallic nickel and cobalt, in agreement with the SAED result. The top of the NTA is made up of the Ni-Co@Ni-Co LDH nanosheets (Figure 7.10), whose SAED pattern is similar to that of the body (Figure 7.6). EDX also confirms the elemental composition of Ni, Co, and O (Figure 7.11). The Barret-Joyner-Halenda (BJH) pore size distribution showed that the sample with Ni:Co=5:5 had a bimodal size distribution, with pore diameters centered at 4.8 and 15.1 nm, respectively (the insert of Figure 7.12). The presence of high mesopores provides large surface area for active species to quickly access the electrode material. The hysteresis

loop belongs to type H4, indicating slit-like pores with mesopore size. And the Brunauer-Emmet-Teller (BET) surface area is $112.2 \text{ m}^2 \text{ g}^{-1}$ (Figure 7.12).

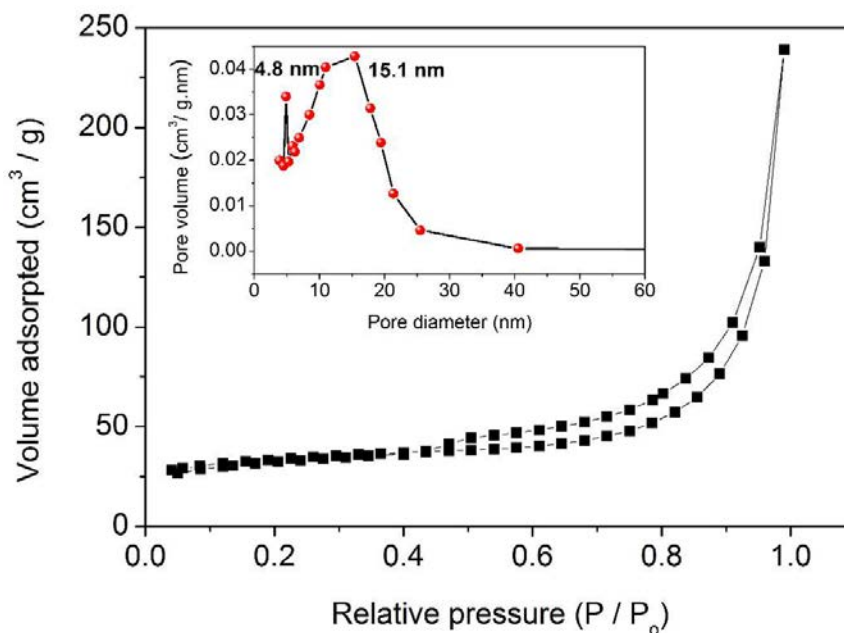


Figure 7.12 The BET isotherm of the the Ni-Co@Ni-Co LDH (Ni:Co=5:5) at 77 K. The inset: the Barret-Joyner-Halenda (BJH) pore size distribution

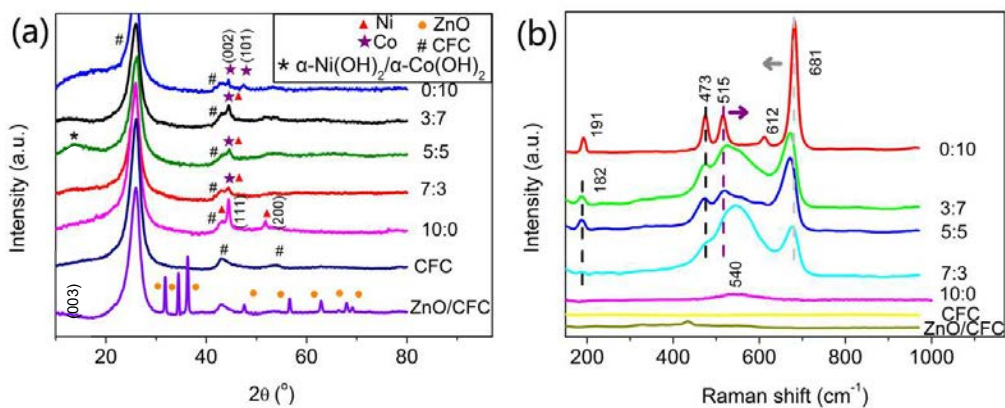


Figure 7.13 (a) XRD patterns and (b) Raman spectra of CFC, ZnO and Ni-Co@Ni-Co LDH NTAs/CFC with different Ni:Co ratios.



Figure 7.13a shows that Ni-Co@Ni-Co LDH NTAs/CFC (of different Ni:Co ratios) contains hexagonal cobalt with a space group of P63/mmc (JCPDS Card No. 05-0727) and cubic nickel with a space group of $Fm\bar{3}m$ (JCPDS Card No. 04-0850), apart from CFC (JCPDS Card No.41-1487).^[64] The characteristic diffraction peak observed around 44.5° is caused by the overlap of the (111) peak from nickel and the (002) peak from cobalt. A wide diffraction peak at around 11.3° in the Ni-Co@Ni-Co LDH NTAs/CFC (Ni:Co=5:5) can be indexed as (001) plane of α -Ni(OH)₂ or α -Co(OH)₂ (hydrotalcite-like LDH phase).^[152] However, no obvious peaks of hydrotalcite-like LDH phase are found in the samples with other Ni:Co ratio, implying their tiny crystals. Meanwhile, the disappearance of ZnO peaks in the Ni-Co@Ni-Co LDH NTAs/CFC indicates that the ZnO NRA template was completely removed by alkaline solution.

Figure 7.13b displays that Ni-Co@Ni-Co LDH NTAs/CFC (Ni:Co=0:10) has the characteristic Raman peaks at 681, 612, 515, 473, and 191 cm^{-1} , corresponding to the A_{1g} , F_{2g} , F_{2g} , E_g , and F_{2g} modes of Co(OH)₂, respectively.^[153] Ni-Co@Ni-Co LDH NTAs/CFC (Ni:Co=10:0) shows weak Raman activity and a wide band at 540 cm^{-1} (corresponding to Ni(OH)₂), suggesting its low crystalline.^[153b] The result is in good agreement with its XRD pattern which reveals no extra peaks other than those of Ni metal. Two Raman peaks of Ni-Co@Ni-Co LDH NTAs/CFC (Ni:Co=3:7, 5:5, and 7:3) located at 473 and 515 cm^{-1} correspond to Ni-OH/Co-OH and Ni-O/Co-O (A_g) stretching modes, respectively.^[151,153b,154] The characteristic peak at 182 cm^{-1} belongs to the LDH phase.^[155] The Raman band at 681 cm^{-1} was observed to red shift with increasing amount of nickel in Ni-Co@Ni-Co LDH NTAs/CFC. The redshift of the

A_{1g} Raman mode is probably due to tensile strain associated with Ni doping into the $\text{Co}(\text{OH})_2$ lattice.^[156] However, the band at 515 cm^{-1} blue shifts with increasing amount of nickel, similar to the observations of Bockman *et al.*^[157] The change of the E_g Raman mode can be ascribed to the increase of lattice distortion and defects induced by nonstoichiometry due to the formation of the LDH phase.^[156,158] Moreover, the shifted peaks became broadened. The peak corresponding to ZnO (437 cm^{-1}) was not found in the samples, indicating the complete removal of ZnO, in agreement with XRD results.

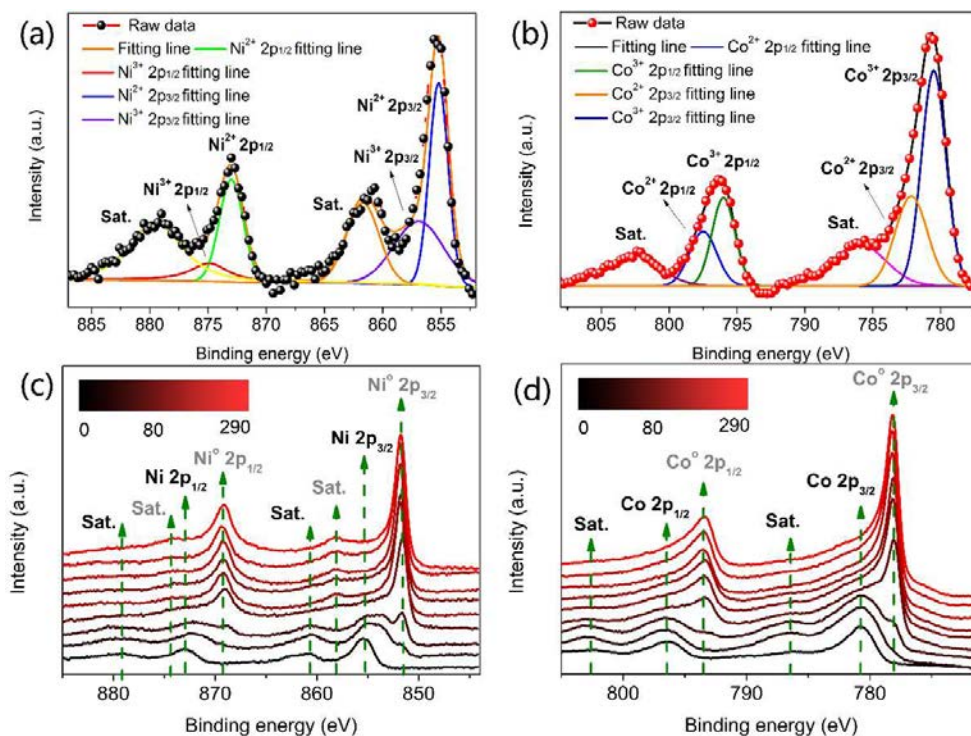


Figure 7.14 (a) Ni 2p XPS, (b) Co 2p XPS, (c) depth profile of Ni 2p XPS, and (d) depth profile of Co 2p XPS of the as-obtained Ni-Co@Ni-Co LDH NTAs/CFC (Ni:Co=5:5). Etching depth is from 0 to 290 nm.

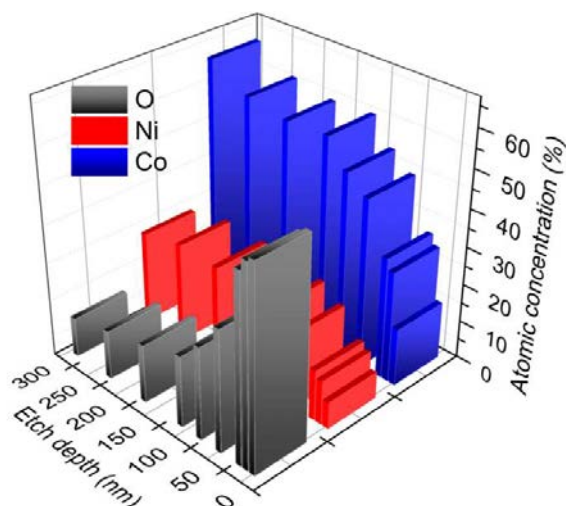


Figure 7.15 Variation of O, Co, and Ni concentrations of the Ni-Co@Ni-Co LDH (Ni:Co=5:5) as a function of etching depth.

To further study the composition of the electrode material, Ni-Co@Ni-Co LDH NTAs/CFC (Ni:Co=5:5) is characterized by X-ray photoelectron spectroscopy (XPS). Ni 2p XPS spectrum (Figure 7.14a) shows two kinds of nickel species, where the two spin-orbit doublets at 873.8 and 855.6 eV correspond to Ni 2p_{1/2} and Ni 2p_{3/2} signals of Ni²⁺, while those at 874.9 and 856.9 eV can be ascribed to Ni 2p_{1/2} and Ni 2p_{3/2} signals of Ni³⁺.^[152,159] In Co 2p XPS spectrum (Figure 7.14b), two main spin-orbit lines and weak satellite signals (indicated as "Sat.") could be observed, suggesting the coexistence of Co²⁺ and Co³⁺ in the Ni-Co@Ni-Co LDH NTAs/CFC.^[152,160] The fitting peaks at 797.5 and 782.1 eV are attributed to Co 2p_{1/2} and Co 2p_{3/2} signals of Co²⁺. The peaks at 795.4 and 780.5 eV are ascribed to Co 2p_{1/2} and Co 2p_{3/2} signals of Co³⁺. However, no signals of Ni or Co can be detected in the XPS spectra, although they can be observed in the XRD pattern. Considering that XPS is a surface sensitive



technique, this result indicates that the Ni-Co@Ni-Co LDH NTAs/CFC may have a core-shell structure with the metallic Ni/Co as the core and the Ni-Co LDHs as the shell. XPS depth profiles of Ni 2p (Figure 7.14c) and Co 2p (Figure 7.14d) show a gradual increase in the amount of metallic Ni/Co with increasing etch depth, along with a gradual decrease in O content (Figure 7.15), which is supportive to the Ni/Co core and Ni-Co LDH shell structure. The formation of Ni-Co@Ni-Co LDHs core/shell structure can be explained by the two-stage electrochemical reaction. At the initial stage, due to the high concentration of Ni^{2+} and Co^{2+} in the SO_4^{2-} -containing electrolyte, metallic Ni and Co are preferentially deposited on the cathode, $\text{Ni}^{2+}/\text{Co}^{2+} + 2e^- \rightarrow \text{Ni}/\text{Co}$. As water is gradually electrolyzed including $2\text{H}_2\text{O} + 2e^- \rightarrow \text{H}_2 + 2\text{OH}^-$ and $\text{O}_2 + 2\text{H}_2\text{O} + 4e^- \rightarrow 4\text{OH}^-$, the local pH value increases and the surface of the electrode is gradually passivated, forming a layer of hydroxide, $\text{Ni}^{2+}/\text{Co}^{2+} + 2\text{OH}^- \rightarrow \text{Ni}(\text{OH})_2/\text{Co}(\text{OH})_2$, to cover the Ni and Co metal core. Thus, the Ni-Co and Ni-Co LDH core/shell structure was finally formed. This metallic core-semiconductor shell structure is beneficial to the electron collection and charge transport in the electrode. The rate capability is thus expected to be enhanced due to the fast charge/discharge kinetics.

7.2.2 Negative electrode: CNFs/CFC

CNFs have attracted wide attention in energy-storage materials because of low cost, high conductivity and high specific surface area. It was reported that KOH-activated CNFs exhibited high specific capacitance (209 F g^{-1}) at 20 A g^{-1} , due to its three-dimensional network and large inter-fiber porosity.^[161] In our work, KOH was as an activating agent to form a porous structure by the oxidation of carbon to CO_2 and carbonate. KOH was then used to increase the surface oxygen-containing groups, which can effectively improve capacitive behavior of electrodes.^[162] TEM images of CNFs showed a long and continuous nano-cylindrical web morphology with an average diameter of 250 nm (**Figure 7.16**). The corresponding SAED pattern (**7.16d**) shows that CNFs are amorphous, rich with many defects and disorders. It is thus expected that the CNFs will present excellent electrochemical performance.

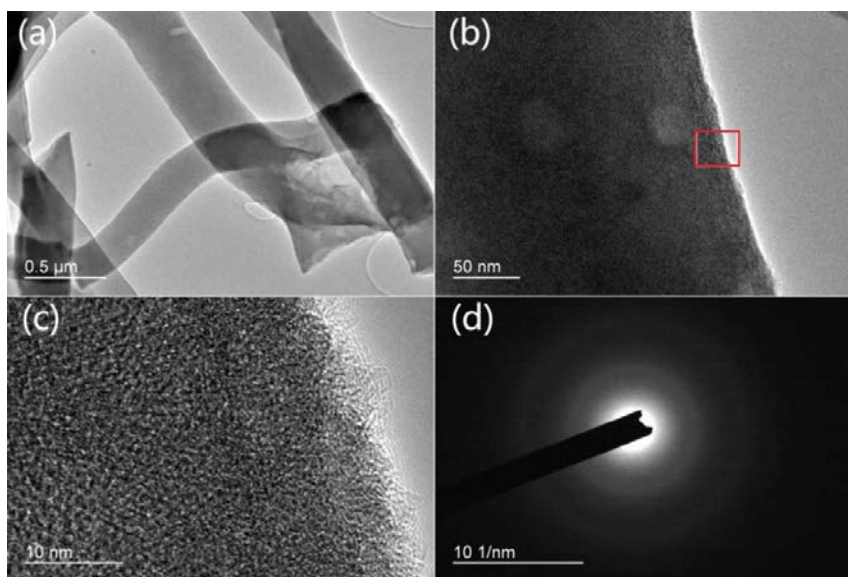


Figure 7.16 CNFs: (a, b, c) TEM images with different magnifications. (d) the SAED pattern of CNFs in a selected area of (b).

7.3 Electrochemical characterizations

7.3.1 Positive electrode: Ni-Co@Ni-Co LDH NTAs/CFC

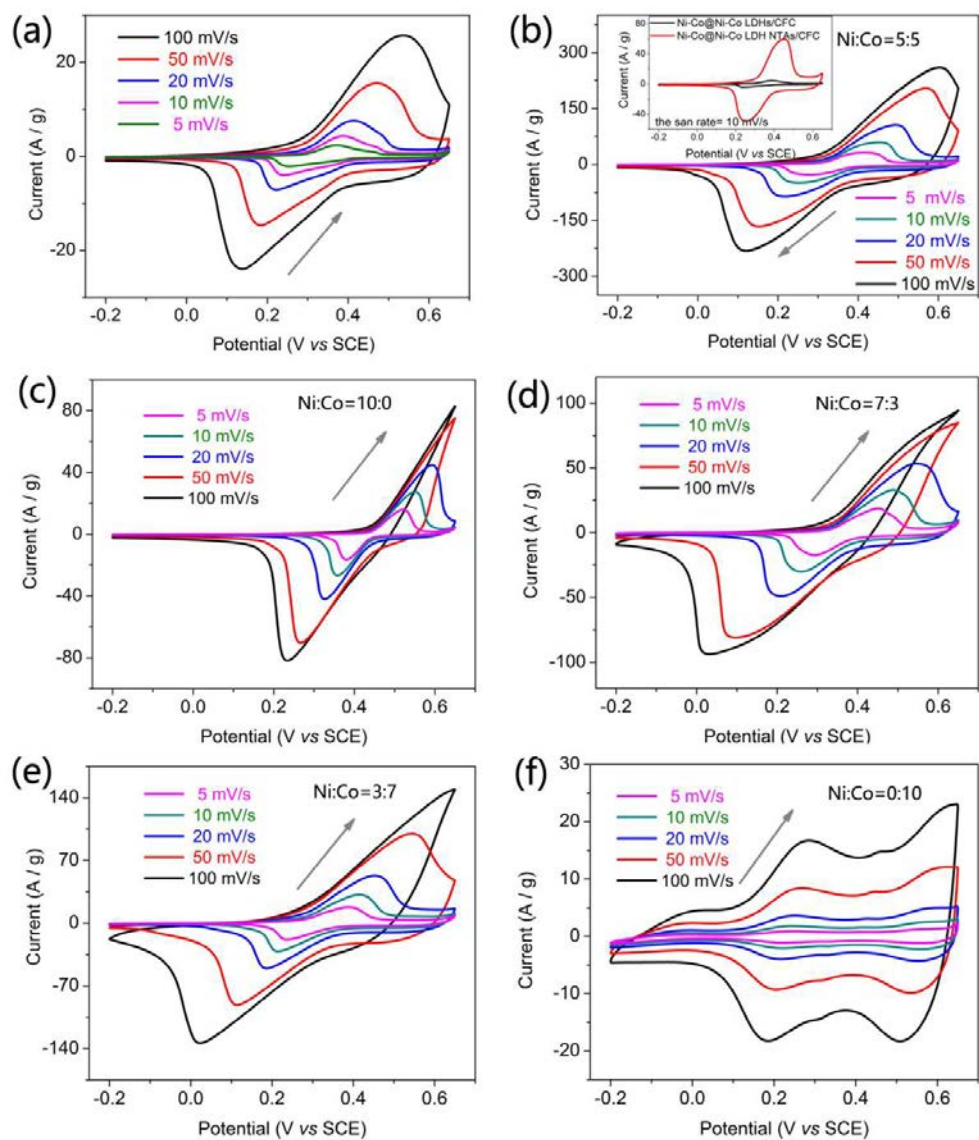


Figure 7.17 (a) CVs of Ni-Co LDHs/CFC, and CVs of Ni-Co@Ni-Co LDH NTAs/CFC at different scan rates in 1 mol L⁻¹ NaOH aqueous solution with different Ni:Co ratios: (b) 5:5, (c) 10:0, (d) 7:3, (e) 3:7, and (f) 0:10. Inset of (b): CVs of Ni-Co@Ni-Co LDH NTAs/CFC and Ni-Co LDHs/CFC at a scan rate of 10 mV s⁻¹.



Figure 7.17 showed typical CV curves of Ni-Co@Ni-Co LDHs/CFC and Ni-Co@Ni-Co LDH NTAs/CFC at scan rates from 5 to 100 mV s⁻¹. All CV curves exhibited a strong pair of well-defined redox peaks, corresponding to the battery-type pseudocapacitive reaction related to Ni(Co)-OH/Ni(Co)-O-OH.^[163] One pair of redox peaks in CV is observed due to the well mixing of Ni and Co ions in the hybrid by electrochemical deposition, as revealed by the EDX mapping results. Comparison of the CV reduction peak area suggests that the sample with Ni:Co=5:5 possesses the highest specific capacitance. Besides, the sample fabricated without ZnO NRA template (Ni-Co@Ni-Co LDHs/CFC) shows very poor pseudo capacitance (Figure 7.17a) due to its collapsed structure (Figure 7.18) with a compact layer of material covering CFC, which is detrimental to electrochemical performance. Therefore, the use of ZnO NRA template is necessary to effectively improve the electrochemical performance of the Ni-Co@Ni-Co LDHs. It is worth noting that the Ni-Co@Ni-Co LDH NTAs/CFC exhibits a single pair of redox peaks (Figure 7.19) that shift with composition. The oxidation peak potential (*vs.* SCE) shifts to higher value with increasing amount of Ni, in agreement with previous reports.^[64,163a,164] Importantly, the maximum redox peak current is found in the sample with Ni:Co=5:5, due to a possible synergistic effect.

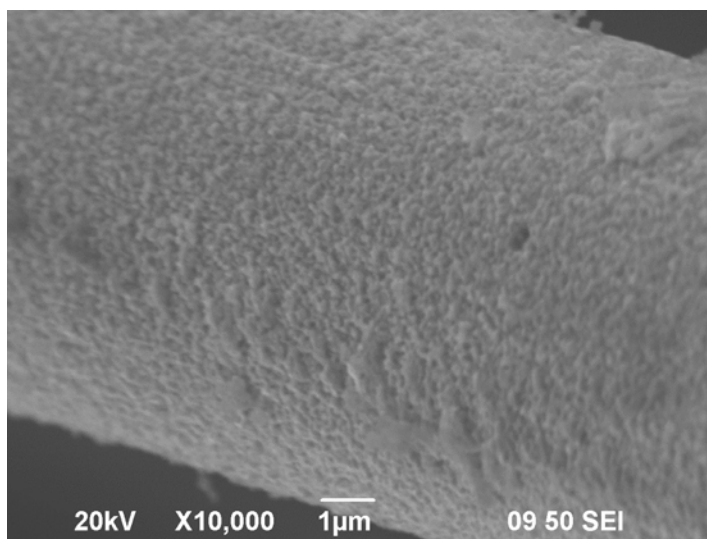


Figure 7.18 SEM image of Ni-Co@Ni-Co LDHs/CFC.

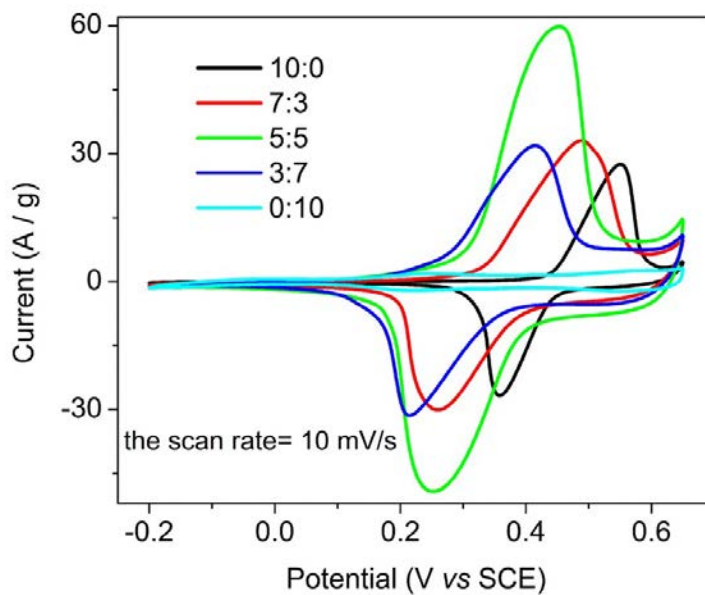


Figure 7.19 CVs of samples of different Ni:Co ratios.



Figure 7.20 show symmetric galvanostatic charge/discharge (GCD) curves of the Ni-Co@Ni-Co LDH NTAs/CFC, indicating excellent reversible redox reactions. The gravimetric capacitances of the Ni-Co@Ni-Co LDH NTAs/CFC at a current density of 5 A g^{-1} are determined to be 120, 1130, 2200, 819, and 609 F g^{-1} for the Ni:Co ratio of 0:10, 3:7, 5:5, 7:3, and 10:0, respectively. Obviously, the sample with Ni:Co=5:5 shows the highest capacitance (Figure 7.20f), consistent with the CV results. The above results show that the electrochemical performance of the sample depends on a proper amount of Ni and Co, which is also reflected in the gradual changes of crystal structure and morphology of the hybrid as a function of Ni:Co ratio. As shown in Figure 7.21a, the sample with Ni:Co=5:5 demonstrates the highest specific capacitance at all the current densities, which decreases from 2414 to 1980 F g^{-1} when the current density is increased from 1 to 20 A g^{-1} , about 82.1% retention rate of its initial value, indicating a high rate capability. Its rate capability and capacitance are the best among all the samples tested (Figure 7.21b), implying the importance of doping the proper amount of cobalt into the active material. The Ni-Co@Ni-Co LDH NTAs/CFC reported here shows excellent electrochemical properties, compared with other nickel-cobalt composites reported (Table 7.2). The excellent properties are resulted from the improved charge transfer due to the increased electrical conductivity, the increased number of electroactive sites due to possible valence interchange or charge hopping between Ni and Co cations,^[53b,165] and the porous core-shell structure developed in the separated NTAs.

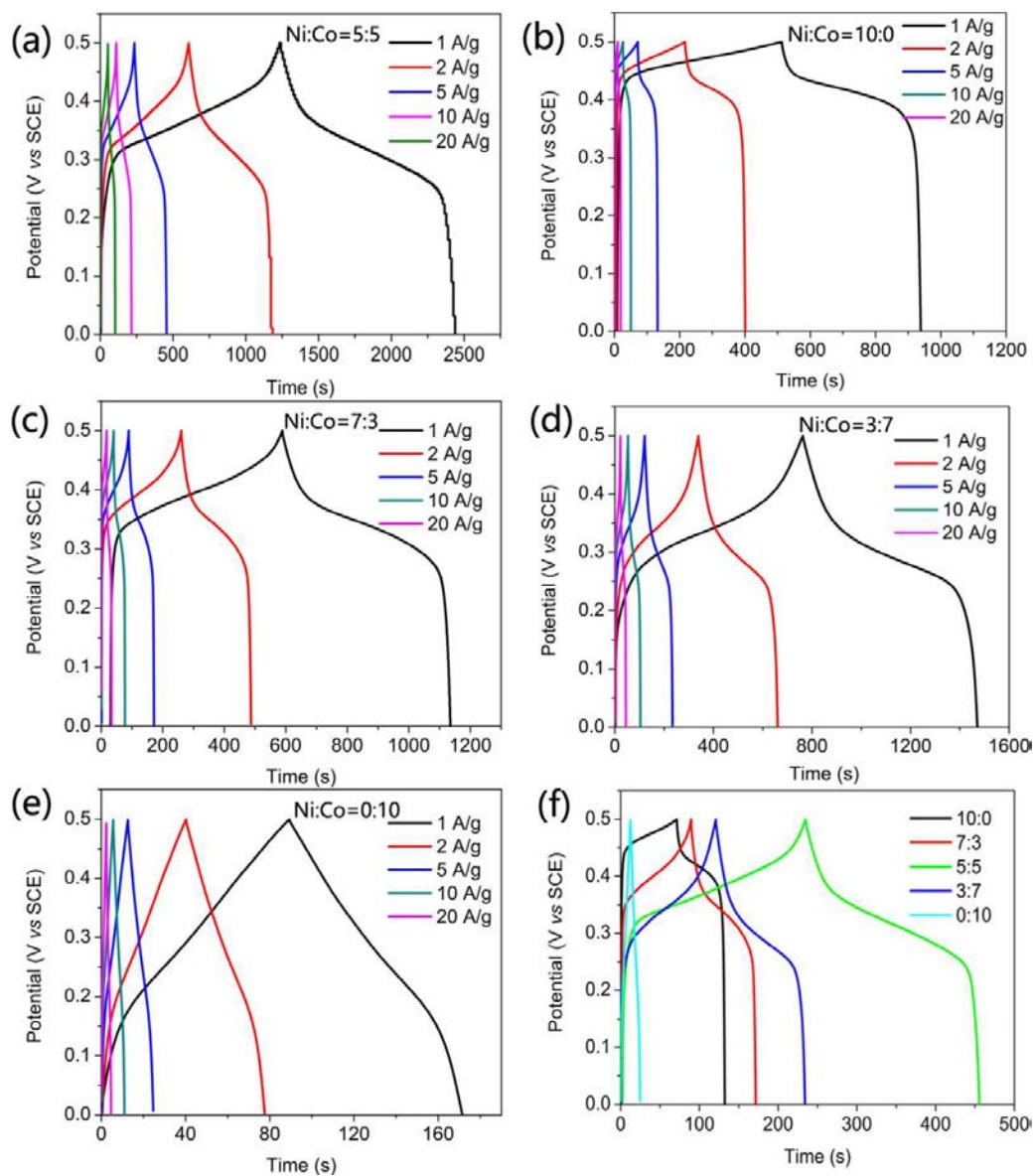


Figure 7.20 GCD curves of Ni-Co@Ni-Co LDH NTAs/CFC at different current densities with different Ni:Co ratios: (a) 5:5, (b) 10:0, (c) 7:3, (d) 3:7, and (e) 0:10. (f) GCD curves of samples with different Ni:Co ratios at a current density of 5 A g^{-1} .



Electrochemical impedance spectroscopy (EIS) (Figure 7.21c) shows that ESRs (equivalent series resistances) of the Ni-Co@Ni-Co LDH NTAs/CFC are about 1.43, 1.37, 1.19, 1.33 and 1.46 Ω , for the Ni:Co ratio of 10:0, 7:3, 5:5, 3:7, and 0:10, respectively. The small ESR for Ni-Co@Ni-Co LDH NTAs/CFC indicates low electrolyte resistance and low contact resistance between active material and the current collector. The low frequency portion of the EIS is a straight line, representing the Warburg resistance, which is related to ion diffusion/migration in the electrolyte. The sample of Ni:Co=5:5 shows a line with a higher slope than other ones, indicating faster ion diffusion between the electrode and the electrolyte. This result is in agreement with its higher specific capacitance and better rate capability. The cycling performance of the Ni-Co@Ni-Co LDH NTAs/CFC (Ni:Co=5:5) (Figure 7.21d) shows that, at a current density of 5 A g⁻¹, 98.8% of the initial capacitance (2200 F g⁻¹) is maintained after 5,000 cycles, also better than other compositions.

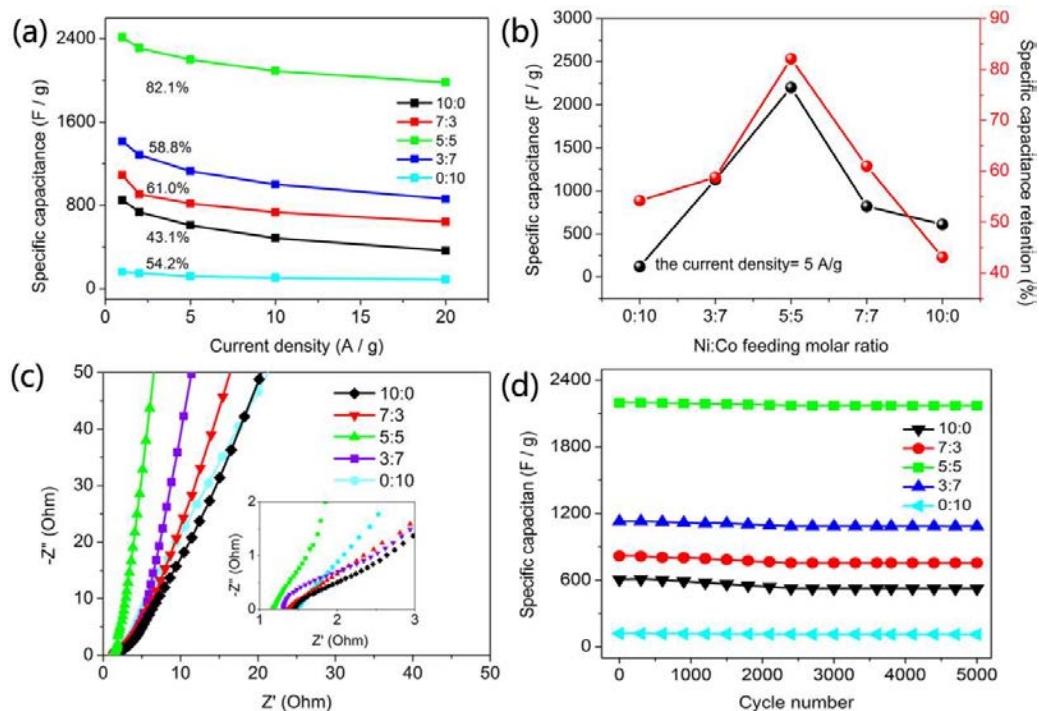


Figure 7.21 (a) Specific capacitance vs. current density. (b) Comparison of the specific capacitance and retention rate. (c) Nyquist plots. Inset: magnified EIS spectra at the high frequency region. (d) Cycling performance at a current density of 5 A g⁻¹. The measurement is based on for Ni-Co@Ni-Co LDH NTAs/CFC with different Ni:Co ratios.



Table 7.2 Comparison of the specific capacitance of the present work with those reported ones based on nickel or cobalt oxide/hydroxide.

Active materials	Current density (A/g)	Electrolyte	Specific capacitance (F/g)	Rate capacity	Ref.
Nickel-cobalt LDH nanocones	10	1M KOH	1580	N/A	[53b]
Ni _{0.3} Co _{2.7} O ₄	0.625	3M KOH	960	83.8% retention after 6.25 A/g	[166]
MnCo ₂ O ₄ @Ni(OH) ₂	5	2M KOH	2154	32.5% retention after 20 A/g	[167]
3D Ni foam/N-CNT/NiCo ₂ O ₄	1	2M KOH	1472	78.3% retention after 20 A/g	[168]
Sponge-like NiCo ₂ O ₄ /MnO ₂	1	1M KOH	935	86.7% retention after 20 A/g	[169]
Our work	5	1M NaOH	2200	82.1% retention after 20 A/g	

7.3.2 Negative electrode: CNFs/CFC

Figure 7.22a shows rectangular CV curves of the as-obtained CNFs/CFC, without obvious distortion with increasing potential scan rate at -1.0 to 0.0 V, indicating typical electric double-layer capacitance behavior. GCD tests were performed at different



current densities from 1 to 20 A g⁻¹ (Figure 7.22b). All curves were symmetric and triangular in shape, and no obvious IR drop can be observed. This indicates that CNFs have excellent electrochemical reversibility and a very small equivalent series resistance, which is essential to the high power requirement of battery-type supercapacitors. The CNFs/CFC showed a specific capacitance of 261, 253, 246, 236, and 231 F g⁻¹ at different current densities of 1, 2, 5, 10 and 20 A g⁻¹, respectively (Figure 7.22c). The high retention of 88.5% of the initial capacitance for a 20 times current density increase demonstrated a good rate performance, which can be explained by good electron conduction of the CNFs/CFC. The interconnected porous structure and rich activated groups due to alkaline treatment facilitated the electrolyte penetration and ion transportation/diffusion. The network of CNFs ensured the high-speed migration of electrons along the carbon fibers. Compared with conventional carbon materials,^[170] the CNFs exhibited a better electrochemical performance with higher capacitance. A good cycle life, with a capacitance retention rate of 98.7% after 5000 charge/discharge cycles, was found for the CNFs/CFC electrode (Figure 7.22d). These results demonstrate that the CNFs/CFC electrode is suitable for battery-type supercapacitor application.

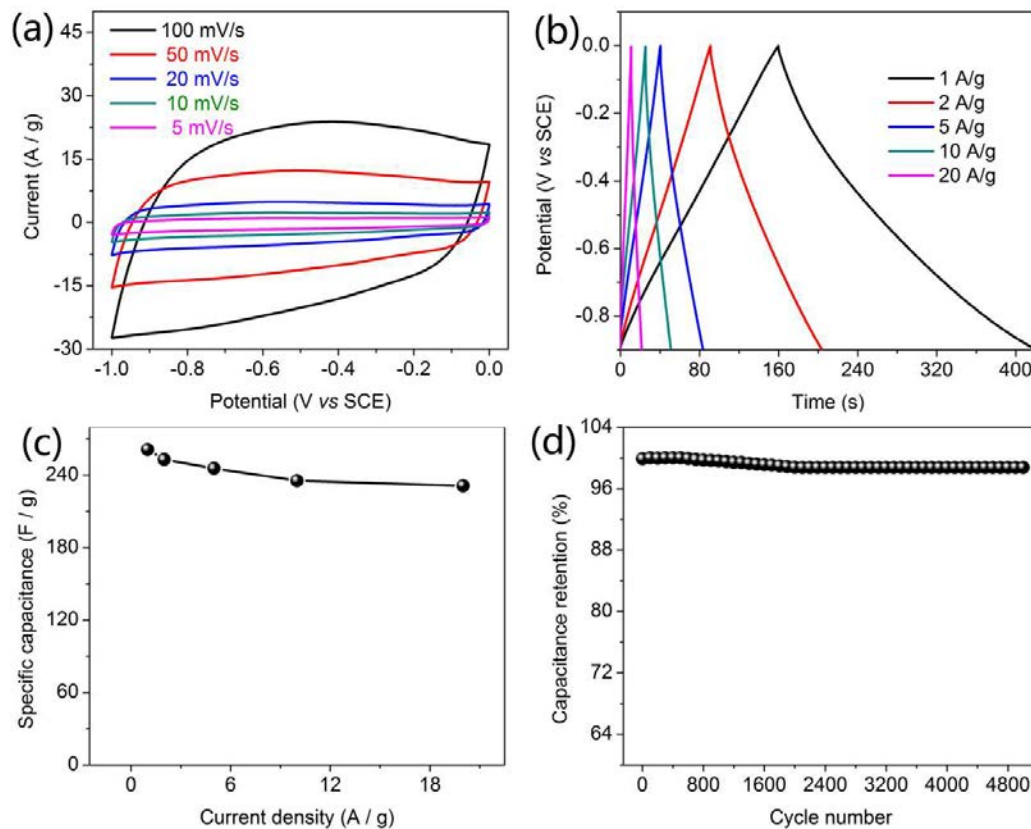


Figure 7.22 (a) CV curves of CNFs/CFC electrode at different scan rates. (b) GCD curves of CNFs/CFC at different current densities. (c) Specific capacitance of CNFs/CFC electrode at different current densities. (d) Cycling performance of CNFs/CFC electrode at a current density of 5 A g^{-1} .

7.3.3 Battery-type supercapacitor

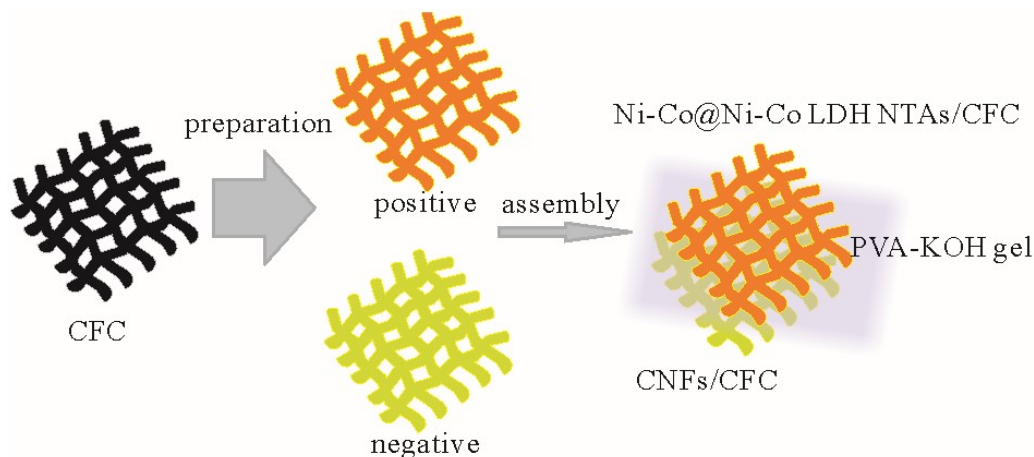


Figure 7.23 A schematic illustration for the preparation process of FBSC Ni-Co@Ni-Co LDH NTAs/CFC and CNFs/CFC and the assembly of FBSC device.

An all-solid-state flexible battery-type supercapacitor (FBSC) with KOH-PVA gel electrolyte was assembled using the as-prepared Ni-Co@Ni-Co LDH NTAs/CFC as the positive electrode and CNFs/CFC as the negative electrode, as illustrated in Figure 7.23. To optimize the FBSC device capacitance with a stable potential window, CV curves of the two electrodes were separately measured at a scan rate of 10 mV s^{-1} (Figure 7.24a). The mass loading on each electrode was determined according to the charge balance (Equation 3.3-3.5).

Figure 7.24b shows the CV curves of an optimized FBSC at different cell voltages. The presence of the redox peaks is due to the Faradaic reactions of Ni-Co LDHs. With increasing cell voltage, the energy stored is also increased. As expected, a stable cell voltage window of the FBSC can be extended to 1.7 V.

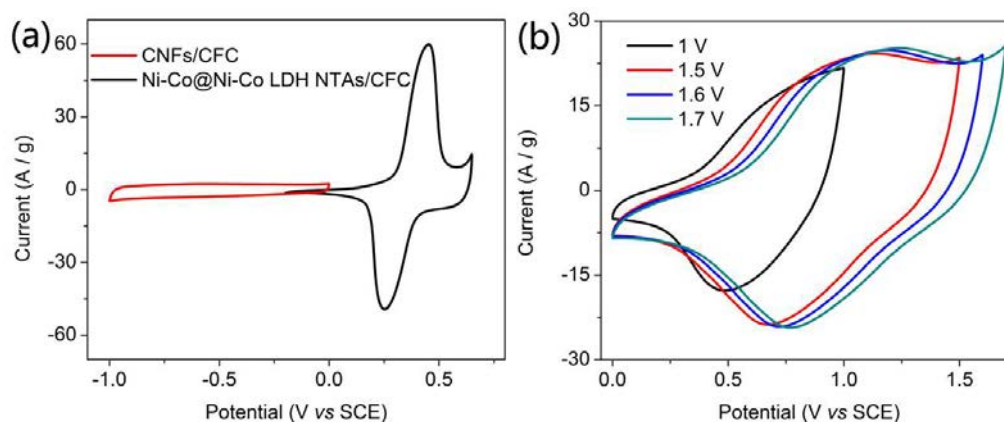


Figure 7.24 CV curves of (a) Ni-Co@Ni-Co LDH NTAs/CFC and CNFs/CFC electrodes at a scan rate of 10 mV s^{-1} , and (b) an optimized FBSC device in various voltage windows at a scan rate of 100 mV s^{-1} .

Figure 7.25a shows the CV curves of an optimized FBSC at different scan rates from 5 to 100 mV s^{-1} between 0 and 1.7 V. There was no obvious shape change in the CV curves, indicating a good rate capability of the assembled device. The specific capacitance of the FBSC calculated based on the GCD curves (Figure 7.25b) reached 319 F g^{-1} at the current density of 2 A g^{-1} , much higher than many flexible supercapacitors reported previously, such as, A-p-BC-N-25 || A-p-BC-N-25 (170 F g^{-1} at 1 A g^{-1}),^[171] rGO-PEDOT/PSS (123 F g^{-1} at 2 A g^{-1}),^[172] NiCoO₄ (77 F g^{-1} at 1 A g^{-1}),^[173] MnO₂/CNF || graphene/CNF (87.1 F g^{-1} at 1.25 A g^{-1}),^[174] and MnO₂/ERGO || CNT-ERGO (69.4 F g^{-1} at 0.25 A g^{-1}).^[175] At higher discharge current densities of 5, 10, and 20 A g^{-1} , the device still delivers high specific capacitance of 280, 253, and 220 F g^{-1} , respectively (Figure 7.25c). The specific capacitance decreases with increasing current density, due to the incomplete redox reaction caused



by sluggish ion diffusion at high current densities.^[176] The cycling life of the as-prepared FBSC was investigated by GCD measurement between 0 to 1.5 V at a current density of 5 A g⁻¹ (Figure 7.25d). Interestingly, the capacitance was first decreased in the initial 200 cycles which may be caused by inadequate wetting between the active material and the gel electrolyte. In the following GCD cycles, the capacitance rose again, which was probably due to the activation of active material and increased contact between the active material and the electrolyte. After 3,000 cycles, the FBSC showed a capacitance retention rate of 96.9%, demonstrating good cycling performance. This result is much better than those devices reported in the literature, such as porous carbon || porous carbon (89.0%, 3,000 cycles),^[177] MnO₂/CNF || graphene/CNF (95.2%, 3,000 cycles)^[174], Ni(OH)₂ || ordered mesoporous carbon (~89%, 3,000 cycles),^[170a] Mo₂N || RGO (85.7%, 4,000 cycles),^[178] MnO₂/CNF || Bi₂O₃/CNF (85%, 4,000 cycles),^[179] Mn₃O₄/NGP || Ni(OH)₂/NGP (~92.0%, 3,000 cycles),^[180] RGO/Ni || RGO/Ni (~95.1%, 3,000 cycles),^[181] hydrogenated-Cu₂WS₄ || hydrogenated-Cu₂WS₄ (95.0%, 3,000 cycles),^[182] MnO₂/ERGO || ERGO/CNT (~89.1%, 3,000 cycles),^[175] and graphene/MnO₂ || CNT (95.0%, 1,000 cycles).^[183]

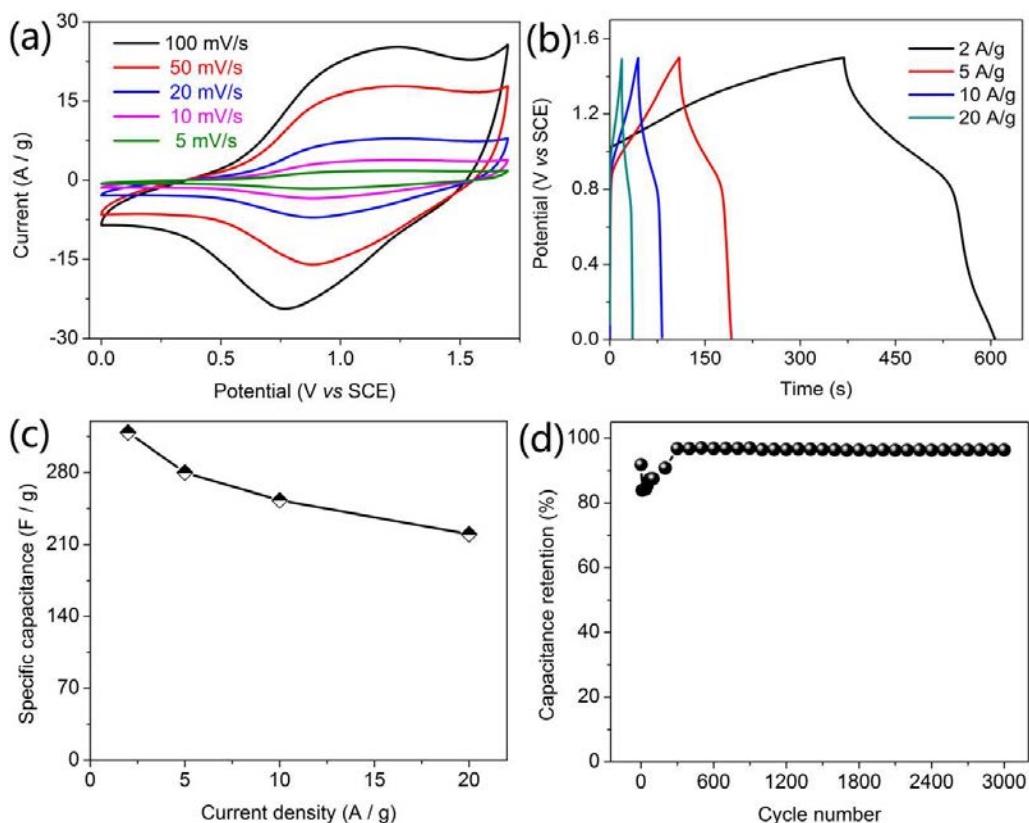


Figure 7.25 (a) CVs at different scan rates, (b) GCD curves at different current densities, (c) specific capacitance at different current densities, and (d) Cycling performance at a current density of 5 A g^{-1} of an optimized FBSC device.

The as-assembled FBSC was subject to a 90° bending test. Figure 7.26a shows that there was almost no change in CV curves before and after the bending, suggesting the good flexibility of the device. As a demonstration for practical application in energy storage, a red light-emitting diode (LED, 1.5 V) was lit up by two FBSCs connected in series (Figure 7.26b). GCD measurement (Figure 7.26c) shows that the discharge time of devices connected in parallel is twice as long as that of a single one within the



same voltage window of 1.5 V. Meanwhile, the output voltage of devices connected in series is twice as high as that of a single one. These results reveal that the fabricated devices have good reproducibility and can be well managed for practical power applications.

Figure 7.26d shows the Ragone plot of our device in comparison with those state-of-the-art reported ones. Our device shows a maximum gravimetric energy density of 100 Wh kg⁻¹ at a power density of 1500 W kg⁻¹, which still remains a high enough value of 69 W h kg⁻¹ at a high power density of 15 kW kg⁻¹. These values are higher than those devices reported recently, such as Ni(OH)₂/graphene || graphene (<78 W h kg⁻¹, <15 kW kg⁻¹),^[170b] Ni(OH)₂/CF || CNT/CF (<45 W h kg⁻¹, <3.5 kW kg⁻¹),^[184] Co(OH)_xCO₃/CF || CNT/CF (<35 W h kg⁻¹, <3.5 kW kg⁻¹),^[184] MnO₂-CNF || Bi₂O₃-CNF (12 W h kg⁻¹, <3.4 kW kg⁻¹),^[179] Co₃O₄/VAGN/CF || Co₃O₄/VAGN/CF (<49 W h kg⁻¹, <10 kW kg⁻¹),^[176] CNTG || MG (< 23 W h kg⁻¹, <9 kW kg⁻¹)^[185], MnO₂/ACT || ACT (<67 W h kg⁻¹, <5 kW kg⁻¹).^[186]

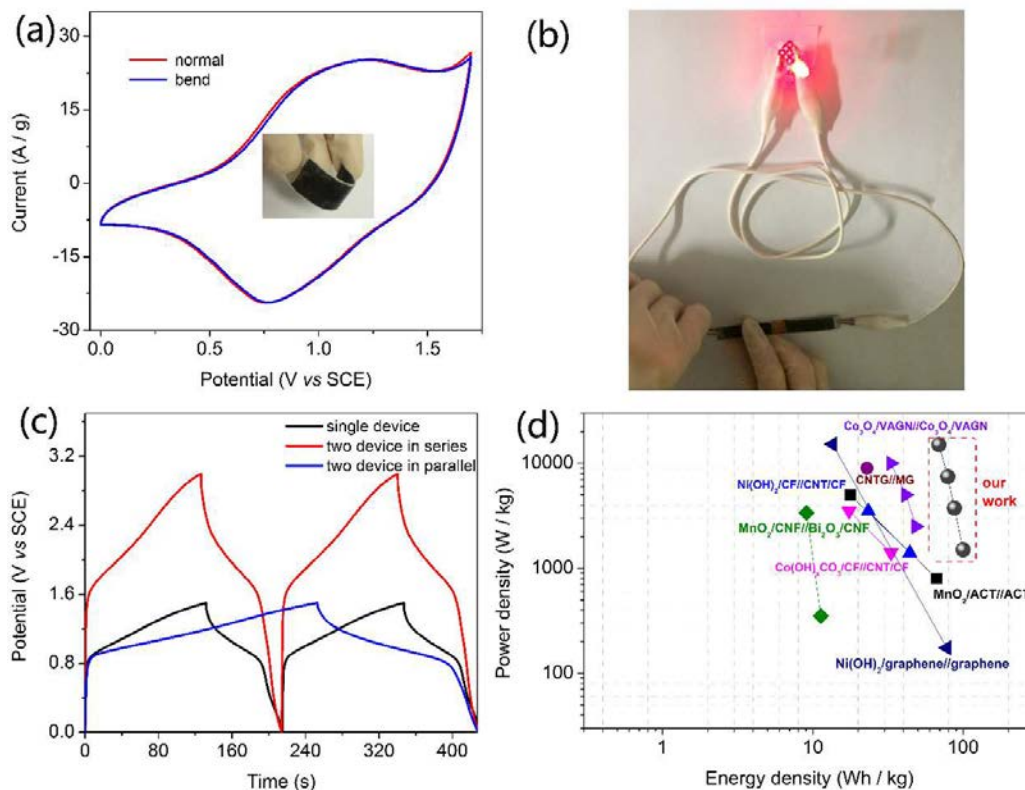


Figure 7.26 (a) CVs of the FBSC device under flat and bending conditions at a scan rate of 100 mV s^{-1} . Inset: digital image of a 90° bended device. (b) Digital image of a LED lit up by two tandem devices. (c) GCD curves of two FBSCs in series and in parallel at a current density of 5 A g^{-1} . A single device is also plotted for comparison. (d) Ragone plot of our device in comparison with those reported ones.

We attribute the excellent electrochemical performance of the assembled FBSC to the unique structural features of the positive electrode, Ni-Co@Ni-Co LDH NTAs/CFC. The well-aligned and separated nanotubes with massive hierarchical active material on the top provide a large amount of electrochemical active sites. The metallic core of



the nanotubes transfers electrons efficiently from the massive top to the current collector on the bottom. Meanwhile, a proper mixture of Ni and Co optimizes the electrochemical properties of the electrode due to the synergistic effect between Ni and Co HDs.

7.4 Relationship between Faradaic reaction active sites and nickel-cobalt composition

To understand why Ni-Co@Ni-Co LDH NTAs/CFC could store/deliver charge with fast kinetics, the electrochemically active sites within Ni-Co@Ni-Co LDH NTAs/CFC were investigated in detail with the help of results of CV measurement. It is well established that in a diffusion-limited electrochemical redox reaction, the current-voltage relationship for a potential scan can be obtained by Randles-Sevcik equation^[187] as follows.

$$i_p = 2.7 \times 10^5 n^{\frac{3}{2}} A D^{\frac{1}{2}} C^0 v^{\frac{1}{2}} \quad (7.1)$$

Where i_p ($A\ cm^{-2}$) is the cathodic peak current during a potential scan as a function of scan rate v of the CV test ($V\ s^{-1}$), A is the electrochemical active area (cm^2), D is the diffusion coefficient of electrolyte ($cm^2\ s^{-1}$), and C^0 is the concentration of electrolyte ($mol\ cm^{-3}$). When the bulk diffusion coefficient and electrolyte concentration are the same for the Ni-Co@Ni-Co LDH NTAs/CFC with different Ni:Co ratios, i_p is mainly affected by the accessible electrode area A . Figure 7.27 shows the relationship between scan rates and corresponding cathodic peak currents of the Ni-Co@Ni-Co



LDH NTAs/CFC. During discharging, the reactive electrode area of Ni-Co@Ni-Co LDH NTAs/CFC (5:5) was 3.1, 2.7, 1.8, and 12.3 times larger than that of Ni-Co@Ni-Co LDH NTAs/CFC (10:0, Figure 7.27b), Ni-Co@Ni-Co LDH NTAs/CFC (7:3, Figure 7.27c), Ni-Co@Ni-Co LDH NTAs/CFC (3:7, Figure 7.27d), and Ni-Co@Ni-Co LDH NTAs/CFC(0:10, Figure 7.27e). The high active area ratio for the Ni-Co@Ni-Co LDH NTAs/CFC (5:5) indicates a large proportion of the charges located at effective sites and a high usage of active materials. TEM images in Figure 7.9 also verified the highly open structure of the Ni-Co@Ni-Co LDH NTAs/CFC (5:5) with separated tubes and hierarchical top. In view of the influence of the geometry change on the redox active sites in the Ni-Co@Ni-Co LDH NTAs/CFC, the difference of the Ni-Co@Ni-Co LDH NTAs/CFC in morphology is very obvious, which was confirmed by SEM images in Figure 7.8. Therefore, Ni-Co@Ni-Co LDH NTAs/CFC (0:10) had the least accessible sites for charge storage due to its poor architecture. It is reasonable to conjecture that a large active reaction area could be achieved by tuning the compositions of nickel-cobalt in the Ni-Co@Ni-Co LDH NTAs/CFC.

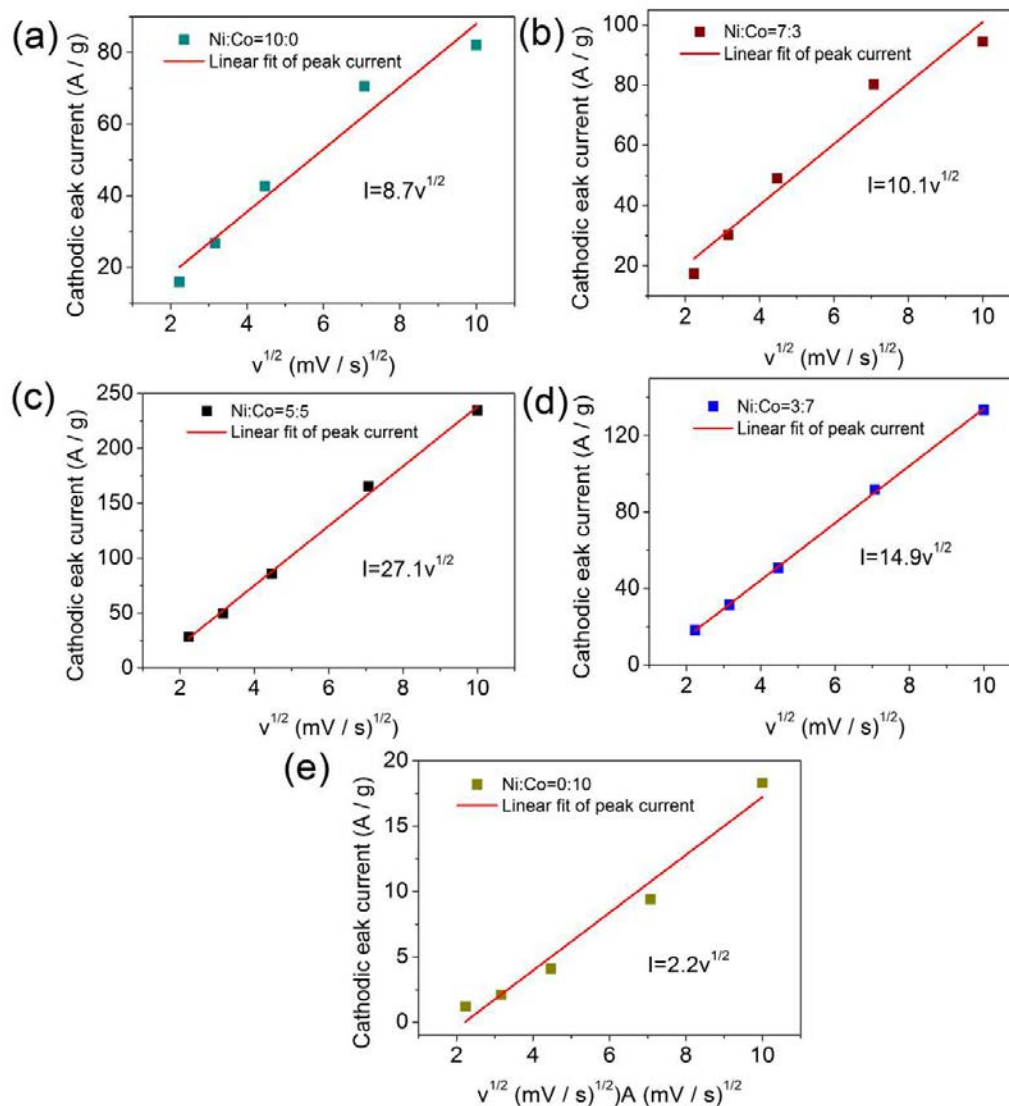


Figure 7.27 The relationship between the cathodic peak current and scan rate fitted using the Randles-Sevcik equation for Ni-Co@Ni-Co LDH NTAs/CFC different Ni:Co ratios: (a) 10:0, (b) 7:3, (c) 5:5, (d) 3:7, and (e) 0:10.



7.5 Summary

An asymmetric battery-type supercapacitor using Ni-Co@Ni-Co LDH NTAs/CFC and CNFs/CFC as the positive and negative electrodes, respectively, was fabricated. The assembled device shows good flexibility, high energy density (100 Wh kg^{-1} at 1500 W kg^{-1}) and good cycling stability (96.9% after 3,000 cycles) at a voltage window of 1.5 V, which are comparable to, or better than many of the state-of-the-art devices reported recently. The attractive properties are resulted from the unique structural features of the positive electrode, such as the metallic Ni/Co core inside the Ni-Co LDH nanotubes and massive active material on the top of nanotube array. The work presented here shows a good example of the combination of the electrode structural design and composition optimization for battery-type supercapacitor applications.



Chapter 8 Conclusion and Future Outlook

8.1 Conclusion

In this thesis, we focused on the investigation of different strategies to improve the electrochemical performance of nickel-based materials by structure and composition control. The core philosophy is to focus on the main factors that restrict the electrochemical kinetic process, such as ion and electron transport. The corresponding strategies are: (i) utilizing electrochemical methods to fabricate nanostructured electrodes with different morphologies to reduce the contact resistance between the substrate and active materials and enhance the intrinsic conductivity; (ii) doping with other metal element to further enhance the electrochemical performance. Several physical/electrochemical factors are very crucial in achieving excellent electrochemical performance of nickel-based electrodes, such as the preparation conditions (electrolyte type and composition, the applied voltage, ...) and the structure design of the electrode materials.

In Chapter 4, the anodization method to prepare porous layered $\text{Ni}(\text{OH})_2/\text{Ni}_2\text{O}_3$ composite grown on the current collector was proposed. The *in-situ* grown active materials have good mechanical/electrical contact with the current collector and the anodic nickel foil can be directly used as supercapacitor electrode. As a result, the



specific capacitance and cycling performance of $\text{Ni}(\text{OH})_2/\text{Ni}_2\text{O}_3$ was greatly enhanced as compared with previous reports.

In Chapter 5, to further improve the electronic conductivity of the material matrix and reduce the charge transfer resistance of the materials, a cathodic deposition method was exploited to prepare core/shell structured $\text{Ni}@\text{NiO}$. It was found that the crystal growth of $\text{Ni}@\text{NiO}$ was greatly affected by electrolyte type and composition. Meanwhile, the electrochemical properties of materials had a close relationship with physical morphologies. Dendritic materials synthesized in nickel-free ethylene glycol electrolyte by cathodic deposition presented excellent electrochemical performance, especially in the cyclic life. What's more, the electrolyte containing F^- ions had a positive impact on the improvement of electrochemical performance.

In Chapter 6, two types of nickel-based composites on the anode and cathode were achieved simultaneously in a cell under optimized preparation conditions. Based on the studies of former chapters, the nickel-free ethylene glycol electrolyte was used to successfully prepare nickel-based composites on both the anode and cathode. As a result, the active materials deposited on the anode and cathode showed good specific capacitance with excellent cycling stability.

In Chapter 7, we doped cobalt into the material matrix by cathodic deposition to further enhance the electrochemical performance of the nickel-based composites. The introduction of cobalt with a proper amount boosted electric conduction of materials to support fast electron transport required by high rates. Meanwhile, the architecture



design using ZnO as a template to prepare aligned nanotubes increased surface area of reaction and shortened the diffusion path for electrons and ions. As a result, the specific capacitance and rate performance of Ni-Co@Ni-Co layered double hydroxide nanotubes were greatly improved. Meanwhile, the as-assembled flexible battery-type supercapacitor based on Ni-Co@Ni-Co layered double hydroxide nanotubes showed high energy density with good power density.

8.2 Future Recommendations

As discussed in this thesis, nickel-based composite materials have been designed and fabricated by electrochemical method such as anodization and cathodic deposition. By utilizing the simple synthesis methods, three-dimension architectures of nickel-based composites with improved electrochemical performance have been demonstrated. Meanwhile, simultaneous fabrication of anodic and cathodic films in a single cell has been achieved, and the as-prepared nickel-based materials exhibit good electrochemical performance. In addition, the doping of cobalt further enhances the performance of nickel-based composite. The as-obtained nickel-cobalt composite was assembled into flexible battery-like supercapacitors. Based on the above mentioned studies, it is proposed to conduct the following work on high-performance energy storage devices in the future:

- (i) Study the underlying mechanism of nickel anodization.



Up to now, it is still difficult to understand the formation of porous nickel-based composite on the anode and the dendrite growth on the cathode at the same time. The processing parameters, such as applied voltage, reaction time, temperature, pH, electrolyte, and substrate, etc. affect the structures of nickel-based composites, and determine the electrochemical performance of the electrodes. In 1963, Weininger^[188] put forward a crystal structure effect on the anodic oxidation of nickel. The work answered the questions such as the mechanism of anodization at the surfaces of nickel crystals, and the loss of crystal surface structure on anodization, etc. The research was confined to the model built on only alkaline solution and a few monolayers of reaction products. Afterwards, MacDougall^[80] continued the research on the anodic nickel film in neutral and acid solutions. Then advanced techniques were used to study the anodic oxidation of nickel, such as in-situ Raman spectroscopy,^[70] spectroelectrochemistry,^[189] and so on. Recently, a number of papers have reported the application of anodic nickel-based composites in supercapacitor electrodes.^[60-61,101,190] A deeper understanding on the anodization mechanism is needed in order to further enhance the electrochemical performance of the anodic materials and widen their applications.

(ii) To design and fabricate three-dimensional current collectors for 3D energy storage devices.

The emergence of microelectromechanical systems in recent years such as biological monitor, micro-air vehicle, and microelectronic pill has requested an urgent need on the miniaturization of energy storage devices. Three-dimensional architectures of the



electrodes should be considered. Different from the conventional two-dimensional parallel plate electrodes, the non-planar electrode configuration design enables the increase of power density due to the improved ion kinetic. Meanwhile, the interpenetrated arrangement of the anode and the cathode makes the power density not affected by the device thickness. The energy density of the device can be increased by simply increasing the three-dimensional electrode thickness. As demonstrated in Chapter 5, the dendritic nickel-based electrode has great potential to be used as a three-dimensional current collector which can significantly increase the electrode-current collector surface contact areas and hence dramatically reduce interfacial resistance. The three-dimensional electrode can be fabricated by coating or growing a layer of active materials on the surface of three-dimensional current collector. The integrated electrode design between the anode and cathode will strongly enhance the charge and mass transfer in electrochemical reactions. The schematic of a three-dimensional architecture is illustrated in Figure 8.1. In the future, we will focus on the development of three dimensional electrodes by periodic nanostructured current collectors, such as nanorod array, nanotube array, and nanocone array. Additionally, the integration of the other electrode is still a great challenge.

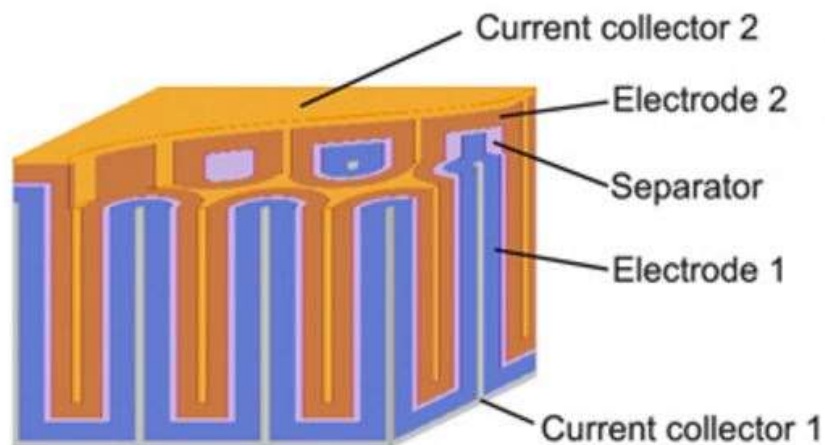


Figure 8.1 The schematic of three-dimensional architecture based on interdigital electrodes.^[191]

(iii) To apply the as-fabricated nickel-based composites to photocatalysis such as photodegradation, photocatalytic hydrogen production and so on.

It is known that nickel can be used in chemical catalysis and photocatalysis. Nickel-based materials have attracted much attention in photodegradation and photocatalytic water splitting in recent years.^[192] Yan *et al.*^[192i] reported on the use of CdS/g-C₃N₄ heterojunction nanorods modified by Ni(OH)₂ as a highly efficient photocatalyst for visible-light driven hydrogen evolution from water. Zhai *et al.*^[192k] successfully synthesized mesoporous nanohybrids of NiO nanoparticles and HTiNbO₅ nanosheets which had good photocatalytic activity. There is a great potential for the application of the as-prepared nickel-based composites in photocatalysis.



(iv) To develop new energy storage chemistry for further enhancement of energy density.

The ability to quickly charge and discharge electrical energy makes supercapacitors ideal devices for high power density energy storage. However, traditional supercapacitors have a much lower energy density than batteries. To solve the problem, using organic electrolytes with a broader operating voltage (e.g., ionic liquids) is an effective method to improve the energy density of the traditional supercapacitors. However, due to the restriction of the charge storage mechanism (ion adsorption or fast faradaic redox reactions), traditional supercapacitors are hard to compete with batteries in energy density. Nickel-based composites in this thesis belong to the special battery-type pseudocapacitive electrode materials (BPMs) which go beyond scope of the traditional supercapacitors. However, the improvement in their rate capability, cyclic life and power density are always accompanied by the loss in energy density and capacitance. Currently, researchers are working to combine the outstanding features of a supercapacitor and a battery, such as high power density, long cycle life and high energy density. Revolutionary ideas in the design of electrode configuration and searching of new materials are needed to accomplish the new-generation of energy storage devices.



References

- [1] J. Chang; M. Jin; F. Yao; T. H. Kim; V. T. Le; H. Yue; F. Gunes; B. Li; A. Ghosh; S. Xie; Y. H. Lee, *Adv. Funct. Mater.* 23 (2013) 5074-5083.
- [2] B. Dunn; H. Kamath; J.-M. Tarascon, *Science* 334 (2011) 928-935.
- [3] a) R. Kotz; M. Carlen, *Electrochim. Acta* 45 (2000) 2483-2498; b) B. L. Ellis; P. Knauth; T. Djenizian, *Adv. Mater.* 26 (2014) 3368-3397.
- [4] L. L. Zhang; X. S. Zhao, *Chem. Soc. Rev.* 38 (2009) 2520-2531.
- [5] H. Ibrahim; A. Ilinca; J. Perron, *Renew. Sust. Energ. Rev.* 12 (2008) 1221-1250.
- [6] G. Wang; L. Zhang; J. Zhang, *Chem. Soc. Rev.* 41 (2012) 797-828.
- [7] O. Barbieri; M. Hahn; A. Herzog; R. Kötz, *Carbon* 43 (2005) 1303-1310.
- [8] H.-Q. Li; J.-Y. Luo; X.-F. Zhou; C.-Z. Yu; Y.-Y. Xia, *J. Electrochem. Soc.* 154 (2007) A731-A736.
- [9] C. Niu; E. K. Sichel; R. Hoch; D. Moy; H. Tennent, *Appl. Phys. Lett.* 70 (1997) 1480-1482.
- [10] J. R. Miller; R. Outlaw; B. Holloway, *Science* 329 (2010) 1637-1639.
- [11] P. Simon; Y. Gogotsi, *Nat Mater* 7 (2008) 845-854.



-
- [12] a) H. Shi, *Electrochim. Acta* 41 (1996) 1633-1639; b) M. Endo; T. Maeda; T. Takeda; Y. J. Kim; K. Koshiba; H. Hara; M. S. Dresselhaus, *J. Electrochem. Soc.* 148 (2001) A910-A914.
- [13] C. Largeot; C. Portet; J. Chmiola; P.-L. Taberna; Y. Gogotsi; P. Simon, *J. Am. Chem. Soc.* 130 (2008) 2730-2731.
- [14] J. Huang; B. G. Sumpter; V. Meunier, *Chem. Eur. J.* 14 (2008) 6614-6626.
- [15] B. E. Conway *Electrochemical Supercapacitors: Scientific Fundamentals and Technological Applications*; Kluwer-Academic: N.Y., **1999**.
- [16] V. Augustyn; P. Simon; B. Dunn, *Energy Environ. Sci.* 7 (2014) 1597-1614.
- [17] V. Augustyn; J. Come; M. A. Lowe; J. W. Kim; P. L. Taberna; S. H. Tolbert; H. D. Abruna; P. Simon; B. Dunn, *Nature Materials* 12 (2013) 518-522.
- [18] V. Srinivasan; J. W. Weidner; J. Newman, *J. Electrochem. Soc.* 148 (2001) A969-A980.
- [19] H. Jiang; T. Zhao; C. Li; J. Ma, *J. Mater. Chem.* 21 (2011) 3818-3823.
- [20] B. E. Conway; V. Birss; J. Wojtowicz, *J. Power Sources* 66 (1997) 1-14.
- [21] K. Ghandi, *Green and Sustainable Chem.* 2014 (2014) 44-53.
- [22] Q. Wang; J. Yan; Z. J. Fan, *Energy Environ. Sci.* 9 (2016) 729-762.



- [23] L. Zhang; F. Zhang; X. Yang; K. Leng; Y. Huang; Y. Chen, *Small* 9 (2013) 1342-1347.
- [24] L. Wei; N. Nitta; G. Yushin, *ACS Nano* 7 (2013) 6498-6506.
- [25] Z. Li; Z. W. Xu; H. L. Wang; J. Ding; B. Zahiri; C. M. B. Holt; X. H. Tan; D. Mitlin, *Energy Environ. Sci.* 7 (2014) 1708-1718.
- [26] J. Chmiola; C. Largeot; P.-L. Taberna; P. Simon; Y. Gogotsi, *Science* 328 (2010) 480-483.
- [27] M. Heon; S. Lofland; J. Applegate; R. Nolte; E. Cortes; J. D. Hettinger; P.-L. Taberna; P. Simon; P. Huang; M. Brunet; Y. Gogotsi, *Energy Environ. Sci.* 4 (2011) 135-138.
- [28] M. Q. Zhao; C. E. Ren; Z. Ling; M. R. Lukatskaya; C. Zhang; K. L. Van Aken; M. W. Barsoum; Y. Gogotsi, *Adv. Mater.* 27 (2015) 339-345.
- [29] Z. S. Wu; K. Parvez; X. Feng; K. Mullen, *Nat Commun* 4 (2013) 2487.
- [30] L. Qie; W. M. Chen; H. H. Xu; X. Q. Xiong; Y. Jiang; F. Zou; X. L. Hu; Y. Xin; Z. L. Zhang; Y. H. Huang, *Energy Environ. Sci.* 6 (2013) 2497-2504.
- [31] Y. Yoon; K. Lee; S. Kwon; S. Seo; H. Yoo; S. Kim; Y. Shin; Y. Park; D. Kim; J.-Y. Choi; H. Lee, *ACS Nano* 8 (2014) 4580-4590.
- [32] D. T. Pham; T. H. Lee; D. H. Luong; F. Yao; A. Ghosh; V. T. Le; T. H. Kim; B. Li; J. Chang; Y. H. Lee, *ACS Nano* 9 (2015) 2018-2027.



- [33] L. Hao; B. Luo; X. Li; M. Jin; Y. Fang; Z. Tang; Y. Jia; M. Liang; A. Thomas; J. Yang; L. Zhi, *Energy Environ. Sci.* 5 (2012) 9747-9751.
- [34] L.-F. Chen; X.-D. Zhang; H.-W. Liang; M. Kong; Q.-F. Guan; P. Chen; Z.-Y. Wu; S.-H. Yu, *ACS Nano* 6 (2012) 7092-7102.
- [35] L. Pan; G. Yu; D. Zhai; H. R. Lee; W. Zhao; N. Liu; H. Wang; B. C.-K. Tee; Y. Shi; Y. Cui; Z. Bao, *Proc. Natl. Acad. Sci.* 109 (2012) 9287-9292.
- [36] J. Huang; K. Wang; Z. Wei, *J. Mater. Chem.* 20 (2010) 1117-1121.
- [37] Z. H. Huang; Y. Song; X. X. Xu; X. X. Liu, *ACS Appl. Mater. Interfaces* 7 (2015) 25506-25513.
- [38] J. W. Long; K. E. Swider; C. I. Merzbacher; D. R. Rolison, *Langmuir* 15 (1999) 780-785.
- [39] V. D. Patake; S. M. Pawar; V. R. Shinde; T. P. Gujar; C. D. Lokhande, *Curr. Appl. Phys.* 10 (2010) 99-103.
- [40] H. B. Li; M. H. Yu; F. X. Wang; P. Liu; Y. Liang; J. Xiao; C. X. Wang; Y. X. Tong; G. W. Yang, *Nat Commun* 4 (2013) 1894.
- [41] B. Wang; J. S. Chen; Z. Y. Wang; S. Madhavi; X. W. Lou, *Adv Energy Mater* 2 (2012) 1188-1192.
- [42] A. K. Singh; D. Sarkar; G. G. Khan; K. Mandal, *ACS Appl. Mater. Interfaces* 6 (2014) 4684-4692.



- [43] Y. Yang; L. Li; G. Ruan; H. Fei; C. Xiang; X. Fan; J. M. Tour, *ACS Nano* 8 (2014) 9622-9628.
- [44] Y. J. Zhang; C. T. Sun; P. Lu; K. Y. Li; S. Y. Song; D. F. Xue, *CrystEngComm* 14 (2012) 5892-5897.
- [45] F. Li; Y. Xing; M. Huang; K. L. Li; T. T. Yu; Y. X. Zhang; D. Losic, *J. Mater. Chem. A* 3 (2015) 7855-7861.
- [46] C. Wei; H. Pang; B. Zhang; Q. Lu; S. Liang; F. Gao, *Science Report* 3 (2013) 2193.
- [47] D. Quyet Huu; Z. Changchun; Z. Chuck; W. Ben; Z. Jim, *Nanotechnology* 22 (2011) 365402.
- [48] H. Y. Lee; J. B. Goodenough, *J. Solid State Chem.* 148 (1999) 81-84.
- [49] C. Z. Yuan; L. Yang; L. R. Hou; L. F. Shen; X. G. Zhang; X. W. Lou, *Energy Environ. Sci.* 5 (2012) 7883-7887.
- [50] Y. Xiao; S. Liu; F. Li; A. Zhang; J. Zhao; S. Fang; D. Jia, *Adv. Funct. Mater.* 22 (2012) 4052-4059.
- [51] C. Mondal; M. Ganguly; P. K. Manna; S. M. Yusuf; T. Pal, *Langmuir* 29 (2013) 9179-9187.



- [52] a) R. K. Sharma; A. C. Rastogi; S. B. Desu, *Electrochim. Acta* 53 (2008) 7690-7695; b) X. Xia; Q. Hao; W. Lei; W. Wang; D. Sun; X. Wang, *J. Mater. Chem.* 22 (2012) 16844-16850.
- [53] a) H. Chen; L. Hu; M. Chen; Y. Yan; L. Wu, *Adv. Funct. Mater.* 24 (2014) 934-942; b) X. Liu; R. Ma; Y. Bando; T. Sasaki, *Adv. Mater.* 24 (2012) 2148-2153; c) L. Yu; G. Zhang; C. Yuan; X. W. Lou, *Chem. Commun. (Camb.)* 49 (2013) 137-139.
- [54] Z. Lu; Z. Chang; W. Zhu; X. Sun, *Chem. Commun.* 47 (2011) 9651-9653.
- [55] D. Su; H.-S. Kim; W.-S. Kim; G. Wang, *Chem. Eur. J.* 18 (2012) 8224-8229.
- [56] Y. F. Yuan; X. H. Xia; J. B. Wu; J. L. Yang; Y. B. Chen; S. Y. Guo, *Electrochim. Acta* 56 (2011) 2627-2632.
- [57] G. H. A. Therese; P. V. Kamath, *Chem. Mater.* 12 (2000) 1195-1204.
- [58] G. R. Li; H. Xu; X. F. Lu; J. X. Feng; Y. X. Tong; C. Y. Su, *Nanoscale* 5 (2013) 4056-4069.
- [59] A. J. Bard; L. R. Faulkner *Electrochemical Methods: Fundamentals and Applications*; Wiley, **2000**. pp. 23.
- [60] G. G. Zhang; W. F. Li; K. Y. Xie; F. Yu; H. T. Huang, *Adv. Funct. Mater.* 23 (2013) 3675-3681.



-
- [61] M. Jin; G. Zhang; F. Yu; W. Li; W. Lu; H. Huang, *Phys. Chem. Chem. Phys.* 15 (2013) 1601-1605.
- [62] G.-W. Yang; C.-L. Xu; H.-L. Li, *Chem. Commun.* (2008) 6537-6539.
- [63] G. Fu; Z. Hu; L. Xie; X. Jin; Y. Xie; Y. Wang; Z. Zhang; Y. Yang; H. Wu, *Int. J. Electrochem. Sci.* 4 (2009) 1052-1062.
- [64] L. Huang; D. Chen; Y. Ding; S. Feng; Z. L. Wang; M. Liu, *Nano Lett.* 13 (2013) 3135-3139.
- [65] C. Yao; T. J. Webster, *J. Nanosci. Nanotechnol.* 6 (2006) 2682-2692.
- [66] Z. Xie; D. Blackwood, *Electrochim. Acta* 56 (2010) 905-912.
- [67] a) M. Paulose; K. Shankar; S. Yoriya; H. E. Prakasam; O. K. Varghese; G. K. Mor; T. A. Latempa; A. Fitzgerald; C. A. Grimes, *J. Phys. Chem. B* 110 (2006) 16179-16184; b) H. Tsuchiya; P. Schmuki, *Electrochem. Commun.* 7 (2005) 49-52; c) I. Sieber; H. Hildebrand; A. Friedrich; P. Schmuki, *Electrochem. Commun.* 7 (2005) 97-100; d) V. P. Parkhutik; V. I. Shershulsky, *J. Phys. D: Appl. Phys.* 25 (1992) 1258.
- [68] G. K. Mor; O. K. Varghese; M. Paulose; K. Shankar; C. A. Grimes, *Sol. Energy Mater. Sol. Cells* 90 (2006) 2011-2075.



- [69] a) I. Sheft; H. H. Hyman; J. J. Katz, *J. Am. Chem. Soc.* 75 (1953) 5221-5223;
b) B. A. Lange; H. M. Haendler, *J. Inorg. Nucl. Chem.* 35 (1973) 3129-3133; c) N. K. Allam; C. A. Grimes, *J. Phys. Chem. C* 111 (2007) 13028-13032.
- [70] C. A. Melendres; S. Xu, *J. Electrochem. Soc.* 131 (1984) 2239-2243.
- [71] N. K. Allam; C. A. Grimes, *Mater. Lett.* 65 (2011) 1949-1955.
- [72] M. R. Sturgeon; P. Lai; M. Z. Hu, *J. Mater. Res.* 26 (2011) 2612-2623.
- [73] L. J. Deng; J. F. Wang; G. Zhu; L. P. Kang; Z. P. Hao; Z. B. Lei; Z. P. Yang; Z. H. Liu, *J. Power Sources* 248 (2014) 407-415.
- [74] A. D. Pauric; S. A. Baig; A. N. Pantaleo; Y. Wang; P. Kruse, *J. Electrochem. Soc.* 160 (2013) C12-C18.
- [75] S. Minagar; C. C. Berndt; J. Wang; E. Ivanova; C. Wen, *Acta Biomater.* 8 (2012) 2875-2888.
- [76] N. K. Allam; K. Shankar; C. A. Grimes, *J. Mater. Chem.* 18 (2008) 2341-2348.
- [77] a) N. K. Allam; X. J. Feng; C. A. Grimes, *Chem. Mater.* 20 (2008) 6477-6481;
b) N. K. Allam; F. Alamgir; M. A. El-Sayed, *ACS Nano* 4 (2010) 5819-5826.
- [78] a) T.-H. Fang; K.-J. Chen, *Mater. Trans.* 48 (2007) 471-475; b) E. M. Yu; V. P. Parkhutik; J. M. Martinez-Duart; J. M. Albella, *J. Phys. D: Appl. Phys.* 27 (1994) 661-669.



- [79] J. M. Macak; H. Tsuchiya; A. Ghicov; K. Yasuda; R. Hahn; S. Bauer; P. Schmuki, *Curr. Opin. Solid State Mater. Sci.* 11 (2007) 3-18.
- [80] a) B. MacDougall; M. Cohen, *J. Electrochem. Soc.* 123 (1976) 191-197; b) B. MacDougall; M. Cohen, *J. Electrochem. Soc.* 121 (1974) 1152-1159.
- [81] T. Gao; B. P. Jelle, *J. Phys. Chem. C* 117 (2013) 17294-17302.
- [82] H. Bode; K. Dehmelt; J. Witte, *Electrochim. Acta* 11 (1966) 1079-1087.
- [83] Y. L. Lo; B. J. Hwang, *Langmuir* 14 (1998) 944-950.
- [84] D. S. Hall; D. J. Lockwood; C. Bock; B. R. MacDougall, *Proc Math Phys Eng Sci* 471 (2015) 20140792.
- [85] J. Cheng; G.-P. Cao; Y.-S. Yang, *J. Power Sources* 159 (2006) 734-741.
- [86] a) L. F. Shen; J. Wang; G. Y. Xu; H. S. Li; H. Dou; X. G. Zhang, *Adv Energy Mater* 5 (2015) ; b) A. Pramanik; S. Maiti; S. Mahanty, *Dalton Trans.* (2015) ; c) S. Peng; L. Li; H. B. Wu; S. Madhavi; X. W. D. Lou, *Adv Energy Mater* 5 (2015) 1401172-1401178; d) L. J. Li; J. Xu; J. L. Lei; J. Zhang; F. McLarnon; Z. D. Wei; N. B. Li; F. S. Pan, *J. Mater. Chem. A* 3 (2015) 1953-1960.
- [87] T. Pauporté; A. Goux; A. Kahn-Harari; N. De Tacconi; C. Chenthamarakshan; K. Rajeshwar; D. Lincot, *J. Phys. Chem. Solids* 64 (2003) 1737-1742.



- [88] a) R. C. V. Piatti; A. J. Arvía; J. J. Podestá, *Electrochim. Acta* 14 (1969) 541-560; b) M. Murthy; G. S. Nagarajan; J. W. Weidner; J. W. Van Zee, *J. Electrochem. Soc.* 143 (1996) 2319-2327.
- [89] A. K. N. Reddy, *J. Electroanal. Chem.* 6 (1963) 141-152.
- [90] J. Macheras; D. Vouros; C. Kollia; N. Spyrellis, *Trans. Inst. Met. Finish.* 74 (1996) 55-58.
- [91] L. P. Bicelli; B. Bozzini; C. Mele; L. D'Urzo, *Int. J. Electrochem. Sci.* 3 (2008) 356-408.
- [92] M. Y. Abyaneh; M. Fleischmann, *J. Electroanal. Chem. Interfacial. Electrochem.* 119 (1981) 187-195.
- [93] G. Zhang; T. Wang; X. Yu; H. Zhang; H. Duan; B. Lu, *Nano Energy* 2 (2013) 586-594.
- [94] L. Li; X. Zhang; G. Wu; X. Peng; K. Huo; P. K. Chu, *Adv. Mater. Interfaces* 2 (2015) n/a-n/a.
- [95] A. K. Singh; D. Sarkar; G. G. Khan; K. Mandal, *J. Mater. Chem. A* 1 (2013) 12759-12767.
- [96] J. Maier *Physical Chemistry of Ionic Materials: Ions and Electrons in Solids*; John Wiley & Sons, **2004**.
- [97] P. Knauth; H. Tuller, *J. Appl. Phys.* 85 (1999) 897-902.



- [98] J. Maier, *Prog. Solid State Chem.* 23 (1995) 171-263.
- [99] J. Maier, *Nature Materials* 4 (2005) 805-815.
- [100] F. Vacandio; M. Eyraud; P. Knauth; T. Djenizian, *Electrochem. Commun.* 13 (2011) 1060-1062.
- [101] L. Yang; L. Qian; X. Tian; J. Li; J. Dai; Y. Guo; D. Xiao, *Chem. Asian J.* 9 (2014) 1579-1585.
- [102] a) C. Johnston; P. Graves, *Appl. Spectrosc.* 44 (1990) 105-115; b) K.-W. Nam; K.-B. Kim, *J. Electrochem. Soc.* 149 (2002) A346-A354.
- [103] A. F. Carley; S. D. Jackson; J. N. O'Shea; M. W. Roberts, *Surf. Sci.* 440 (1999) L868-L874.
- [104] V. Srinivasan; J. W. Weidner, *J. Electrochem. Soc.* 144 (1997) L210-L213.
- [105] a) H. B. Li; M. H. Yu; F. X. Wang; P. Liu; Y. Liang; J. Xiao; C. X. Wang; Y. X. Tong; G. W. Yang, *Nat Commun* 4 (2013) 1894-1900; b) B. Wang; J. S. Chen; Z. Wang; S. Madhavi; X. W. Lou, *Adv Energy Mater* 2 (2012) 1188-1192; c) H. B. Li; Y. Q. Gao; C. X. Wang; G. W. Yang, *Adv. Energy Mater.* 5 (2015) 1401767-1401775.
- [106] P. V. Kamath; M. Dixit; L. Indira; A. Shukla; V. G. Kumar; N. Munichandraiah, *J. Electrochem. Soc.* 141 (1994) 2956-2959.
- [107] S. Ci; Z. Wen; Y. Qian; S. Mao; S. Cui; J. Chen, *Sci. Rep.* 5 (2015) 11919.



- [108] H. Jiang; C. Li; T. Sun; J. Ma, *Chem. Commun.* 48 (2012) 2606-2608.
- [109] B. Zhao; J. Song; P. Liu; W. Xu; T. Fang; Z. Jiao; H. Zhang; Y. Jiang, *J. Mater. Chem.* 21 (2011) 18792-18798.
- [110] Z. Lu; Q. Yang; W. Zhu; Z. Chang; J. Liu; X. Sun; D. Evans; X. Duan, *Nano Res* 5 (2012) 369-378.
- [111] C. Wei; H. Pang; C. Cheng; J. Zhao; P. Li; Y. Zhang, *CrystEngComm* 16 (2014) 4169-4175.
- [112] Y. Zhu; W. Chu; N. Wang; T. Lin; W. Yang; J. Wen; X. S. Zhao, *RSC Advances* 5 (2015) 77958-77964.
- [113] a) N. Liu; J. Li; W. Ma; W. Liu; Y. Shi; J. Tao; X. Zhang; J. Su; L. Li; Y. Gao, *ACS Appl. Mater. Interfaces* 6 (2014) 13627-13634; b) H. Wu; M. Xu; H. Wu; J. Xu; Y. Wang; Z. Peng; G. Zheng, *J. Mater. Chem.* 22 (2012) 19821-19825.
- [114] C. Shang; S. Dong; S. Wang; D. Xiao; P. Han; X. Wang; L. Gu; G. Cui, *ACS Nano* 7 (2013) 5430-5436.
- [115] a) J.-C. Chen; C.-T. Hsu; C.-C. Hu, *J. Power Sources* 253 (2014) 205-213; b) M.-S. Wu; Y.-A. Huang; C.-H. Yang, *J. Electrochem. Soc.* 155 (2008) A798-A805.
- [116] H. Wang; H. S. Casalongue; Y. Liang; H. Dai, *J. Am. Chem. Soc.* 132 (2010) 7472-7477.



- [117] C. H. Lien; C. C. Hu; Y. D. Tsai; D. S. H. Wang, *J. Electrochem. Soc.* 159 (2012) D260-D264.
- [118] a) Z. Pi; T. Tian; X. Tian; C. Yang; S. Zhang; J. Zheng, *J. Nanosci. Nanotechnol.* 7 (2007) 673-676; b) X. Xia; J. Tu; Y. Zhang; X. Wang; C. Gu; X. B. Zhao; H. J. Fan, *ACS Nano* 6 (2012) 5531-5538.
- [119] a) A. N. Mansour, *Surf. Sci. Spectra* 3 (1994) 231-238; b) J. A. Schreifels; P. C. Maybury; W. E. Swartz Jr, *J. Catal.* 65 (1980) 195-206.
- [120] D. Chadwick; T. Hashemi, *Corros. Sci.* 18 (1978) 39-51.
- [121] W. T. Becker; R. J. Shipley *Failure analysis and prevention*; ASM International: UC, CA, USA, **2002**. pp. 1094.
- [122] a) A. N. Mansour, *Surf. Sci. Spectra* 3 (1994) 221-230; b) M. H. Yu; W. Wang; C. Li; T. Zhai; X. H. Lu; Y. X. Tong, *NPG Asia Mater.* 6 (2014) e129-e136.
- [123] E. Westsson; G. J. Koper, *Catalysts* 4 (2014) 375-396.
- [124] a) N. Mironova-Ulmane; A. Kuzmin; I. Steins; J. Grabis; I. Sildos; M. Pärss, *Journal of Physics: Conference Series* 93 (2007) 012039; b) A. C. Gandhi; C. Y. Huang; C. C. Yang; T. S. Chan; C. L. Cheng; Y. R. Ma; S. Y. Wu, *Nanoscale Research Letters* 6 (2011) 485.



- [125] a) Z. Tang; C. H. Tang; H. Gong, *Adv. Funct. Mater.* 22 (2012) 1272-1278;
b) P. Lin; Q. J. She; B. L. Hong; X. A. J. Liu; Y. N. Shi; Z. Shi; M. S. Zheng; Q. F. Dong, *J. Electrochem. Soc.* 157 (2010) A818-A823.
- [126] M. Yang; H. Cheng; Y. Gu; Z. Sun; J. Hu; L. Cao; F. Lv; M. Li; W. Wang; Z. Wang; S. Wu; H. Liu; Z. Lu, *Nano Res.* 8 (2015) 2744-2754.
- [127] K. Xu; R. Zou; W. Li; Y. Xue; G. Song; Q. Liu; X. Liu; J. Hu, *J. Mater. Chem. A* 1 (2013) 9107-9113.
- [128] X. Ma; Y. Li; Z. Wen; F. Gao; C. Liang; R. Che, *ACS Appl. Mater. Interfaces* 7 (2015) 974-979.
- [129] Q. Li; C.-L. Liang; X.-F. Lu; Y.-X. Tong; G.-R. Li, *J. Mater. Chem. A* 3 (2015) 6432-6439.
- [130] S. Bag; C. R. Raj, *J. Mater. Chem. A* 2 (2014) 17848-17856.
- [131] X. Cao; Y. Shi; W. Shi; G. Lu; X. Huang; Q. Yan; Q. Zhang; H. Zhang, *Small* 7 (2011) 3163-3168.
- [132] a) D.-B. Kuang; B.-X. Lei; Y.-P. Pan; X.-Y. Yu; C.-Y. Su, *J. Phys. Chem. C* 113 (2009) 5508-5513; b) M. Wehrens-Dijksma; P. H. L. Notten, *Electrochim. Acta* 51 (2006) 3609-3621.
- [133] X. Dai; D. Chen; H. Q. Fan; Y. Zhong; L. Chang; H. B. Shao; J. M. Wang; J. Q. Zhang; C. N. Cao, *Electrochim. Acta* 154 (2015) 128-135.



- [134] a) S. Chen; J. Duan; Y. Tang; S. Zhang Qiao, *Chemistry* 19 (2013) 7118-7124; b) H. Chen; L. F. Hu; Y. Yan; R. C. Che; M. Chen; L. M. Wu, *Adv Energy Mater* 3 (2013) 1636-1646.
- [135] C. Johnston; P. Graves, *Appl. Spectrosc.* 44 (1990) 105-115.
- [136] W. Z. Wang; Y. K. Liu; C. K. Xu; C. L. Zheng; G. H. Wang, *Chem. Phys. Lett.* 362 (2002) 119-122.
- [137] C. C. Hu; J. C. Chen; K. H. Chang, *J. Power Sources* 221 (2013) 128-133.
- [138] A. K. N. Reddy; S. K. Rajagopalan, *J. Electroanal. Chem.* 6 (1963) 153-158.
- [139] I. Epelboin; M. Jousselein; R. Wiart, *J. Electroanal. Chem.* 119 (1981) 61-71.
- [140] a) J. Barton; J. M. Bockris, *Proceedings of the Royal Society of London. Series A.* 268 (1962) 485-505; b) J. K. Kawasaki; C. B. Arnold, *Nano Lett.* 11 (2011) 781-785.
- [141] a) K. Zhuo; M. G. Jeong; C. H. Chung, *RSC Advances* 3 (2013) 12611-12615; b) S. Eugénio; T. M. Silva; M. J. Carmezim; R. G. Duarte; M. F. Montemor, *J. Appl. Electrochem.* 44 (2013) 455-465.
- [142] A. K. N. Reddy; S. R. Rajagopalan, *J. Electroanal. Chem.* 6 (1963) 159-163.
- [143] a) H. J. You; F. Chen; S. C. Yang; Z. M. Yang; B. J. Ding; S. H. Liang; X. P. Song, *Crystal Growth & Design* 11 (2011) 5449-5456; b) S. H. Ahn; S. J. Hwang;



S. J. Yoo; I. Choi; H. J. Kim; J. H. Jang; S. W. Nam; T. H. Lim; T. Lim; S. K. Kim; J. J. Kim, *J. Mater. Chem.* 22 (2012) 15153-15159.

[144] a) Y. D. Gamburg; G. Zangari *Theory and Practice of Metal Electrodeposition*; Springer, **2011**; b) L.-P. Zhu; H.-M. Xiao; W.-D. Zhang; Y. Yang; S.-Y. Fu, *Crystal Growth & Design* 8 (2008) 1113-1118; c) L. D. Rafailović; D. M. Minić, *Hem. ind* 63 (2009) 557-569; d) M. E. Glicksman; A. O. Lupulescu, *J. Cryst. Growth* 264 (2004) 541-549.

[145] M. H. Yu; W. Wang; C. Li; T. Zhai; X. H. Lu; Y. X. Tong, *Npg Asia Mater* 6 (2014) e129.

[146] J. Yan; Z. Fan; W. Sun; G. Ning; T. Wei; Q. Zhang; R. Zhang; L. Zhi; F. Wei, *Adv. Funct. Mater.* 22 (2012) 2632-2641.

[147] A. K. Singh; D. Sarkar; G. G. Khan; K. Mandal, *ACS Appl. Mater. Interfaces* 6 (2014) 4684-4692.

[148] A. Izadi-Najafabadi; D. N. Futaba; S. Iijima; K. Hata, *J. Am. Chem. Soc.* 132 (2010) 18017-18019.

[149] X.-F. Lu; J. Lin; Z.-X. Huang; G.-R. Li, *Electrochim. Acta* 161 (2015) 236-244.

[150] Z. Yin; S. Wu; X. Zhou; X. Huang; Q. Zhang; F. Boey; H. Zhang, *Small* 6 (2010) 307-312.



- [151] W. Yan; D. Wang; G. G. Botte, *Electrochim. Acta* 61 (2012) 25-30.
- [152] H. Chen; L. Hu; M. Chen; Y. Yan; L. Wu, *Adv. Funct. Mater.* 24 (2014) 934-942.
- [153] a) M. A. Sayeed; T. Herd; A. P. O'Mullane, *J. Mater. Chem. A* 4 (2016) 991-999; b) J. Yang; H. Liu; W. N. Martens; R. L. Frost, *J. Phys. Chem. C* 114 (2010) 111-119.
- [154] S. Deabate; F. Fourgeot; F. Henn, *J. Power Sources* 87 (2000) 125-136.
- [155] C. Zhang; J. Zhao; L. Zhou; Z. Li; M. Shao; M. Wei, *J. Mater. Chem. A* 4 (2016) 11516-11523.
- [156] B. Santara; B. Pal; P. K. Giri, *J. Appl. Phys.* 110 (2011) 114322.
- [157] O. Bøckman; T. Østvold; G. A. Voyiatzis; G. N. Papatheodorou, *Hydrometallurgy* 55 (2000) 93-105.
- [158] H. B. Li; M. H. Yu; X. H. Lu; P. Liu; Y. Liang; J. Xiao; Y. X. Tong; G. W. Yang, *ACS Appl. Mater. Interfaces* 6 (2014) 745-749.
- [159] X.-F. Lu; D.-J. Wu; R.-Z. Li; Q. Li; S.-H. Ye; Y.-X. Tong; G.-R. Li, *J. Mater. Chem. A* 2 (2014) 4706-4713.
- [160] Y. Zhao; L. Hu; S. Zhao; L. Wu, *Adv. Funct. Mater.* 26 (2016) 4038-4038.
- [161] C. Ma; Y. Li; J. Shi; Y. Song; L. Liu, *Chem. Eng. J.* 249 (2014) 216-225.



- [162] V. Barranco; M. A. Lillo-Rodenas; A. Linares-Solano; A. Oya; F. Pico; J. Ibañez; F. Agullo-Rueda; J. M. Amarilla; J. M. Rojo, *J. Phys. Chem. C* 114 (2010) 10302-10307.
- [163] a) X. Zheng; Z. Gu; Q. Hu; B. Geng; X. Zhang, *RSC Advances* 5 (2015) 17007-17013; b) R. R. Salunkhe; K. Jang; S.-w. Lee; H. Ahn, *RSC Advances* 2 (2012) 3190-3193.
- [164] Y. Cheng; H. Zhang; C. V. Varanasi; J. Liu, *Energy Environ. Sci.* 6 (2013) 3314-3321.
- [165] a) V. Gupta; S. Gupta; N. Miura, *J. Power Sources* 175 (2008) 680-685; b) R. D. Armstrong; E. A. Charles, *J. Power Sources* 25 (1989) 89-97.
- [166] H. B. Wu; H. Pang; X. W. Lou, *Energy Environ. Sci.* 6 (2013) 3619-3626.
- [167] Y. Zhao; L. Hu; S. Zhao; L. Wu, *Adv. Funct. Mater.* 26 (2016) 4085-4093.
- [168] J. Wu; P. Guo; R. Mi; X. Liu; H. Zhang; J. Mei; H. Liu; W.-M. Lau; L.-M. Liu, *J. Mater. Chem. A* 3 (2015) 15331-15338.
- [169] G. Li; W. Li; K. Xu; R. Zou; Z. Chen; J. Hu, *J. Mater. Chem. A* 2 (2014) 7738-7741.
- [170] a) X. Dong; Z. Guo; Y. Song; M. Hou; J. Wang; Y. Wang; Y. Xia, *Adv. Funct. Mater.* 24 (2014) 3405-3412; b) J. Yan; Z. Fan; W. Sun; G. Ning; T. Wei; Q. Zhang; R. Zhang; L. Zhi; F. Wei, *Adv. Funct. Mater.* 22 (2012) 2632-2641.



- [171] L.-F. Chen; Z.-H. Huang; H.-W. Liang; W.-T. Yao; Z.-Y. Yu; S.-H. Yu, *Energy Environ. Sci.* 6 (2013) 3331-3338.
- [172] Y. Liu; B. Weng; J. M. Razal; Q. Xu; C. Zhao; Y. Hou; S. Seyedin; R. Jalili; G. G. Wallace; J. Chen, *Sci. Rep.* 5 (2015) 17045-17055.
- [173] R. K. Gupta; J. Candler; S. Palchoudhury; K. Ramasamy; B. K. Gupta, *Sci. Rep.* 5 (2015) 15265-15275.
- [174] N. Yu; H. Yin; W. Zhang; Y. Liu; Z. Tang; M.-Q. Zhu, *Adv. Energy Mater.* 6 (2016) 1501458-1501466.
- [175] Z. Zhang; F. Xiao; L. Qian; J. Xiao; S. Wang; Y. Liu, *Adv. Energy Mater.* 4 (2014) 1400064-1400072.
- [176] Q. Y. Liao; N. Li; S. X. Jin; G. W. Yang; C. X. Wang, *ACS Nano* 9 (2015) 5310-5317.
- [177] F. Zhang; Y. Lu; X. Yang; L. Zhang; T. Zhang; K. Leng; Y. Wu; Y. Huang; Y. Ma; Y. Chen, *Small* 10 (2014) 2285-2292.
- [178] G. Ma; Z. Wang; B. Gao; T. Ding; Q. Zhong; X. Peng; J. Su; B. Hu; L. Yuan; P. K. Chu; J. Zhou; K. Huo, *J. Mater. Chem. A* 3 (2015) 14617-14624.
- [179] H. H. Xu; X. L. Hu; H. L. Yang; Y. M. Sun; C. C. Hu; Y. H. Huang, *Adv. Energy Mater.* 5 (2015) 1401882-1401888.



- [180] J. X. Feng; S. H. Ye; X. F. Lu; Y. X. Tong; G. R. Li, *ACS Appl. Mater. Interfaces* 7 (2015) 11444-11451.
- [181] L. Liu; Y. Yu; C. Yan; K. Li; Z. Zheng, *Nat. Commun.* 6 (2015) 8260-8268.
- [182] X. Hu; W. Shao; X. Hang; X. Zhang; W. Zhu; Y. Xie, *Angew. Chem.* (2016) n/a-n/a.
- [183] Z. Fan; J. Yan; T. Wei; L. Zhi; G. Ning; T. Li; F. Wei, *Adv. Funct. Mater.* 21 (2011) 2366-2375.
- [184] D. Ghosh; M. Mandal; C. K. Das, *Langmuir* 31 (2015) 7835-7843.
- [185] H. Gao; F. Xiao; C. B. Ching; H. Duan, *ACS Appl. Mater. Interfaces* 4 (2012) 7020-7026.
- [186] L. Bao; X. Li, *Adv. Mater.* 24 (2012) 3246-3252.
- [187] D. M. MacArthur, *J. Electrochem. Soc.* 117 (1970) 422-426.
- [188] J. L. Weininger; M. W. Breiter, *J. Electrochem. Soc.* 110 (1963) 484-490.
- [189] C. Zhang; S. M. Park, *J. Electrochem. Soc.* 134 (1987) 2966-2970.
- [190] a) M.-m. Chen; X.-b. Xiong; C. Yi; J. Ma; X.-r. Zeng, *J. Inorg. Organomet. Polym. Mater.* 25 (2015) 739-746; b) M. Chiku; M. Toda; E. Higuchi; H. Inoue, *J. Power Sources* 286 (2015) 193-196; c) G. Zhang; L. Wang; Y. Liu; W. Li; F. Yu;



- W. Lu; H. Huang, *J. Mater. Chem. A* (2016) ; d) R. Hang; Y. Liu; L. Zhao; A. Gao; L. Bai; X. Huang; X. Zhang; B. Tang; P. K. Chu, *Sci. Rep.* 4 (2014)
- [191] T. S. Arthur; D. J. Bates; N. Cirigliano; D. C. Johnson; P. Malati; J. M. Mosby; E. Perre; M. T. Rawls; A. L. Prieto; B. Dunn, *MRS Bull.* 36 (2011) 523-531.
- [192] a) M. Islam; N. Zalikha; H. Kosslick; M. T. Zainuddin; Z. A. Zubir; A. A. Nazri; S. Azrolsani; A. Malek; M. Zahid; M. Ezwan *Advanced Materials Research*, 2016; p 527-531; b) Z. Han; W. R. McNamara; M. S. Eum; P. L. Holland; R. Eisenberg, *Angew. Chem. Int. Ed.* 51 (2012) 1667-1670; c) A. Khosravi; F. Bigdeli; M. Yousefi; M. Abdikhani; S. Taheri Otaqsara, *Environ. Prog. Sustain. Energy* 33 (2014) 1194-1200; d) H. N. Kagalwala; E. Gottlieb; G. Li; T. Li; R. Jin; S. Bernhard, *Inorg. Chem.* 52 (2013) 9094-9101; e) M. A. Gross; A. Reynal; J. R. Durrant; E. Reisner, *J. Am. Chem. Soc.* 136 (2013) 356-366; f) H. Lv; W. Guo; K. Wu; Z. Chen; J. Bacsá; D. G. Musaev; Y. V. Geletii; S. M. Lauinger; T. Lian; C. L. Hill, *J. Am. Chem. Soc.* 136 (2014) 14015-14018; g) E. Nurlaela; T. Shinagawa; M. Qureshi; D. S. Dhawale; K. Takanahe, *ACS Catalysis* 6 (2016) 1713-1722; h) Z. Yan; X. Yu; A. Han; P. Xu; P. Du, *The Journal of Physical Chemistry C* 118 (2014) 22896-22903; i) Z. Yan; Z. Sun; X. Liu; H. Jia; P. Du, *Nanoscale* 8 (2016) 4748-4756; j) Y. Zhao; B. Zhao; J. Liu; G. Chen; R. Gao; S. Yao; M. Li; Q. Zhang; L. Gu; J. Xie; X. Wen; L.-Z. Wu; C.-H. Tung; D. Ma; T. Zhang, *Angew. Chem. Int. Ed.* 55 (2016) 4215-4219; k) Z. Zhai; X. Yang; L. Xu; C. Hu; L. Zhang; W. Hou; Y. Fan, *Nanoscale* 4 (2012) 547-556.